APPLIED COMPUTATIONAL ELECTROMAGNETICS SOCIETY JOURNAL

Special Issue on Magnetic Levitation and Bearings 2018

Guest Editors:
Antonino Musolino, Rocco Rizzo, and Luca Sani
DESTEC, University of Pisa, Italy

THE APPLIED COMPUTATIONAL ELECTROMAGNETICS SOCIETY JOURNAL

SPECIAL ISSUE ON MAGENTIC LEVITATION AND BEARIGNS 2018

Numerical Analysis and Preliminary Experimental Validation of a Heteropolar Electrodynamic Bearing

V. Kluyskens [1], B. Dehez [1], C. Dumont, A. Musolino [2], and R. Rizzo [2]

[1] Université Catholique de Louvain, Center for Research in Mechatronics, Louvain, Belgium
{virginie.kluyskens; bruno.dehez}@uclouvain.be

[2] University of Pisa, DESTEC, Department of Energy and Systems Engineering, Italy
{antonino.musolino; rocco.rizzo}@unipi.it

Abstract ─ In this paper we describe the numerical simulations of a Heteropolar Electrodynamic Bearing and compare them with some experimental data taken on a prototype in quasi-static state. The device is composed of a cylindrical permanent magnet rotor and six coils fixed onto the stator. The system has been simulated by means of a dedicated numerical code ("EN4EM" - Electric Network for Electromagnetics), previously developed for research purposes. The software is based on a 3D integral formulation and it is able to numerically simulate coupled multi-degree of freedom electro/mechanical problems. The comparison between computed and measured data are fully satisfactory.

Index Terms ─ Coupled analysis, electrodynamic bearings, integral formulation, permanent magnets.

I. INTRODUCTION

The modern technologies of Magnetic Levitation systems (MAGLEV) allow developing contact-free bearings which are appealing in many technological applications like high-speed drives, high-precision or vacuum devices, and so on [1]. Active magnetic bearings [2] offer great possibilities in terms of control and can achieve high stiffness. Although they operate quite well, some drawbacks, such as the complexity, overall dimensions, and cost of the control system, limit their diffusion. On the other hand, passive magnetic bearings [3], which do not require control system, seem to be a valid alternative. Unfortunately, passive magnetic suspensions suffer from the intrinsic instability (Earnshaw's theorem [4]) and great efforts must be devoted to design reliable stabilization devices.

Passive Electrodynamic Bearings (EDBs) belong to the latter category [5]. The EDBs can be classified into two groups depending on whether the magnetic field produced by the permanent magnets (PM) is homopolar or heteropolar. In these devices the forces that restore the rotor in the equilibrium position arise from currents induced by the relative motion between the permanent magnets and the conductive parts of the bearing. In many cases the null-flux coils can be used in order to achieve a higher energy efficiency [6]. In such kind of configurations, when the rotor is in the equilibrium position, the coils experience no varying magnetic flux and no current flows in the system. On the contrary, if the rotor is not in the equilibrium position the varying magnetic flux produces a non-zero electromotive force and consequently a current flows in the coils. Then, if properly designed, a restoring force can be obtained, allowing the rotor to come back to its equilibrium position. To properly design null flux centering heteropolar EDB, guidelines are given in [6]: the identity $q = p \pm 1$ has to be respected, where q and p are the number of pole pairs of the winding and permanent magnets, respectively.

In order to design passive magnetic bearings and to investigate their performance, many analytical and numerical models have been developed [7]–[12].

However, they have some limitations especially when dealing with the dynamic operation of electro-mechanical systems, under six degree of freedom (DOF). Also the application of the finite-element method (FEM) to systems with moving conductors presents some difficulties, mainly due to the coupling of meshes attached to bodies in relative motion [13]. They usually require a large number of unknowns to obtain a desired accuracy in multi-degree of freedom problems [14]. Moreover, the meshes and consequently the matrices involved in the calculations have to be updated during the motion and the analysis of unbounded domains requires special treatments [15].

In this paper an alternative approach is used to develop a numerical model capable to investigate the complex operation of passive magnetic bearings. This approach is based on an integral formulation [16] in which the problem of coupling moving meshes does not arise since only the discretization of the active regions is required. However, the integral formulations also present some limitations, usually related to the numerical

solution of the model. In fact, the main drawbacks are the matrix setup time and matrix solution time. The paper is organized as follows: the proposed device, and the numerical formulation are described in Sections II and III. Section IV briefly describes the test bench, while Section V discusses the comparison between the computed and the experimental data.

II. PROPOSED DEVICE

The Heteropolar Electrodynamic Bearing under investigation with the main dimensions is shown in Figs. 1 and 2.

The main characteristics of the device are:

- The rotor is a 1 pole pair annular NdFeB magnet, with diametrical magnetization and remanence Br=1.3 T.
- The stator is composed of a 3-phase system with 2 pole pairs. Each phase is made of series connection of 2 coils, in the way that when the rotor is perfectly centered the induced electromotive force (EMF) is zero, respecting criteria given in [6]. Each coil has 560 turns of 0.2 mm copper wire. There is no ferromagnetic yoke behind the coils.
- The nominal airgap when the rotor is centered is 4 mm.

The analysis of the system requires the use of numerical models able to simulate coupled electro/mechanical problems with up to six degree of freedom (6 DOF).

III. THE NUMERICAL FORMULATION

The device has been analyzed by means a numerical code ("EN4EM" - Electric Network for Electromagnetics), previously developed for research purposes [17]. It is based on a 3D integral formulation that reduces the diffusion equation to an equivalent network with time varying parameters. The values of the parameters in the electrical equations are function of the position of the rotor. The equations describing the rotor dynamics with 6 DOF are inherently nonlinear because of the dependence of the force on the position of the rotor itself.
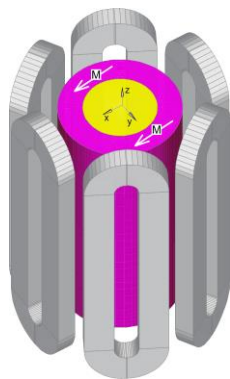
Fig. 1. A 3D view of the analyzed device.

Stator:	Rotor:
q = 2 pole pairs, 3 phases made of 2 coils of 560 turns of 0,2 mm wire No ferromagnetic yoke	p = 1 pole pair, Annular NdFeB magnet **Magnetic airgap** 4 mm
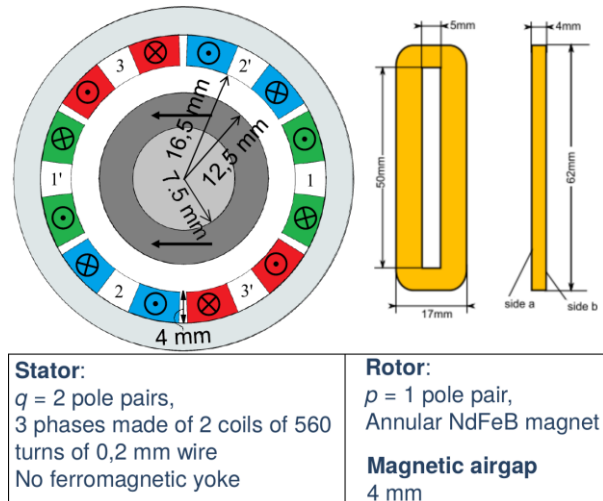
Fig. 2. Cross section and coils dimensions.

Furthermore, the problem of rigid body dynamics is coupled with the diffusion equation of the magnetic field. The main numerical formulation characteristics are: (a) only active (usually conductive) parts of a device must be discretized; (b) coupling with external lumped circuits is straightforward. The main drawbacks, instead, are the matrix setup time and the matrix solution time. These matrices are densely populated, and this may require (relatively) long computational times to get the solution. Anyhow, since this formulation is highly parallelizable, recent improvements in multicore CPUs or GPUs, allows to reduce the computation time.

The details of the adopted formulation and the development of a C-code exploiting the GPGPU Nvidia CUDA libraries is extensively described in [17].

Figure 3 shows the mesh used by the EN4EM numerical code to simulate the Heteropolar Electro-dynamic Bearing. The whole system has been discretized with 500 elementary volumes and the time to simulate the system at a fixed out-centered position and at a given angular speed was about 120 s.
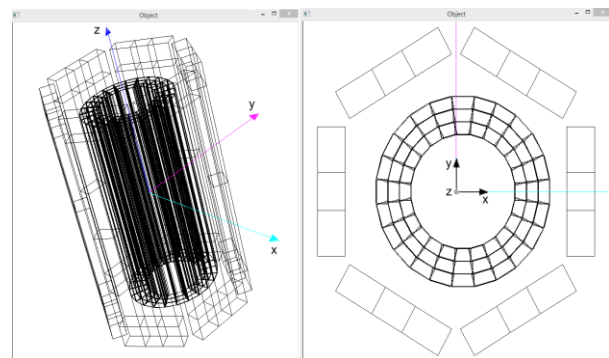
Fig. 3. The mesh used by the numerical code EN4EM to simulate the device.
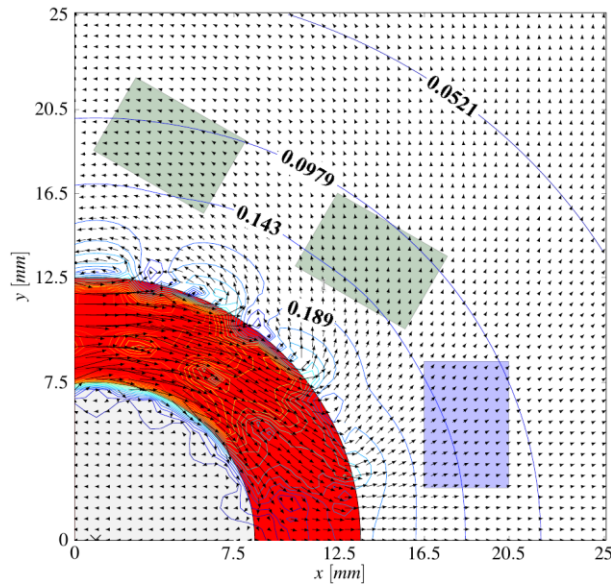
Fig. 4. The magnetic flux density B vectors in the system (dx=1 mm), produced only by the PM.
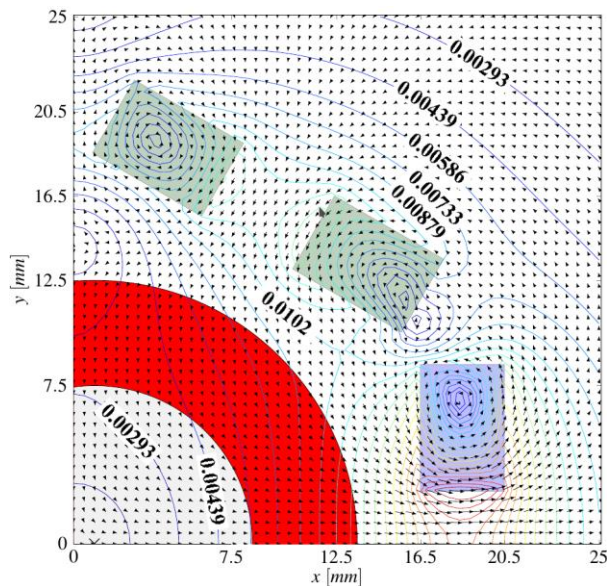
Fig. 5. The magnetic flux density B vectors in the system (dx=1 mm), produced only by the currents induced in the coils when the rotor spins at 7200 rpm. The currents in the coils are: $i_1=0.096$ A, $i_2=i_3=-0.047$ A. Coils are numbered according to Fig. 2.

As an example of software capabilities, Fig. 4 and 5 show the magnetic flux density vectors in the symmetry plane (z=0) of the system obtained by using the EN4EM code (for the sake of readability only a quarter of the system is shown). Although the code is able to simulate all the 6 DOF, in order to allow the comparison with the experimental results, the rotor has

been constrained in some fixed out-centered positions. Then, several configurations of the device have been simulated by varying the spin speed and the center shift along the x and y directions. Other applications of the codes are reported in [17-20].

IV. THE TEST BENCH

The test bench is designed to operate in quasi-static conditions, i.e., the rotor spins in a fixed out-centered position relatively to the stator. Although the test bench was initially designed to operate up to 60.000 rpm, in order to reduce vibrations it has been used up to 7200 rpm only [21]. The rotor is driven by an external motor. The stator coils are glued inside a plastic structure. This plastic structure is mounted on a xy manual stage, allowing displacing the stator with respect to the rotor with a micrometer precision. The prototype is encased inside an enclosure for safety. The test bench is also equipped with a 6-axis force sensor, measuring the reaction forces on the stator winding. The test bench, with the safety enclosure opened, is represented in Fig. 6.
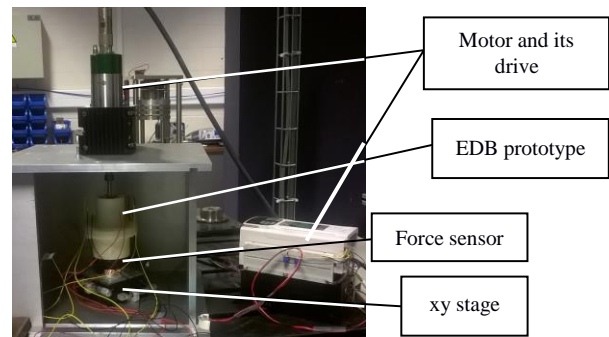
Fig. 6. The test bench.

V. RESULTS

The numerical formulation described in Section 3 has been used to perform the analysis of the described device operating under different conditions.

A first set of simulations has been performed in order to investigate the induced EMF in the open-circuited coils, as a function of spin speed and for different center shifts. Figure 7 shows the comparison between the computed results and the experimental data of the resultant induced EMF at the series connection of coils 1 and 1' (connected with discordant fluxes) as a function of time for a center shift $dx=1$ mm and at a spin speed of 6000 rpm (counterclockwise). The results are fully satisfactory. Figure 8 reports the induced EMF (peak-to-peak) as a function of the center shift dx at the speed of 7200 rpm. The results show that the maximum errors obtained in the comparison with the experimental measurements are below 4%, confirming a good agreement between the simulations and the experimental

data. The computed results for $V_2(dx)$ and $V_3(dx)$ differ from those of $V_1(dx)$ for less than 1% and are not reported in the figure.
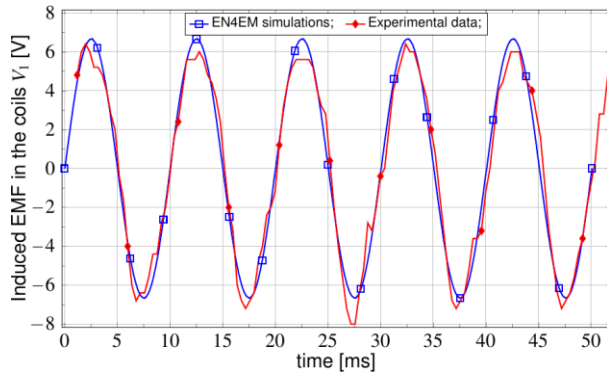
Fig. 7. Induced EMF V_1 in the (open-circuited) coils 1 1' as a function of time (dx=1mm, @6000 rpm).
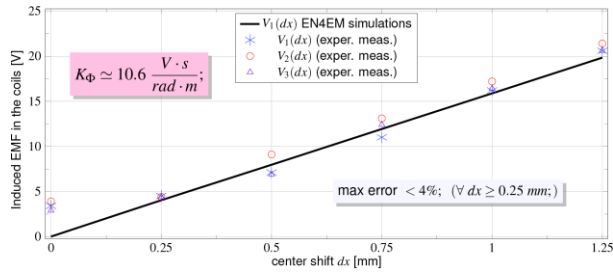
Fig. 8. Induced EMF in the (open-circuited) coils as a function of center shift dx (@7200 rpm).

The induced EMF should be zero when the rotor is centered, referring to the null-flux criterion, and it can be observed in Fig. 8 that it is indeed the case for the numerical model but not for the experimental data. This is due to some asymmetry between the phases, due for instance to their geometric precision, which leads to a magnetic center which is not coincident for each phase. This asymmetry can also been observed on the spreading of the EMF measured for each center shift.

Furthermore, the simulated value of coefficient for the induced EMF is K_ϕ=10.6 [Vs/rad m], with an error of about 9% w.r.t. the measurements.

A second set of simulations has been performed with the windings short-circuited. In this case, the rotor is fixed in some out-centered positions dx=[0; 0.25; 0.50; 0.75; 1.0; 1.25] mm and rotates at different constant spin speeds. Figure 9 shows the time varying currents in the short-circuited windings for a center shift $dx=1$ mm, @ 7200 rpm. Figure 9 confirms the great similarity of the simulation results on each phase announced on the analysis of Fig. 7. Since the rotor spin speed has been kept constant, the transient behavior of the currents

takes into account only the electrical time constant.
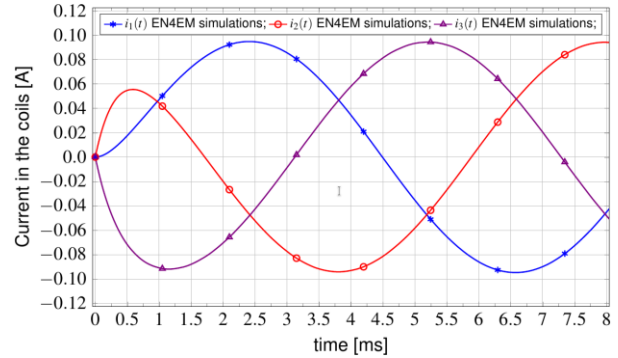
Fig. 9. Currents in the (short-circuited) coils as a function of time (dx=1mm, @7200 rpm).

In particular the reported waveforms are obtained by simultaneously shorting the three windings by closing three switches when the polar axis of the flux density distribution of the PMs on the rotor is aligned with the axis of the coils 1 and 1'. The left part of Fig. 2 shows the position of the rotor with respect to the windings at the moment of closing the switches.

We have not taken experimental measurements of the currents, but the accuracy of the computations can be indirectly assumed by the values of the forces produced by the interaction of these currents with the flux density by the PM as shown by Figs. 10 and 11.

These figures respectively show the centering $F_x(dx)$, $F_y(dy)$ (i.e., the forces acting along the direction of the displacement of the rotor) and perpendicular forces $F_x(dy)$, $F_y(dx)$ as a function of center shift dx or dy. In the same figures the experimental measurements have also been reported. The comparison shows a maximum error of about 5% for the centering force, and an error of about 10% for the perpendicular one, confirming a good agreement between the simulations results and the measurements.
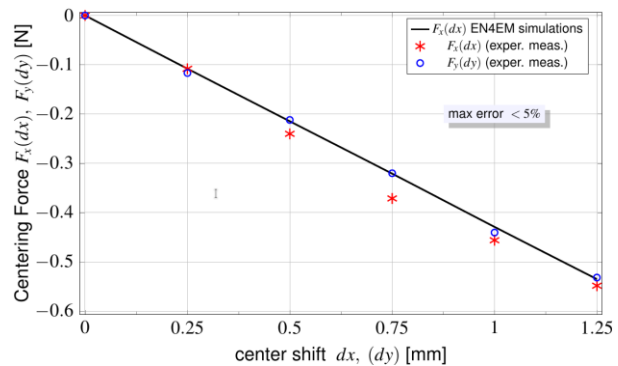
Fig. 10. Centering forces $Fx(dx)$ and $Fy(dy)$ as a function of center shift dx (@7200 rpm).
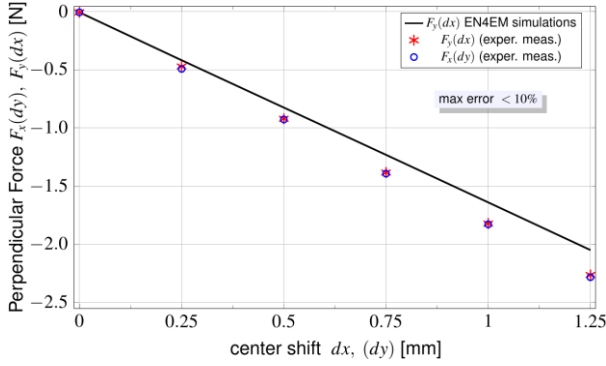
Fig. 11. Perpendicular forces $Fx(dy)$, $Fy(dx)$ as a function of center shift dx (@7200 rpm).

Only one centering and one perpendicular computed forces are reported in the figures, since the others are very close to the reported ones (the differences are less than 1%). During the simulations we noticed that the perpendicular force is very sensitive to the distance between the rotor and the coils. This is due to the profile of the magnetic flux density B produced by the permanent magnet.

Figure 12 shows the profiles of the centering $Fx(dx)$ and perpendicular force $Fy(dx)$ for different center shifts dx as a function of spin speed in the range *[0 - 7200] rpm*.

About the accuracy of the computed data reported in Fig. 12, let us consider Figs. 10 and 11, which report the forces in correspondence of several displacements at the speed of *7200 rpm*. Also Figs. 13 and 14 show the comparison at the displacement of *1.25 mm* for several spin speeds. The agreement between experimental and computed data in the range of displacement and speed as in Fig. 12 is comparable with the ones shown on Figs. 10, 11, 13 and 14, and is fully satisfactory.
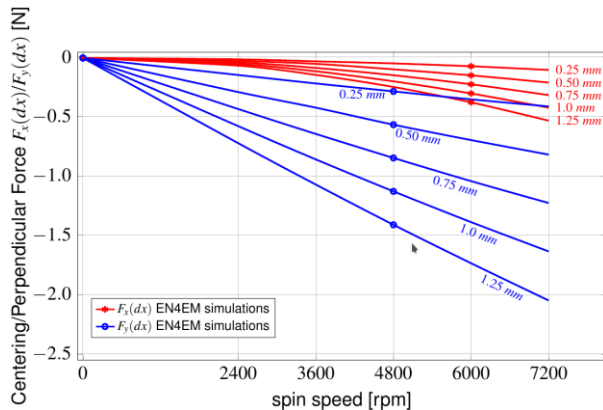
Fig. 12. Centering/perpendicular force $Fx(dx)/Fy(dx)$ as a function of speed at different center shift dx.
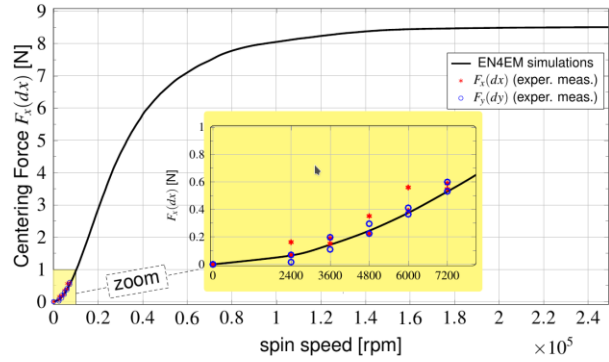
Fig. 13. Centering forces $Fx(dx)$ as a function of the speed (in rpm) and with the center shift *dx = 1.25 mm*.
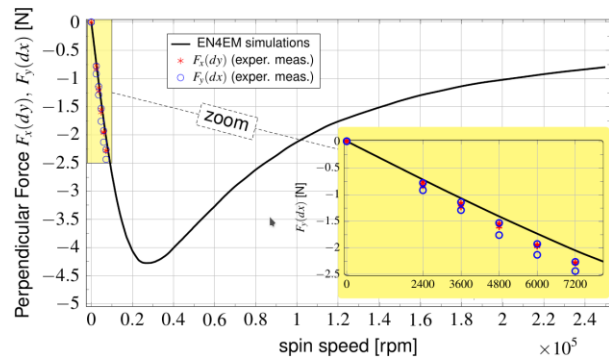
Fig. 14. Perpendicular forces $Fy(dx)$ as a function of the speed (in rpm) and with the center shift *dx = 1.25 mm*.

The same figures also report the comparison with the experimental measurements in the range *[0 - 7200] rpm*, showing a good agreement. It can also be observed on these figures that at the spin speed of 7200 rpm, the parasitic force, perpendicular to the center shift is more important than the restoring force. This is due to the fact that, at that spin speed, the rotor is not spinning fast enough in comparison to the electrical pole. The restoring force becomes more important and the parasitic perpendicular force becomes smaller when the spin speed becomes higher than the electrical pole of the system [7]. For this prototype to be able to work in dynamic conditions, the spin speed should be higher, and additional external damping should also be added [8].

VI. CONCLUSIONS

A numerical analysis of a Heteropolar Electrodynamic Bearing has been presented. The simulations have been performed by the use of a numerical code based on a 3D integral formulation, previously developed at the University of Pisa for research purposes, and

capable to simulate coupled electro/mechanical problems with up to six degree of freedoms. The code shares a number of features of integral formulations, in particular the capability of producing acceptable results with very poor discretizations which require short computation times. For the magnetic bearing under test we used a model with about 500 elementary volumes which was able to produce results in very good agreement with the experimental measurements. The ongoing work is aimed to investigate the behavior of the HEDB taking into account further degrees of freedom during dynamic operation.

ACKNOWLEDGMENT

REFERENCES

[1] G. Schweitzer and E. H. Maslen, *Magnetic Bearings: Theory, Design and Application to Rotating Machinery*. New York, NY, USA: *Springer*, 2009.

[2] A. Looser and J. W. Kolar, "An active magnetic damper concept for stabilization of gas bearings in high-speed permanent-magnet machines," *IEEE Trans. Ind. Electron.*, vol. 61, no. 6, pp. 3089-3098, June 2014.

[3] R. F. Post and D. D. Ryutov, "Ambient-temperature passive magnetic bearings: Theory and design equations," *in Proc. 6th Int. Symp. Magn. Bearings*, pp. 110-122, Aug. 1998.

[4] S. Earnshaw, "On the nature of the molecular forces which regulate the constitution of the luminiferous ether," *Trans. Cambridge Philosoph. Soc.*, vol. 7, pp. 97-112, 1842.

[5] J. G. Detoni, "Progress on electrodynamic passive magnetic bearings for rotor levitation," *Proc. Inst. Mech. Eng. C, J. Mech. Eng. Sci.*, vol. 228, no. 10, pp. 1829-1844, 2014.

[6] C. Dumont, V. Kluyskens, and B. Dehez, "Null-flux radial electrodynamic bearing," *IEEE Trans. Magn.*, vol. 50, no. 10, Oct. 2014.

[7] N. Amati, X. De Lépine, and A. Tonoli, "Modeling of electrodynamic bearings," *J. Vibrat. Acoust.*, vol. 130, no. 6, p. 061007, Oct. 2008.

[8] V. Kluyskens and B. Dehez, "Dynamical electro-mechanical model for magnetic bearings subject to eddy currents," *IEEE Trans. Magn.*, vol. 49, no. 4, pp. 1444-1452, Apr. 2013.

[9] A. V. Filatov and E. H. Maslen, "Passive magnetic bearing for fly-wheel energy storage systems," *IEEE Trans. Magn.*, vol. 37, no. 6, pp. 3913-3924, Nov. 2001.

[10] J. G. Detoni, F. Impinna, A. Tonoli, and N. Amati, "Unified modelling of passive homopolar and heteropolar electrodynamic bearings," *J. Sound Vibrat.*, vol. 331, no. 19, pp. 4219-4232, Sep. 2012.

[11] A. Rahideh and T. Korakianitis, "Analytical open-circuit magnetic field distribution of slotless brushless permanent-magnet machines with rotor eccentricity," *IEEE Trans. Magn.*, vol. 47, no. 12, pp. 4791-4808, Dec. 2011.

[12] A. Tonoli, N. Amati, F. Impinna, J. G. Detoni, H. Bleuler, and J. Sandtner, "Dynamic modeling and experimental validation of axial electrodynamic bearings," in *Proc. of the 12th Int. Symposium on Magnetic Bearings*, p. 68-73, 2011.

[13] B. Davat, Z. Ren, and M. Lajoie-Mazenc, "The movement in field modeling," *IEEE Trans. on Mag.*, vol. 21, no. 6, pp. 2296-2298, Nov. 1985.

[14] A. Bossavit, *Computational Electromagnetism: Variational Formulations, Complementarity, Edge Elements*. Academic Press, 1998.

[15] D. Rodger, H. C. Lai, and P. J. Leonard, "Coupled elements for problems involving movement," *IEEE Trans. on Mag.*, vol. 26, no. 2, pp. 548-550, Mar. 1990.

[16] R. Albanese and G. Rubinacci, "Integral formulation for 3D eddy-current computation using edge elements," *IEEE Proceedings A (Physical Science, Measurement and Instrumentation, Management and Education, Reviews)*, vol. 135, no. 7, pp. 457-462, 1988.

[17] E Tripodi, A Musolino, R Rizzo, and M Raugi, "A new predictor-corrector approach for the numerical integration of coupled electromechanical equations," *Int. J. for Num. Meth. in Eng.*, vol. 105, no. 4 pp. 261-285, 2016.

[18] A. Musolino, R. Rizzo, M. Toni, and E. Tripodi, "Modeling of electromechanical devices by GPU-accelerated integral formulation," *Int. Jour. of Num. Mod. in Electron. Network, Dev. and Field*, vol. 26, pp. 376-396, 2013.

[19] V. Di Dio and L. Sani, "Coupled electromechanical analysis of a permanent-magnet bearing," *ACES Journal*, vol. 32, no. 8, pp. 736-741, Aug. 2017.

[20] M. G. Iachininoto, et al., "Effects of exposure to gradient magnetic fields emitted by nuclear magnetic resonance devices on clonogenic potential and proliferation of human hematopoietic stem cells," *Bioelectromagnetics*, vol. 37, no. 1 pp. 201-211, 2016.

[21] C. Dumont, V. Kluyskens, and B. Dehez, "Design and experimental testing of a heteropolar electro-dynamic bearing," *2nd IEEE Conference on Advances in Magnetics*, LaThuile, Italy, Feb. 2018.

Analysis of Unbalanced Response of Rigid Rotor Supported by AMBs under Coupling Dynamic and Control Methods

Guowei Du [1,2,3], Zhengang Shi [1,2,3], Haoyu Zuo [1,2,3], Lei Zhao [1,2,3], and Zhe Sun*[1,2,3]

[1] Institute of Nuclear and New Energy Technology
[2] Collaborative Innovation Center of Advanced Nuclear Energy Technology
[3] The Key Laboratory of Advanced Reactor Engineering and Safety
dgw13@mails.tsinghua.edu.cn, sun_zhe@mail.tsinghua.edu.cn*

Abstract ─ The main helium circulator is the core component of the High Temperature Reactor (HTR). Mechanical machining errors and assembly errors can cause uneven distribution of rotor mass. When the rotor rotates, the unbalanced mass will generate unbalanced force which will change the rotor's axis trajectory. By coupling the rotor dynamics method and the electromagnetic bearing system control theory, the motion of the rotor is modeled. Three representative unbalanced conditions of the impeller position, the bearing position and the centroid position are assumed to simulate the unbalance response of the rotor, and the influence of changes in the stiffness and damping on the unbalance response of the rotor is analyzed by adjusting the stiffness and the damping of the rotor. The results of the analysis show that the bearings farther from the unbalanced position (UBP) have larger rotor displacements and bearing loads. Increasing Active Magnetic Bearings (AMBs) stiffness and damping will increase the bearing load and reduce the response displacement of the rotor. Therefore, the stiffness and damping of AMBs must be designed by considering the bearing capacity and the displacement limit of the rotor.

Index Terms ─ Active magnetic bearing, bearing stiffness and damping, coupling dynamic and control methods, rigid rotor, unbalance response.

I. MODEL INTRODUCTION

A. The rotor model

The main helium circulator model of the HTR is shown in Fig. 1. The vertical rotor (red part) is supported by two radial electromagnetic bearings (yellow sections). Because the first-order bending frequency of the rotor exceeds the rated rotation speed of the rotor, the rotor is simplified as a rigid rotor and placed in a rectangular coordinate system, as shown in Fig. 2, the dynamic parameters of the rotor are shown in Table 1.

In Fig. 2, The notation x_a represents the rotor displacement in the x direction at bearing A, the notation y_a represents the rotor displacement in the y direction at

bearing A, and the notation F_{xa} represents the bearing force applied to the rotor by the bearing A in the x direction, the notation F_{ya} represents the bearing force applied to the rotor by the bearing A in the y direction, as is the case for the bearing B. The notation x_c represents the displacement of the centroid in the x direction, notation y_c represents the displacement of the centroid in the y direction, and the notation θ_x represents the rotation angle of the rotor around the x axis, the notation θ_y represents the rotation angle of the rotor around the y axis. The notation P represents the external load, the notation C represents the centroid, the notation l represents the force arm of the force from the centroid, and the notation Ω represents the rotational speed.
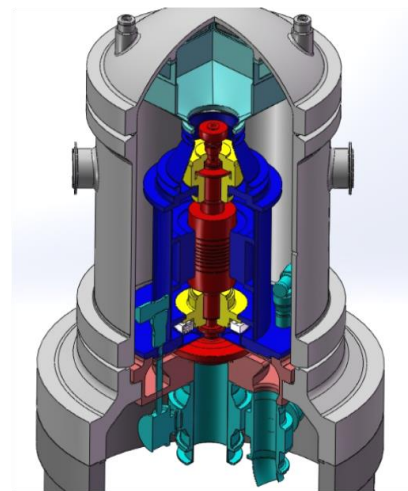
Fig. 1. The model of HTR.

Table 1: Rotor dynamics parameters

Parameters	Value	Unit
Total mass(m)	4230	kg
Centroid position	Z=1.5	m
Equatorial moment of inertia $J_x = J_y$	2690	kgm^2
Polar moment of inertia J_z	215	kgm^2
Rotor diameter at bearing (D)	0.3	m
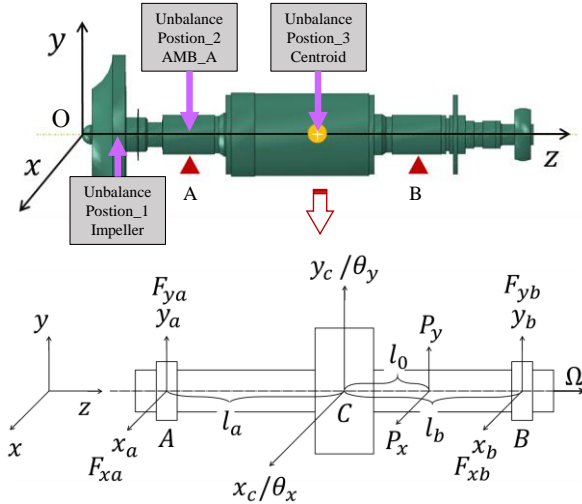
Fig. 2. The model of rigid rotor.

B. The AMB model

The design of the radial bearing is shown in Fig. 3. It is an 8-poles bearing. The design parameters of the bearing are shown in Table 2.
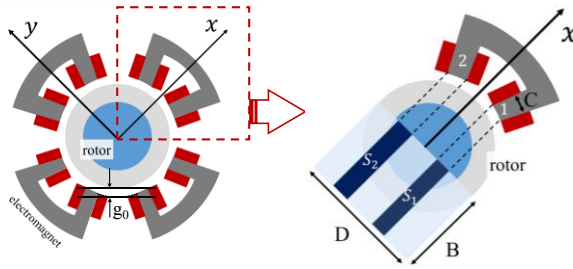
Fig. 3. The model of AMB.

Table 2: Design parameters of AMBs

Parameters	Value	Unit
AMB-A position	Z=0.8	m
AMB-B position	Z=2.6	m
AMB-A arm(l_a)	0.7	m
AMB-A arm(l_b)	1.1	m
Magnetic permeability(μ_0)	$4\pi/10^7$	H/m
Number of coil turns(N)	30	-
Bearing thickness(B)	0.3	m
Single pole width(C)	0.06	m
Bias current(I_0)	20	A
AMB Gap (g_0)	0.001	m
Pole projected area S_1=S_2	0.243	m^2
Bearing projected area A_j	0.09	m^2
Radio of projected area r_p	0.37	-

In Fig. 3, the notations S_1 and S_2 represent the projected area of the magnetic pole 1 and the magnetic pole 2 on the rotor in the y-plane. The notation A_j represent the projected area of the magnetic bearing on

the rotor in the y-plane, $A_j = B \times D$, and the notation r_p is the ratio of the projected area of magnetic pole to the projected area of the bearing, where $r_p = \frac{S_1+S_2}{B \times D}$.

C. Rotor unbalanced load

In the ISO 1940-1 standard [1], there is a double logarithmic linear relationship between the maximum permissible radial imbalance e_{per}（g.mm/kg）and the maximum rotation speed n_{max} (r/min) for the same unbalance level:

$$\log_{10}(e_{per}) = A \times \log_{10}(n_{max}) + B.$$

According to the ISO1940-1 standard, the unbalanced level of the rotor is G6.3. The relationship between the radial unbalance and the maximum rotation speed is as follows:

$$\log_{10}(e_{per}) = -\log_{10}(n_{max}) + 4.778,$$

i.e.,

$$e_{per} = \frac{10^{4.778}}{n_{max}} = \frac{6281 \times 10^{-6}}{\Omega_{max}} (\text{kg} \cdot \text{m}),$$

where Ω_{max} is angular speed(rad/s). Through rotor mass of m=4230kg, the unbalance U can be obtained:

$$U = e_{per} \times m = \frac{26.569}{\Omega_{max}} (\text{kg} \cdot \text{m}).$$

According to the centrifugal force equation $F_P = m\Omega^2 r$, the centrifugal force produced by the rotor at this unbalanced amount is as:

$$F_P = U \times \Omega^2 = \frac{26.57\Omega^2}{\Omega_{max}} (\text{N}).$$
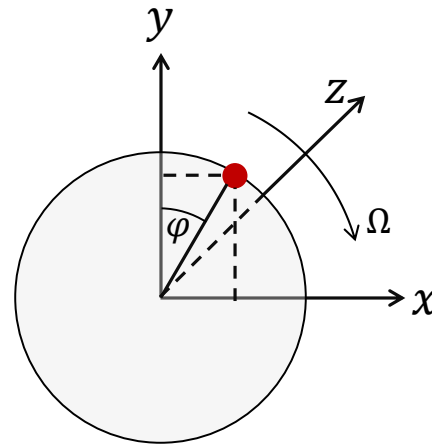
Fig. 4. Rotor initial phase angle.

The initial phase angle of the unbalanced mass of the rotor is defined in Fig. 4. The components of the centrifugal force in the x and y directions can be obtained [2]:

$$P_x = F_P \sin(\Omega t + \varphi),$$
$$P_y = F_P \cos(\Omega t + \varphi).$$

In the three typical unbalanced positions in Fig. 2, unbalances are respectively set to analyze the effects of

unbalances at different positions on the rotor response results. Specific unbalanced arms are shown in Table 3.

Table 3: Design parameters of AMBs

Unbalance Position Number	Arm	Unit
UBP1:Impeller position (l_{01})	-1.2	m
UBP2:AMB-A position (l_{02})	-0.7	m
UBP3:Centroid position(l_{03})	0	m

II. COUPLING DYNAMIC AND CONTROL METHODS

A. Rotor dynamic equation

The radial load of the rotor is perpendicular to the rotational speed, so a change of radial load produces a gyroscopic moment, resulting in the four degrees of freedom of the two radial bearings being coupled together. Therefore, the four degrees of freedom of the two radial bearings need to be analyzed together. The axial load is parallel to the rotational speed, so the change of the axial load does not produce a gyroscopic moment and can be analyzed separately. The analysis of axial bearing is similar to radial bearings, but with less freedom and simple analysis, which is not described.

According to Fig. 2 to establish the rotor dynamics equation, the first is the rotor force balance equation:

$$m\ddot{x}_c = F_{xa} + F_{xb} + P_x, \tag{1}$$
$$m\ddot{y}_c = F_{ya} + F_{yb} + P_y. \tag{2}$$

Secondly, the torque balance equation of the rotor is considered, considering the gyroscopic effect of the rotor:

$$J_x\ddot{\theta}_x - J_z\Omega\dot{\theta}_y = -F_{ya}l_a + F_{yb}l_b + P_yl_0, \tag{3}$$
$$J_y\ddot{\theta}_y + J_z\Omega\dot{\theta}_x = F_{xa}l_a - F_{xb}l_b - P_xl_0. \tag{4}$$

Combining equations 1-4 and representing them with a matrix equation:

$$M\ddot{X}_c + C\dot{X}_c = T_fF + P. \tag{5}$$

Where,

$$M = \begin{bmatrix} m & & & \\ & m & & \\ & & J_x & \\ & & & J_y \end{bmatrix},$$

$$C = \begin{bmatrix} 0 & & & \\ & 0 & & \\ & & 0 & -J_z\Omega \\ & & J_z\Omega & 0 \end{bmatrix},$$

$$T_f = \begin{bmatrix} 1 & 1 & 0 & 0 \\ 0 & 0 & 1 & 1 \\ 0 & 0 & -l_a & l_b \\ l_a & -l_b & 0 & 0 \end{bmatrix},$$

$$F = \begin{bmatrix} F_{xa} \\ F_{xb} \\ F_{ya} \\ F_{yb} \end{bmatrix}; P = \begin{bmatrix} P_x \\ P_y \\ P_yl_0 \\ -P_xl_0 \end{bmatrix}; X_c = \begin{bmatrix} x_c \\ y_c \\ \theta_x \\ \theta_y \end{bmatrix}.$$

The displacement and the rotation angle of the

centroid are transformed into displacements in the four directions of AMB-A and AMB-B by the transformation matrix T_t, i.e., $X_c = T_tX$, where,

$$X = \begin{bmatrix} x_a \\ x_b \\ y_a \\ y_b \end{bmatrix},$$

$$T_t = \begin{bmatrix} \frac{l_b}{l_a+l_b} & \frac{l_a}{l_a+l_b} & 0 & 0 \\ 0 & 0 & \frac{l_b}{l_a+l_b} & \frac{l_a}{l_a+l_b} \\ 0 & 0 & -\frac{1}{l_a+l_b} & \frac{1}{l_a+l_b} \\ \frac{1}{l_a+l_b} & -\frac{1}{l_a+l_b} & 0 & 0 \end{bmatrix}.$$

Equation 5 is converted to equation 6 by $X_c = T_tX$:

$$MT_t\ddot{X} + CT_t\dot{X} = T_fF + P. \tag{6}$$

B. The relationship between AMB force and rotor displacement under PD control

The equation for the electromagnetic force generated by a single electromagnet is:

$$F_{magnetic} = \frac{\mu_0N^2I^2A_jr_p}{8g^2} = k\frac{I^2}{g^2}. \tag{7}$$

Where $k = \frac{\mu_0N^2A_jr_p}{8}$, the notation g is the gap between the AMB and the rotor as shown in Fig. 3, the notation I is the current of the AMB [3].

Take the relationship between F_{xa} and x_a as an example to derive the relationship between electromagnetic force and displacement in each direction. Assume that the initial gap of the bearing is g_0, then the gap of the bearing after the rotor moves is:

$$\begin{cases} g_{xa+} = g_0 - x_a \\ g_{xa-} = g_0 + x_a \end{cases}. \tag{8}$$

Where the notation g_{xa+} is the gap between the rotor and the magnetic poles of bearing A in x positive direction. The notation g_{xa-} is the gap between the rotor and the magnetic poles of bearing A in x reverse direction.

Two magnetic poles symmetrical at the x_a direction use differential control, i.e.:

$$\begin{cases} I_{xa+} = I_0 + I_{xa} \\ I_{xa-} = I_0 - I_{xa} \end{cases}. \tag{9}$$

Where the notation I_{xa+} is the control current of the magnetic poles of bearing A in x positive direction and the notation I_{xa-} is the control current of the magnetic poles of bearing A in x reverse direction.

Therefore, the relationship between bearing force and displacement is as follows:

$$F_{xa} = k\left[\frac{(I_0+I_{xa})^2}{(g_0-x_a)^2} - \frac{(I_0-I_{xa})^2}{(g_0+x_a)^2}\right]. \tag{10}$$

The relationship between force and displacement and current is linearized. The two order Taylor expansion is performed at $x_a = 0$ and $I_{xa} = 0$ and the second-order and higher-order terms are ignored:

$$\left[\frac{(I_0+I_{xa})^2}{(g_0-x_a)^2} - \frac{(I_0-I_{xa})^2}{(g_0+x_a)^2}\right] \approx I_{xa}\frac{4I_0}{g_0^2} + x_a\frac{4I_0^2}{g_0^3}. \tag{11}$$

The relationship between AMB force and control current and rotor displacement at direction of x_a is obtained:

$$F_{xa} = k \left(I_{xa} \frac{4I_0}{g_0^2} + x_a \frac{4I_0^2}{g_0^3} \right). \tag{12}$$

Finally, the relationship between AMB force F and X is as follows:

$$F = k \frac{4I_0}{g_0^2} I_C + k \frac{4I_0^2}{g_0^3} X. \tag{13}$$

Where I_C is the control current:

$$I_C = \begin{bmatrix} I_{xa} \\ I_{xb} \\ I_{ya} \\ I_{yb} \end{bmatrix}.$$

PD control is adopted between control current I_C and displacement X, as shown in Fig. 5 [4]:

$$I_C = -pX - d\dot{X}, \tag{14}$$

Where,

$$p = \text{diag}[p_a, p_b, p_a, p_b],$$
$$d = \text{diag}[d_a, d_b, d_a, d_b].$$
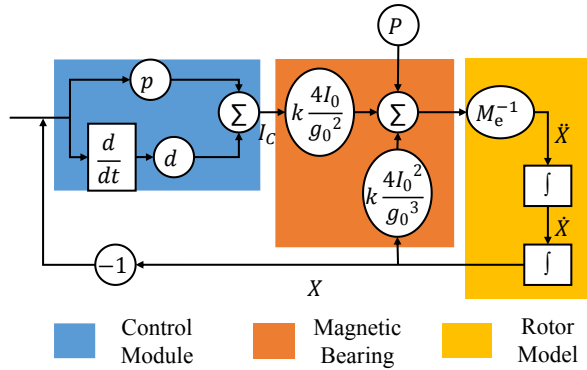
Fig. 5. the block diagram of the closed loop controlled system.

By combining equations 6, 13, and 14, the rotor dynamics equation that coupled dynamic equations and control methods are obtained:

$$M_e \ddot{X} + C_e \dot{X} + K_e X = P. \tag{15}$$

Where,

$$M_e = MT_t,$$
$$C_e = CT_t + k \frac{4I_0}{g_0^2} T_f d,$$
$$K_e = k \frac{4I_0}{g_0^2} T_f p - k \frac{4I_0^2}{g_0^3} T_f.$$

By setting the equivalent stiffness and the equivalent damping ratio to determine the control matrix p and d. Setting $K_e(1,1) = K_e(1,2) = K$, the p can be obtained and setting damping ratio is ζ, the d can be obtained through equations 16,17:

$$C_e(1,1) = 2M_e(1,1)\sqrt{\frac{K_e(1,1)}{M_e(1,1)}}\zeta, \tag{16}$$

$$C_e(1,2) = 2M_e(1,2)\sqrt{\frac{K_e(1,2)}{M_e(1,2)}}\zeta. \tag{17}$$

III. NUMERICAL SIMULATION RESULTS

A. Time response results

The numerical solution method of time domain equation mainly includes mode superposition method and direct integration method. The mode superposition method needs to first obtain the mode shape of the model, which is suitable for calculating the seismic response that discard the influence of higher-order modes. This method is limited to applications within the elastic range and takes more time to calculate. The direct integration method does not require vibration mode analysis, and the equation is directly integrated by discrete time. The general direct integration methods include linear acceleration method, Wilson-θ method and Newmark-β method. For the linear integration method, the stability condition depends on the step size, and the step size depends on the minimum period of the discrete structure, which is difficult to determine. The Wilson-θ method improves the linear integration method by introducing the θ factor, and the convergence of the method can be ensured by defining the θ. The Newmark-β method is another variant of the linear acceleration method. Compared with the Wilson-θ method, its calculation accuracy and computational stability are more controllable, but the calculation process is more complicated [5,6].

The rotor's time-domain result of unbalanced response is solved by equation 15 and Wilson-θ method. The initial condition of the rotor at time 0 s is $\dot{X}(0) = \dot{X}_0$, $X(0) = X_0$. $\ddot{X}_0$ can be solved by $\dot{X}_0$, X_0 and equation 15 as $\ddot{X}_0 = M_e^{-1}(P_0 - K_e X_0 - C_e \dot{X}_0)$.

Dissipate the entire analysis time into multiple Δt, and assume that the acceleration in each $\theta \Delta t$ period changes linearly, where θ is time magnification factor, that is shown in Fig. 6.
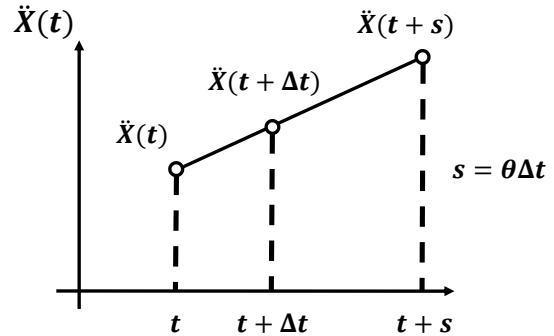
Fig. 6. Linear change of acceleration.

Set,

$$\Delta \ddot{X}_s(t) = \ddot{X}(t+s) - \ddot{X}(t), \tag{18}$$

define the function of $\ddot{X}$ about τ,

$$\ddot{X}(t + \tau) = \ddot{X}(t) + \frac{\tau}{s}\Delta\ddot{X}_S(t). \quad (19)$$

Perform one and two integrals for τ and take $\tau = s$:

$$\dot{X}(t + s) = \dot{X}(t) + s\ddot{X}(t) + \frac{s}{2}\Delta\ddot{X}_S(t), \quad (20)$$

$$X(t + s) =$$
$$X(t) + s\dot{X}(t) + \frac{s^2}{2}\ddot{X}(t) + \frac{s^2}{6}\Delta\ddot{X}_S(t). \quad (21)$$

Bring equation 18 into equations 20 and 21:

$$\dot{X}(t + s) =$$
$$\dot{X}(t) + \frac{s}{2}\ddot{X}(t) + \frac{s}{2}\ddot{X}(t + s), \quad (22)$$

$$X(t + s) =$$
$$X(t) + s\dot{X}(t) + \frac{s^2}{6}[\ddot{X}(t + s) + 2\ddot{X}(t)]. \quad (23)$$

At $t+s$, the equation of motion of the rotor is:

$$M_e\ddot{X}(t + s) + C_e\dot{X}(t + s) + K_eX(t + s)$$
$$= P(t + s). \quad (24)$$

Combining equations 22, 23, and 24 and eliminating $\dot{X}(t + s)$ and $\ddot{X}(t + s)$:

$$\left(\frac{6M_e}{s^2} + \frac{3C_e}{s} + K_e\right)X(t + s) =$$
$$[\left(\frac{6M_e}{s^2} + \frac{3C_e}{s}\right)X(t) + \left(\frac{6M_e}{s} + 2C_e\right)\dot{X}(t)$$
$$+ \left(2M_e + \frac{sC_e}{2}\right)\ddot{X}(t) + P(t + s)]. \quad (25)$$

Equation 26 can be obtained from Fig. 6:

$$\ddot{X}(t + s) = \theta\ddot{X}(t + \Delta t) + (1 - \theta)\ddot{X}(t). \quad (26)$$

Substitute equation 26 into equation 23, and set $s = \theta\Delta t$:

$$\ddot{X}(t + \Delta t) = \frac{6}{\theta^3\Delta t^2}[X(t + s) - X(t)]$$
$$- \frac{6}{\theta^2\Delta t}\dot{X}(t) + (1 - \frac{3}{\theta})\ddot{X}(t). \quad (27)$$

In equation 22 and equation 23, set $s = \theta\Delta t$:

$$\dot{X}(t + \Delta t) =$$
$$\dot{X}(t) + \frac{\Delta t}{2}\ddot{X}(t) + \frac{\Delta t}{2}\ddot{X}(t + \Delta t), \quad (28)$$

$$X(t + \Delta t) =$$
$$X(t) + \Delta t\dot{X}(t) + \frac{\Delta t^2}{6}[\ddot{X}(t + \Delta t) + 2\ddot{X}(t)]. \quad (29)$$

The entire iterative solution process is as follow five steps:

Step1: $X(t + s)$ is solved by $X(t)$, $\dot{X}(t)$, $\ddot{X}(t)$, $P(t + s)$ and equation 25;

Step2: $\ddot{X}(t + \Delta t)$ is solved by $X(t)$, $\dot{X}(t)$, $\ddot{X}(t)$, $X(t + s)$ and equation 27;

Step3: $\dot{X}(t + \Delta t)$ is solved by $\dot{X}(t)$, $\ddot{X}(t)$, $\ddot{X}(t + \Delta t)$ and equation 28;

Step4: $X(t + \Delta t)$ is solved by $X(t)$, $\dot{X}(t)$, $\ddot{X}(t)$, $\ddot{X}(t + \Delta t)$ and equation 29;

Step5: Replace t with $t + \Delta t$, repeat step1 to step4.

For the wilson $- \theta$ method, the calculation is stable when $\theta > 1.37$, generally taking $\theta = 1.4$ [6].

When the rotation speed is 4000 r/min and the unbalanced position is UBP1. The K is 1×10^7 N/m and the damping ratio is 0.5. The time-domain response results of rotor displacement and AMB force within 0.2 s are shown in Fig. 7 and Fig. 8.
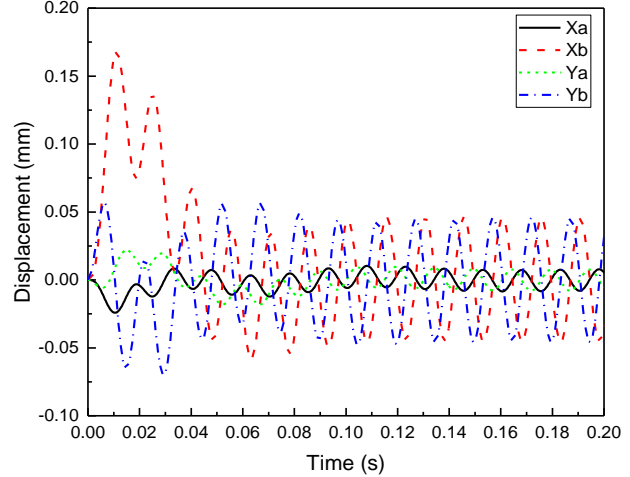
Fig. 7. Time-domain response results of rotor displacement (4000r/min).
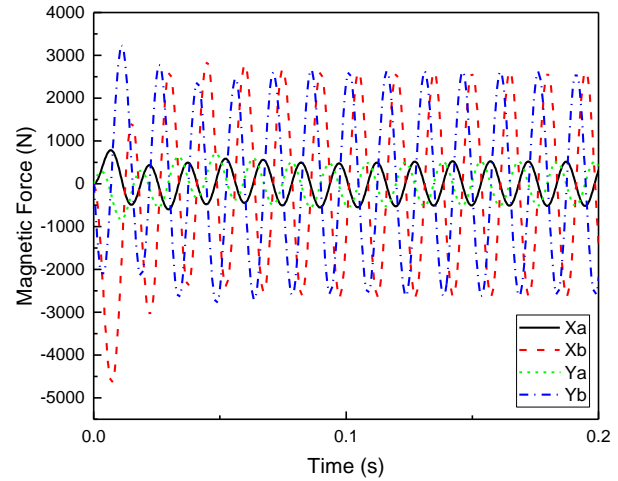
Fig. 8. Time-domain response results of AMB force (4000r/min).

B. The effect of unbalanced position on the response result

In order to analyze the rotor displacement response and bearing load response during the entire speed-up process (from 0r/min to 4000r/min), the 81 time-domain response curves of the rotor is calculated at intervals of 50r/min. A Fourier transform is performed on each time-domain response curve to obtain a frequency-domain curve of the rotor at a fixed rotational speed (the Fig. 9 and the Fig. 10 show the frequency-domain curve, which is obtained through Fourier transform from Fig. 7 and Fig. 8). The 81 frequency-domain curves are drawn together, and the envelope curves of 81 curves are the frequency-domain curves during the rotor speed-up process, and the peaks of Fig. 9 and Fig. 10 are indicated by red circles in Figs. 9-16 [7].
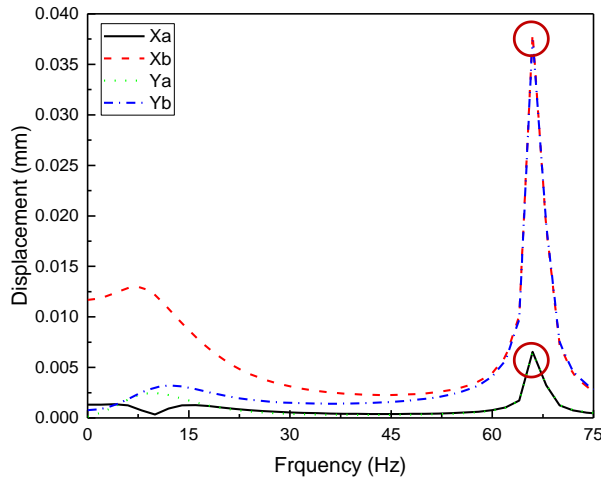
Fig. 9. Frequency-domain response results of rotor displacement (4000r/min).

Fig. 10. Frequency-domain response results of AMB force (4000r/min).

Fig. 11. Rotor displacement frequency response curve (different unbalance position).
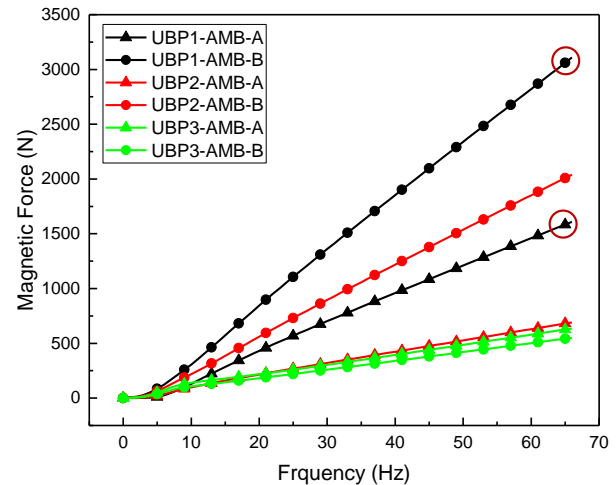
Fig. 12. AMB force frequency-domain curve (different unbalance position).

The AMB stiffness is $K = 1 \times 10^7$ N/m and the damping ratio is $\zeta = 0.5$. The frequency-domain effect of the unbalance position (UBP) on the rotor displacement and AMB force is analyzed, which is shown in Fig. 11 and Fig. 12.

From Fig. 11 and Fig. 12, it can be seen that when the stiffness and damping ratio are the same, the farther the unbalance mass deviates from the centroid of the rotor, the greater the displacement of rotor and force of AMB. Compared with AMB-A and AMB-B, it can be found that for the condition of UBP1 and UBP2, because the position of AMB-B is farther from the unbalanced load than the position of AMB-A, this means that its arm is longer and the bearing force it needs to bear is greater, and its displacement response is also more pronounced.

C. The effect of AMB stiffness on the response result

Select the unbalance condition UBP1 with maximum rotor displacement and bearing load according to section B and fix damping ratio $\zeta = 0.5$ to analyze the frequency-domain effect of different bearing stiffness on rotor displacement and AMB force. The results are shown in Fig. 13 and Fig. 14.

From Fig. 13 and Fig. 14, it can be seen that as the stiffness increases, the rotor displacement decreases and the AMB force increases, but the reduction of the rotor displacement is not obvious and the increase of the AMB force is significant which may lead to saturation of the magnetic actuator. [8] By selecting an appropriate bearing stiffness, both rotor displacement and bearing load can be guaranteed.
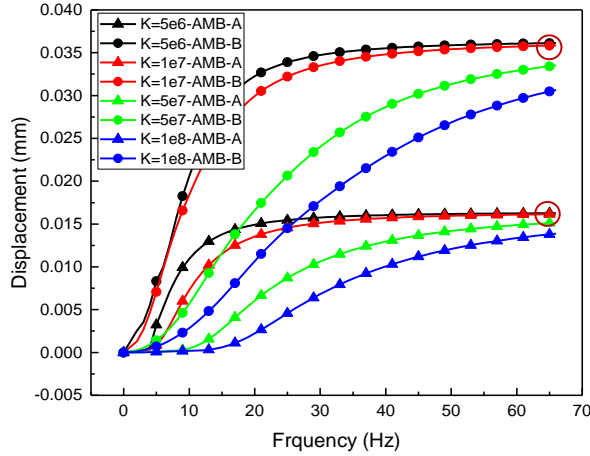
Fig. 13. Rotor displacement frequency response curve.
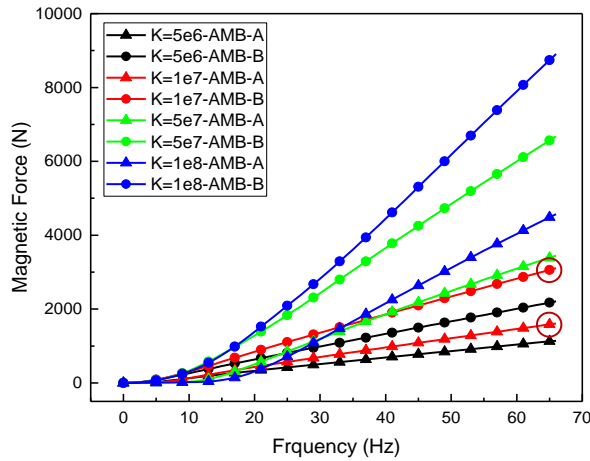
Fig. 14. AMB force frequency response curve.

D. The effect of damping ratio on the response result

The unbalance condition is same as section C, and fix stiffness $K = 1 \times 10^7 \text{N/m}$ to analyze the effect of different stiffness ratio on rotor displacement and AMB force. The results are shown in Fig. 15 and Fig. 16.
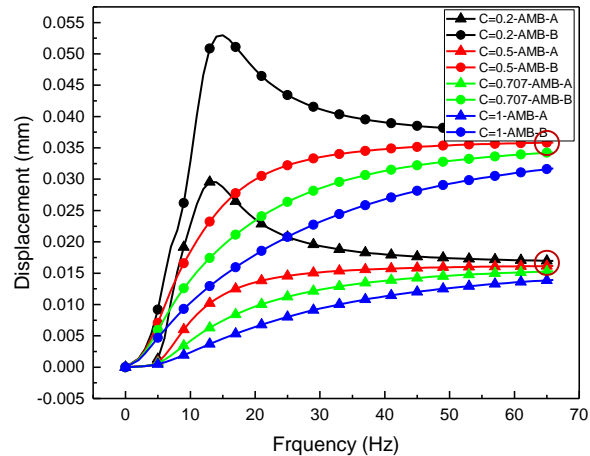
Fig. 15. Rotor displacement frequency response curve.
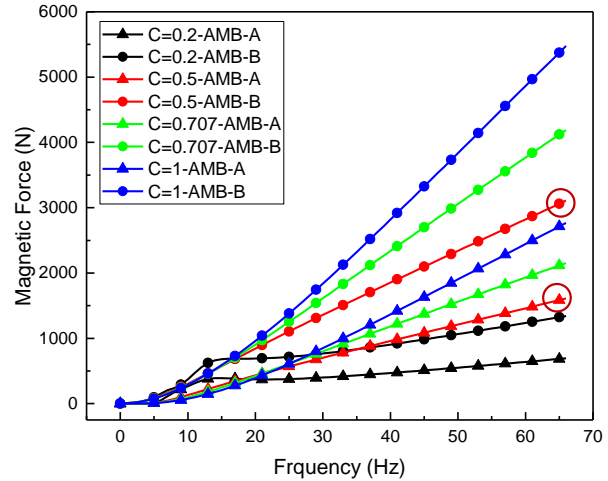
Fig. 16. AMB force frequency response curve.

From Figs. 15 and 16, it can be seen that the results are similar to Section C. As the damping ratio increases, the rotor displacement decreases and the AMB force increases. By selecting appropriate damping ratio, both rotor displacement and bearing load can be guaranteed.

IV. CONCLUSION

When the stiffness and damping ratio are the same, the farther the unbalance mass deviates from the centroid of the rotor, the greater the displacement of rotor and force of AMB. The arm from the bearing to the unbalance position is longer and the bearing force it needs to bear is greater, and its displacement response is also more pronounced.

Increasing the stiffness and damping ratio of bearings can effectively reduce the unbalance response of the rotor, but it will significantly increase the bearing load. Therefore, when determining the bearing stiffness and damping ratio, it is necessary to consider the bearing load and displacement comprehensively and select the optimal solution.

The follow-up work of this paper mainly includes: 1) Using the method of this paper to calculate the unbalanced response of the system under different conditions, and compare it with the actual running data to realize the correction of the system model. This work can be combined with the linear identification method [9]. 2) When a rotor-drop occurs, the system may exhibit nonlinearity [10-12], and it is necessary to consider extending the work of this paper to a nonlinear model.

REFERENCES

[1]   ISO Standard 1940, "Balance Quality of Rotating

Rigid Bodies," *International Organization for Standardization ISO*, 1973.

[2] J. Yu and C. Zhu, "A multi-frequency disturbances identification and suppression method for self-sensing AMB rotor system," *[J]. IEEE Transactions on Industrial Electronics*, p. (99):1-1, 2017.

[3] G. Schweitzer and E. H. Maslen, "Magnetic bearings: Theory, design, and application to rotating machinery," 2009.

[4] R. Herzog, P. Bühler, C. Gähler, and R. Larsonneur, "Unbalance compensation using generalized notch filters in the multivariable feedback of magnetic bearings," *IEEE Trans. Control Sys. Tech.*, vol. 4, no. 5, pp. 580-586, 1996.

[5] I. Gladwell and R. Thomas, "Stability properties of the Newmark, Houbolt and Wilson θ methods," *International Journal for Numerical and Analytical Methods in Geomechanics*, vol. 4, no. 2, pp. 143-158, 1980.

[6] L. Aiqun and D. Youliang, *Aseismic Analysis of Engineering Structures* [M]. High Education Press, 2010.

[7] C. R. Burrows and M. N. Sahinkaya, "Vibration control of multi-mode rotor bearing systems," *In Proceedings of the Royal Society of London (Series A)*, vol. 386, 1983.

[8] B. Shafai, S. Beale, P. Larocca, et al., Magnetic bearing control systems and adaptive forced balancing, *[J]. Control Systems IEEE*, vol. 14, no. 2, pp. 4-13, 1994.

[9] Z. Sun, Y. He, J. Zhao, Z. Shi, L. Zhao, and S. Yu, "Identification of active magnetic bearing system with a flexible rotor," *Mechanical Systems & Signal Processing*, vol. 49, no. 1-2, pp. 302-316, 2014.

[10] Z. Sun, J. Zhao, Z. Shi, et al., "Soft sensing of magnetic bearing system based on support vector regression and extended Kalman filter," *[J]. Mechatronics*, vol. 24, no. 3, pp. 186-197, 2014.

[11] Z. Sun, X. Yan, J. Zhao, et al., "Dynamic behavior analysis of touchdown process in active magnetic bearing system based on a machine learning method," *[J]. Science & Technology of Nuclear Installations*, 2017 (5):1-11, 2017.

[12] C. A. Fonseca, I. F. Santos, and H. I. Weber, "Influence of unbalance levels on nonlinear dynamics of a rotor-backup rolling bearing system," *[J]. Journal of Sound & Vibration*, 394:482-496, 2017.

Guowei Du graduated from School of Aerospace, and now is a fifth year Ph.D. candidate at the Institute of Nuclear and New Energy Technology of Tsinghua University. His main research direction is rotor dynamics and active magnetic bearing control.

Zhe Sun is currently an Associate Professor and Ph.D. Supervisor of Tsinghua University. His research interests are control and monitoring of active magnetic levitation system, rotor dynamics, statistical learning theory and its engineering application, etc.

Semi-Analytical 3D Force Calculation of an Ironless Cylindrical Permanent Magnet Actuator for Magnetic Levitation Systems

Mousa Lahdo [1,2], Tom Ströhla [2], and Sergej Kovalev [1]

[1] Department of Informatics, Electrical Engineering and Mechatronics
University of Applied Sciences Mittelhessen, Friedberg, 61169, Germany
mousa.lahdo@iem.thm.de, sergej.kovalev@iem.thm.de

[2] Department of Mechatronics
Ilmenau University of Technology, Ilmenau, 98693, Germany
tom.stroehla@tu-ilmenau.de

Abstract ─ The semi-analytical calculation of magnetic forces is currently an interesting alternative to the time-consuming three-dimensional finite-element modeling (3D-FEM) due to its high accuracy and low computational cost. This paper presents novel equations for determining the magnetic forces of a cylindrical permanent magnet actuator used in high precision magnetic levitation positioning systems. Compared to the already available equations in literature, these equations consider the magnetic forces as a function of the current magnet position. Moreover, these equations are also suitable for designing and analyzing the cylindrical permanent magnet actuator. The results of our force equations and the verification by 3D-FEM and measurements are presented in this paper.

Index Terms ─ Cylindrical permanent magnet actuator, electromagnetic analysis, Lorentz force, magnetic levitation.

I. INTRODUCTION

Magnetic levitation is a key technology used in order to achieve vacuum compatible high precision positioning systems since friction, backlash, and wear are eliminated. Positioning systems based on magnetic levitation are characterized by a simple compact structure with highest positioning accuracy, excellent repeatability and high control bandwidth. Thus, six degrees-of-freedom (6-DoF) magnetic levitation positioning systems are currently investigated and developed for applications in the semiconductor industry, nanotechnology or microscopy, where highest dynamics, highest precision and absolutely friction-free operation are desired [1-5].

Due to the non-linear current-force and position-force relation in reluctance actuators, which complicates controller design, most existing solutions of magnetic levitation positioning systems are based on ironless actuators which use Lorentz forces to levitate and drive the moving element (mover).

The main advantages of ironless actuators based on Lorentz forces are its inherent linear relation between the currents and forces and its high positioning accuracy [6-7].

Designing, analyzing and optimizing such ironless high precision positioning systems require electromagnetic models that are very fast and accurate. Three-dimensional finite element modeling (3D-FEM) is often used for the calculation of magnetic fields and forces of such systems because they provide a very accurate solution. However, 3D-FEM is not suitable for designing and optimizing such systems because of its extremely high computation time. Thus, other calculation approaches are needed. A very fast and accurate alternative to the conventional 3D-FEM modeling is a semi-analytical-based modeling approach. The semi-analytical approach describes the magnetic fields and forces as a function of physical parameters, e.g., magnet and coil dimensions and thus, provides a good insight in the physical system properties. Moreover, for the design and optimization of electromagnetic actuators, such equations are more efficient compared to 3D-FEM. Beyond that, researchers do not always have the possibility to use a cost-intensive 3D-FEM software, therefore, a precise semi-analytical equation is a good alternative since it can be implemented in every mathematical program.

Due to these reasons, many researchers calculate the magnetic fields and forces in electromagnetic systems semi-analytically instead of using 3D-FEM. This can be seen by the huge number of publications dealing with semi-analytical calculation of magnetic fields and forces [8-14]. For instance, in a recent publication, [15] derives analytical expressions in order to optimize a magnetically levitated planar motor. The analytical calculation of repulsive levitation forces between Halbach arrays and

magnetic guiding coils in high precision magnetic levitation systems is presented in [16]. An overview of different analytical calculation methods is given in [17].

In high precision magnetic levitation systems, ironless rectangular coils [18], square coils [19] or circular coils [20] are commonly used in order to generate repulsive levitation forces. Until now, many papers published in literature deal with the semi-analytical force calculation between a cuboidal permanent magnet and a rectangular [21] or square air-core coil [22]. The derived force equations for the rectangular and square coils consider also the position dependence of the magnetic forces and thus provide the basis for fast and accurate analysis and design tools [21-22]. Moreover, these equations can also be used for the derivation of model-based commutation algorithms as well as real-time motion control of magnetic levitation positioning systems [23-25].

The semi-analytical force calculation between circular air-core coils and cylindrical permanent magnets are also known, but these equations are only valid in cases where the center axis of cylindrical magnet and the circular coil are coaxial [26-29]. However, in 6-DoF magnetic levitation system, a movement of the permanent magnet in the horizontal plane is indispensable, i.e., the center of the cylindrical magnet and the circular coil are not coaxial and thus the force equations known in literature are not valid for the non-coaxial case. Since this case has not yet been investigated in the context of high precision magnetic levitation systems, it is rare to find equations which consider the Cartesian magnetic force components (F_x, F_y, F_z) as a function of the current mover position (x_p, y_p). Previous efforts to determine the magnetic forces between a circular coil and a cylindrical permanent magnet are mostly done by experiments [30] or by 3D-FEM [31].

As such, this paper aims to provide a semi-analytical calculation of the repulsive magnetic levitation force between a cylindrical moving magnet and a stationary circular coil.

Moreover, the calculation of the destabilizing propulsion forces is also presented. The main contributions of this paper are new semi-analytical expressions which consider the Cartesian magnetic force components as a function of the current mover position.

This paper is organized as follows: Section II explains briefly the force generation principle of the cylindrical magnet actuator. The generation and calculation of the levitation and propulsion force as a function of the mover position is described in Section III. In Section IV, the calculated levitation and propulsion forces using the new expressions are compared with the calculated forces using 3D-FEM and with our measured forces obtained from the prototype. Section V concludes this paper.

II. ANALYSIS AND MAGNETIC FIELD CALCULATION

In high precision magnetic levitation systems, the active magnetic guidance coil has a significant weight that must be levitated, e.g. the weight of the magnet, the plate to which it is fixed and the weight of an additional payload. Hence, the calculation of the levitation forces is an important task in such positioning systems. Compared with cost-intensive experiments and time-consuming 3D-FEM software, the proposed approach in this paper ensures the possibility of calculating quickly the levitation force as a function of the coil and magnet dimensions and thus is suitable for parameter studies.

A. Force generation principle

The permanent magnet actuator usually used in magnetic levitation systems in order to generate the repulsive levitation force can be seen in Fig. 1. It consists of a fixed circular air-core coil and a moving cylindrical permanent magnet.
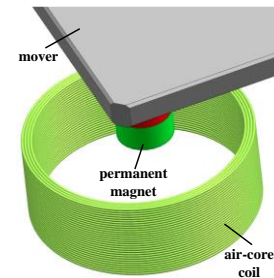
Fig. 1. Cylindrical permanent magnet actuator.

However, such topologies based on static magnetic forces are inherently unstable. This means that the permanent magnet actuator generates, in addition to the desired stable repulsive levitation force, an undesired destabilizing propulsion force that tends to push the permanent magnet laterally away from the equilibrium position. Figure 2 shows a more detailed illustration of this unstable behavior.
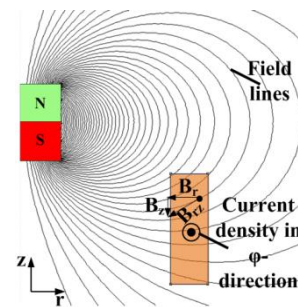
Fig. 2. Generated force components by the permanent magnet actuator.

As can be seen from this figure, the magnetic field generated by the cylindrical permanent magnet creates flux density components in the r- and z-directions. The interaction of the r-component of the magnetic flux density with the φ-component of the current density in the circular coil generates a levitation force in the z-direction.

An equilibrium position occurs, when the repulsive levitation force in $+z$-direction exactly compensates the gravitational force of the mover in the $-z$-direction. As a result, this equilibrium position is stable, i.e., the motion of the mover along the z-direction is stable. This is because as the air gap increases, the generated repulsive levitation force decreases. Thus, the gravitational force restore the mover in the equilibrium position. Nevertheless, the z-component of the magnetic flux density generates with the same current density in the coil a destabilizing propulsion force in the r-direction. This instability is consistent with Earnshaw's theorem predicted by S. Earnshaw in the early 1800 and Braunbek's theorem, which states that a stable levitation based only on static magnetic forces between coils and permanent magnets is never stable in all directions simultaneously [32,34]. Thus, this destabilizing force must be compensated by additional propulsion actuators in order to restore the lateral stability and to move and position the mover simultaneously as it is proposed among others in [1], [19],[20],[22],[29],[30],[31].

Consequently, a stable levitation can only be achieved with additional propulsion actuators in combination with a control system.

The total force which acts on the fixed circular air-core coil can be calculated using the Lorentz force formula:

$$\mathbf{F} = \int_V \mathbf{J} \times \mathbf{B} \, dV, \tag{1}$$

which states that the Lorentz force is the volumetric integral of the cross product of the current density $\mathbf{J}$ in the coil with the external magnetic flux density $\mathbf{B}$ generated by the permanent magnet over the whole volume $dV = dxdydz$ of the coil. However, since the Lorentz force formula can only applied to the current carrying coil, the permanent magnet will experience according to Newton's third law the same force in opposite direction (*action = reaction*).

B. Calculation of the magnetic flux density

The first important step for the prediction of the Lorentz force according to (1) is the calculation of the magnetic flux density of the permanent magnet inside the coil volume. In literature, many 3D-field equations are presented for different permanent magnet shapes. These equations are based on either the current sheet model or on the surface charge model [33]. Both approaches can be derived from the Maxwell equations under the assumption that the relative permeability $\mu_r = 1$. Moreover, both allow an extremely accurate and fast field calculation, provide a good insight into the system properties and leads to the same results in free space [28].

In this paper, the magnetic flux density for an axial magnetized permanent magnet with a uniform magnetization is determined using the surface charge model and this is given by [22]:

$$\mathbf{B} = \frac{\mu_0}{4\pi} \, \mathbf{\nabla_r} \oint_S \frac{\mathbf{M}(\mathbf{r'}) \cdot \mathbf{n}}{|\mathbf{r} - \mathbf{r'}|} \, dS, \tag{2}$$

where $\mathbf{M}(\mathbf{r'})$ is the magnetization of the permanent magnet, $\mathbf{n}$ is the normal vector on the surface, μ_0 is the vacuum permeability, S is the surface of the permanent magnet, $\mathbf{\nabla_r}$ is the vector operator, $\mathbf{r}$ describes the position where the field is evaluated and $\mathbf{r'}$ describes the position of the permanent magnet.

III. FORCE CALCULATION

Using (2) and inserting into (1), the total force can be generally written as:

$$\mathbf{F} = \int_V \mathbf{J} \times \left(\frac{\mu_0}{4\pi} \, \mathbf{\nabla_r} \oint_S \frac{\mathbf{M}(\mathbf{r'}) \cdot \mathbf{n}}{|\mathbf{r} - \mathbf{r'}|} \, dS \right) \, dV. \tag{3}$$

This quintuple integral expression can be generally used in order to calculate the total force generated between a permanent magnet and an air-core coil. For the circular air-core coil, the current density in a cylindrical coordinate system only has a component in the tangential direction. Hence, in order to obtain a formula for the levitation force, only the flux density component in the radial direction is needed because only this component is responsible for the levitation force generation. Therefore, this radial component is given as:

$$B_r = \frac{\mu_0}{4\pi} \frac{\partial}{\partial \mathbf{r}} \oint_S \frac{\mathbf{M}(\mathbf{r'}) \cdot \mathbf{n}}{|\mathbf{r} - \mathbf{r'}|} \, dS. \tag{4}$$

Furthermore, if we assume that the current density is uniform and constant:

$$J_\varphi = \frac{N_c \cdot I_c}{(r_a - r_i) \cdot h_c}, \tag{5}$$

where N_c is the number of coil turns, I_c the current through the coil, $(r_a - r_i) \cdot h_c$ the cross sectional area of the coil and under consideration of the parameters shown also in Fig. 3, the expression for the levitation force F_z at the magnet position $x = y = 0$ can be simplified to a scalar function in z-direction:

$$F_z = \frac{N_c \cdot I_c}{(r_a - r_i) \cdot h_c} \frac{\mu_0}{4\pi} \int_V \left(\frac{\partial}{\partial \mathbf{r}} \oint_S \frac{\mathbf{M}(\mathbf{r}') \cdot \mathbf{n}}{|\mathbf{r} - \mathbf{r}'|} dS \right) dV. \quad (6)$$
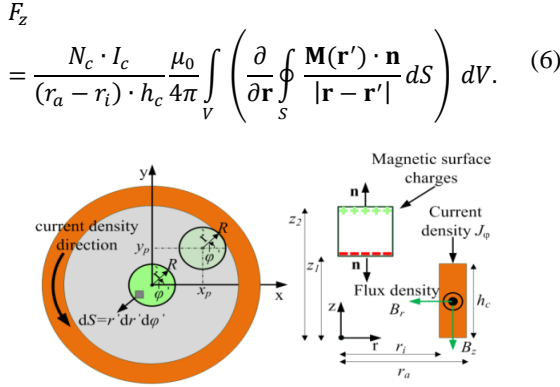
Fig. 3. Top view (left) and side view (right) of the permanent magnet actuator.

The difference vector $\xi_\beta = |\mathbf{r} - \mathbf{r}'|$ expressed in cylindrical coordinates using the relation $\mathbf{r} = \{x, y, z\} = \{r\cos\varphi, r\sin\varphi, z\}$ and $\mathbf{r}' = \{x', y', z'\} = \{r'\cos\varphi, r'\sin\varphi, z'\}$ yields:

$$\begin{aligned} \xi_\beta &= |\mathbf{r} - \mathbf{r}'| \\ &= \sqrt{(x - x')^2 + (y - y')^2 + (z - z'_\beta)^2} \quad (7) \\ &= \sqrt{r^2 + r'^2 - 2rr'\cos(\varphi - \varphi') + (z - z'_\beta)^2}. \end{aligned}$$

In addition to that, if the infinitesimal volume element dV as well as the infinitesimal surface element dS is also expressed in cylindrical coordinates as $dV = r\,dr\,d\varphi\,dz$ and $dS = r'dr'd\varphi'$ respectively, and under consideration of Fig. 3, the levitation force F_z now becomes:

$$F_z = \frac{N_c \cdot I_c}{(r_a - r_i) \cdot h_c} \frac{\mu_0 M}{4\pi} \int_0^{h_c} \int_0^{2\pi} \int_{r_i}^{r_a} \frac{\partial}{\partial r} \int_0^{2\pi} \int_0^R \left(\frac{r'}{\xi_2} - \frac{r'}{\xi_1} \right)$$
$$\cdot dr'd\varphi' \cdot r\,dr\,d\varphi\,dz. \quad (8)$$

However, this equation allows determining the levitation force only if the center of the permanent

magnet is coaxial with the center of the circular coil as can be seen in Fig. 3.

Despite this, in 6-DoF magnetic levitation system, the magnet moves in the horizontal plane x_p and y_p from the central position (Fig. 3). Therefore, the analytical equation must consider the actual mover position (x_p, y_p) over the whole travel range.

This can be done by modifying the integrand of (6) with the relationship $\mathbf{r}' = \{x', y', z'\} = \{x_p + r'\cos\varphi, y_p + r'\sin\varphi, z'\}$ as shown in the final form (9) at the bottom of this page.

At this point, it should be noted that the derivation of semi-analytical expressions for the destabilizing forces in the horizontal direction can be done in the same manner. Thus, the force equations for the Cartesian force components in the x- and y-direction can be derived in the final form as shown in (11) and (12), respectively.

Based on the derived expressions, which are easily implemented in MATLAB, and under consideration of the parameters and dimensions shown in Table 1, the levitation and the destabilizing propulsion forces can be calculated at every value of x_p and y_p in millimeters in the horizontal plane $(x_p, y_p) \in \mathbb{R}$.

Table 1: Dimensions and parameters for the levitation force calculation

Parameter	Symbol	Value	Unit
Number of turns	N_c	200	
Current	I_c	1	A
Remanence of PM	$\mu_0 M$	1.44	Vs/m^2
Coil height	h_c	24	mm
Magnet radius	R	10	mm
Coil inner side	r_i	23.5	mm
Coil outer side	r_a	33.5	mm
Neg. magnetic charges height	z_1	26	mm
Pos. magnetic charges height	z_2	31	mm

$$F_z(x_p, y_p) = \frac{N_c \cdot I_c}{(r_a - r_i) \cdot h_c} \frac{\mu_0 M}{4\pi} \int_0^{h_c} \int_0^{2\pi} \int_{r_i}^{r_a} \frac{\partial}{\partial r} \int_0^{2\pi} \int_0^R \left(\sum_{\beta=1}^2 \frac{(-1)^\beta \cdot r'}{\Upsilon_\beta} \right) dr'd\varphi' \cdot r\,dr\,d\varphi\,dz, \quad (9)$$

where

$$\Upsilon_\beta = \sqrt{\xi_\beta^2 + x_p^2 + y_p^2 - 2r(x_p \cos(\varphi) + y_p \sin(\varphi)) + 2r'(x_p \cos(\varphi') + y_p \sin(\varphi'))}, \quad (10)$$

$$F_x(x_p, y_p) = \frac{N_c \cdot I_c}{(r_a - r_i) \cdot h_c} \frac{\mu_0 M}{4\pi} \int_0^{h_c} \int_0^{2\pi} \int_{r_i}^{r_a} \frac{\partial}{\partial z} \int_0^{2\pi} \int_0^R \left(\sum_{\beta=1}^2 \frac{(-1)^\beta \cdot r' \cos(\varphi)}{\Upsilon_\beta} \right) dr'd\varphi' \cdot r\,dr\,d\varphi\,dz, \quad (11)$$

$$F_y(x_p, y_p) = \frac{N_c \cdot I_c}{(r_a - r_i) \cdot h_c} \frac{\mu_0 M}{4\pi} \int_0^{h_c} \int_0^{2\pi} \int_{r_i}^{r_a} \frac{\partial}{\partial z} \int_0^{2\pi} \int_0^R \left(\sum_{\beta=1}^2 \frac{(-1)^\beta \cdot r' \sin(\varphi)}{\Upsilon_\beta} \right) dr'd\varphi' \cdot r\,dr\,d\varphi\,dz. \quad (12)$$

Figures 4 to 6 show exemplary the calculation of the force components in the horizontal square plane from -10 mm to $+10$ mm.
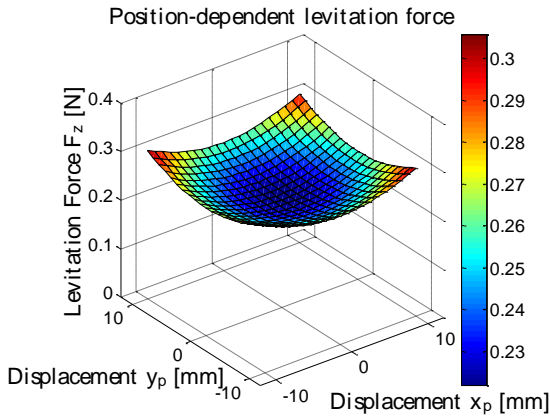
Fig. 4. F_z as a function of the mover position (x_p, y_p).
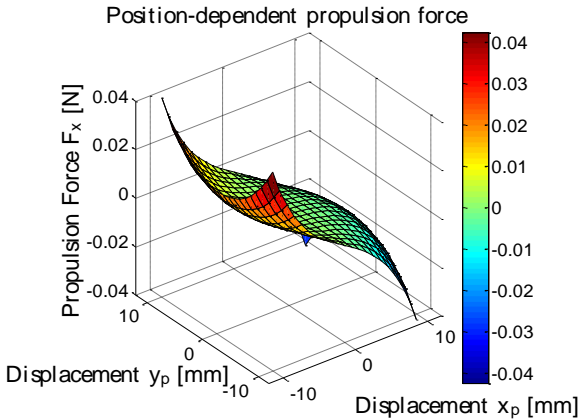
Fig. 5. F_x as a function of the mover position (x_p, y_p).
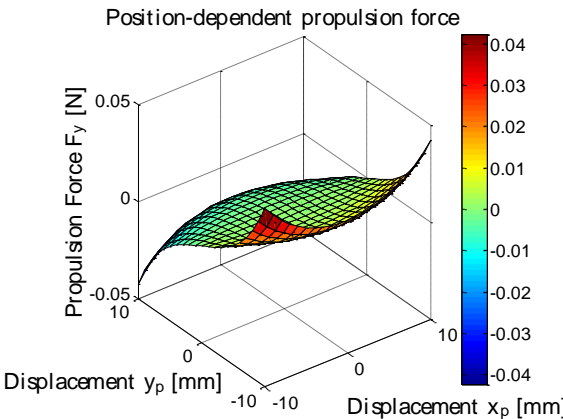
Fig. 6. F_y as a function of the mover position (x_p, y_p).

As can be seen in these figures, all force components are strongly position-dependent due to the non-uniform magnetic field generated by the cylindrical permanent magnet. The force that the circular coil can generate in order to levitate the moving element is minimal at the central position, i.e., $x_p = y_p = 0$. However, this levitation force increases when the magnet deviates laterally away from the central position. The same behavior shows also the destabilizing force curves.

In general, the derived force equations are semi-analytical, i.e., after two consecutive analytical integrations and one analytical derivation with the Symbolic Math Toolbox of MATLAB, it is difficult to express the remaining expression in an analytical form. Therefore, the remaining analytical expression must be converted to a function handle using *matlabFunction* and calculated numerically using the intern numerical integration function *integral3*. In order to simplify the calculation procedure, a MATLAB program is written which contains the analytical and numerical calculation.

IV. VERIFICATION OF THE EQUATIONS

In order to verify the derived equations, a 3D-FEM model of the cylindrical permanent magnet actuator has been implemented in Maxwell 3D. Moreover, a prototype of the permanent magnet actuator was developed in order to measure the generated forces using a precision load cell. The 3D-FEM model and the prototype can be seen in Fig. 7.
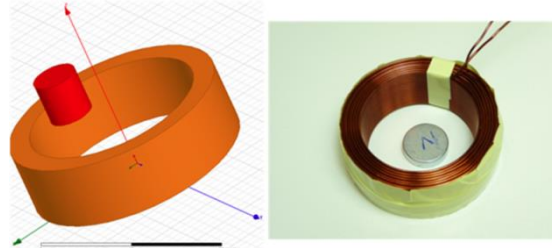
Fig. 7. 3D-FEM model (left) and prototype of the permanent magnet actuator (right).

The permanent magnet used in this study is a neodymium–iron–boron (*NdFeB*) magnet, which has a relative square hysteresis loop with high coercivity and high remanence [33].

Figure 8 (a) compares the current-levitation force curve using the derived equation (9) with the measured results and with 3D-FEM in cases where the mover is at the centered position and the air gap is equal to $z=1$mm.

As can be observed, all curves show a linear relation between the current and the levitation force. This linear relation is as expected, because according to (9), the coil current is directly proportional to the levitation force. A further explanation for the linear relationship is that there are no ferromagnetic materials that can cause a non-linear relationship due to hysteresis and saturation, i.e., from an electromagnetic point of view it is a linear system.

Compared to reluctance actuators, where the

levitation force decreases rapidly as the air gap grows the levitation force in the ironless actuator decreases slightly (Fig. 8 (b)). This advantageous characteristic allows compensating the force variation along the *z*-axes easily using control algorithms.

Figure 8 (c) shows the influence of the horizontal movement on the levitation force. It can be observed that the force increases when the magnet deviates laterally from the central position (similar to Fig. 5 and Fig. 6).
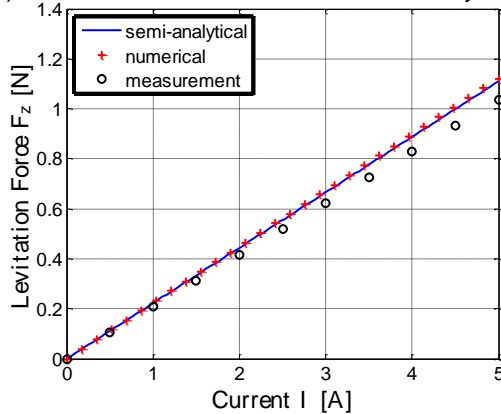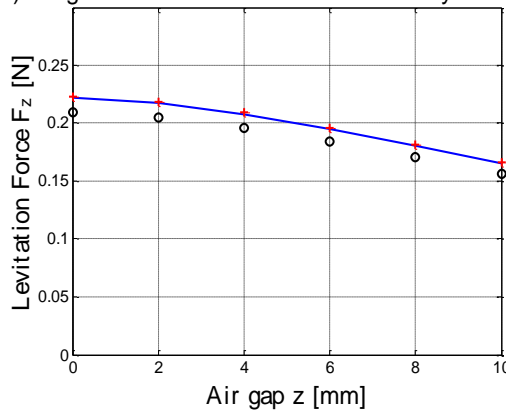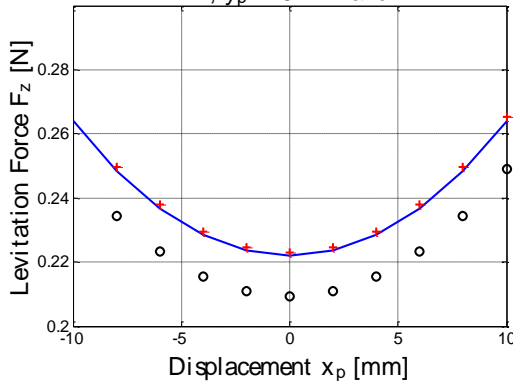
Fig. 8. Measured and calculated curves of the permanent magnet actuator.

If the center of the moving permanent magnet is coaxial with the center of the circular coil, then the destabilizing force components in the *x*- and *y*-direction are zero due to symmetry. However, when the magnet moves from the central position, it experiences also in addition to the levitation force a destabilizing (propulsion) force that tends to push the permanent magnet laterally away from the center position. This unstable behavior can be seen in Fig. 9.
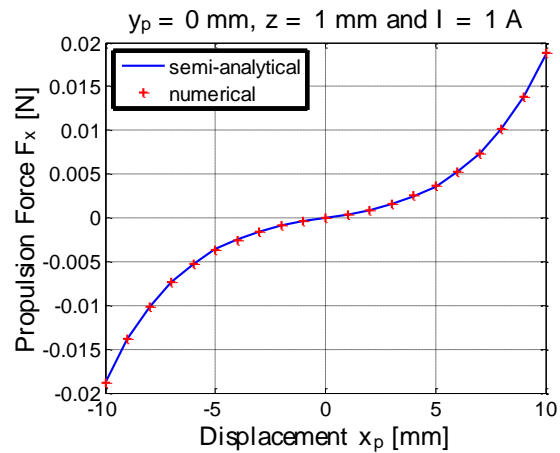
Fig. 9. Destabilizing force F_x.

Since the magnitude of the destabilizing force is too small to measure accurately, we verified the derived equation only with 3D-FEM in case the magnet moves only along the *x*-axes (the *y*-component of the force is zero in this case).

As evident from all the figures, there is an excellent agreement between the calculated forces using the derived equations (9)-(12) and 3D-FEM as well as the measurements.

The maximum error between the solutions of 3D-FEM and our equations is below 1%, whereas the maximum error between our equation and the measurements is below 6%. Apart from the manufacturing tolerances in the magnet and coil dimensions as well as the mechanical and mounting tolerances of our experimental setup, the main reason for the observed error is that our equation assumes an ideal magnet with $\mu_r = 1$. However, the magnetization of the magnet is not perfectly uniform and the relativel permeability of real available *NdFeB* permanent are close to 1 ($\mu_r = 1.05 \ldots 1.1$) with 5% tolerance on magnetization strength [33]. In [21], it is shown that the assumption of an ideal magnet cause an error of approximately 3%.

Despite this, our proposed equations can be used for studying the characteristics of the permanent magnet actuator and these results can be used in the design and real-time control for high precision 6-DoF magnetic levitation systems, e.g., shown in [30] and [31]. Compared to 3D-FEM software, the calculation of the magnetic

fields and the generated forces as well as the optimization of the permanent magnet actuator can be obtained in a very short calculation time.

V. CONCLUSION

In this paper, new and compact equations for calculating the magnetic force components of a cylindrical permanent magnet for ironless magnetic levitation systems were derived and presented. These equations can help to evaluate quickly and precisely the performance of the proposed actuator. Moreover, the derived equations consider also the position-dependent characteristic of the force components. They provide an interesting alternative to 3D-FEM software since they are also accurate and easily applicable for researchers. The semi-analytical results are verified with 3D-FEM and with our prototype which illustrate the accuracy of these force equations.

REFERENCES

[1] S. Verma, H. Shakir and W.-J. Kim, "Novel electro-magnetic actuation scheme for multiaxis nano-positioning," *IEEE Trans. Magn.*, vol. 42, no. 8, pp. 2052-2062, May 2006.

[2] X. Lu and I. Usman, "6D direct-drive technology for planar motion stages," *CIRP Ann.-Manuf. Technol.*, vol. 61, no. 1, pp. 359-362, 2012.

[3] W.-J. Kim and D. L. Trumper, "High-precision magnetic levitation stage for photolithography," *Precis. Eng.*, vol. 22, no. 2, 1998, pp. 66-77, Apr. 1998.

[4] J. W. Jansen, C. M. M. van Lierop, E.A. Lomonova and A. J. A. Vandanput, "Magnetically levitated planar actuator with moving magnets," *IEEE Trans. Ind. Appl.*, vol. 44, no. 4, pp. 1108-1115, July 2008.

[5] L. Guo, H. Zhang, M. Galea, J. Li, W. Lu, and C. Gerada, "Analysis and design of a magnetically levitated planar motor with novel multilayer windings," *IEEE Trans. Magn.*, vol. 51, no. 8, art. no. 8106909, Aug. 2015.

[6] A. C. P. de Klerk, G. Z. Angelis, and J. van Eijk, "Design of a next generation 6 Dof stage for scanning application in vacuum with nanometer accuracy and mGauss magnetic stray field," *Proc. Annu. Meeting-Amer. Soc. Precis. Eng.*, pp. 60-63, 2004.

[7] T. J. Teo, I.-M. Chen, G. Yang, and W. Lin, "Magnetic field modeling of a dual-magnet config-uration," *J. Appl. Phys.*, vol. 102, art. no. 074924, 2007.

[8] M. Lahdo, T. Ströhla, and S. Kovalev, "Magnetic propulsion force calculation of a 2-DoF large stroke actuator for high-precision magnetic levitation system," *ACES Journal*, vol. 32, no. 8, Aug. 2017.

[9] A. Shiri and A. Shoulaie, "Calculation of the magnetic forces between planar spiral coils using concentric rings," *ACES Journal*, vol. 25, no. 5,

May 2010.

[10] R. Muscia, "Magneto-mechanical model of passive magnetic axial bearings versus the eccentricity error - Part 1: physical mathematical model," *ACES Journal*, vol. 32, no. 8, Aug. 2017.

[11] J. L. G. Janssen, J. J. H. Paulides, and E. A. Lomonova, "3-D analytical calculation of the torque between perpendicular magnetized magnets in magnetic suspensions," *IEEE Trans. Magn.*, vol. 47, no. 10, pp. 4286-4289, Oct. 2011.

[12] S. Wu, S. Zuo, X. Wu, F. Lin, and J. Shen, "Magnet modification to reduce pulsating torque for axial flux permanent magnet synchronous machines," *ACES Journal*, vol. 31, no. 3, Mar. 2016.

[13] R. Bjork, A. Smith, and C. R. H. Bahl, "Analysis of the magnetic field, force and torque for two-dimensional Halbach cylinders," *J. Magn. Magn. Mater.*, vol. 322, no. 1, pp. 131-141, 2010.

[14] T. R. N. Mhiócháín, D. Weaire, S. M. McMurry, and J. M. D. Coey, "Analysis of torque in nested magnetic cylinders," *J. Appl. Phys.*, vol. 86, no. 11, pp. 3412-3424, 1999.

[15] L. Guo, H. Zhang, M. Galea, J. Li, and C. Gerada, "Multiobjective optimization of a magnetically levitated planar motor with multilayer windings," *IEEE Trans. Ind. Elect.*, vol. 63, no. 6, pp. 3522-3532, June 2016.

[16] J. W. Jansen, J. L. G. Janssen, J. M. M. Rovers, J. J. H. Paulides, and E. Lomonova, "(Semi-) analytical models for the design of high precision permanent magnet actuators," *Int. Compumag. Soc. Newslett.*, vol. 16, no. 02, pp. 4-17, 2009.

[17] J. W. Jansen, J. P. C. Smeets, T. T. Overboom, J. M. M. Rovers, and E. A. Lomonova, "Overview of analytical models for the design of linear and planar motors," *IEEE Trans. Magn.*, vol. 50, no. 11, art. no. 8206207, Dec. 2014.

[18] H. Zhang, B. Kou, H. Zhang, and Y. Xi, "A three-degree-of-freedom short-stroke Lorentz-force-driven planar motor using a Halbach permanent magnet array with unequal thickness," *IEEE Trans. Ind. Elect.*, vol. 62, no. 6, pp. 3640-3650, June 2015.

[19] K. S. Jung and Y. S. Baek, "Study on a novel contact-free planar system using direct drive DC coils and permanent magnets," *IEEE/ASME Trans. Mech.*, vol. 7, no. 2, pp. 35-43, Mar. 2002.

[20] M.-Y. Chen, T.-B. Lin, S.-K. Hung, and L.-C. Fu, "Design and experiment of a macro-micro planar maglev positioning system," *IEEE Trans. Ind. Elect.*, vol. 59, no. 11, pp. 4128-4139, Nov. 2012.

[21] J. M. M. Rovers, J. W. Jansen, and E. A. Lomonova, "Analytical calculation of the force between a rectangular coil and a cuboidal permanent magnet," *IEEE Trans. Magn.*, vol. 46, no. 6, pp. 1656-1659, June 2010.

[22] M. Lahdo, T. Ströhla, and S. Kovalev, "Repulsive

magnetic levitation force calculation for a high precision 6-DoF magnetic levitation positioning system," *IEEE Trans. Magn.*, vol. 53, no. 3, Mar. 2017.

[23] J. Peng, Y. Zhou, and G. Liu, "Calculation of a new real-time control model for the magnetically levitated ironless planar motor," *IEEE Trans. Magn.*, vol. 49, no. 4, pp. 1416-1422, Apr. 2013.

[24] F. Liu, M. Zhang, Y. Zhu, and C. Hu, "A real-time model of ironless planar motors with stationary circular coils," *IEEE Trans. Magn.*, vol. 51, no. 7, art. no. 8203110, July 2015.

[25] C. M. M. van Lierop, J. W. Jansen, A. A. H. Damen, E. A. Lomonova, P. P. J. van den Bosch, and A. J. A. Vandenput, "Model-based commutation of a long-stroke magnetically levitated linear actuator," *IEEE Trans. Ind. Appl.*, vol. 45, no. 6, pp. 1982-1990, Nov./Dec. 2009.

[26] S. Verma, W.-J. Kim, and H. Shakir, "Multi-axis maglev nanopositioner for precision manufacturing and manipulation applications," *IEEE Trans. Ind. Appl.*, vol. 41, no. 5, pp. 1159-1167, Sep./Oct. 2009.

[27] W. Robertson, B. Cazzolato, and A. Zander, "Axial force between a thick coil and a cylindrical permanent magnet: Optimizing the geometry of an electromagnetic actuator," *IEEE Trans. Magn.*, vol. 48, no. 9, pp. 2479-2487, Sep. 2012.

[28] R. Ravaud, G. Lemarquand, S. Babic, V. Lamarquand, and C. Akyel, "Cylindrical magnets and coils: Fields, forces, and inductances," *IEEE Trans. Magn.*, vol. 46, no. 9, pp. 3585-3590, Sep. 2010.

[29] H. Zhang, B. Kou, Y. Jin, and H. Zhang, "Modeling and analysis of a new cylindrical magnetic levitation gravity compensator with low stiffness for the 6-DOF fine stage," *IEEE Trans. Ind. Elect.*, vol. 62, no. 6, pp. 3629-3639, June 2015.

[30] P. Berkelman and M. Dzadovsky, "Magnetic levitation over large translation and rotation ranges in all directions," *IEEE/ASME Trans. Mech.*, vol. 18, no. 1, pp. 44-52, Feb. 2013.

[31] Y. C. Lai, Y. L. Lee, and J. Y. Yen, "Design and servo control of a single-deck planar maglev stage," *IEEE Trans. Magn.*, vol. 43, no. 6, pp. 2600-2602, June 2007.

[32] S. Earnshaw, "On the nature of the molecular forces which regulate the constitution of the luminiferous ether," *Trans. Cambridge Philos. Soc.*, vol. 7, pp. 97-112, Mar. 1839.

[33] E. P. Furlani, *Permanent Magnet and Electro-mechanical Devices: Materials, Analysis and Application*. 6th Edition, Academic Press, London, 2001.

[34] W. Braunbek, "Freischwebende Körper im elektrischen und magnetischen Feld," Z. Physik, vol. 112, pp. 753-763, 1939.

Mousa Lahdo received the diploma degree in Electrical Engineering from the University of Applied Sciences Mittelhessen in Friedberg, Germany, in 2012. Since 2015, he is a Research Associate and Ph.D. student at the Department of Mechatronics, Ilmenau University of Technology. His current research interests include magnetic bearings and magnetic levitation systems and novel integrated electromechanical actuators and motors.

Tom Ströhla researches at the Department of Mechatronics, Ilmenau University of Technology. He teaches Electrical Drive Systems as well as Mechanical and Fluid Actuators. He completed his Ph.D. on the subject of model-based design of electromagnets and he was involved in the development of the draft for the software SESAM. In numerous research and industrial projects, he gained experience in the design of electromagnetic drives and the magnetic measurement technology. He is co-author of several books on electromagnets and theoretical electrical engineering.

Sergej Kovalev is Professor for Electrical Drives, Electrical Engineering and Measurement Systems at the University of Applied Sciences in Friedberg, Germany, since 2012. He enrolled as a Ph.D. candidate in the Mechatronics Department at Technical University Ilmenau, Germany, in 1995 and received his Ph.D. degree in 2001. He has 14 years industrial experience in the R&D departments at different firms in Germany. His research interest is the mechatronics of precision engineering, especially direct drives.

Identification of the Structural Deviations Impacting the Dynamics of a Flexible Multispan Rotor on Full Electromagnetic Suspension

Viktor F. Ovchinnikov, Mikhail Y. Nikolaev, Vasily N. Litvinov, and Denis V. Kapitanov

Research Institute of Mechanics
Lobachevsky State University of Nizhny Novgorod, Russia
minick@mech.unn.ru

Abstract ─ An algorithm for accounting for identification of the structural deviations impacting the dynamics of a flexible multispan rotor on full electromagnetic suspension in an actively developed computer model of dynamics of a flexible rotor on active magnetic bearings is presented. The algorithm is illustrated by applying it against the scale model of a rotor on active magnetic bearings.

Index Terms ─ Active magnetic bearing, computer model of dynamics of a flexible rotor on active magnetic bearings, dynamics influenced by structural deviations, flexible rotor.

I. INTRODUCTION

There are rather strict requirements maintained for the vibration level of rotor systems, as the lower vibration level is, the higher are rotor's running qualities and reliability. The problem of lowering the vibration level is relevant for all rotor systems, especially for the systems suspended on active magnetic bearings (AMB) as the rigidity of AMB is substantially lower compared to traditional sliding bearings, thus same level of impact on the rotor on AMB leads to higher vibration level.

The main cause of rotor vibration during normal operation is the imbalance, so to minimize it there is always a mandatory balancing procedure performed during the assembly of the rotor. Though residual imbalance is still always present, it could be partially compensated for after the rotor is installed in place.

Today a multispan flexible rotor on AMB is seen as a tool for solving relevant issues of energy efficiency and energy savings in the nuclear power engineering [1, 2]. Such rotors could also be utilized in vertical axial wind power plants allowing for efficient transformation of wind energy into electricity [3-5].

The multispan flexible rotor is intended to be a core part of the turbomachine of new nuclear power plant having high-temperature gas-cooled reactor. During the balancing procedure of the scale model of the rotor on AMB [6] it was found that certain structural parameters, despite being in tolerable limits according to design documentation, produce substantial effects on the dynamics of the rotor and thusly on the procedure of identification of the residual imbalance. Discovered effects showed that the previously developed method of balancing the rotor [7, 8] needs to be improved taking into account identification of the structural deviations affecting dynamics of the multispan flexible rotor on full electromagnetic suspension.

II. THE DESCRIPTION OF THE IDENTIFICATION METHOD

The method includes both numerical and experimental parts. The numerical one uses a discrete mathematical model of dynamics of a multispan flexible rotor on AMB [9, 10 and their references] adapted for the rundown mode. The input parameters of the model could be divided in two groups. First ones are the parameters with known values, and second ones are the parameters which are unpredictable and cannot be reliably computed but have to be obtained by solving the reverse problem.

The experimental part is based on utilizing the regular control system of AMB which allows for simultaneous recording of the following parameters of dynamics of the rotor:

- rotation angle and angular speed of the rotor;
- displacements of the rotor in the cross-sections where horizontal sensors are installed;
- currents in the AMB coils.

The oscillograms of the sensors are the input data for solving the reverse problem and for defining the unknown input parameters of the model.

To minimize the dependency of the solution of the reverse problem from the accuracy of measuring the experimental data it is advised to minimize the number of defined parameters. This is done by selecting and processing modes which are affected only by the desired parameters. One of such modes is the rundown mode during which no external forces except the ones from axial and radial AMB are impacting the rotor.

To solve the reverse problem portions of the rundown recordings where rotation frequency could be considered constant are used; such portions could be

seen as stable modes with constant angular speed. The portions that are close to critical rotation frequencies are excluded because at such frequencies dynamics of the rotor is impacted by inner and outer dissipation forces which are very hard to measure for complex structures.

A. The model of dynamics of a multispan flexible rotor

During the formulation of the discrete mathematical model of dynamics of a multispan flexible rotor on AMB the rotor is taken as elastic heterogeneous rod with piecewise characteristics with circular sections. For description of deformations and displacements of each of the rotor sections the oscillation equations of elastic rod is used (the Timoshenko model of a beam [11]). These elements are coupled by three types of concentrated elements: rigid joint, elastic joint and support point of the rotor (AMB). To create the mathematical model of the machine certain combination of the aforementioned basic elements is used.

In the mechanical model of the rotor Cartesian coordinate system $0xyz$ is used for describing the movements of the rotor. $0x$ axis is taken as vertical one coinciding with the rotation axis of the unstrained rotor. It is assumed that for all the rotor characteristics and for the radial AMB axial symmetry conditions stand. Current position of the elements of the rotor is defined by: linear displacement U; vector of angular displacements of the normal cross-section Θ, angular displacements incurred by own rotation with angular speed ω. The deformation of material of the rotor elements creates the tension in the normal cross-section which are statically equivalent to inner torque M and inner force Q applied in the center of the bending. Vector Q includes intersecting stress, and M includes bending torque in two directions. As the rotor element moves it is being affected by a distributed force q applied on the axis of the element.

When projected to horizontal axes $0y$ and $0z$, the motion equations of the element of the rotor including gyroscopic forces are:

$$\frac{\partial Q_y}{\partial x} = m\frac{\partial^2 U_y}{\partial t^2} - q_y,$$

$$\frac{\partial M_z}{\partial x} = -Q_y + \rho I\frac{\partial^2 \Theta_z}{\partial t^2} + 2\omega\rho I\frac{\partial \Theta_y}{\partial t},$$ (1)

$$\frac{\partial \Theta_z}{\partial x} = \frac{1}{EI}M_z, \quad \frac{\partial U_y}{\partial x} = \Theta_z + \frac{1}{GFk^*}Q_y,$$

$$\frac{\partial Q_z}{\partial x} = m\frac{\partial^2 U_z}{\partial t^2} - q_z,$$

$$\frac{\partial M_y}{\partial x} = Q_z + \rho I\frac{\partial^2 \Theta_y}{\partial t^2} - 2\omega\rho I\frac{\partial \Theta_z}{\partial t},$$

$$\frac{\partial \Theta_y}{\partial x} = \frac{1}{EI}M_y, \quad \frac{\partial U_z}{\partial x} = -\Theta_y + \frac{1}{GFk^*}Q_z.$$

Here ρ, E, G are density, modulus of elasticity and shear modulus of the material of the element. F, I are area and axial moment of inertia of the normal cross-section of the element. $m=\rho{\cdot}F$ is the distributed mass of the tube. k^* is the coefficient accounting for nonuniformity of distribution of tangential stress over the cross-section of the element. x is the coordinate along the rotation axis; t is time. Lower index stands for projection on respective axis ($0y$ or $0z$).

The presented model of transverse oscillations of the rotor is used to develop the method of identification of imbalance characteristics when the following are present: non-orthogonality of disc of the axial AMB to the rotation axis; misalignment of the rotor elements in the elastic joints of the elements (elastic clutches). The studied effects lead to amplitude-constant harmonic impact on the rotor on the frequency of the rotor revolution. If the only effects present in the system are these, and the rotor and AMB are axisymmetric, then the rotor movements in $0xy$ and $0xz$ planes will be harmonic and identical except that $0xz$ movements will lag by a quarter of the period. Using complex representation of the bending forms of the rotor in the stationary forced oscillation mode the equations (1) could be written as follows:

$$Q_y = Q(x)\cdot\exp j\omega t, \quad M_z = M(x)\cdot\exp j\omega t,$$

$$\Theta_z = \Theta(x)\cdot\exp j\omega t, \quad U_y = U(x)\cdot\exp j\omega t,$$

$$q_y = q(x)\cdot\exp j\omega t, \quad \mu_z = \mu(x)\cdot\exp j\omega t,$$

$$\Theta_y = -\Theta(x)\cdot\exp j(\omega t - \pi/2) = j\Theta_z,$$

$$\frac{dQ}{dx} = -\omega^2\cdot m\cdot U - q,$$

$$\frac{dM}{dx} = -Q - 3\cdot\omega^2\rho I\cdot\Theta,$$ (2)

$$\frac{d\Theta}{dx} = \frac{1}{EI}M,$$

$$\frac{dU}{dx} = \Theta + \frac{1}{GFk^*}Q.$$

To solve the differential equations (2) we used the expansion of the solution by the basis of orthogonal functions $Q_k(x), M_k(x), \Theta_k(x), U_k(x)$ defined by solving the boundary problem of the rotor where the dependency between the inner forces and movements at the elements is expressed by:

$$\frac{dQ_k}{dx} = -\omega_k^2\cdot m\cdot U_k,$$

$$\frac{dM_k}{dx} = -Q_k - 3\cdot\omega_k^2\cdot\rho I\cdot\Theta_k,$$ (3)

$$\frac{d\Theta_k}{dx} = \frac{1}{EI}M_k,$$

$$\frac{dU_k}{dx} = \Theta_k + \frac{1}{GFk^*}Q_k.$$

The form number k corresponds to Eigen frequency ω_k. Equations (3) differ from same equations for Eigen oscillation modes of a nonrotating rotor by a factor of "3" in the second addendum in the right-hand member of the second equation. This difference is caused by the impact of gyroscopic forces. It is assumed that the AMB control system forms a linear control law of generating the force depending on the rotor displacement [12], so the boundary conditions placed in the cross-sections where radial AMB are installed correspond to the rotor resting on elastic supports. The rigidity of these supports is defined by the parameters of the AMB and the used control laws. Also the forms account for the impact from axial AMB which is equivalent to the one from springs of negative rigidity [10] appearing on rotor inclinations. The rigidity of such springs is defined by the structure of the axial AMB and by the forces they generate.

The shafting in question is taken as L elastically coupled rotors. Elastic joints are located at cross-sections with coordinate $x = x_i$ ($i = \overline{1, L}$). It is assumed that at each elastic joint there are linear and angular displacements of axes of the elements of rotors, which are characterized by components U_{1i}^0, U_{2i}^0 and $\Theta_{1i}^0, \Theta_{2i}^0$ in the coordinate system attached to the rotor. The shafting has N radial AMB in the cross-section with coordinates $x = x_n$ which are characterized by rigidity c_n ($n = \overline{1, N}$). The shafting is supported in the vertical direction by N_0 axial AMB placed at $x = x_\nu$ ($\nu = \overline{1, N_0}$). Due to non-orthogonality of the disc of axial AMB to rotation axis the rotor is impacted by a constant torque which is defined by M_1^ν, M_2^ν components in the coordinate system attached to the rotor. The rotor structure is characterized by the imbalance which creates a distributed force along $0y$ axis:

$$q_y = \omega^2 m[e_1(x) \cdot \cos\varphi - e_2(x) \cdot \sin\varphi]. \tag{4}$$

Here $e_i(x)$ are components of the eccentricity vector in the coordinate system attached to the rotor ($i=1,2$); φ is the rotation angle of the rotor $\left(\dfrac{d\varphi}{dt} = \omega\right)$.

To compose the numerical discrete model of dynamics of the rotor, the movements of the rotor along the $0y$ axis are expanded by eigenmodes:

$$U_y = \sum_{k=1}^{K} a_k U_k(x), \ \Theta_z = \sum_{k=1}^{K} a_k \Theta_k(x),$$
$$M_z = \sum_{k=1}^{K} a_k M_k(x), \ Q_y = \sum_{k=1}^{K} a_k Q_k(x). \tag{5}$$

Here a_k are time-dependent expansion coefficients filling the role of generalized coordinates in the discrete model; K is the amount of eigenmodes used in the approximation of the solution. By using Lagrange equations we have defined the discrete model of movement equations of the rotor:

$$m_0 \frac{d^2 a}{dt^2} + m_0 \Omega_K a = \alpha \cdot D^*(d, I_0)$$
$$+ \omega^2[f_1 \cos\phi - f_2 \sin\phi] + R_1 \cos\phi - R_2 \sin\phi,$$
$$D^*(d, I_0) = c \cdot d + D(d, I_0),$$
$$\alpha = \{\alpha_{kn}\}, \quad \alpha_{kn} = U_k(x_n),$$
$$c = diag(c_1, ..., c_N), \quad \Omega_K = diag(\omega_k^2),$$
$$f_j = \{f_{kj}\}, \quad f_{kj} = \int_0^l m \cdot e_j(x) \cdot U_k(x) dx,$$
$$k = \overline{1, K}, \quad j = 1, 2,$$
$$R_1 = \Theta_0 \cdot M_2 + Q_0 \cdot U_1^0 + M_0 \cdot \Theta_2^0,$$
$$R_2 = -\Theta_0 \cdot M_1 + Q_0 \cdot U_2^0 - M_0 \cdot \Theta_1^0,$$
$$M_1 = \left(M_j^1, ..., M_j^\nu, ..., M_j^{N_0}\right)^T,$$
$$U_j^0 = \left(U_{j1}^0, ..., U_{ji}^0, ..., U_{jL}^0\right)^T,$$
$$\Theta_j^0 = \left(\Theta_{j1}^0, ..., \Theta_{ji}^0, ..., \Theta_{jL}^0\right)^T, \quad j = 1, 2,$$

$$\Theta_0 = \begin{vmatrix} \Theta_1(x_1) & ... & \Theta_1(x_{N_0}) \\ ... & ... & ... \\ \Theta_K(x_1) & ... & \Theta_K(x_{N_0}) \end{vmatrix},$$

$$Q_0 = \begin{vmatrix} Q_1(x_1) & ... & Q_1(x_L) \\ ... & ... & ... \\ Q_K(x_1) & ... & Q_K(x_L) \end{vmatrix},$$

$$M_0 = \begin{vmatrix} M_1(x_1) & ... & M_1(x_L) \\ ... & ... & ... \\ M_K(x_1) & ... & M_K(x_L) \end{vmatrix}. \tag{6}$$

Here $a=(a_1, ..., a_K)$ is the K-dimensioned vector of generalized coordinates; d is the N-dimensioned vector representing displacements of the rotor in the cross-sections where radial AMB are placed; m_0 is the mass of the rotor. $D(d, I_0)$ is the vector of active forces generated by AMB; I_0 is the $4N$-dimensioned vector describing the currents in the AMB coils. R_j is the vector of generalized forces accounting for non-orthogonality of discs of axial AMB to rotation axis and misalignment in the elastic clutches. Upper index "T" stands for operation of transposing of a matrix. It is worth noting that equations (6) also describe the movements of the rotor along the $0z$ axis.

B. Mathematical statement of the identification problem

It is assumed that transversal movements of the rotor are monitored by P sensors ($P \geq N$) placed at the cross-sections with coordinates x_p ($p = \overline{1, P}$). The case of $P=N$ corresponds to the situation when the machine has only regular sensors of the control system of the AMB. As shown in (5), dynamic movements of the rotor in the cross-sections of the sensors $U = (U^1, U^2, ..., U^P)^T$ are bound to the introduced vector of generalized coordinates by the equation:

$$U = \beta \cdot a, \quad \beta = \{\beta_{pk}\}, \quad \beta_{pk} = U_k(x_p),$$
$$k = \overline{1,K}, \; p = \overline{1,P}. \tag{7}$$

The mathematical problem of identification of the imbalance, forces and torques from the axial AMB, misalignment characteristics in the elastic clutches is placed by utilizing the equations (6) and (7) and by using known (experimentally measured) vector functions $U(t)$ and $I(t)$ and to define the components of the vectors $f_j, M_j, U_j^0, \Theta_j^0$ ($j=1,2$). The vector of active forces $D(d, I_0)$ is computed using known properties of the AMB, measured currents in the coils of the AMB, and rotor displacements in the cross-sections where axial AMB are installed.

To exclude the errors caused by the presence of high-frequency noise in the real-world data it makes sense to consider equations (6) and (7) in the frequency region. Forced oscillations of the system on the constant rotation frequency could be viewed as harmonic as a first approximation:

$$a(t) = a^{(1)} \cos\varphi + a^{(2)} \sin\varphi,$$
$$U(t) = U_1 \cos\varphi + U_2 \sin\varphi. \tag{8}$$

The vector $D^*(d, I_0)$ has complex time dependency because the control system is nonlinear in nature, but it is possible to extract harmonic part on the rotation frequency of the rotor, and as a first approximation the following is true:

$$D^*(t) = D_1 \cos\varphi + D_2 \sin\varphi. \tag{9}$$

After substitution of (8) and (9) to (6) and (7) we can get the following:

$$m_0 \cdot \left(\Omega_K - \omega^2 \cdot E_K\right) \cdot a^{(1)} - \alpha^T \cdot D_1 =$$
$$\omega^2 \cdot f_1 + \Theta_0 \cdot M_2 + Q_0 \cdot U_1^0 + M_0 \cdot \Theta_2^0,$$
$$m_0 \cdot \left(\Omega_K - \omega^2 \cdot E_K\right) \cdot a^{(2)} - \alpha^T \cdot D_2 = \tag{10}$$
$$-\omega^2 \cdot f_2 + \Theta_0 \cdot M_1 - Q_0 \cdot U_2^0 + M_0 \cdot \Theta_1^0,$$
$$U_1 = \beta \cdot a^{(1)}, \quad U_2 = \beta \cdot a^{(2)}.$$

By elimination of vectors $a^{(1)}, a^{(2)}$ we can get matrix equations against unknown vectors $f_j, M_j, U_j^0, \Theta_j^0$ ($j=1,2$):

$$U_1 - H \cdot \alpha^T \cdot D_1 = \omega^2 \cdot H \cdot f_1 + H \cdot \Theta_0 \cdot M_2$$
$$+ H \cdot Q_0 \cdot U_1^0 + H \cdot M_0 \cdot \Theta_2^0,$$
$$U_2 - H \cdot \alpha^T \cdot D_2 = -\omega^2 \cdot H \cdot f_2 + H \cdot \Theta_0 \cdot M_1$$
$$- H \cdot Q_0 \cdot U_2^0 + H \cdot M_0 \cdot \Theta_1^0,$$
$$H = \beta \cdot G, \quad G = diag\left(\frac{1}{m_0 \cdot \left(\omega_k^2 - \omega^2\right)}\right),$$
$$A(\omega) \cdot g_j = l_j(\omega), \tag{11}$$
$$l_j(\omega) = U_j - H \cdot \alpha^T \cdot D_j, \quad j = 1,2,$$
$$A(\omega) = \left(\omega^2 \cdot H, H \cdot \Theta_0, H \cdot Q_0, H \cdot M_0\right),$$
$$g_1 = \left(f_1^T, M_2^T, U_1^{0T}, \Theta_2^{0T}\right)^T,$$
$$g_2 = \left(-f_2^T, M_1^T, -U_2^{0T}, \Theta_1^{0T}\right)^T.$$

Equations (11) define the connection between the structural deviations and measured characteristics of the movements of the rotor.

The P amount in equations in (11) is usually less than the amount of unknown quantities ($K+N^0+2L$). The unknown are components of the vectors $f_j, M_j, U_j^0, \Theta_j^0$. Also, some of the equations might be linearly dependent, so to solve the practical problem it is necessary to perform measurements over a series of frequencies $\omega^{(i)}$, combine the equations for all those series and solve the combined equations set as a whole:

$$A(\omega^{(i)}) \cdot g_j = l_j(\omega^{(i)}), \quad i = \overline{1, I^*}, \quad j = 1,2. \tag{12}$$

Here I* is the amount of taken portions of recordings of the rotor rundown. It is obvious that, when we increase the amount of experimental data, the accuracy of identification of residual imbalance of the rotor also increases. However, in such case the amount of equations in the set (12) is going to be bigger than amount of unknown quantities (overdetermined system), and due to noises and errors in the measurement some of the equations will become contradictory. To solve such problems there are special mathematical methods based on least-squares method [13].

III. VERIFICATION OF THE COMPUTER IMPLEMENTATION OF THE METHOD

The described method was implemented in the software to identify the residual imbalance of a rotor. Verification of the method and the implementation was conducted against the shafting comprised by two elastically coupled rotors 140 mm in diameter (see Fig. 1).
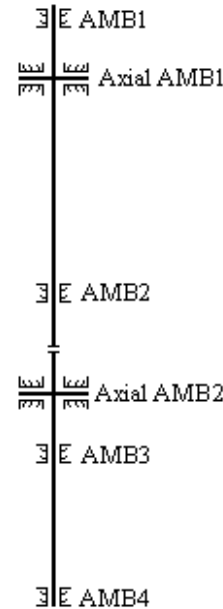
Fig. 1. Scheme of the experimental shafting.

Mass of the upper rotor is 600 kg, length is 4.86 m. Mass of the lower rotor is 420 kg, length is 3.37 m. Centers of radial AMS are located at 0.05 m, 4.62 m, 5.4 m and 8.18 m from the upper end of the shafting. Axial AMB are located at 0.35 m and 5.09 m. Outer radii of the discs of the axial AMB are 0.235 m. Rigidity of radial AMB is 800 N/mm. Elastic clutch shear stiffness is 40 N/mm, bending stiffness 700 N/mm. Computed lowest critical frequencies are (in Hz): 7.18, 9.51, 13.02, 13.81, 29.32, 54.47, 72.27, 139.50. Operational rotation frequency of the shafting is 60 Hz.

For verification the numerical model of the shafting had the following structural deviations introduced:

- Imbalance of 6.042 kg*mm in the upper rotor, placed at 0.025 m from the upper end; directed at angle $\psi = 0^0$ in the coordinate system attached to the rotor.
- Imbalance 1.813 kg*mm in the lower rotor placed at 6.625 m from the upper end of the shafting; directed at $\psi = 270^0$.
- Non-orthogonality of the disc of axial AMB1 to the rotation axis with angle being $\Theta^* = 0.0005$ rad. The direction of horizontal rotation of the disc in the coordinate system attached to the rotor is described as $\psi = 0^0$.
- Non-orthogonality of the disc of axial AMB2 to the rotation axis with angle being $\Theta^* = 0.0008$ rad. Directed at $\psi = 90^0$.
- Linear shear of two rotors' axes in the elastic clutch is 1 mm. The direction of the shear in the coordinate system attached to the rotor is described as $\psi = 0^0$.
- Angular shear of two rotors' axes in the elastic clutch is 0.1 rad. The shear's plane is characterized by $\psi = 90^0$.

Using the computer model of dynamics of multispan flexible rotor on AMB we had conducted the calculations of spin-up mode of the shafting with acceleration of 0.25 Hz/s to rotation frequency 70 Hz. Figure 2, black curves depict dependencies of displacement amplitudes from rotation frequency at the cross-sections where the radial AMBs are installed.

It is obvious from the picture that displacement amplitudes are close to the clearance in the retainer bearings (0.4 mm) when passing critical frequencies. This is unacceptable for the rotors on AMB as, based on recommendations [14], rotor displacements should be no more than half of the clearance in the retainer bearings. Therefore, for the shafting in question it is necessary to conduct certain measures aimed at reducing the impact on the rotor dynamics from the structural deviations. It could be done based on the knowledge of the properties of the aforementioned deviations determined by the identification method shown above. In this example displacement sensors are installed at AMB cross-sections

as well as at 2.42 m and 6.61 m from the upper end of the shafting. The identification method used 13 portions of the rundown recordings (with rotation frequency, Hz): 3.0, 4.0, 5.0, 8.0, 12.0, 16.0, 20.0, 25.0, 35.0, 40.0, 45.0, 50.0, 60.0, 65.0. Each portion is 16.0 m long. The identification results for the components of the vector of the modal imbalance f_{kj}^* and comparison with the "precise" values f_{kj}, computed using (6), are presented in the Table 1.
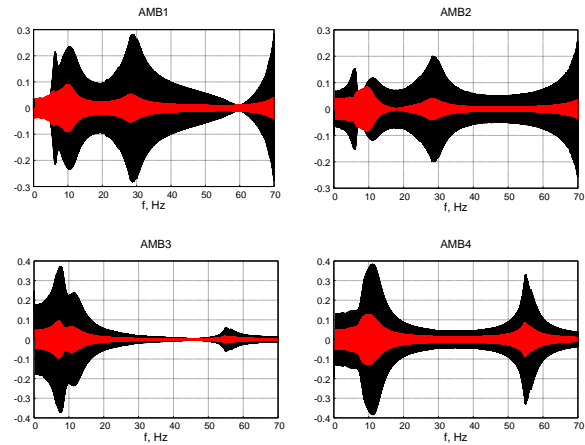
Fig. 2. Dependency of the displacement amplitudes from rotation frequency. Black curves: deviations are present; red curves: deviations are compensated by reducing the imbalance and misalignments.

Table 1: Comparison of the identified and the "precise" imbalance

k	"Precise" Values, kg*mm		Identified, kg*mm		Difference	
	f_{k1}	f_{k2}	f_{k1}^*	f_{k2}^*	Δf_k	δ_k, %
1	-5.63	0.11	-5.39	0.29	0.3	5.3
2	0.81	2.81	0.40	3.14	0.53	18.0
3	-11.82	0.49	-11.42	-0.80	1.35	11.4
4	-3.29	-0.95	-3.50	-1.30	0.41	11.9
5	15.47	0.02	15.22	-0.01	0.25	1.6
6	0.07	-3.27	0.11	-3.11	0.17	5.0
7	-14.49	0.11	-14.27	-1.31	1.44	9.9
8	-13.99	-0.02	-13.66	1.20	1.26	9.0

As modal imbalance, generalized forces, torques from axial AMB, linear and angular shears of rotors' axes in the elastic clutch are vector values. The difference in Table 1 is computed using the following formula:

$$\Delta A = \sqrt{\left(A_1^* - A_1 \right)^2 + \left(A_2^* - A_2 \right)^2},$$

$$\delta = 100 \cdot \Delta A / A, \quad A = \sqrt{A_1^2 + A_2^2},$$

where it is clear that for all modes except k=2, the relative difference is less than 12%. For mode k=2 high

level of relative difference is caused by small value of the modal imbalance – absolute difference for this mode is on par with other modes.

Table 2 presents the values of torques M_j^ν from axial AMB calculated by using the given structural parameters as well as identified using the method presented.

Table 2: Comparison of the identified and the "precise" torques

ν	"Precise" Value, N*m		Identified, N*m		Difference	
	M_1^ν	M_2^ν	$M_1^{*\nu}$	$M_2^{*\nu}$	ΔM_ν	δ_ν, %
1	0	108.3	-2.3	125.5	17.4	16.0
2	-123.3	0	-121.4	13.5	13.6	11.1

Table 3 presents linear and angular shears of rotors' axes in the elastic clutch U_j^0, Θ_j^0 and respective properties U_j^{*0}, Θ_j^{*0} retrieved by identification.

The results that are displayed in Tables 1-3 show that the developed method presented in this paper could be satisfactory used to identify structural deviations impacting the dynamics of the rotor. The information obtained by the method allows implementing specific measures for compensating or minimizing those deviations. The measures include mechanical work for improving the physical rotor structure (placing balance weights, straightening of the elastic clutch) and using control laws for AMB that compensate for the effect of harmonic forces caused by structural deviations [10].

Table 3: Comparison of the "precise" and the identified shear

Shear	"Precise"		Identified		Difference	
	j=1	j=2	j=1	j=2	Δ	δ, %
U_j^0, mm	1,0	0	0.961	0.006	0.04	3.9
Θ_j^0, rad	0	0.1	0.0017	0.075	0.025	25.0

For the example used in the verification by utilizing the data from the tables it is possible to: reduce the imbalance by 88%; reduce the non-orthogonality angle of upper axial AMB by 84%, and to lower axial AMB by 88%; reduce linear and angle shears in the elastic clutch by 96% and 75%, respectively. The displacement amplitudes after such measures are depicted on Fig. 2 by red curves. These red curves show that in all the frequency range during spin-up the displacements are no more than 130 microns. In the stable operation mode displacements at the cross-sections of AMB are no more than 30 microns. Such level of displacement according to [14] is in the "A" zone which is typical vibration for new machines being introduced in the operation.

IV. CONCLUSION

We have developed the numerical-experimental method to identify structural deviations of a multispan flexible rotor on full electromagnetic suspension. Examples of the structural deviations taken into account are: rotor imbalance, non-orthogonality of the discs of the axial AMB to the rotation axis, misalignment of the elements of the rotor in the elastic clutch. Such structural deviations are creating harmonic forces with the frequency equal to rotation frequency. The identification method is based on solving the reverse dynamics problem: from experimentally measured rotor displacement we calculate the properties of the forces which caused those displacements. The model and the software implementation are verified against the sample shafting comprised by two rotors coupled by an elastic clutch.

ACKNOWLEDGMENT

REFERENCES

[1] S. Lei, Y. Suyuan, Y. Guojun, S. Zhengang, and X. Yang, "Technical design and principle test of active magnetic bearings for the compressor of HTR-10GT," in *Proc. HTR 2010, Prague, Czech Republic*, no. 285, Oct.18-20, 2010.

[2] F. M. Mitenkov, N. G. Kodochigov, A. V. Vasyaev, V. F. Golovko, N. N. Ponomarev-Stepnoi, N. E. Kukharkin, and A. Y. Stolyarevskii, "High-temperature gas-cooled reactors - energy source for industrial production of hydrogen," *Atomic Energy*, vol. 97-6, pp. 432-446, 2004.

[3] F. M. Mitenkov, A. S. Chistov, V. F. Ovchinnikov, M. Y. Nikolaev, E. V. Kiryushina, V. N. Litvinov, E. V. Fadeeva, and O. G. Savikhin, "Electromagnetic suspension in vertical axial wind-driven generators," *Journal of Machinery Manufacture and Reliability*, vol. 44, no. 3, pp. 195-199, 2015.

[4] N. X. Wang, J. G. Zhang, G. and P. Ding, "Influence of magnetic bearing stiffness on rotor in wind turbine generator," *Applied Mechanics and Materials*, vol. 150, pp. 57-62, Jan. 2012.

[5] F. M. Mitenkov, V. F. Ovchinnikov, M. Y. Nikolaev, E. V. Kiryushina, V. N. Litvinov, E. V. Fadeeva, and A. S. Chistov, "The effect of wind speed on dynamics of vertical-axial rotor of wind power unit with electromagnetic suspension," *Problems of Strength and Plasticity*, vol. 78, pp. 5-12, 2016.

[6] I. V. Drumov, N. G. Kodochigov, S. E. Belov, D. S. Znamensky, et al., "Studies of the electro-magnetic suspension system for the GT-MHR turbo machine rotor model," *Proceedings of HTR*,

Prague, Czech Republic, no. 41, pp. 1-7, Oct. 18-20, 2010.

[7] F. M. Mitenkov, V. V. Znyshev, Y. V. Kiryushina, M. Y. Nikolaev, and V. F. Ovchinnikov, "Specific features of the dynamics of a vertical flexible rotor with an electromagnetic suspension," *Journal of Machinery Manufacture and Reliability*, vol. 36, no. 5, pp. 397-399, 2007.

[8] V. Ovchinnikov, M. Nikolaev, and V. Litvinov, "Algorithm for compensation of residual imbalance of a flexible rotor on active magnetic bearings," *Cybernetics and Physics*, vol. 6, no. 2, pp. 76-79, 2017.

[9] V. F. Ovchinnikov, M. Y. Nikolaev, and V. N. Litvinov, "Algorithm for accounting for inner damping in a computer model of dynamics of a flexible rotor on active magnetic bearings," *Applied Computational Electromagnetics Society Journal*, vol. 32, no. 8, pp. 726-730, 2017.

[10] V. F. Ovchinnikov, M. Y. Nikolaev, V. N. Litvinov, N. G. Kodochigov, and I. V. Drumov, "The impact of design deviations on dynamic characteristics of a flexible multispan rotor on complete electromagnetic suspension," *Thermal Engineering*, vol. 65, no. 9, pp. 589-596, 2018.

[11] S. Timoshenko, D. H. Young, and W. Weaver, Jr., *Vibration Problems in Engineering*. New York, Chichester, Brisbane, Toronto, Singapore, John Wiley & Sons, 1974.

[12] D. V. Balandin and M. M. Kogan, "Controlling the motion of a vertical rigid rotor rotating in electromagnetic bearings," *Izv. Ross. Akad. Nauk. Teor. Sist. Upr.*, no. 5, pp. 3-17. 2011.

[13] G. H. Golub and C. F. Van Loan, *Matrix Computations*. JHU Press, 1996.

[14] ISO 14839-2:2004 Mechanical vibration - Vibration of rotating machinery equipped with active magnetic bearings - Part 2: Evaluation of vibration (IDT).

Mikhail Nikolaev graduated from Lobachevsky State University of Nizhny Novgorod. Leading Researcher at Research Institute of Mechanics of Lobachevsky State University of Nizhny Novgorod. Ph.D. (Engineering Science). Field of interest: studying and modelling dynamics of complex unique systems.

Vasily Litvinov graduated from Lobachevsky State University of Nizhny Novgorod. Junior Researcher at Research Institute of Mechanics of Lobachevsky State University of Nizhny Novgorod. Field of interest: studying and modelling dynamics of magnetic and mechanical systems.

Denis Kapitanov graduated from Lobachevsky State University of Nizhny Novgorod. Researcher at Research Institute of Mechanics of Lobachevsky State University of Nizhny Novgorod. Ph.D. (Physics and Mathematics). Field of interest: studying and modelling dynamics of elastic systems.

Viktor Ovchinnikov graduated from Lobachevsky State University of Nizhny Novgorod. Leading Researcher of Research Institute of Mechanics of Lobachevsky State University of Nizhny Novgorod. Ph.D. (Physics and Mathematics). Field of interest: studying and modelling dynamics of flexible-body systems.

Dynamics of an Electromechanical Touchdown Bearing Mechanism

Janne E. Heikkinen [1], Henri Kauppila [1], Alexander Smirnov [2], Teemu Sillanpää [3], Eerik Sikanen [1], and Jussi Sopanen [1]

[1] Department of Mechanical Engineering
Lappeenranta University of Technology, Lappeenranta, FI-53850, Finland
janne.heikkinen@lut.fi, henri.kauppila@student.lut.fi, eerik.sikanen@lut.fi, jussi.sopanen@lut.fi

[2] VTT Technical Research Centre of Finland, Espoo, FI-02044, Finland
alexander.smirnov@vtt.fi

[3] Department of Electrical Engineering
Lappeenranta University of Technology, Lappeenranta, FI-53850, Finland
teemu.sillanpaa@lut.fi

Abstract ─ Safety bearings are used as a back-up system for the rotor-systems that use active magnet bearings for supporting the rotor. When the control fails due to unexpected events, the rotor drops on the safety bearings that prevent further damages of the system. This paper presents dynamic studies of a novel electromechanical safety bearing solution. The parts of the studied system are modeled as rigid bodies and the purpose is the study the dynamics of a real system in means of simulation. The safety bearing mechanism is manufactured and measured in the laboratory environment. The study shows that the dynamic behavior of the system can be repeated using the simulation tools that combines mechanical description of the system, electromagnetics and control system. Also, the electromechanical safety bearing solution seems to be feasible from the dynamic perspective.

Index Terms ─ Electromechanical system, mechanism, multibody dynamics, multidisciplinary simulation, safety bearings.

I. INTRODUCTION

Active magnetic bearings are widely used for promoting higher rotational speeds. Higher rotational speeds brings multiple advantages such as higher power density and savings on material costs. Actively controlled magnetic bearings are able to maintain high performance level through the full operational speed range contradicting the difficulties of other non-contacting bearings types such as air foil bearings. Contactless operation enables higher system efficiency and the regular maintenance of the bearing components is unnecessary. Active control requires a position feedback of the system that requires position sensors, but

that brings advantage of monitoring the performance of the system without additional on-line sensors or regular on-site monitoring intervals.

The downside of the magnetic bearings is the unavoidable need for using an auxiliary systems that ensures the safe operation of the rotor system in emergency cases when control of the rotor-bearing system fails due to sudden event such as exceeding load limits or disturbances in the electric circuit. The regularly used approach is to use regular types of bearings that catch the rotor in case of dropdown. Regular bearing types such as deep groove ball bearings or angular contact ball bearings are used for this purpose. The inner bearing diameter is few hundred micrometers larger than the rotor diameter enabling the contactless regular operation. The effects of the most important parameters of touchdown bearings were studied by Ishii and Kirk in 1996 [1]. In case of dropdown, the rotor drops the distance of the airgap and the very first moments of the contact event between the rotor and the bearing inner bore are dramatic due to extreme peak stresses in the bearing components and high angular acceleration of the bearing inner ring and individual rollers in the bearings as shown by Neisi et al. [2].

The paper introduces a novel electromechanical actuator that can be used for safety mechanism of AMB supported rotor system. Previous studies has presented other types of active auxiliary systems such as piezo-hydraulic actuators [3] and controllable electromagnetic actuators [4]. Jiang et al. [5] studied two different control strategies of radially active auxiliary bearings in means of simulation. Our paper presents a study investigating the dynamics of an active touchdown bearing mechanism using a multibody simulation approach. Multibody simulation is regularly used tool for studying mechanisms

and machines having multiple parts interacting through joints and forces [6]. It allows combining different disciplines in the system as long as the physical phenomena to be investigated can be modeled either analytically or numerically.

The main objective of the study is to explore the dynamical characteristics of the mechanism. It is vital for the operation that the launch is fast enough to catch the rotor before it hits on the bottom of the bearing ring. The launch can be accelerated by controlling the voltage of the electromagnetic actuator, pre-loading and selecting the mechanical springs appropriately and designing the mechanism properly to ensure smooth and direct translational movement of the touchdown bearing. The mechanism is manufactured and tested in a laboratory environment where three position probes were assembled circumferentially to measure the displacement of each point with respect to the main body.

The study contributes to the existing knowledge by introducing an interesting electromechanical device for increased safety that is studied in means of simulation and laboratory experiments for confirming the functionality of the mechanism. The simulation results and the experiments confirm that the electromechanical touchdown bearing mechanism is able to capture the rotor before it completely drops on the bearings.

II. TOUCHDOWN BEARING MECHANISM

The novel electromechanical touchdown bearing mechanism is launched, when a sudden undesired event of the system is identified. Figure 1 shows the schematics of the touchdown bearing mechanism including the list of parts [7]. The mechanism comprises electromagnetic actuators that are used for loading the mechanical springs and holding the mechanism in place. Once the mechanism is launched, the voltage of the electromagnetic actuators are driven to negative value resulting zero electromagnetic force. The parameters were selected based on fastest experimentally obtained launch event. The mechanical springs push the lid where the touchdown bearing sits to catch the rotor before it drops on the bottom of the touchdown bearings. The inner sleeve of the bearing is conical which angle match with the conical sleeve angle of the rotor that ensures the centering of the rotor when it is captured.

The conventional touchdown bearings with regular cylindrical inner bore may result in whirling motions of the rotor in a dropdown where the rotor orbits the centerline on the inner ring of the bearing. The inner ring should accelerate as fast as possible to meet the rotational speed at which the surface speed of the rotor and the inner ring bore would be equal. The proposed mechanism would completely close the airgap of the touchdown bearing disabling completely the whirling motion of the rotor.

101 = mechanism
102 = touchdown bearing
103 = moving lid
104 = stator of the mechanism
107 = conical bearing surface
109 = rotating shaft
116 = conical shaft shoulder
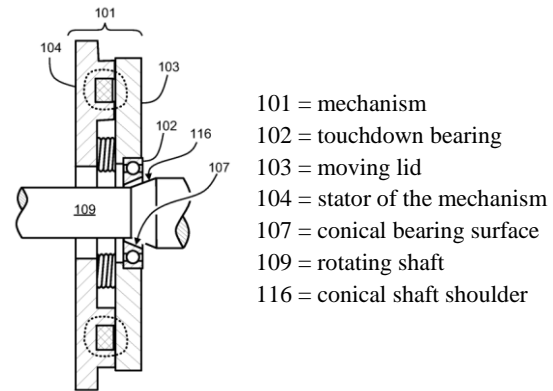
Fig. 1. Schematics and a part list of the studied touchdown bearing mechanism [7].

The studied mechanism is a simplified version of an actual system comprising a stationary part including the windings of the electromagnetic actuator that would be mounted to the end-plate of the machine, six mechanical springs (type Sodemann C04800810620M), and the moving lid that would include the touchdown bearing in the actual application. In the proof-of-concept, the stationary part is attached to a plate that is held in a screw bench and the lid does not have the touchdown bearings since the main objective is to study the release mechanism. The mechanism is loaded by increasing the current in the windings that generates a force field that is larger than the mechanical spring force. As the released lid is in the maximum distance from the stator and the electromagnetic attractive force is proportional to distance square, loading the lid requires much higher current than the required current for holding the airgap closed in the regular operation. The laboratory prototype and the 3D model of the studied system is illustrated in Fig. 2. The locations of displacement measurements are highlighted with yellow dots including the number of the proximity probe that will be used later to specify the observation point.

Fig. 2. Proof-of-concept electromechanical touchdown bearing mechanism in left and 3D model in right. Yellow points illustrate the location of eddy-current sensors.

III. SIMULATION MODEL

The actuator was modeled in MSC Adams 2017.1 and the simulation results were compared against the laboratory measurements. Simulation model was parametric enabling system testing with different initial values such as air gap length and varying spring coefficient of mechanical springs. The parts are modeled as rigid bodies comprising mass properties. The simulation model included the following parts:

- 2 bodies: frame and lid;
- 2 frictional contacts between bodies, radial and axial;
- 6 springs with individual spring coefficients;
- Electromagnetic pulling force distributed to points of mechanical springs.

A. Electrical modeling in simulation

Electrical modeling point of view the system is seen as variable inductor with breaking resistor making series RL-circuit. Resistance value and initial current are given as input parameter. Circuit inductance and force depend on current and position of lid thus look-up tables have been created for force and inductance based on electrical simulation.

Considering variable inductance, RL-circuit current can be calculated:

$$U_L + U_R = 0, \tag{1}$$

where U_L is voltage over the inductance and U_R voltage over the resistance. The sum of voltages can be also described as an equation:

$$L\frac{di}{dt} + i\frac{dL}{dt} + iR = 0, \tag{2}$$

where $L\frac{di}{dt}$ corresponds voltage generated over the inductance related to change of current, $i\frac{dL}{dt}$ voltage over the inductance generated by the changing inductance (mechanical movement of the lid) and iR the voltage loss related to resistive losses.

The system is studied in means of multibody dynamics simulation in time domain. The electromagnetic and mechanical forces are located in the same six points. Springs are assumed to have a linear spring coefficients whereas the electromagnetic forces and inductances are modeled as splines according to the look-up tables that are presented in Fig. 3. The state of the system is solved using time integration using a step size of $2.5 \cdot 10^{-6}$ s. Displacements are recorded in the locations of eddy current sensors that were used to measure the displacement in the experiments.

IV. RESULTS

Release was tested with differences in spring coefficients that were fine-tuned according the measured results. The used spring coefficients are presented in Table 1. The variation in spring coefficients is unrealistically large, but the unrealistic coefficients were used for compensating the effect of sliding friction and other non-linear effects that causes uneven motion of the lid. Initial current was set to 1.5 A, and 20 Ohm breaking resistor was used. Obtained release result can be seen from Fig. 4. The curves show the displacement of the lid that are observed from the same locations where the displacement probes are located in the prototype mechanism. The studied locations are referred as Place 1, 2 and 3, respectively. The result curve starts from the time step, where the system is launched. The lid hits in hard stop approximately 5 ms from the release. The first 3 ms is spent for waiting the electromagnetic force drop. Once the mechanical force exceeds the electromagnetic force and the static friction, the lid starts to move and reach the destination in 2 ms.
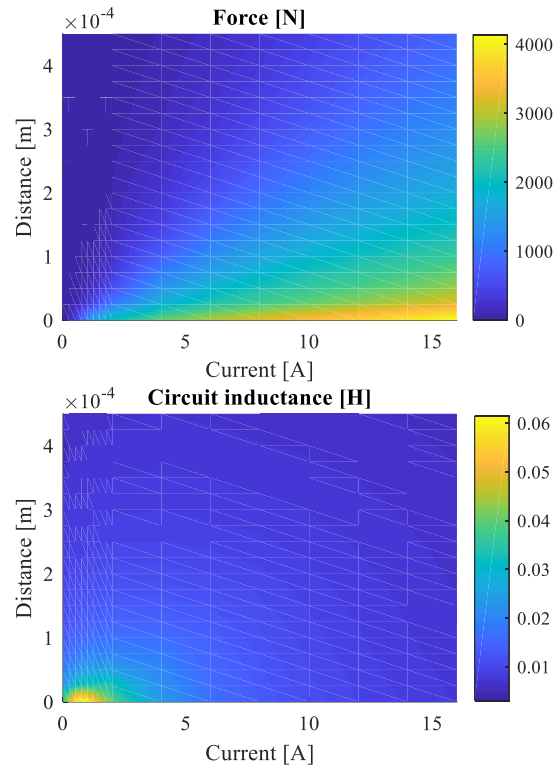
Fig. 3. Look-up tables for electro-mechanical pulling force and circuit inductance.

Table 1: Simulation spring coefficients

Spring Number	Angle	Spring Rate
1	30°	17.2 N/mm
2	90°	14.2 N/mm
3	150°	17.2 N/mm
4	210°	23.2 N/mm
5	270°	23.2 N/mm
6	330°	12.2 N/mm
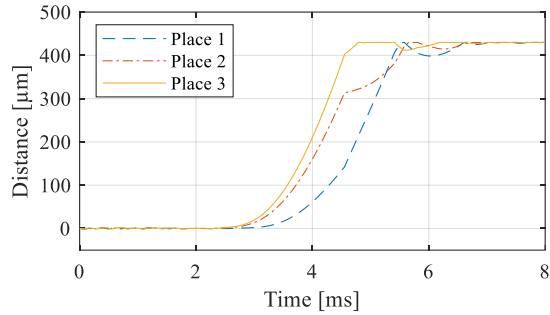
Fig. 4. Displacement in the simulated release.

A. Laboratory tests

The proposed electromechanical touchdown bearing mechanism was studied in the laboratory in order to study the performance and key parameters of the system in an adjustable and well-known environment. The system was adjusted by current in the electromagnetic actuator. The system was loaded using current of 8 A that was enough to produce force that exceeded the mechanical spring force. The obtained release current was 1.9 A and the current level of 4.5 A was selected for holding the lid in place replicating the typical operational conditions. The system was released by actively adjusting the current to a negative value enabling the fastest possible drop in electromagnetic force. Figure 5 shows the current profile during the launch, whereas Fig. 6 shows the corresponding voltage profile.
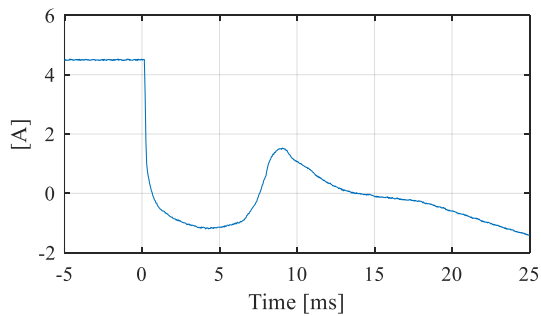
Fig. 5. Current profile of the system during a launch.
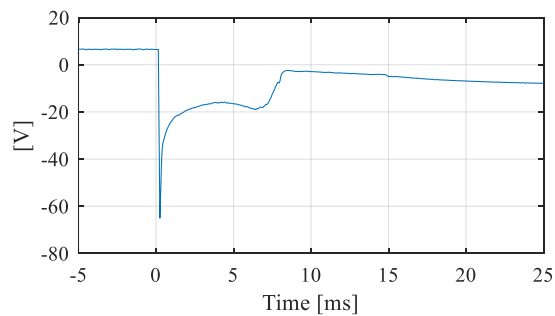
Fig. 6. Voltage profile of the system during a launch.

The displacement of the lid is observed in three positions. The displacement curves are presented in Fig. 7. The shape of the displacement curves are very close to the displacement curves of the simulated system. One of the reasons for such is the unrealistic spring coefficients, but still the overall results indicate clearly that the simulation model is able to predict the force interactions and the dynamics of the system well. The main differences in the curves are the time between the launch and the first motions and the time span that is required for closing the gap. In simulation model, the time from the launch to the first motions is 2.5 ms whereas in the measurement the lid experiences some motion instantly after the release. The simulation model is able to close the gap in 2 ms whilst the measurement indicates approximately 3-4 ms time span depending on the start and end points of observation. Table 2 tabulates the different phases of the release in both simulated and measured case. It can be also observed that the measured curves show more flexibility in the system when compared to simple rigid multibody simulation model. The system is attached in the laboratory in a screw bench from one side enabling some motion due to the flexibility of the system structure.
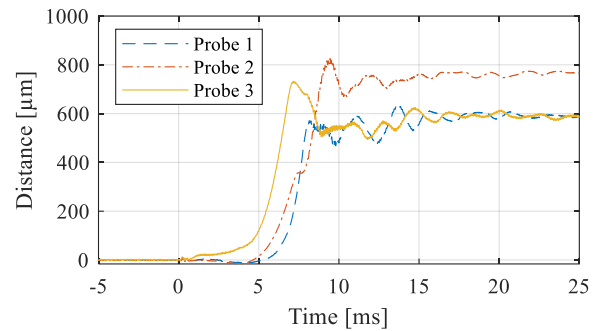
Fig. 7. Measured displacements during a launch.

Table 2: Phases of the release

Release Time	Simulated	Measured
Current drops to release point	< 1 ms	< 1 ms
Waiting lid to start moving	2.5 ms	1 ms
First side reaches 430 μm	4.5 ms	7 ms
Other side reaches 430 μm	5.5 ms	8 ms

In the actual rotating application with the introduced specifications, the rotor would drop approximately 50% of the airgap distance before the designed electro-mechanical system would catch the rotor. Naturally, the time and distance of the drop would depend on the combinations of touchdown bearing airgap, initial position, orientation and velocity of the rotor, and the rotor unbalance.

V. CONCLUSION

This paper studies a novel electromechanical system that is used for a safety system of an AMB supported rotor system. The mechanism comprises mechanical spring that will be loaded by an electromagnetic actuator. Once the current of the electromagnetic circuit is actively driven to negative value, the electromagnetic force is removed and the mechanical springs push the moving part of the system for catching the dropping rotor. The system is studied in means of simulation and experiments. The simulation uses rigid multibody dynamics approach where the electromagnetic forces are modeled as simple analytical equations. The spring coefficients of the mechanical springs were varied due to measured results showing that the moving lid tilts during the launch. The simulation results are close to the measured results in terms of the time span that is required for launching the system. The launch is that fast that it is able to capture the rotor from the air and smooth the drop enabling safe run down.

ACKNOWLEDGMENT

REFERENCES

[1] T. Ishii and R. G. Kirk, "Transient response technique applied to active magnetic bearing machinery during rotor drop," *J. Vib. Acoust*, vol. 118, no. 2 pp. 154-163, 1996.

[2] N. Neisi, E. Sikanen, J. Heikkinen, and J. Sopanen, "Effect of off-sized balls on contact stresses in a touchdown bearing," *Trib. Int.*, vol. 120, pp. 340-349, 2018.

[3] I. Cade, M. N. Sahinkaya, C. Burrows, and P. S. Keogh, "On the design of an active auxiliary bearing for rotor/magnetic bearing systems," *11th International Symposium on Magnetic Bearings*, Nara, Japan, Aug. 2008.

[4] L. Ginzinger and H. Ulbrich, "Control of a rubbing rotor using an active auxiliary bearing," *J. Mech. Sci. Technol.*, vol. 21, no. 6, pp. 851-854, 2007.

[5] J. Jiang, H. Ulbrich, and A. Chavez, "Improvement of rotor performance under rubbing conditions through active auxiliary bearing," *Int. J. Nonlinear Mech.*, vol. 41, no. 8, pp. 949-957, 2006.

[6] A. A. Shabana, *Dynamics of Multibody Systems*. Cambridge University Press, 2005.

[7] J. Heikkinen, R. S. Semken, O. Pyrhönen, J. Sopanen, and A. Smirnov, "*A controllable bearing system*," Patent WO2016139389 A1, 2016.

Janne E. Heikkinen received M.Sc. degree in Mechanical Engineering from Lappeenranta University of Technology (LUT), Finland, in 2010. After the Master's studies, he started his research career as a Ph.D. student at LUT. He defended successfully his Doctoral Dissertation and received D.Sc. degree from LUT in 2014. He is currently working as a Post-Doctoral Researcher in Laboratory of Machine Dynamics at LUT. His research interests are in the field of rotating electric machines especially high-speed machinery. His main expertise is on rotordynamics, structural vibrations, and vibration measurements.

Henri Kauppila is studying M.Sc. degree from Lappeenranta University of Technology (LUT) in Mechanical Engineering and having minor in Electrical Engineering. He is interested in system dynamics and computer-aided engineering, especially multi-physics simulations and control engineering. Currently he is doing his master's thesis work related to co-simulation in industry.

Alexander Smirnov received the M.Sc. and the D.Sc. degree in Electrical Engineering from Lappeenranta University of Technology (LUT), Lappeenranta, Finland in 2008 and in 2012, respectively. He has been working at LUT as a Post-doctoral Researcher from 2012 to 2016. Currently he is working in VTT Technical Research Centre of Finland. His research mainly concerns high-speed electrical machines and drives, active magnetic bearings, and vehicle electrification.

Teemu Sillanpää received B.Sc. and M.Sc. degrees in Electrical Engineering in 2012 and 2013, respectively, from Lappeenranta University of Technology (LUT), Lappeenranta, Finland, where he is currently working toward the Ph.D. degree in the Control Engineering and Digital Systems Laboratory. His research interests include control systems, digital signal processing and power electronic circuits related to active magnetic bearing suspended high-speed electrical machines.

Eerik Sikanen received his M.Sc. degrees in Mechanical Engineering from Lappeenranta University of Technology (LUT), Lappeenranta, Finland, in 2014. Currently, he is working as Doctoral Student in the Laboratory of Machine Dynamics at LUT. His research interests are rotor dynamics and mechanical design of rotating machines. He is mainly concentrating on three-dimensional finite element modeling of high-speed machinery and in systems including thermomechanical effects.

Jussi Sopanen received his M.Sc. Degree in Mechanical Engineering and D.Sc. (Technology) degree from Lappeenranta University of Technology (LUT), Lappeenranta, Finland, in 1999 and 2004, respectively. Hi is currently serving as a Professor in Machine Dynamics at LUT. His research interests are mechanical vibrations, rotor dynamics, multi-body dynamics and mechanical design of electrical machines.

Torque and Bearing Reaction Forces Simulation of Micro-Magnetic Gears

M. Muñoz-Martínez [1], E. Diez-Jimenez [1], M. J. Gómez-García [2], R. Rizzo [3], and A. Musolino [3]

[1] Mechanical Engineering Area, Universidad de Alcalá, Spain
miriam.martinezm@uah.es, efren.diez@uah.es

[2] Mechanical Engineering Department, Universidad Carlos III de Madrid, Spain
mjggarci@ing.uc3m.es

[3] Department of Energy and Systems Engineering, University of Pisa, Largo Lucio Lazzarino, 56122, Pisa, Italy
rocco.rizzo@unipi.it, antonino.musolino@unipi.it

Abstract ─ Specific torque and bearing reaction forces are simulated for two models of axial flux magnetic gears. The models cover simulation in two scale ranges: hundreds of microns and tenths of microns. The simulations presented are performed considering currently available magnetic properties in the microscale and potentially achievable ones. Specific torque of the models is between 2.76 up to 8.24 Nm/kg. This range is large enough to overpass conventional toothed microgear specific torque. This means that micro magnetic gears can not only provide conversion of speed and torque without friction but also to be more compact.

Index Terms ─ Axial flux rotary machines, FEM simulation, magnetic gear, microgears, micromagnets.

I. INTRODUCTION

MEMS (MicroElectroMechanical Systems) contain moving parts that are susceptible to friction, wear and fatigue. Friction and wear are undesired phenomena in machines because they reduce their efficiency and lifetime. In the microscale, friction and wear are primarily imposed by surface forces (capillary, van der Waals, electrostatic, or frictional forces) and surface parameters (i.e., surface roughness or adhesion) [1]–[3].

In the macroscale, friction forces are much lower than inertial ones, thus lubrication is good enough to keep a high efficiency and long lifetime of mechanisms. Nevertheless, when the size is reduced, friction forces become more important and the efficiency decreases dramatically. Many MEMS are impossible or impractical to protect from external contamination. Thus, not only water vapour but also other contaminants chemically interact and stick. Friction and wear are the most crucial phenomena that finally determine the reliability of MEMS [4]–[6].

Wear and friction in MEMS depend on size, surface roughness, coatings and lubricants. Previous research works have studied these effects explaining the differences in tribological aspects from micro to nanoscale [7], [8]. Although the results of these studies show interesting enhancements, friction and wear is unavoidable since contact forces always appear.

Magnetomechanical components can be a good choice in order to reduce or even completely avoid wear in MEMS. Any kind of mechanism is susceptible of conversion to its magneto-mechanical equivalent. Spur gears [9], planetary gears [10], harmonic-drives [11]–[13] couplings [14], bevel gear, cycloidal gear, can be converted to its magnetic equivalent. Not only gears can be converted but also bearings, springs [15]–[17], suspensions and even structures can be created.

These types of components have already been tested in macroscale [18]–[22] preventing from wear and friction in the teeth transmission or in the bearings. Even more, they have been combined (bearings, gear and coupling) as demonstrated in the first fully contactless machine ever built [23]. All these components are completely passive; they behave as conventional mechanical elements but with additional advantages.

All the benefits of magneto-mechanical components are inherent to the lack of contact. Nevertheless, the main pitfall for their wide adoption in the macroscale has always been their lower specific capacity for torque/force transmission with respect to conventional ones [24]. For magneto-mechanical components, the transmitted force/torque, in first term, depends directly on the amount of magnetic material in the mechanism. This implies that the specific force/torque (Nm/kg) remains constant for any scale. On the contrary, for conventional mechanical elements the miniaturization increases friction/inertial force ratio, thus specific force/torque decreases when reducing size. This effect permits to establish a frontier wherein micromagnetic gears also would perform better in terms of specific torque. This frontier has been set in 2 mm characteristic diameter with currently available

magnetic material properties and around 9 mm diameter if best magnetic material properties were achieved [25].

In this work, the specific torque and bearing reaction forces are simulated for two models of axial flux magnetic gears. The models cover simulation in two scale ranges: hundreds of microns and tenths of microns. The simulations presented are performed considering currently available magnetic properties in the microscale and potentially achievable ones.

II. PERMANENT MAGNETS FOR MEMS

The fabrication of high-quality permanent magnets with size in the 1-1000 μm range is still very challenging. Permanent Magnets are essential components for MEMS devices such as motors, generators, pumps, sensors, acoustic speakers and others. After magnetization, PM provide "free" constant source of magnetic fields, requiring no external power. PM are often coupled with soft magnetic cores to guide and concentrate the fields in certain regions as for example in magnetic gears

Current micromanufacturing techniques for PM are divided into deposited micromagnets (from 0.5 to 50 μm thickness) and powder micromagnets (from 10 μm to 1 mm thickness). Deposition of micromagnets includes physical vapour deposition (sputtering, evaporation and pulse-laser deposition) [27]. Since high magnetic product rare earth micromagnets cannot be electroplated from aqueous baths, the available techniques for deposition are sputtering and PLD [28].

Using powder techniques as sintering or bonding PM can be done in the range of 10 μm to 1 mm. With this method, powders size determine the minimum PM size. Likewise for macroscale PM, bonded micro-magnets properties are usually weaker than those of the original magnetic powder. The coercivity remains constant but the remanence is directly related to the particle fill factor, reaching at best 80%. The values obtained even in the best solution found in literature are low (for NdFeB not larger than remanence 0.7 T and remanence 1090 kA/m, separately). Table 1 summarizes methods, thickness and highest magnetic properties of micro permanent magnets [29].

Table 1: NdFeB Permanent Magnets properties for different micro-manufacturing techniques

Method	E (μm)	Br (T)	Hc (kA/m)	BH$_{mx}$ (kJ/m^3)	Assem.
Deposition	0.5-50	0.5-1.4	600-1035	150-400	Integral
Powder	50-1000	0.2 – 0.7	300-800	14-250	Integral
Bulk μmachining	25-1000	1 – 1.4	860-1035	342-406	Manual Brittle
Macroscale	>1000	1 – 1.4	860-1035	342-406	Manual

III. MICRO-MAGNETIC GEAR DESIGN

Axial flux micro-magnetic gear topology is chosen because it has demonstrated high specific torque performance in the macroscale and because its stack type topology is very adequate to typical epitaxial MEMS fabrication processes.

The magnetic gear design consists of an input or fast rotary element made by several PM, an intermediate element, typically static, made of soft magnetic material and a third element acting as output or slow rotary element made again of a set of PM.
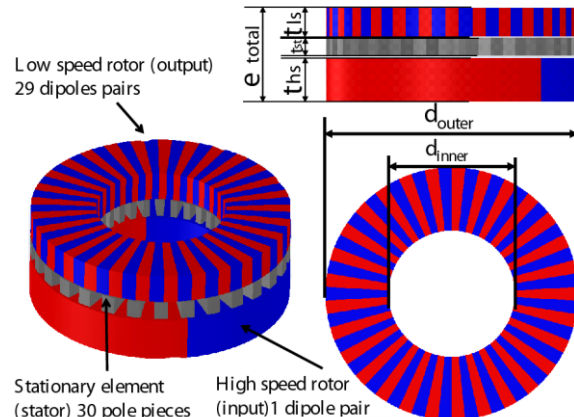
Fig. 1. Micro-magnetic gear geometrical parameters.

The permanent magnet arrangement is done in alternative polarizations, (red and blue in Fig. 1). All the polarizations of the PM are oriented towards the vertical direction (blue-north pole, red-south pole). The number of dipole-pairs in low speed rotor is N$_{output}$=29; the number of stationary steel pole-pieces is N$_{stator}$=30; and the number of dipole-pairs in high-speed rotor is N$_{input}$=1. Gear ratio (Gr) is given by the relationship between the different elements. It is calculated as:

$$G_r = \frac{N_{output} - N_{stator}}{N_{output}}. \qquad (1)$$

This expression is valid if the number of dipole pairs in the input is equal to the difference between N$_{output}$ and N$_{stator}$, i.e., N$_{stator}$=1. In this case, G$_r$ = -1/29. Bearings, axles and frames will contribute with extra weight. Therefore, it is necessary to estimate final corrected specific torque values. Considering previous magnetic gear developments, a correction factor of 1.1 is reasonable for the final device weight [22], [30].

Two ranges of application are explored: hundreds of microns and tenths of microns. Thus, two different models have been created. The geometrical parameters of each model are listed in Table 2.

Vacoflux 48 (Bsat=2.35 T) is considered as soft magnetic material of the stator and NdFeB material for the tow rotors. As already mentioned, the simulations presented are performed considering currently available magnetic properties in the microscale ones and potentially achievable ones. Available selection of properties depends on thickness of the rotor. Permanent magnetic material properties used are listed in Table 3.

Table 2: Geometrical parameters of the magnetic gears

Definition	Sym.	Model 1 (Submilimetric)	Model 2 (Micrometric)
Outer diameter (µm)	d_{outer}	700	140
Inner diameter (µm)	d_{inner}	350	70
Total length (µm)	e_{total}	260	52
Low speed rotor thickness (µm)	t_{ls}	80	16
Stator thickness (µm)	t_{st}	50	10
High speed rotor thickness (µm)	t_{hs}	120	24
Airgap Low Speed roto-Stator (µm)	g_{ls-st}	4	0.8
Airgap Stator-High Speed rotor (µm)	g_{st-hs}	6	1.2
Magnetic parts weight (mg)	W_{mag}	0.5478	0.0044
Estimated weight (mg)	W_{tot}	0.6028	0.0048

Table 3: Magnetic material properties

Material Name	Br (T)	Hc (kA/m)
NdFeB ideal	1.42	1035
NdFeB real thin film (< 50 µm)	1.3	955
NdFeB real submilimetric	0.7	800
Vacoflux 48	1.5	0.150

IV. FEM MODEL AND SIMULATIONS

All the calculations are done using a finite element model (FEM) software for electromagnetic fields. The solver chosen is the magneto-static solver. The magneto-static field solution verifies the following two Maxwell's equations:

$$\nabla \times \vec{H} = \vec{J} \text{ and } \nabla \cdot \vec{B} = 0.$$

With the following relationship at each material:

$$\vec{B} = \mu_0(\vec{H} + \vec{M}) = \mu_0 \cdot \mu_r \cdot \vec{H} + \mu_0 \cdot \vec{M}_p. \quad (2)$$

Where H is the magnetic field intensity, B is the magnetic field density, J is the conduction current density, M_p is the permanent magnetization, μ_0 is the permeability of vacuum and µr is the relative permeability [31].

The geometrical 3D model is shown in Fig. 2. In this model, the angular position of the low speed rotor can be automatically modified by the software at each simulation. The mesh of the model is more refined in the magnetic material interfaces and also within the airgaps. An example of the mesh is also shown in Fig. 2.

The materials considered are dependent on the thickness of the rotor. The combination of models and materials leads to four parametric magneto-static simulations. The summary of the simulations and

materials selected for each element is given in Table 4.
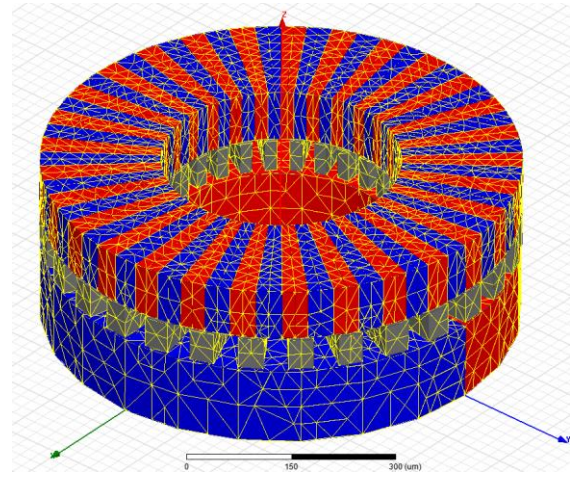
Fig. 2. 3D view of the FEM model: geometry and mesh.

Table 4: Simulation list

Nº	Model	Low Speed Rotor Material	High Speed Rotor Material	Stator Material
1R	Model 1	NdFeB real submilimetric	NdFeB real submilimetric	Vacoflux 48
1I	Model 1	NdFeB ideal	NdFeB ideal	Vacoflux 48
2R	Model 2	NdFeB real thin film	NdFeB real thin film	Vacoflux 48
2I	Model 2	NdFeB ideal	NdFeB ideal	Vacoflux 48

As boundary conditions a "Zero tangential Field" type condition is applied in the external surfaces of the surrounding region volume. No current or field excitation is used, only permanent magnetization excitation according to the material properties table.

Each simulation corresponds to a single combination of the model and material properties. Forces and torques are obtained in post-processing by using the virtual forces principle. The output and input torque and corresponding reaction forces at each element are calculated for every angular position. Each simulation has been done considering a stationary condition.

The solver uses an adaptive meshing solver. Typically 11-13 iterations on the mesh are sufficient for a correct convergence of the simulation. The total number of tetrahedral elements is around 200000. The mesh is refined for achieving less than 2% of energy error within a simulation time of less than 20 seconds per simulation. All the simulations have been done in a workstation with an Intel Core i4-4690 with 8Gb of RAM memory.

The selection of this computational working point has been chosen after performing a sensitivity analysis of the FEM results, Fig. 3. In this figure, it is shown that error highly decreases from more than 150000 elements while computational time is still low.
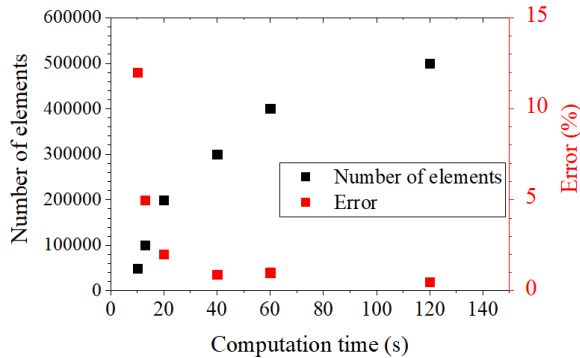
Fig. 3. Number of elements sensitivity analysis.

V. RESULTS AND DISCUSSION

The results present, in next figures, torques and axial forces for each model as a function of the rotation angle of the corresponding input rotor. The radial forces are negligible due to the axial geometry of the gear.

Figure 4 shows torques of input and output rotor of model 1 for both material combination 1R and 1I with respect to the angle of rotation of the input rotor. The maximum output torque is achieved at 90 degrees for both combinations, in agreement with the topology of the gear. The maximum output torque for the real material combination is 1.66 µNm and the one for the ideal material combination is 4.95 µNm. The torque in the input rotor is 29 times smaller than the one in the output as expected.
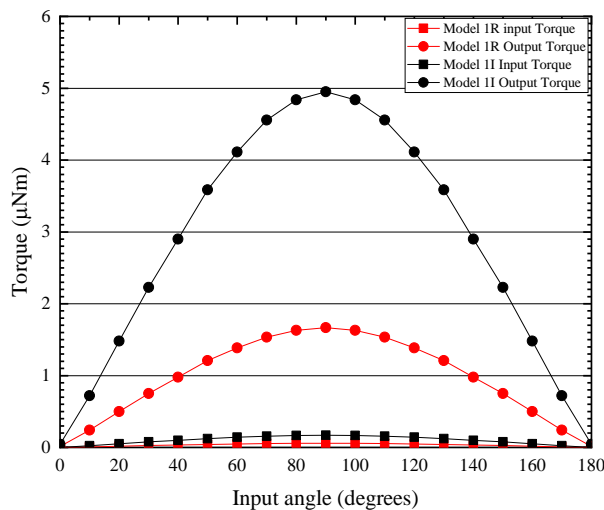
Fig. 4. Torques for Model 1R and 1I.

Figure 5 shows the axial forces acting on input and output rotor of model 1 for both material combination 1R and 1I with respect to the angle of rotation of the input rotor. The maximum axial force is 63.22 mN achieved at 0 degrees of input rotation in the output element corresponding to the ideal materials case. The maximum axial force for the real material case is 18.75 mN obtained also at 0 degrees of rotation of the input rotor.

Figure 6 shows torques of input and output rotor of model 2 for both material combination 2R and 2I with respect to the angle of rotation of the input rotor. The maximum output torque is achieved at 90 degrees for both combinations, in agreement with the topology of the gear. The maximum output torque for the real material combination is 0.0331 µNm and the one for the ideal material combination is 0.0397 µNm. The torque in the input rotor is 29 times smaller than the one in the output.
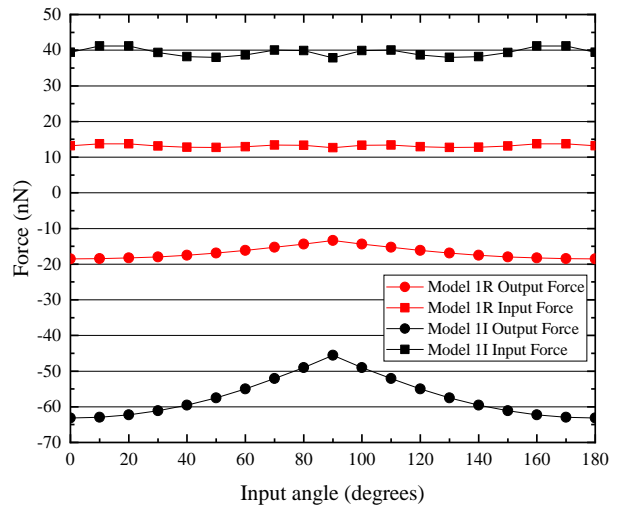
Fig. 5. Axial forces for Model 1R and 1I.
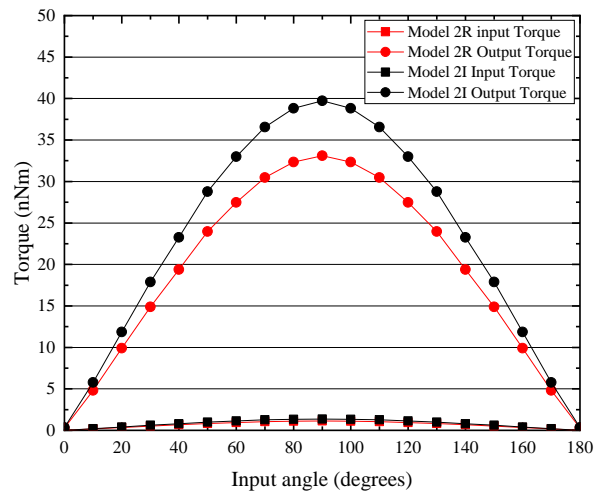
Fig. 6. Torques for Model 2R and 2I.

Figure 7 shows the axial forces acting on input and output rotor of model 2 for both material combination 2R and 2I with respect to the angle of rotation of the input rotor. The maximum axial force is 2.11 mN achieved at 0 degrees of input rotation in the output element corresponding to the ideal materials case. The maximum axial force for the real material case is 2.10 mN obtained also at 0 degrees of input rotation.

Specific torque of the models is between 2.76 up to 8.24 Nm/kg. This range is large enough to overpass conventional toothed microgear specific torque [25]. This means that micro magnetic gears can not only provide conversion of speed and torque without friction but also be more compact. It is important to notice that specific torque for both ideal models is almost equal for both sizes, demonstrating that specific torque is independent of the order of magnitude of the size. A summary of the results is presented in Table 5.
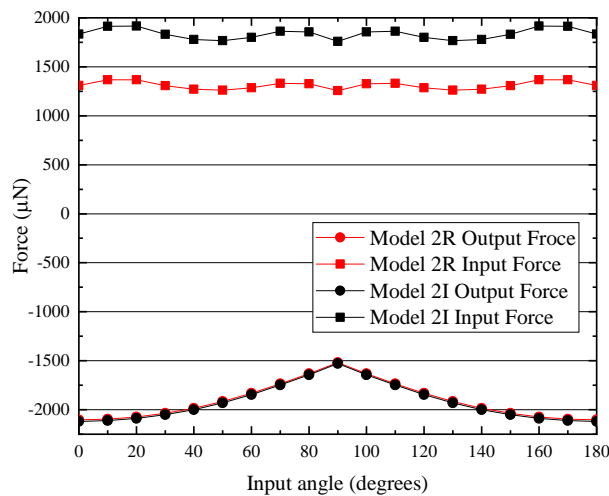
Fig. 7. Axial forces for Model 2R and 2I.

Table 5: Results summary

| Model	Output Torque Max. (μNm)	Axial Force Max. (mN)	Specific Torque (Nm/kg)
Model 1 Real	1.66	18.75	2.76
Model 1 Ideal	4.95	63.22	8.21
Model 2 Real	0.0331	2.10	6.86
Model 2 Ideal	0.0397	2.11	8.24

For model 1 the difference between the model with ideal material and with real material is significant. The maximum output torque in the ideal materials model is 2.98 times larger than with real materials properties, so it happens with the specific torque and axial force. Thus, it can be interesting for science material researchers to keep on working on enhancement of NdFeB properties for magnets in the submilimetric range. For model 2

the difference between the model with ideal material and with real material is smaller, just a 1.2. Therefore, micromagnetic gears in the micrometric range would have an outstanding specific torque capacity. Hence, it can be interesting to develop manufacturing systems for such devices.

VI. CONCLUSION

MEMS contain moving parts that are susceptible to friction, wear and fatigue. Friction and wear are undesired phenomena in machines because they reduce their efficiency and lifetime. Magnetic gears can be a good choice in order to reduce wear in MEMS since they transmit torques without contact.

In this work, the specific torque and bearing reaction forces are simulated for two models of axial flux magnetic gears. The models cover simulation in two scale ranges: hundreds of microns and tenths of microns. The simulations presented are performed considering currently available magnetic properties in the microscale and potentially achievable ones.

Specific torque of the models is between 2.76 up to 8.24 Nm/kg. This range is large enough to overpass conventional toothed microgear specific torque. This means that not only micro magnetic gears can provide conversion of speed and torque without friction but also that they can be more compact.

REFERENCES

[1] G. Subhash, A. D. Corwin, and M. P. de Boer, "Evolution of wear characteristics and frictional behavior in MEMS devices," *Tribol. Lett.*, vol. 41, no. 1, pp. 177-189, Jan. 2011.

[2] M. Kawano, K. Sahrani, S. Mori, T.; Kuroda, and M. Tentzeris, "Numerical modeling of reconfigurable RF MEMS-based structures involving the combination of electrical and mechanical force," *Appl. Comput. Electromagn. Soc. J.*, vol. 21, no. 1, pp. 1-8, 2006.

[3] R. Barmada, S. Musolino, and A. Rizzo, "Equivalent network approach for the simulation of MEMS devices," *Appl. Comput. Electromagn. Soc. J.*, vol. 21, no. 1, pp. 16-25, 2006.

[4] J. Iannacci, "Reliability of MEMS: A perspective on failure mechanisms, improvement solutions and best practices at development level," *Displays*, vol. 37, pp. 62-71, 2015.

[5] H.-W. Wu, Y.-Y. Chen, and J.-H. Horng, "The analysis of three-body contact temperature under the different third particle size, density, and value of friction," *Micromachines*, vol. 8, no. 10, p. 302,

Oct. 2017.

[6] O. Penkov, M. Khadem, A. Nieto, T.-H. Kim, and D.-E. Kim, "Design and construction of a micro-tribotester for precise in-situ wear measurements," *Micromachines*, vol. 8, no. 4, p. 103, Mar. 2017.

[7] M. Tauviqirrahman, R. Ismail, J. Jamari, and D. J. Schipper, "Friction reduction in lubricated-MEMS with complex slip surface pattern," *Procedia Eng.*, vol. 68, pp. 331-337, 2013.

[8] R. W. Carpick, E. E. Flater, J. R. VanLangendon, and M. P. De Boer, "Friction in MEMS: From single to multiple asperity contact," *Proc. SEM VIII Int. Congr. Expo. Exp. Appl. Mech.*, p. 282, 2002.

[9] F. Jorgensen and T. Andersen, "Two dimmensional model of a permanent magnet spur gear," *Conf. Rec. 2005 IEEE Ind. Appl. Conf.*, vol. 1-4, pp. 261-265, 2005.

[10] C.-C. Huang, M.-C. Tsai, D. G. Dorrell, and B.-J. Lin, "Development of a magnetic planetary gearbox," *IEEE Trans. Magn.*, vol. 44, no. 3, pp. 403-412, Mar. 2008.

[11] B. Majidi and J. Milimonfared, "Design and analysis of an interior continuous magnetic gear box using finite element method," *Appl. Comput. Electromagn. Soc. J.*, vol. 30, no. 1, pp. 109-116, 2015.

[12] N. Niguchi and K. Hirata, "Cogging torque analysis of magnetic gear," *IEEE Trans. Ind. Electron.*, vol. 59, no. 5, pp. 2189-2197, 2012.

[13] R. C. Holehouse, K. Atallah, and J. Wang, "A linear magnetic gear," *Proc. - 2012 20th Int. Conf. Electr. Mach. ICEM 2012*, pp. 563-569, 2012.

[14] Y. D. Yao, D. R. Huang, C. M. Lee, S. J. Wang, D. Y. Chiang, and T. F. Ying, "Magnetic coupling studies between radial magnetic gears," *IEEE Trans. Magn.*, vol. 33, no. 5, pp. 4236-4238, 1997.

[15] J. Zhang, L. L. Huang, "Stability analysis for a flywheel supported on magnetic bearings with delayed feedback control," *Appl. Comput. Electromagn. Soc. J.*, vol. 32, no. 8, pp. 642-649, 2017.

[16] R. Muscia, "Magneto-mechanical model of passive magnetic axial bearings versus the eccentricity error - Part I: Physical mathematical model," *Appl. Comput. Electromagn. Soc. J.*, vol. 32, no. 8, pp. 670-677, 2017.

[17] E. Diez-Jimenez, A. Musolino, R. Rizzo, and E. Tripodi, "Analysis of the static and dynamic behavior of a non hysteretic superconductive passive magnetic linear bearing by using an electromagnetic integral formulation," *Prog. Electromagn. Res. M*, vol. 50, pp. 183-193, 2016.

[18] E. Diez-Jimenez, J.-L. Perez-Diaz, and J. C. Garcia-Prada, "Local model for magnet–super-conductor mechanical interaction: experimental verification," *J. Appl. Phys.*, vol. 109, no. 6, pp. 063901-063901-5, 2011.

[19] S. A. Afsari, H. Heydari, and B. Dianati, "Cogging torque mitigation in axial flux magnetic gear system based on skew effects using an improved quasi 3-D analytical method," *IEEE Trans. Magn.*, vol. 51, no. 9, pp. 1-11, 2015.

[20] C. Cristache, E. Diez-Jimenez, I. Valiente-Blanco, J. Sanchez-Garcia-Casarrubios, and J. L. Perez-Diaz, "Aeronautical magnetic torque limiter for passive protection against overloads," *Machines*, vol. 4, no. 3, 2016.

[21] E. Diez-Jimenez, "Design and analysis of a non-hysteretic passive magnetic linear bearing for cryogenic environments," *Proc. Inst. Mech. Eng. Part J J. Eng. Tribol.*, 2014.

[22] J. Esnoz-Larraya, *et al.*, "OPTIMAGDTRIVE: High-performance magnetic gears development for space applications," in *ESMATS*, 2017.

[23] J. L. Perez-Diaz and E. Diez-Jimenez, "Performance of magnetic-superconductor non-contact harmonic drive for cryogenic space applications," *Machines*, vol. 3, no. 3, pp. 138-156, 2015.

[24] P. In, "Comparison of magnetic-geared permanent magnet machines," *Prog. Electromagn. Res.*, vol. 133, no. 2013, pp. 177-198, 2013.

[25] E. Diez-Jimenez, R. Sanchez-Montero, and M. Martinez-Muñoz, "Towards miniaturization of magnetic gears: Torque performance assessment," *Micromachines*, vol. 9, no. 1, p. 16, Dec. 2017.

[26] M. L. Chan, *et al.*, "Design and characterization of MEMS micromotor supported on low friction liquid bearing," *Sensors Actuators, A Phys.*, vol. 177, pp. 1-9, 2012.

[27] Y. Su, H. Wang, G. Ding, F. Cui, W. Zhang, and W. Chen, "Electroplated hard magnetic material and its application in microelectromechanical systems," *IEEE Trans. Magn.*, vol. 41, no. 12, pp. 4380-4383, 2005.

[28] N. M. Dempsey, A. Walther, F. May, D. Givord, K. Khlopkov, and O. Gutfleisch, "High performance hard magnetic NdFeB thick films for integration into micro-electro-mechanical systems," *Appl. Phys. Lett.*, vol. 90, no. 9, 2007.

[29] D. P. Arnold and N. Wang, "Permanent magnets for MEMS," *J. Microelectromechanical Syst.*, vol. 18, no. 6, pp. 1255-1266, 2009.

[30] E. Diez-Jimenez, J. Esnoz-Larraya, I. Valiente-Blanco, and C. Cristache, "Lubrication free magnetic harmonic drives for harsh space environments," in *Space Robotics Symposium*, 2015.

[31] "Ansoft Ansys Maxwell v15 - Help assistant." 2018.

Stability Experiment of the High-Speed Active Magnetic Bearing-Flywheel System in the Rotating Frame

Jinpeng Yu [1,2,3], Yan Zhou [1,2,3], Haoyu Zuo [1,2,3], Kai Zhang [4], Pingfan Liu [2,3], Yanbao Li [5], Pengcheng Pu [1,2,3], Lei Zhao [1,2,3], and Zhe Sun[*1,2,3]

[1] Institute of Nuclear and New Energy Technology
[2] Collaborative Innovation Center of Advanced Nuclear Energy Technology
[3] The Key Laboratory of Advanced Reactor Engineering and Safety
[4] Department of Engineering Physics
Tsinghua University, Beijing, 100084, China
yu-jp15@mails.tsinghua.edu.cn, sun_zhe@mail.tsinghua.edu.cn*

[5] Shanghai Aerospace Control Technology Institute
Shanghai, 200000, China

Abstract ─ The active magnetic bearings (AMBs) can greatly improve the stability of the flywheel system and increase the maximum flywheel speed. However, if the active magnetic bearing-flywheel system (AMB-FS) is placed in a rotating frame, the strong gyroscopic effect of high-speed flywheel will greatly affect the system stability. In this study, to realize the high stability of the AMB-FS at ultra-high flywheel speed with low power consumption, the cross feedback PID control was applied in the AMB-FS. The system stability and the performance of AMBs were studied. In the experiment, the gyroscopic effect of the flywheel was effectively suppressed. In the vacuum environment, the flywheel could runs stably at any speed within the range of 0 to 30000 rpm, and the power consumption of AMBs was only 17.82 W and the system had no need of cooling measures. The flywheel speed could exceed 31200 rpm and still possessed the speeding potential. The rotating frame test showed that the maximum frame rotational speed could reach 3.5 deg/s at the rated flywheel speed of 30000 rpm, and the AMB-FS run stably.

Index Terms ─ Active magnetic bearing, cross feedback control, gyroscopic effect, system stability.

I. INTRODUCTION

The active magnetic bearing-flywheel system (AMB-FS) is a nonlinear system with multiple coupling variables. The rotor imbalance, gyroscopic effect and external disturbance will bring about high control requirement for AMBs. Especially in the high-speed AMB-FS, the strong gyroscopic effect of the flywheel will impose a great burden on AMBs and bring about the problem of stability and stability margin [1]. The AMB controller will fail to meet the control requirements and only small external disturbance acting on the high-speed flywheel will lead to the instability of the AMB-FS.

Combining PID controller with other control methods can achieve good control performance. Displacement cross feedback and speed cross feedback can suppress the gyroscopic effect of the flywheel significantly [2]. Zhang [3] implemented the control arithmetic which included cross feedback based on PD controller on the spacecraft attitude control. Reference [4] designed an H∞ controller with gain adjustment, which could suppress the gyroscopic effect significantly. Studies in [5-6] combined variable gain controller with other control methods to stabilize the AMB-FS. All the methods could effectively suppress the gyroscopic effect and improved the system stability. Meanwhile, accounting the uncertainty and robust control will also contribute to improve the control performance and system stability. Reference [7] derived the nominal model of active magnetic suspension of rotor and the uncertainty model, and proposed a robust control with a multi-objective controller to achieve good robust stability when the model of a plant was uncertain. Reference [8] presented the sensitivity and stability margin analyses of the flexible rotor supported by AMBs with the robust optimal vibrations control, and the μ-controller was verified in experimental tests and possessed good performance. References [9-10] proposed an identification method for flexible rotor suspended by magnetic bearings to estimate the unknown parameters and establish the transfer function matrix model of the AMB system, and finally eliminated the influence of bearing stiffness and improved the system stability.

The study in this paper mainly focused on the stability

of the AMB-FS on movable base. The rotating frames accounting the gyroscopic effects is a typical problem, so the AMB-FS in the rotating frame was studied. Furthermore, the PID controller with cross feedback was studied to discover if the controller worked well in the proposed AMB-FS. And with the optimized design of the structure and controller, the performance of AMBs was studied in the experiment. In the second section, the flywheel stability and cross feedback PID controller is analyzed and designed. The third section shows the experiment result of the stability of AMB-FS under cross feedback PID control. The experiment of the high-speed AMB-FS in rotating frame is presented in section four.

II. STABILITY ANALYSIS AND CONTROLLER DESIGN

If the system frame rotates in the different direction from flywheel, the gyroscopic effect of the high-speed flywheel will impose a great burden on AMBs, which will seriously affect the flywheel stability and raise strict control requirements for AMBs. Therefore, for the AMB-FS, the rotating frame can also be equivalent to the external disturbance. The system stability is analyzed based on the horizontal AMB-FS, whose weight is supported by radial AMBs.

A. Stability Analysis

The system mainly includes flywheel, AMB system, drive motor, frame, and other appended structures. The three-dimensional (3D) structure of the AMB-FS is shown in Fig. 1. The system has an inner rotor structure with radial AMBs mounted on the outside of the flywheel, which achieves high inertia ratio of 1.93. The rated flywheel speed is 500 Hz.
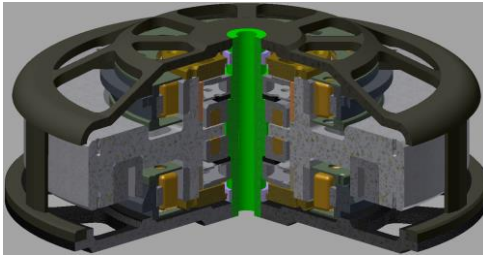
(a) 3D structure of the AMB-FS

(b) The flywheel

Fig. 1. The structure of AMB-FS and flywheel.

Neglecting the influence of the flexible modes of the flywheel, the rigid body model and the force conditions are shown in Fig. 2. The high-speed flywheel is placed horizontally. Since the radial and axial AMBs in the system are decoupled, only the radial AMBs are analyzed.
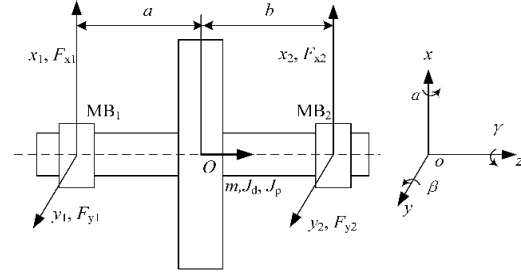
Fig. 2. The flywheel model and the force condition.

$MB_i (i = 1,2)$ are radial AMBs. The flywheel coordinate is $q = [x, \beta, y, -\alpha]^T$ and the AMB coordinate is $q_b = [x_1, x_2, y_1, y_2]^T$, which have the transformation relation $q_b = L_q q$, where,

$$L_q = \begin{bmatrix} 1 & -a & 0 & 0 \\ 1 & b & 0 & 0 \\ 0 & 0 & 1 & -a \\ 0 & 0 & 1 & b \end{bmatrix}. \quad (1)$$

a and b are the distance between radial AMBs and the flywheel centroid. In order to simplify the calculation, it is considered that the displacement sensor and AMBs have the same position. So the motion differential equation of the flywheel is:

$$\begin{cases} m\ddot{x} = F_{x_1} + F_{x_2} + F_{x1}^t + F_{x2}^t \\ m\ddot{y} = F_{y_1} + F_{y_2} + F_{y1}^t + F_{y2}^t \\ J_d\ddot{\alpha} = a(F_{y_1} + F_{y1}^t) - b(F_{y_2} + F_{y2}^t) - J_p\Omega\dot{\beta} \\ J_d\ddot{\beta} = b(F_{x_2} + F_{x1}^t) - a(F_{x_1} + F_{x2}^t) + J_p\Omega\dot{\alpha} \end{cases} \quad (2)$$

with m the mass of flywheel, x and y the displacements of the flywheel centroid, α and β the rotation angles in the x and y directions, J_d and J_p the diameter and polar moment of inertia and Ω the flywheel speed. $F_{x_1}, F_{x_2}, F_{y_1}$ and F_{y_2} are the electromagnetic forces. $F_{tx_1}, F_{tx_2}, F_{ty_1}$ and F_{ty_2} are the external forces (disturbances). The flywheel is place in the closed frame, so $F_{x1}^t = F_{x2}^t = F_{y1}^t = F_{y2}^t = 0$.

The motion differential equation of the AMB-FS can be rewrite in matrix form:

$$M\ddot{q} + G\dot{q} = L_F F, \quad (3)$$

where $M = \text{diag}(m, J_d, m, J_d)$, $F = [F_{x_1}, F_{x_2}, F_{y_1}, F_{y_2}]^T$, $L_F = L_q^T$ and,

$$G = \begin{bmatrix} 0 & 0 & 0 & 0 \\ 0 & 0 & 0 & 1 \\ 0 & 0 & 0 & 0 \\ 0 & -1 & 0 & 0 \end{bmatrix} J_p\Omega. \quad (4)$$

Let $I = \text{diag}(1,1,1,1)$. The AMB force can be linearized as $F = K_x q_b + K_i I_c$, where $K_x = k_x I$ and

$K_i = k_i I$ are force-displacement and force-current stiffness matrices respectively. Under PID current feedback control, the AMB current is:

$$I_c = -G_s G_i \left(K_p q_b + K_d C \dot{q}_b \right.$$
$$\left. + K_I \int q_b \, dt \right), \tag{5}$$

where $G_s = g_s I$ and $G_i = g_i I$ the coefficients of the displacement sensor and power amplifier, $K_p = k_p I$ and $K_d = k_d I$ the parameter matrices of the PID controller. The matrix C is the cross feedback coefficient. Substitute the AMB force into equation (3) and obtain equation (6):

$$M\ddot{q} + N\dot{q} + Vq + W \int q \, dt = 0, \tag{6}$$

where $W = L_F K_i G_s G_i K_I L_q$, $N = G + L_F K_i G_s G_i K_d C L_q$, and $V = L_F K_i G_s G_i K_p L_q - L_F K_s L_q$. The state space equation of the system can be obtained as:

$$\dot{p} = Ap, \tag{7}$$

where $p = (\dot{q}, q, \int q \, dt)^T$ and,

$$A = \begin{bmatrix} -M^{-1}N & -M^{-1}V & -M^{-1}W \\ I & 0 & 0 \\ O & I & O \end{bmatrix}. \tag{8}$$

Figure 3 shows the PID closed loop system and Table 1 shows the parameters in the simulation.
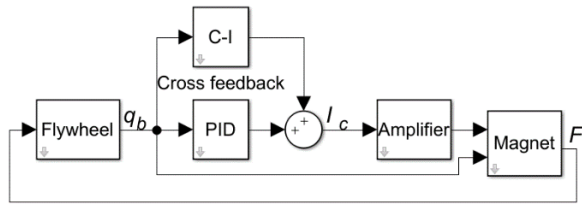
Fig. 3. The closed loop system with cross feedback.

Under dynamic condition, the flywheel speed has $\Omega \neq 0$. Suppose that the flywheel is under the decentralized PID control ($C = C_d = I$). When the flywheel speed increases from $0 \, \text{Hz}$ to $500 \, \text{Hz}$, the eigenvalues of matrix A change with the flywheel speed. During the acceleration period, matrix A has three negative real eigenvalues and three pairs of conjugate eigenvalues. The negative real eigenvalues, $a_1^d = -141.2218$, $a_2^d = -96.1456$ and $a_3^d = -1.0178$ remain unchanged. However, the three pairs of conjugate eigenvalues, a_{4i}^d, a_{5i}^d and $a_{6i}^d (i = 1,2)$, are greatly affected by the flywheel speed, as shown in Fig. 4.

Table 1: The parameters in the simulation

Parameter	Value	Parameter	Value
$a(\text{m})$	0.02	$m(\text{kg})$	5.2
$b(\text{m})$	0.02	$k_x(\text{N/m})$	8982.6
$J_d(\text{kg}\cdot\text{m}^2)$	0.014	$k_i(\text{N/A})$	4.5
$J_p(\text{kg}\cdot\text{m}^2)$	0.027	k_p	9980.7
g_i	1	k_{in}	0.0138
g_s	1	k_d	13.8

(a) a_{4i}^d

(b) a_{5i}^d

(c) a_{6i}^d
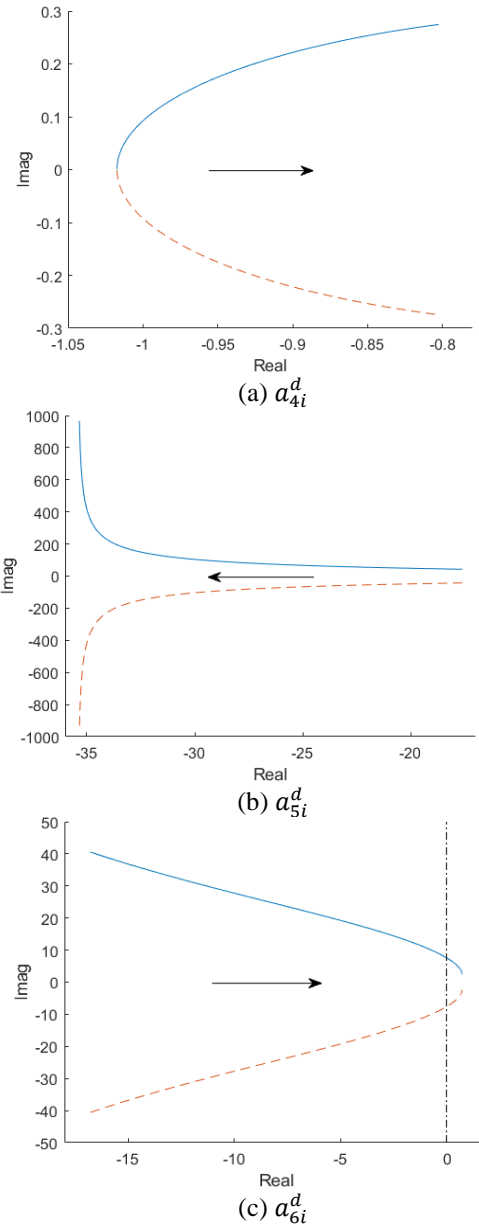
Fig. 4. The conjugate eigenvalues change as the flywheel speed up.

As the flywheel speeds up, a_{5i}^d moves away from the imaginary axis, while a_{4i}^d and a_{6i}^d approach the imaginary axis. Therefore, a_{4i}^d and a_{6i}^d become the dominant eigenvalues for the system as the flywheel speeds up. When a_{4i}^d and a_{6i}^d approach the imaginary axis, the absolute value of the real part decrease and the system stability will be decreased significantly. When the flywheel speed is near 450 Hz, the real part of a_{6i}^d turns into positive value and the AMB-FS is instability. Therefore, the original PID controller possesses good robustness under static state but fails to ensure the stability of AMB-FS at high flywheel speed.

B. Controller design

In order to improve the stability of the high-speed AMB-FS, the decentralized PID control was combined with cross feedback control in the actual experiment. The cross feedback suppressed the precession and nutation frequency by taking the displacement signal in the orthogonal direction as the feedback, as shown in Fig. 5.
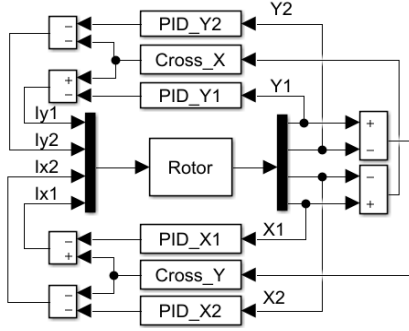
Fig. 5. PID controller with cross feedback.

As for precession, the cross feedback with low-pass characteristics, whose gain in the middle and high frequency band is very low, can effectively damp the precession and has little effect on nutation:

$$G_l = \frac{k_{cl}}{T_{lp}s + 1}. \tag{9}$$

As for nutation, the cross feedback with high-pass characteristics, whose gain in the low frequency band is very low, can effectively damp the nutation and has little effect on procession:

$$G_h = \frac{k_{ch}s}{T_{hp}s + 1}. \tag{10}$$

In order to suppress both the nutation and precession, it is necessary to add the both displacement cross feedback simultaneously, and connect the low-pass and high-pass filters to the corresponding control channel. Therefore, the actual transfer function of the cross feedback is:

$$G(s) = \frac{k_d}{T_{lp}s + 1} + \frac{k_{ch}s}{T_{hp}s + 1}. \tag{11}$$

III. STABILITY EXPERIMENT

Figure 6 shows the AMB-FS experiment platform. The horizontal AMB-FS was placed in the frame, and the frame was placed on a rotatable base. During the running of the AMB-FS, the frame could rotate in the x direction.

A. Static suspension

Figure 7 shows the axis orbit of the flywheel in static suspension. It can be seen that AMBs could suspend the flywheel stably in the static state, and the radial displacement of the flywheel was less than 1 μm.

Fig. 6. Experiment platform.

(a) Displacement at MB_1 (b) Displacement at MB_2
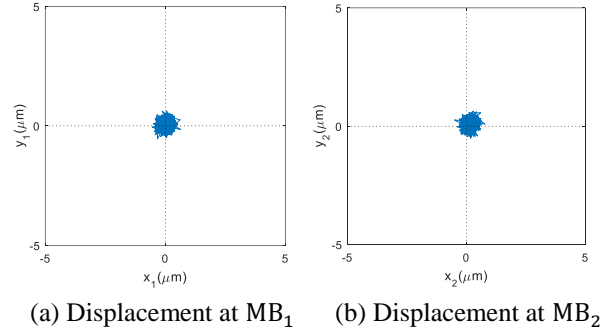
Fig. 7. Flywheel axis orbit under static suspension.

B. Gyroscopic effect suppression

When the flywheel speed is high, the precession frequency gradually drops to zero, and the nutation frequency increases continually. It is difficult for the decentralized PID controller to effectively suppress the procession and nutation simultaneously. The performance of the cross feedback PID control on the gyroscopic effect was studied in the following experiment.

Figure 8 shows the axis orbit and displacement spectrum of the flywheel without cross feedback control. When the flywheel speed was 40 Hz, the precession was unstable and the decentralized PID controller cannot provide enough damping for the precession mode.

Similarly, without cross feedback control, the nutation was unstable when the flywheel speed was 110 Hz, as is shown in Fig. 9. The nutation frequency is 210 Hz, and the ratio between the nutation frequency and the rotor speed is 1.91, which is basically equal to the inertia ratio of the flywheel [11].

(a) Displacement at MB$_1$ (b) Displacement at MB$_2$

(c) Flywheel displacement spectrum
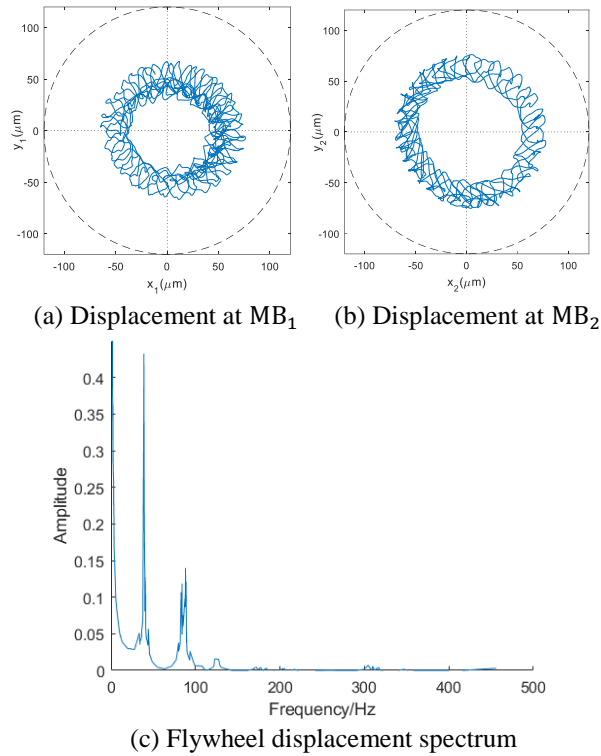
Fig. 8. Precession instability in the experiment.

(a) Displacement at MB$_1$ (b) Displacement at MB$_2$

(c) Flywheel displacement spectrum
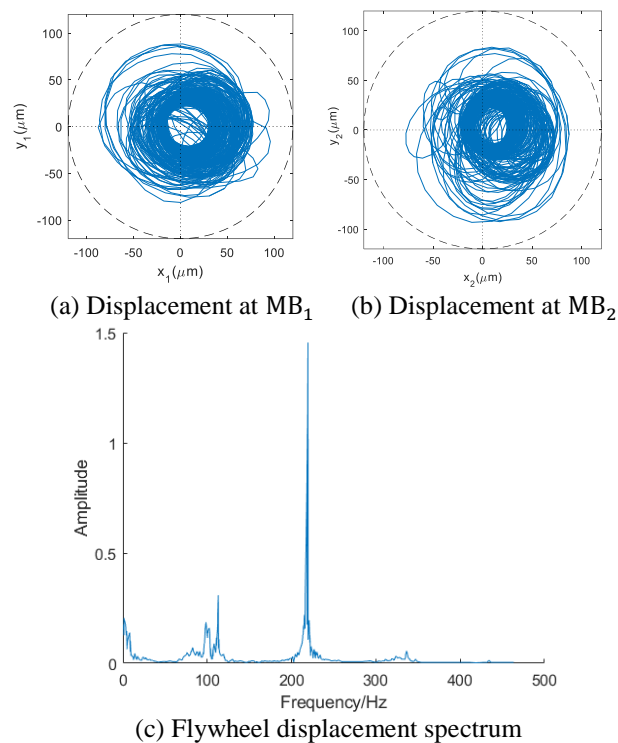
Fig. 9. Nutation instability in the experiment.

In order to effectively suppress the nutation and precession modes of the flywheel simultaneously, the cross feedback control was introduced. The speed-up experiment of AMB-FS was carried out after selecting the appropriate parameters for the cross feedback PID controller. Figure 10 shows the axis orbit and displacement spectrum of the flywheel. It can be seen that under cross feedback PID control, the procession and nutation modal frequencies were effectively suppressed simultaneously. The AMB controller showed good performance and the AMB-FS was highly stable.

(a) Displacement at MB$_1$ (b) Displacement at MB$_2$

(c) Flywheel displacement spectrum
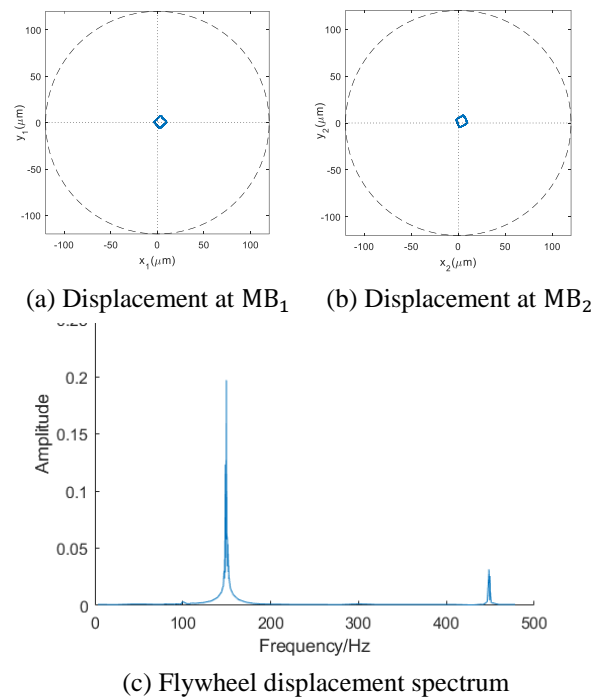
Fig. 10. Stable suspension with cross feedback.

The dashed circle in Figs. 7 and 8 represent the clearance of AMBs. Before the flywheel was totally unstable and had contact with the touchdown bearings, we recorded the data shown in Figs. 7 and 8 and stopped accelerating the flywheel in case of serious damage to the system. If the flywheel runs stably, its axis orbit should be similar with Fig. 6, which means the flywheel has very little displacement in x and y directions. However, in the experiment, as the flywheel speeds up without cross feedback control, its axis orbit changed from Fig. 6 to Figs. 7 and 8, which is the divergent behavior before the flywheel is totally unstable.

In the experiment, the flywheel speed could exceed 31200 rpm and still possessed the speeding potential. When the flywheel rotated at the rated speed of 500 Hz in the vacuum environment, the power consumption of AMBs was only 17.82 W and the system had no need of cooling measures. The radial vibration amplitude of the flywheel was less than 2 μm, and the shaking intensity of the AMB-FS base is less than 0.016 mm/s.

C. Rotating frame experiment

From the theoretical analysis above, it can be seen that the rotating frame leads to strong gyroscopic effect of the flywheel at high speed, which will reduce the AMB controller performance significantly. The flywheel may collide with the touchdown bearings, leading to the instability of the AMB-FS. Therefore, in the rotating frame, the stability of the AMB-FS was analyzed in the experiment.

In the experiment, the flywheel was suspended stably at the rated speed of 500 Hz, and the frame rotated in the x direction at different angular velocity. The axial orbit of both ends of the flywheel and the flywheel displacement spectrum is shown in Fig. 11, where the angular velocity of the frame is 1 deg/s, 1.5 deg/s and 2.5 deg/s, respectively.

(a) 1 deg/s

(b) 1.5 deg/s

(c) 2.5 deg/s
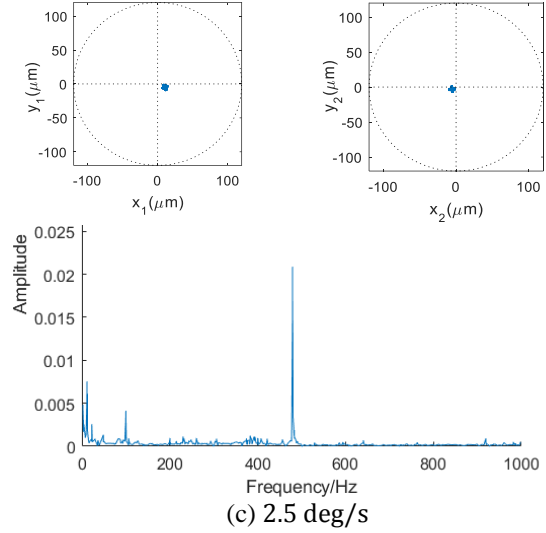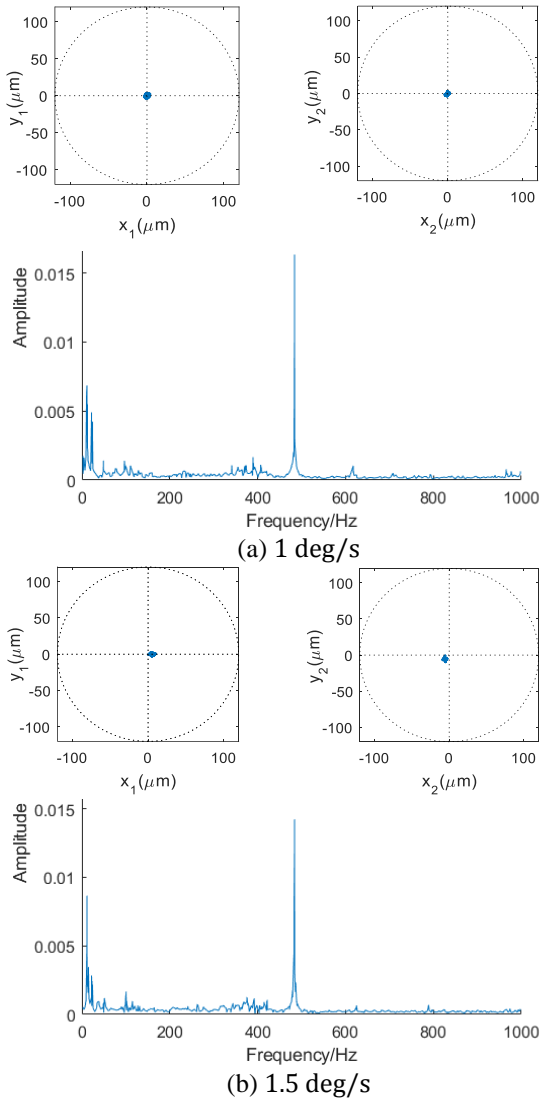
Fig. 11. Axis orbit and displacement frequency.

From the experimental results, it can be seen that the increase of the frame rotational speed had no effect on the stability of the AMB-FS. There as little change in the flywheel axis orbit and the displacement spectrum. It proves that the cross feedback PID controller possessed good robustness and had high performance in resisting the disturbance of the rotating frame. The dynamic stability of the ultra-high AMB-FS was fully verified under the disturbance of the rotating frame in the experiment.

IV. AMB-FS ANALYSIS IN ROTATING FRAME

Since the power amplifier has maximum current and the ferromagnetic material has saturation magnetization, AMBs have the maximum force. Influenced by the gyroscopic effect and limited by the maximum AMB force, the frame has the maximum rotational speed when the AMB-FS is stable. Therefore, the experiment of the AMB-FS in the rotating frame was studied.

Assume that the rotational angle of the frame is $\theta = \omega_n t + \theta_0$, where θ_0 is the initial angle and ω_n is the frame rotational speed. Under the conditions of small-angle change, the AMB force at time t is:

$$\begin{cases} F_{x_1} = -(k_1 x_1 + d_1 \dot{x}_1) \\ F_{x_1} = -(k_2 x_2 + d_2 \dot{x}_2) \\ F_{y_1} = -[k_3(y_1 - a\theta) + d_3(\dot{y}_1 - a\omega_n)]' \\ F_{y_2} = -[k_4(y_2 + b\theta) + d_4(\dot{y}_2 + b\omega_n)] \end{cases} \quad (12)$$

where k_j $(j = 1, 2, 3, 4)$ and d_j are the stiffness and damping of AMBs. Substitute the equation (12) into the (2) and obtain the ordinary differential equations with

the bearing coordinates $q_b = [x_1, x_2, y_1, y_2]^T$ as the variables, and the solution of equation is:

$$\begin{cases} x_1 = -\dfrac{J_p \Omega \omega_n}{(a+b)k_1} \\ x_2 = \dfrac{J_p \Omega \omega_n}{(a+b)k_2} \\ y_1 = a(\omega_n t + \theta_0) \\ y_2 = -b(\omega_n t + \theta_0) \end{cases} \quad (13)$$

Therefore, the AMB force can be obtained by substituting equation (13) into equation (12):

$$\begin{cases} F_{x_1} = \dfrac{J_p \Omega \omega_n}{(a+b)} \\ F_{x_1} = -\dfrac{J_p \Omega \omega_n}{(a+b)} \\ F_{y_1} = F_{y_2} = 0 \end{cases} \quad (14)$$

It can be seen from the result that when the frame rotates in x direction at speed ω_n, there is no force in y direction while the forces in x direction have the same values and opposite directions. The AMB force in x direction is proportional to the product of flywheel speed and frame rotational speed. Therefore, when the flywheel speed is high, only a small frame rotational speed will consume a large amount of AMB force and lead to the force saturation, which will affect the stability of the AMB-FS significantly.

A. Maximum frame speed

AMBs in this study can provide a maximum electromagnetic force of 1200 N. Therefore, with equation (11) and the model in Fig. 5, the relationship between flywheel speed and maximum frame rotational speed can be obtained in Fig. 12, where the solid line is theoretical result and the dotted line is simulation result.

The maximum frame rotational speed was verified in the experiment. The flywheel was placed horizontally, which means its axis was in the horizontal direction and its weight was supported by the radial AMBs. The AMB-FS was placed on a rotatable base.

   A.   The flywheel accelerated to a certain speed and run stably.
   B.   As the flywheel rotated stably, accelerated the base slowly.
   C.   When the base accelerated to the speed at which the flywheel vibrated violently, recorded the speeds of the flywheel and base.
   D.   Changed the speed of flywheel and repeated the step A to C.

The dashed line in Fig. 12 shows the experiment result. It can be seen that the results of theory, simulation and experiment agree well. As the flywheel speed increases, the maximum frame rotational speed decreases rapidly.
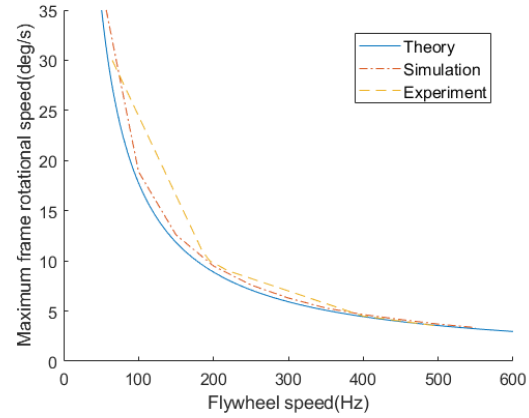
Fig. 12. Relationship between flywheel speed and frame rotational speed.

The experimental results show the high stability of the AMB-FS at high flywheel speed. And the maximum frame rotational speed could reach 3.5 deg/s at the rated flywheel speed of 500 Hz. In the experiment, AMBs needed to provide extra force to offset the flywheel gravity. Therefore, If the flywheel is placed vertically, which means the axis of the flywheel is vertical direction and the weight is supported by axial AMBs, the robustness of AMB controller and the maximum frame rotational speed will be further improved.

B. Features of the AMB Force

In can be seen in the theoretical analysis that the AMB force had different performance in different directions. Therefore, the simulation and the experiment were carried out to observe the features of the AMB force when the frame rotational speed increased. In the simulation, the flywheel rotated at the rated speed of 500 Hz, and the frame rotational speed gradually increased from 0 deg/s to 3.5 deg/s. Figure 13 shows the simulation results of frame rotational speed and the AMB force.

According to theoretical analysis, when the frame rotates in the x direction, AMBs will generate force in x direction to suppress the gyroscopic effect of the flywheel. As shown in Fig. 13 (b), the AMB electromagnetic forces in x direction increased as the frame rotational speed increase, and the force direction of two AMB is opposite. While in the y direction there was only a certain exciting force at the start and stop state of the frame acceleration. The results are consistent with theoretical analysis. Furthermore, in the simulation, the acceleration of the frame was reflected by the flywheel rotating in x direction. Therefore, there was no AMB force in the y direction during the acceleration of the frame.

(a) Frame rotational speed

(b) AMB force in x direction

(c) AMB force in y direction
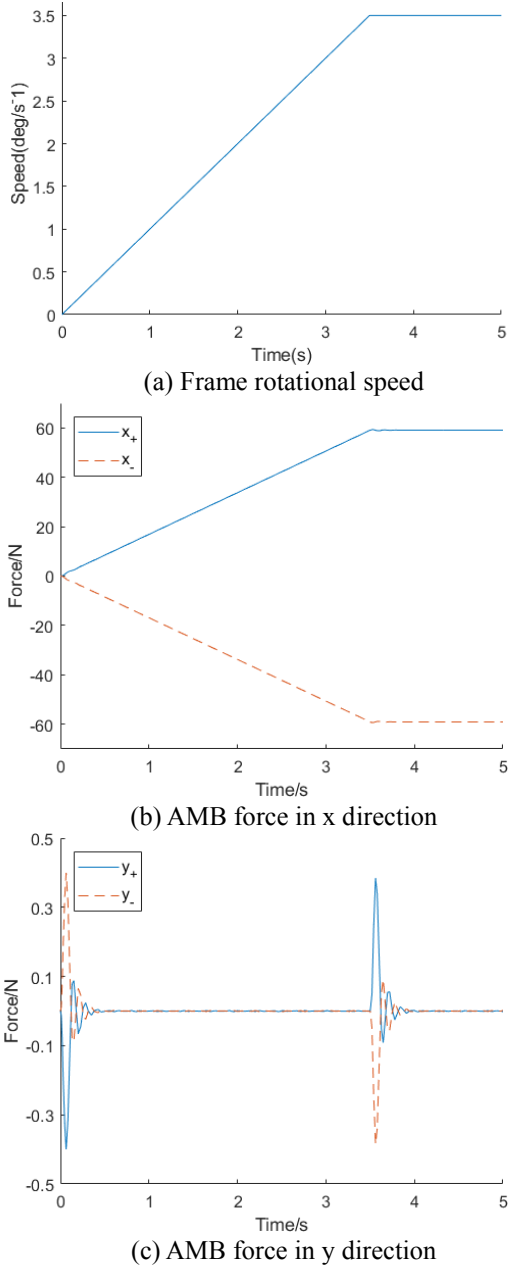
Fig. 13. Frame rotational speed and AMB force.

Similarly, in the experiment, the flywheel was suspended stably and rotates at 100 Hz. Recorded the control current of radial AMB when the frame rotated at different rotational speeds. According to the theoretical analysis, when the flywheel rotated in the rotating frame, there is no AMB force in y direction. Therefore, only the control current in x direction was studied in the experiment. By gradually increasing the frame rotational speed until the AMB force was saturate, the features of the AMB force was obtained as Fig. 14 shows.

From the experimental results, it can be seen that the AMB control current changed with the frame rotational

speed. The high-speed flywheel could be suspended stably and the axis orbit was small, so the flywheel displacement could be regarded as a constant. The features of the AMB force can be obtained as Fig. 15 shows. F_{x_1} and F_{x_2} are the AMB force of MB$_1$ and MB$_2$, and the $F_{x_i}^+$ points to the positive direction of the x-axis while the $F_{x_i}^-$ points to the negative.

1) When the frame rotational speed is low, the influence of the gyroscopic effect on the AMB-FS is small. The AMB forces $F_{x_1}^+$ and $F_{x_2}^+$ are large, while $F_{x_1}^-$ and $F_{x_2}^-$ are zero. Therefore, the electromagnetic force is mainly used to offset the flywheel gravity.

2) As the frame rotational speed increases, $F_{x_1}^+$ increase rapidly and $F_{x_2}^+$ decreases to zero. The flywheel is in the cantilever state, with the flywheel gravity is use to suppress the gyroscopic effect.

3) When frame rotational speed is high, the external disturbances caused by the gyroscopic effect aggravates. $F_{x_1}^+$ continues to increase while $F_{x_2}^-$ starts to increase. AMBs at both ends of the flywheel provide electromagnetic force to suppress the gyroscopic effect.

Fig. 14. The AMB control current in x direction.

(a) Low speed   (b) Medium speed

(c) High speed
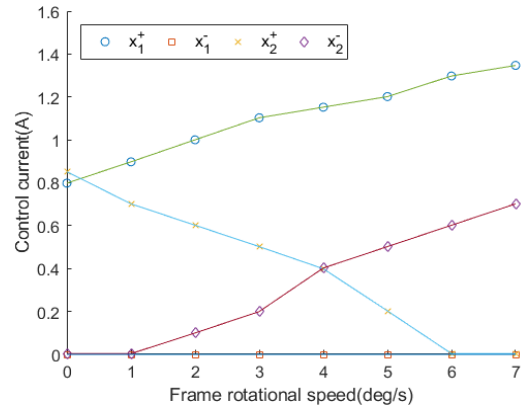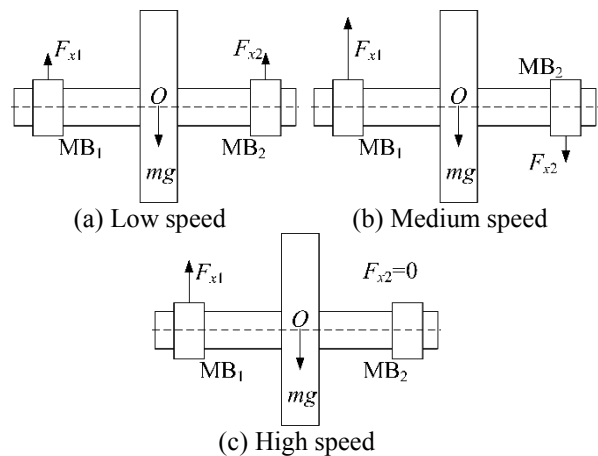
Fig. 15. The AMB force under different frame rotational speed.

The resultant force of AMBs is constant, but the resultant moment about the flywheel centroid increases as the frame speeds up to suppress gyroscopic effect. The experimental results agree with the theoretical analysis and show the features of the AMB force when the frame rotational speed increases.

C. Stability at maximum frame speed

As AMBs suppresses the gyroscopic effect caused by the rotating frame, it still need to resist the external disturbance loaded on the flywheel. So the simulation was carried out to observe the influence of external disturbance on the AMB-FS in the rotating frame. When the flywheel rotated at the rated speed of 500 Hz and the frame rotated at the maximum speed of 3.5 deg/s, loaded the external disturbance on the flywheel in the x direction at 6 s. Increased the frame rotational speed to 3.5 deg/s before 4 s, and loaded 58 N external disturbance when the AMB-FS runs stably as shown in Fig. 16 (a), The AMB-FS could return to steady state. However, to suppress the gyroscopic effect, the AMB control current in the x direction was very large and the control current reached saturation during the flywheel returning to the steady state. When the external disturbance came to 60 N, the system was unstable and AMBs cannot meet the control requirement, as shown in Fig. 16 (b).

(a) 58 N in x direction
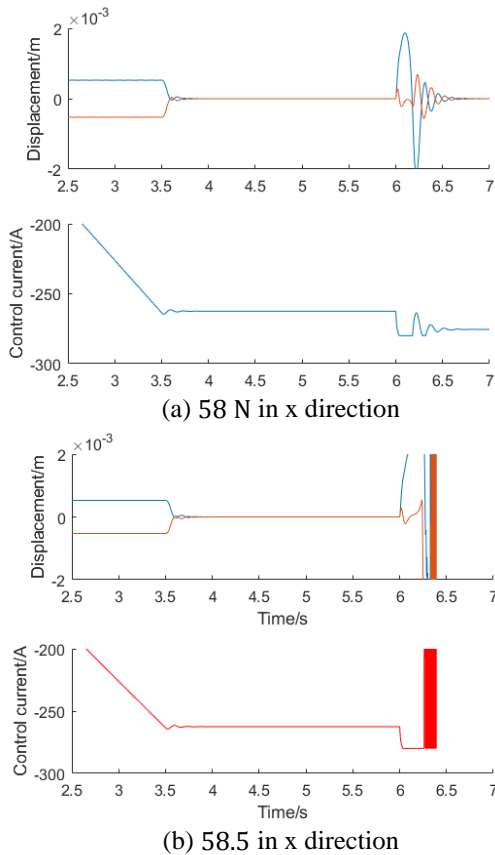
(b) 58.5 in x direction

Fig. 16. Displacement and control current in x direction.

Similarly, repeated the experiment and loaded the external disturbance on the flywheel in the y direction. Increased the frame rotational speed to 3.5 deg/s before 4 s, and loaded 17.5 N external disturbance on the flywheel at 6s. As the Fig. 17 (a) shows, the AMB-FS could return to the steady state. However, the AMB control current in the x direction still reached saturation. When the external disturbance was only 18 N, the system was unstable.

As is known in the theoretical analysis, when the AMB-FS runs in the rotating frame, AMBs in y direction need not to provide electromagnetic force. Therefore, theoretically, the external disturbance loaded in the y direction can be large. However, due to the gyroscopic effect of the flywheel, the external disturbance loaded in the y direction will still seriously affect AMBs in x direction.

(a) 17 N in y direction

(b) 17.5 N in y direction
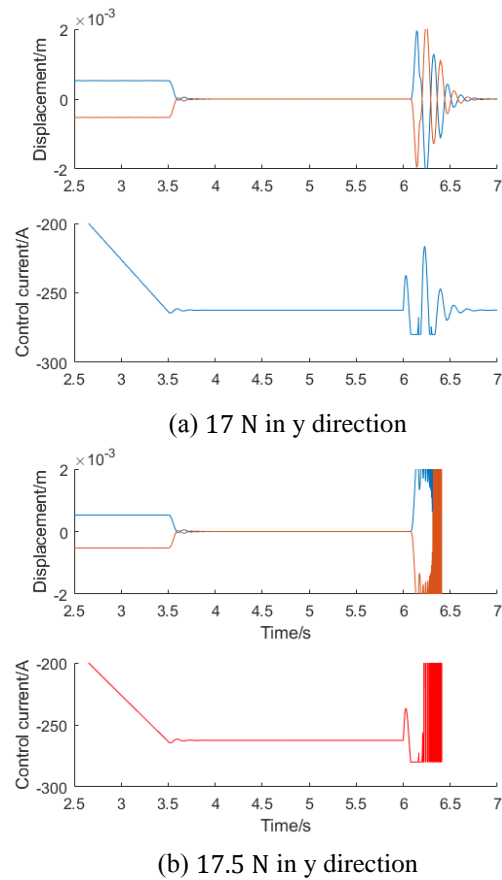
Fig. 17. Displacement and control current in x direction.

From the simulation and the analysis, it can be seen that AMBs in the x direction is under seriously requirement regardless of direction of the external disturbance. The external disturbance is against the frame rotational speed. The larger the frame rotational speed, the more the electromagnetic force is consumed to suppress the gyroscopic effect. Therefore, AMBs will

be weak to resist the external disturbance when the frame speed is high. Limited by the experimental conditions, the experiment of external disturbance will be carried out after optimizing the experiment platform.

V. CONCLUSION

In this paper, through stability analysis, AMB controller design, stability experiment and AMB-FS performance experiment, the AMB-FS was designed and studied. The stability of the AMB-FS and the high performance of AMBs were studied in the rotating frame.

➢ Under cross feedback PID control, the gyroscopic effect of the flywheel was effectively suppressed.

➢ The flywheel could be suspended stably at any speed within the range of 0 to 30000 rpm in the vacuum environment, and the AMB-FS showed high stability.

➢ The flywheel speed could exceed 31200 rpm and still possessed the speeding potential.

➢ When the flywheel rotated at the rated speed of 500 Hz in the vacuum environment, the power consumption of AMBs was only 17.82 W and the system had no need of cooling measures.

➢ The radial vibration amplitude of the flywheel was less than 2 μm, and the shaking intensity of the AMB-FS base was less than 0.016 mm/s.

➢ The maximum frame rotational speed at different flywheel speeds was analyzed, and the maximum frame speed could reach 3.5 deg/s at the rated flywheel speed of 500 Hz.

The dynamic and parametric uncertainties of the AMB-FS would be carried out in the further experiment. To reduce the energy loss and improving the stability of the high-speed AMB-FS, the study about the resistance moment of AMBs would be carried out.

ACKNOWLEDHGMENT

REFERENCE

[1] P. C. Pu, J. P. Yu, and L. Zhao, "Analysis of stiffness and damping properties of active magnetic bearing using cross feedback control," *International Conference on Mechanics and Mechanical Engineering*, 2017.

[2] Z. Kai, Z. Lei, and H. Zhao, "Research on control of flywheel suspended by active magnetic bearing system with significant gyroscopic effects," *Chinese Journal of Mechanical Engineering*, pp. 63-66, 2004.

[3] K. Zhang, R. Zhu, and H. Zhao, "Experimental research on a momentum wheel suspended by active magnetic bearings," *Proceedings of the 8th ISMB, Mito*, 2002.

[4] S. Sivrioglu, "Lmi based gain scheduled h_∞ controller design for amb systems under gyroscopic and unbalance disturbance effect," *Proc. Int. Symp. on Magnetic Bearings*, pp. 191-196, 1996.

[5] F. Matsumura, T. Namerikawa, K. Hagiwara, and M. Fujita, "Application of gain scheduled H∞ robustness controllers to a magnetic bearing," in *IEEE Transactions on Control Systems Technology*, vol. 4, no. 5, pp. 484-493, Sep. 1996.

[6] P. Tsiotras and S. Mason, "Self-scheduled H∞ controllers for magnetic bearings," *International Mechanical Engineering Congress and Exposition*, Atlanta, GA, pp. 151-158, Nov. 1996.

[7] Z. Gosiewski and A. Mystkowski, "The robust control of magnetic bearings for rotating machinery," *Solid State Phenomena*, vol. 113, pp. 125-130, 2006.

[8] A. Mystkowski, "Sensitivity and stability analysis of mu-synthesis AMB flexible rotor," *Solid State Phenomena*, vol. 164, pp. 313-318, 2010.

[9] Z. Sun, J. Zhao, Z. Shi, and S. Yu, "Identification of flexible rotor suspended by magnetic bearings," *International Conference on Nuclear Engineering*, pp. V002T03A043 - V002T03A043, 2013.

[10] Z. Sun, Y. He, J. Zhao, et al., "Identification of active magnetic bearing system with a flexible rotor," *Mechanical Systems & Signal Processing*, vol. 49, no. 1-2, pp. 302-316, 2014.

[11] F. Jiancheng, *Technology of Magnetic Suspension Control Moment Gyroscope*. Nationnal Defense Industry Press, 2012.

Jinpeng Yu received his B.Sc. degree in 2015 from Dalian University of Technology. Now he is studying for a Ph.D. at the Institute of Nuclear and New Energy Technology, Tsinghua University. He is mainly engaged in active magnetic bearing and its application in flywheel system.

Zhe Sun is currently an Aassociate Professor and Ph.D. Supervisor of Tsinghua University. His research interests are control and monitoring of active magnetic levitation system, rotor dynamics, statistical learning theory and its engineering application, etc. He has published more than 20 SCI/EI index papers and 10 national patents. He presides over and participates in a series of National Science and Technology Major Project of China, National Natural Science Foundation of China and National High-tech Research and Development Program of China.

Nonlinear Analysis of Rotor-AMB System with Current Saturation Effect

Xiaoshen Zhang [1,2,3], Tianpeng Fan [1,2,3], Zhe Sun[*1,2,3], Lei Zhao [1,2,3], Xunshi Yan [1,2,3], Jingjing Zhao [1,2,3], and Zhengang Shi [1,2,3]

[1] Institute of Nuclear and New Energy Technology
[2] Collaborative Innovation Center of Advanced Nuclear Energy Technology
[3] Key Laboratory of Advanced Reactor Engineering and Safety of Ministry of Education
Tsinghua University, Beijing, 100084, China
zxs16@mails.tsinghua.edu.cn, sun_zhe@mail.tsinghua.edu.cn*

Abstract ─ The analysis on nonlinear dynamics of a rotor-AMB system is conducted in this paper. The nonlinearity of electromagnetic force and current saturation effect are taken into account. The nonlinear model of the rotor-AMB system is built and the nonlinear dynamic behaviors of the system in both resonance region and non-resonance region are investigated through numerical integration method. This paper shows that the rotor-AMB system can exhibit some complicated nonlinear dynamic behaviors, such as soft spring characteristic of the amplitude-frequency response curve, the jump phenomenon, and pitchfork bifurcation. And the effects of exciting force and current saturation on these nonlinear dynamic behaviors of the system are discussed.

Index Terms ─ Current saturation, nonlinear analysis, numerical integration, pitchfork bifurcation.

I. INTRODUCTION

As a typical mechatronic product, active magnetic bearings (AMBs) can achieve the suspension support of the rotor through the electromagnetic forces. An AMB system consists of sensors, controllers, power amplifiers, and mechanical components. The rotor displacement is adjusted by the cooperation of these components. During operation, as the rotor deviates from the reference position, the displacement is measured by the sensor, then measurement signal is transformed into a control signal through the calculation of the controller, which is imported into the power amplifier hereafter. Based on the control signal, the power amplifier exports the control current which will play a key role in magnetic bearings to generate appropriate electromagnetic force to suspend the rotor. Compared with conventional bearings, AMBs have a lot of advantages, such as no mechanical friction between rotor and stator, no wear, lubrication free, long operation life with low maintenance cost, etc. What is more, dynamic characteristics of the rotor can be controlled through the AMBs during system operation. Due to these advantages, AMBs have been widely applied in high-speed rotating machinery, especially those working in special environments.

The modeling, dynamics analysis, and controller design of the rotor-AMBs system were usually based on linearized models which described the characteristics of the system approximately in the linear region near to static levitation position [1], and system identifications were also based on the linearized models [2,3]. The linearized model can meet the research needs of vibration modal analysis and controller design under the condition of small rotor displacements. However, the rotor-AMB systems are substantially nonlinear. The electromagnetic force is a nonlinear function of currents and rotor displacement, and there may exist hysteresis, voltage saturation, and current saturation effects in the system. With the increasing of rotating speed and more extensive use of new structures and materials, the nonlinearities of the rotor-AMB system have become increasingly prominent. Thus the system may exhibit many complicated nonlinear phenomena, such as jump phenomenon, co-existence of multiple solutions, sensitivity to initial conditions, bifurcations and even chaos [4]. The dynamic characteristics of the rotor-AMBs systems are so complicated that linear models could not predict the dynamic behaviors and the stability of the system accurately under various operating conditions [5]. Therefore, it is essential to carry out the nonlinear dynamics analysis of the rotor-AMBs system.

There have been extensive publications about nonlinear characteristics of rotor-bearing systems. For example, Refs. [6,7] investigated the nonlinear dynamics of rotor-film bearing systems and got some valuable results, which were heuristic for the nonlinear dynamics analysis of rotor-AMB systems. However, rotor-AMB systems have some special nonlinear factors because of features of the AMBs, such as the delay of control force [8,9], current, voltage and magnetic saturation [10], and time-varying stiffness [11].

The nonlinear phenomena of rotor-AMB systems have been the focuses of researchers. Many analysis

methods have been developed and many interesting results have been found. Nonlinear analysis methods applied to rotor-AMB systems can be divided into two categories, namely numerical methods and analytical methods. References [12-14] analyzed the bifurcations of a flexible rotor supported by AMBs numerically. The dynamic behaviors of the system under different operating conditions were studied using the trajectory diagrams, bifurcation diagrams, power spectra and Poincaré maps in [12]. The effects of the system parameters on dynamic characteristics were analyzed and the key factors affecting system performance were identified and demonstrated. References [13,14] investigated the nonlinear dynamic responses of the flexible rotor-AMBs system numerically and proved that nonlinear phenomena such as period-doubling motion, quasi-periodic motion, and even chaotic motion might appear. Moreover, the approximate analytical methods including harmonic balance method, asymptotic perturbation method [15], the method of multiple scales [4], and KBM method [16,17], have been applied widely in nonlinear analysis of rotor-AMB systems. The nonlinear oscillations of a rigid rotor-AMB system taking the time delay into account were studied using the approximate analytical method in [18], and the effects of system parameters on the dynamic behaviors were analyzed. Reference [4] applied the method of multiple scales to obtain an analytical approximate solution of a rotor-AMB system subjected to primary resonance excitations in the presence of 1:1 internal resonance. Based on the analytical approximate solution, a verity of nonlinear phenomena were studied and the analysis results were validated by numerical simulation. References [15,19] utilized the asymptotic perturbation method and the method of multiple scales respectively to investigate the responses of the rotor-AMB system with periodic time-varying stiffness and the system exhibited some typical nonlinear phenomena. References [16,17] utilized KBM method to investigate the nonlinear dynamics of the rotor-bearing system with hysteretic characteristics.

These aforementioned reports about the nonlinear analysis of rotor-AMB systems focused on rotor vibration amplitudes, which will have a significant effect on system stability. However, the rotor-AMB system has a larger air gap between the rotor and stator than rotor systems supported by conventional bearings due to the non-contact suspension support feature. Under certain operating conditions, the nonlinear rotor-AMB system may have multiple equilibrium solutions, namely, the rotor may vibrate in different equilibrium positions. In this case, the rotor's maximal instantaneous displacement is dependent on both rotor equilibrium position and vibration amplitude. And if rotor displacement is large, the rotor-AMB system may lose its stability. Therefore, equilibrium solutions also have an important influence on system stability as well as the vibration amplitude. There were few reports

about rotor equilibrium positions of the rotor-AMB system. Nevertheless, the rotor-AMB system is expected to operate in non-resonance regions, where the rotor doesn't exhibit complicated characteristics in vibration amplitude generally. Whereas there may exist some other nonlinear phenomena in non-resonance regions, which also have effect on the system performance but didn't attract enough attention. For example, the pitchfork bifurcation phenomenon was discovered in site-commissioning of a rotor-AMB system with current saturation effect, which meant that new equilibrium solutions occurred in the system. It was detrimental to system performance.

In this paper, a single-degree-of-freedom rotor-AMB system with current saturation effect is investigated through numerical integration method. The nonlinear model of the rotor-AMB system considering current saturation effect is deduced firstly. Then the amplitude-frequency response characteristics and rotor dynamic behaviors in the non-resonance region are analyzed numerically based on the system differential equation of motion. The system exhibits soft-spring characteristics, jump phenomena, and pitchfork bifurcation. The effects of exciting force and current saturation on system dynamic behaviors are illustrated and controller parameter modification is conducted. This paper concentrates on nonlinear phenomena of the rotor-AMB system in both non-resonance and resonance regions, which extends the nonlinear dynamic analysis of the rotor-AMB system to full speed range and enriches the nonlinear dynamic theory of the rotor-AMB system. The investigation of pitchfork bifurcation in non-resonance can supply the research gap in nonlinear analysis of the rotor-AMB system and help to understand the system's nonlinear dynamics in the round. And through the comprehensive nonlinear dynamics analysis of the system with current saturation, the nonlinear dynamic behaviors are illustrated in detail and the causes of the nonlinear phenomenon are explored in depth. The analysis result can play an important role in the efforts to improve system performance. For example, the controller adjustment based on nonlinear analysis results can achieve the goal of improving system performance that the efforts based on linear analysis couldn't do.

II. THEORETICAL MODEL

This paper takes an actual rotor-AMB system as a research object. During commissioning, the system lost its stability and the current saturation phenomenon was discovered by analyzing the operational data. In order to explore the instability mechanism, the nonlinear model is built and nonlinear analysis through cell mapping method is conducted by authors of this paper [20]. In this paper, the nonlinear dynamics of the rotor-AMB system is investigated using numerical integration method and dynamic behaviors in both resonance and non-resonance

regions are analyzed. Just as Ref. [20], the rotor-AMB system is simplified into a single-degree-of-freedom model for simplicity of the analysis in this paper, which focuses on the direction where nonlinear phenomena occur.

A. System model

The diagram of the simplified system model is shown in Fig. 1.
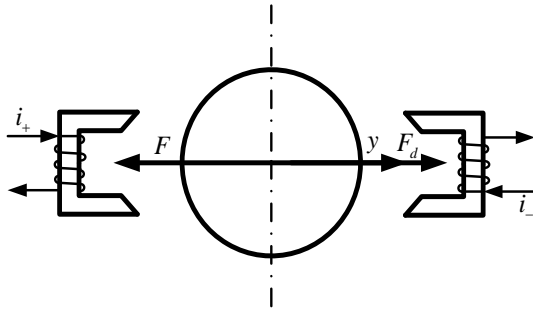
Fig. 1. Schematic diagram of single-degree-of-freedom rotor-active magnetic bearings system.

Where, y represents the displacement of the rotor, i_+, i_- represents the currents from the power amplifier to the magnets respectively, F represents the electromagnetic force, and F_d represents the exciting force. The exciting force is assumed to be sinusoidal, as shown in equation (1):

$$F_d = |F_d|\cos(\Omega t). \tag{1}$$

The open-loop system is inherently unstable. For the analyzing the dynamic characteristics of the system, a PD controller is adopted to keep the system stable. The magnetic hysteresis and fringing effect are not taken into account. The sensor is taken as a proportional component whose gain is k. And a current-type power amplifier is employed in the system, in which the current saturation is taken into account. The closed-loop diagram of the system is shown in Fig. 2.
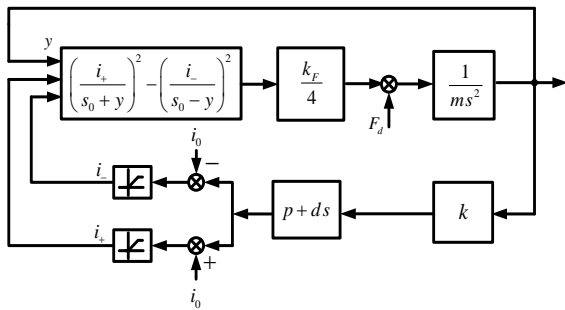

Fig. 2. Closed-Loop Diagram of Rotor-AMB System.

In the actual system, the currents in the power amplifier are limited to a certain range. Thus, the currents

of the two magnets, namely, i_+, i_-, can be expressed as a piecewise function shown in equation (2):

$$i_+ = \mathrm{med}(0, i_0 + i, i_m) = \begin{cases} 0 & i_0 + i < 0 \\ i_0 + i & 0 \le i_0 + i \le i_m, \\ i_m & i_m \le i_0 + i \end{cases}$$

$$i_- = \mathrm{med}(0, i_0 - i, i_m) = \begin{cases} 0 & i_0 - i < 0 \\ i_0 - i & 0 \le i_0 - i \le i_m, \\ i_m & i_m \le i_0 - i \end{cases} \tag{2}$$

$$i = k(py + d\dot{y}),$$

where, i_0 represents the bias current of the magnetic bearing and i represents the control current, $\dot{y}$ represents the first order derivative of rotor displacement, and 'med' means the median value of the three values in the bracket.

In the rotor-AMB systems, the electromagnetic force is a nonlinear function of the rotor displacement and the currents in magnetic bearings. The electromagnetic force model in Ref. [1] is adopted and can be formulated as equation (3):

$$F = \frac{1}{4}k_F\left(\left(\frac{i_+}{s_0 + y}\right)^2 - \left(\frac{i_-}{s_0 - y}\right)^2\right), \tag{3}$$

where, s_0 is the air gap of the bearing at the reference position, and k_F is the force coefficient related to the system. It can be seen from equation (3) that the existence of the current saturation makes nonlinear characteristics of the system more complicated.

Based on basic laws of the classical mechanics, the governing equation of the closed-loop system shown in Fig. 2 is deduced, as shown in equation (4):

$$\ddot{y} = \frac{1}{m}\left(-F + |F_d|\cos(\Omega t)\right), \tag{4}$$

where m is the mass of the rotor.

Then the mathematical model of the rotor-AMB system is made up of the equations (1), (2), (3), (4).

B. Nondimensionalization

In order to facilitate analysis and obtain the visualized results, the governing equations of the system obtained above are transformed into the dimensionless form by introducing the following dimensionless variables and corresponding notations:

$$y' = \frac{y}{s_0}, \ \Omega' = \frac{\Omega}{\Omega_0}, \ \tau = \Omega_0 t,$$

$$i' = \frac{i}{i_m}, \ i_0' = \frac{i_0}{i_m}, \ i_\pm' = \frac{i_\pm}{i_m},$$

$$p' = \frac{ps_0}{i_m}, \ d' = \frac{\Omega_0 ds_0}{i_m}, \ \tilde{k}_F = \frac{k_F}{4}\frac{i_m^2}{\Omega_0^2 s_0^3}, \tag{5}$$

$$|\tilde{F}_d| = \frac{1}{\Omega_0^2 s_0}|F_d|,$$

where, Ω_0 is the rated operating speed of the rotor. Substitute equation (5) into equations (1), (2), (3), and (4), then dimensionless form model of the system is obtained, as shown in equation (6):

$$i'_{\pm} = \mathrm{med}\left(0, i'_0 \pm i', 1\right),$$

$$i' = k\left(p'y' + d'\frac{\mathrm{d}}{\mathrm{d}\tau}y'\right),$$

$$\tilde{F} = \tilde{k}_F\left(\left(\frac{i'_+}{1+y'}\right)^2 - \left(\frac{i'_-}{1-y'}\right)^2\right),$$

$$\frac{\mathrm{d}^2}{\mathrm{d}\tau^2}y' = \frac{1}{m}\left(-\tilde{F}\right) + \left|\tilde{F}_d\right|\cos\left(\Omega'\tau\right).$$

In the non-dimensional model, i'_0=0.5, $k = 45000$, $\tilde{k}_F$=0.0099. In the following, the values of these variables are fixed at these values and other parameters will be assigned.

III. RESULTS AND DISCUSSIONS

Based on the dimensionless form model obtained in the previous section, the nonlinear dynamics of the rotor-AMB system is investigated numerically. In this section, equation (6) is solved to get time series solutions of multiple variables by Runge-Kutta 5(4) algorithm [21] under different conditions. Then the time responses of rotor displacement, currents, and electromagnetic force are obtained. Based on the rotor displacement time series responses, the displacements at chosen Poincaré points of motion periods are gotten by Poincaré map and vibration amplitude a is calculated according to equation (7):

$$b_1 = 2\int y'(\tau)\sin\Omega'\tau\,\mathrm{d}\tau,$$

$$b_2 = 2\int y'(\tau)\cos\Omega'\tau\,\mathrm{d}\tau,$$

$$a = \sqrt{b_1^2 + b_2^2}.$$

In the following of this section, the amplitude-frequency response of the system is acquired and the pitchfork bifurcation phenomenon is discovered and interpreted. Based on analysis results, the controller parameters are adjusted to avoid pitchfork bifurcation, which has a detrimental effect on system stability.

A. Amplitude-frequency response of system

The amplitude-frequency response is one of the important characteristics of the rotor-AMB system, which play a key role in the system performance analysis and controller design. However, the amplitude-frequency response based on nonlinear model differs from that based on the linear model.

In this subsection, parameters of the PD controller are fixed at $p' = 4.232\times10^{-5}$, $d' = 1.0668\times10^{-4}$. Then amplitude-frequency response curves of the rotor-AMB system for different exciting magnitudes are obtained.

When the exciting force's magnitudes are 0.354, 0.4132, 0.4722, the amplitude-frequency response curves are shown in Fig. 3 respectively. In Fig. 3, a is the dimensionless vibration amplitude of rotor situated in zero equilibrium position. In this case, the rotor's maximal instantaneous displacement only depends on vibration amplitude and is just the vibration amplitude. It contrasts with that in case of pitchfork bifurcation which will be described in the next subsection.
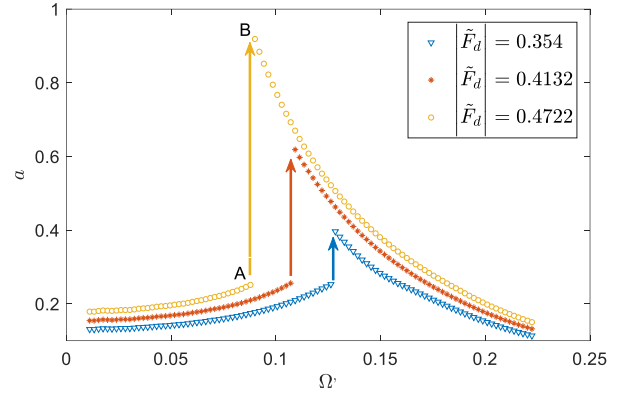
Fig. 3. The amplitude-frequency response of the rotor-AMB system.

It can be seen from Fig. 3 that the vibration amplitude of the rotor is not only dependent on exciting magnitudes, but also related to exciting frequencies. With the increase of exciting force, the vibration amplitude magnifies. Meanwhile, as the exciting frequency increases, the rotor amplitude first increases and then decreases after some specific frequency where there is a resonance peak. This result is consistent with that based on the linear system. However, the nonlinear system also exhibits more complicated phenomena, such as soft-spring characteristics and jump phenomenon. As shown in Fig. 3, the frequencies where resonance peaks occur are different for different exciting magnitudes. As the exciting magnitude increases, the resonance peak moves to low-frequency zone, i.e., the resonant frequency becomes smaller. In addition, there is another nonlinear phenomenon in Fig. 3. In the vicinity of resonance peaks, the vibration amplitudes mutate with a slight exciting frequency change. Take $\left|\tilde{F}_d\right|$=0.4722 as an example, the amplitude a increases gradually as frequency increases until it reaches the point A. However, at the point A, as frequency increases lightly, the amplitude a jumps from the point A to the point B and the rotor vibration amplitude reaches the peak value. Subsequent to that, the amplitude decreases gradually with the increase of exciting frequency. It is a typical jump phenomenon of nonlinear systems. Furthermore, it can be seen in Fig. 3 that, the larger exciting force is, the more obvious the

jump phenomenon and soft-spring characteristics are.

In order to explore the causes of nonlinear phenomena in the resonance region of the rotor-AMB system, the current and electromagnetic force at point B are shown in Fig. 4 and Fig. 5. In Fig. 5, $\tilde{F}_+, \tilde{F}_-$ represent the attractive force generating by the two magnets respectively, which can be formulated as $\tilde{F}_\pm = \tilde{k}_F \left(\dfrac{i'_\pm}{1 \pm y'} \right)^2$.

It can be seen that severe current saturation has occurred and the electromagnetic force acting as restoring force in the system distort. It leads to the soft-spring characteristic and jump phenomenon, which have detrimental influences on the stability of the rotor-AMB system. In brief, the nonlinearity of electromagnetic force and current saturation existing in the system are the causes of complicated dynamic behaviors when the rotor-AMB system is subjected to the exciting force.
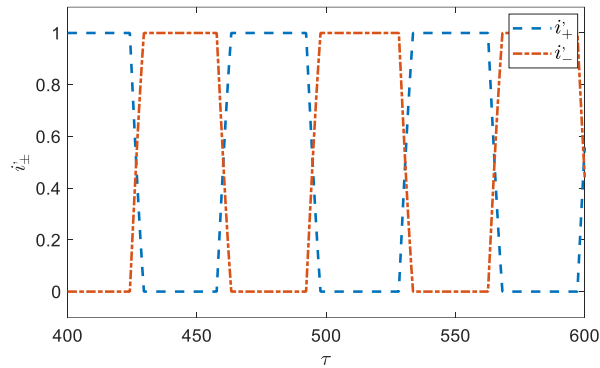
Fig. 4. The partial enlarged detail of current at point B of Fig. 3.
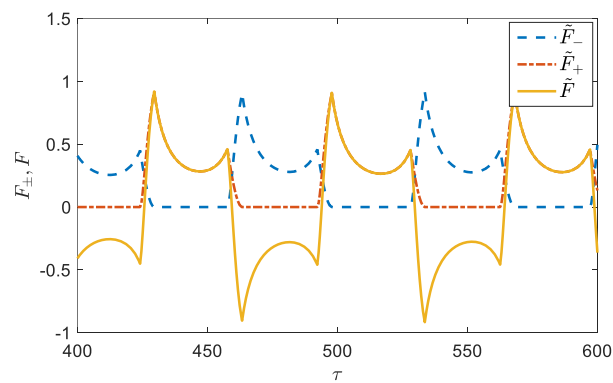
Fig. 5. The partial enlarged detail of electromagnetic force at point B of Fig. 3.

B. Pitchfork bifurcation

When the system is running stably, the rotor speed is generally far from the resonance zone. However, the rotor-AMB system with current saturation effect still exhibits the nonlinear phenomenon when the system is operating in the non-resonance region. In this subsection, the oscillations of the rotor under different initial conditions are investigated and the bifurcation diagram of the rotor versus the exciting force is obtained. The effects of the exciting force and the current saturation in the power amplifier on the vibration of the rotor are also illustrated.

In the analysis, these parameters of the system are fixed at $p' = 4.232 \times 10^{-5}$, $d' = 1.0668 \times 10^{-4}$, $\Omega' = 1$. Two different initial conditions are respectively set as $[y'_{10} = 0.0536, \dot{y}'_{10} = 0.0093]$, $[y'_{20} = 0.403, \dot{y}'_{20} = 0.0093]$. The dynamic behaviors of the system for different exciting forces are analyzed. The time series responses of the rotor-AMB system subjected to exciting forces under different initial conditions are solved by Runge-Kutta 5(4) method with variable step size. And the rotor displacements at Poinceré map points which are the specific time instants of motion periods are obtained from corresponding time series responses through Poincaré map. Then the bifurcation diagram versus the amplitude of the exciting force is obtained, as shown in Fig. 6. The abscissa of the Fig. 6 is the magnitude of the exciting force, while the ordinate is the displacement at the specific Poincaré map point. Different from that in subsection A, the rotor displacements at Poincaré map points y'_1, y'_2 in Fig. 6 depend on both rotor equilibrium positions and vibration amplitudes. In order to explain the relationship between the rotor displacements at Poincaré map points shown in Fig. 6 and time series response, taking $\left| \tilde{F}_d \right| = 16.83$ as an example to point out the correspondence between Fig. 6 and Fig. 10. The displacements shown in Fig. 6 are the mean values of the Poincaré map points' displacements in Fig. 10 after system enters steady state. It is noted that Fig. 10 is the partial enlarged drawing of the time series response and the mapping points shown in Fig. 10 are only part of all mapping points. Because of the chosen mapping points, y'_1 is the maximal instantaneous displacement under corresponding initial condition, while y'_2 is not. But, the maximal instantaneous displacements for two different initial conditions are both the sum of the absolute value of equilibrium positions and vibration amplitude.

It can be seen in Fig. 6 that when the exciting force is small, the amplitudes of the rotor vibration are small and rotor displacements of the Poincaré map points for different initial conditions are consistent, i.e., both rotor equilibrium positions and vibration amplitudes for two different initial conditions are the same. The rotor vibrates at zero equilibrium position for small exciting force and with the increase of the exciting force, the vibration amplitude tends to be larger. In case of small exciting forces, the responses of the rotor-AMB system based on the nonlinear model are consistent with those

based on the linearized model and rotor displacements depend only on vibration amplitudes. However, as the exciting force continues to magnify, the pitchfork bifurcation appears in the vicinity of $\left| \tilde{F}_d \right| = 16.04$, where rotor displacements for different initial conditions are different. The rotor deviates from zero equilibrium position and vibrates at either of two new different equilibrium positions. This is a typical supercritical pitchfork bifurcation. With further increase of exciting force, the pitchfork bifurcation aggravates. In the case of pitchfork bifurcation, the Poincaré map points' rotor displacements are not only dependent on vibration, but also dependent on rotor vibration positions.
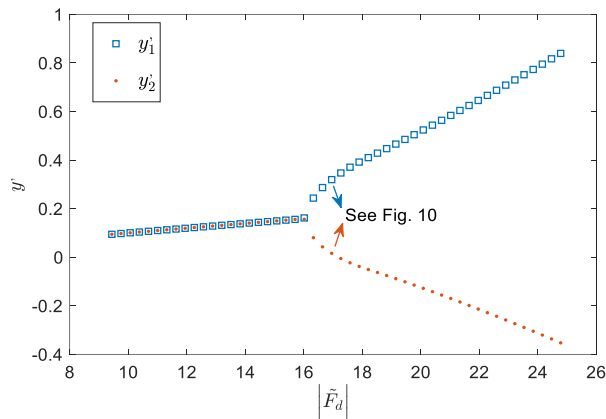

Fig. 6. Pitchfork bifurcation: rotor displacement at Poincaré map points versus exciting magnitude.

In order to understand the bifurcation further and reveal the causes of this phenomenon, two different exciting forces in Fig. 6 are taken as examples to illustrate the influences of the exciting force and current saturation on the dynamic behaviors of the rotor.

For $\left| \tilde{F}_d \right| = 9.44$, the pitchfork bifurcation doesn't appear. The system time series responses, currents in the system, and electromagnetic forces are shown in Fig. 7, Fig. 8, and Fig. 9, respectively. It is noted that for the same exciting force, currents and electromagnetic forces in the system for two different initial conditions are the same after the system enters steady state. So this paper just takes the currents and the electromagnetic forces under one initial condition to show the current and electromagnetic force state of the system in Fig. 8 and Fig. 9. And the same drawing way is used below.

Figure 7 shows the dynamic response of the rotor for $\left| \tilde{F}_d \right| = 9.44$. It can be seen that as the exciting force is small, the responses of the rotor for two different initial conditions tend to be consistent and rotor vibrates periodically with the same constant amplitude at the zero equilibrium position. According to Fig. 8 and Fig. 9, the current saturation doesn't occur and electromagnetic force

generated by the current is sinusoidal as expected. In a word, as the exciting force is sufficiently small, the system can generate sufficient currents and electromagnetic force to keep rotor vibrating at zero equilibrium position. And the rotor's maximal instantaneous displacements are the rotor vibration amplitudes. It can be seen from Fig. 7 that rotor displacements are small during operation.
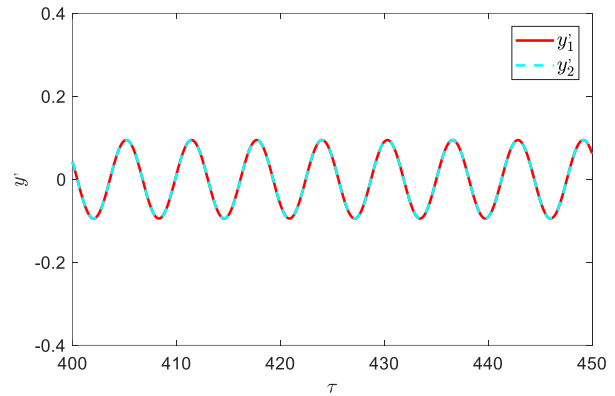
Fig. 7. The partial enlarged detail of system time series responses for $\left| \tilde{F}_d \right| = 9.44$.
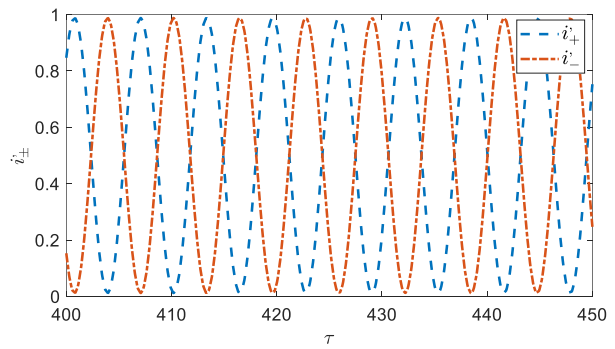
Fig. 8. The partial enlarged detail of currents for $\left| \tilde{F}_d \right| = 9.44$.
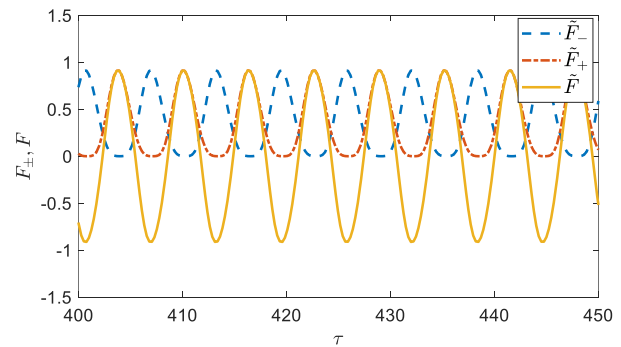
Fig. 9. The partial enlarged detail of electromagnetic force for $\left| \tilde{F}_d \right| = 9.44$.

However, as the exciting force becomes larger, the bifurcation appears. For $\left|\tilde{F}_d\right|=16.83$, the system time series response, currents in the system, and electromagnetic force are shown in Fig. 10, Fig. 11, and Fig. 12, respectively.
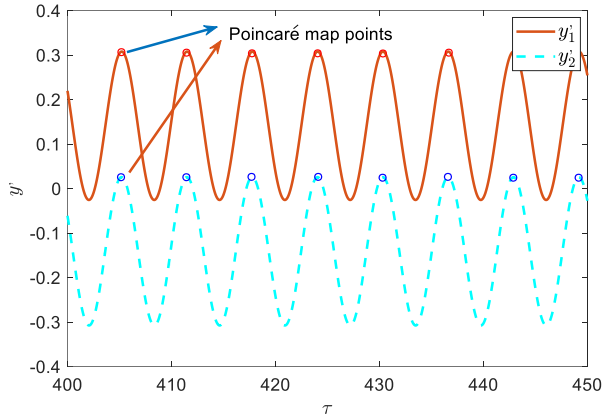

Fig. 10. The partial enlarged detail of system time series responses for $\left|\tilde{F}_d\right|=16.83$.
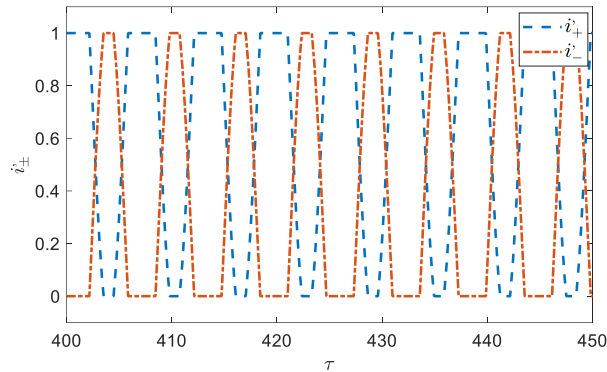
Fig. 11. The partial enlarged detail of current for $\left|\tilde{F}_d\right|=16.83$.
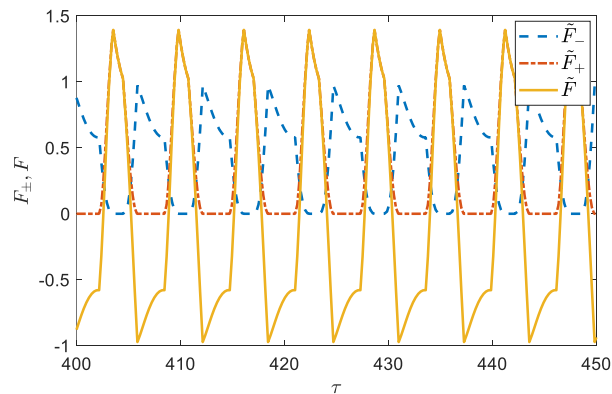

Fig. 12. The partial enlarged detail of electromagnetic force for $\left|\tilde{F}_d\right|=16.83$.

It can be seen from Fig. 10 that system time series responses for slightly different initial conditions are very different for $\left|\tilde{F}_d\right|=16.83$. The rotor may vibrate at different positions deviating from the zero equilibrium position and the new possible equilibrium positions are symmetrical about the original equilibrium position. Figure 11 shows conspicuous current saturation has occurred. And the electromagnetic force shown in Fig. 12 has distorted seriously. In case of current saturation, as the exciting force continues to magnify, the vibration amplitude of the rotor tends to increase, and the needed restoring force calculated by the controller is larger. That means the current in the magnetic bearings should have continued to magnify. However, the existence of the current saturation has limited the increase of the electromagnetic force. At zero equilibrium position, the electromagnetic force contributed by the currents and displacement of the rotor is not enough to suppress the vibration effectively. In order to keep the balanced state, another factor affecting the electromagnetic force, namely the displacement of the rotor, should be larger in the presence of current saturation. Hence, the rotor deviates from the zero equilibrium position to new equilibrium positions. It follows that the sensitivity of the nonlinear system to initial conditions leads to the pitchfork bifurcation.

In this case, the pitchfork bifurcation occurs. The rotor deviates from zero equilibrium position. The rotor's maximal instantaneous displacement is the sum of the absolute value of new equilibrium and vibration amplitude. As Fig. 6, Fig. 7 and Fig. 10 show, the rotor equilibrium position has a prominent effect on the rotor's maximal instantaneous displacement. So, in order to keep rotor-AMB system stable during operation, the equilibrium positions of the system are important as well as vibration amplitudes.

It can be concluded that: as exciting force is small, there is no current saturation in the rotor-AMB system and the zero equilibrium solution exists and is stable. The rotor displacement is only dependent on vibration amplitude. However, with the increase of exciting force, the current saturation occurs gradually and the electromagnetic force generated in the system is not large enough to keep rotor vibrating at zero equilibrium position. The zero equilibrium solution loses its stability and two new equilibrium solutions come up. And it is a typical supercritical pitchfork bifurcation. So, as exciting force is large, the rotor's maximal instantaneous displacement, which has a great effect on the system stability, is dependent on both equilibrium position and vibration amplitude of the rotor-AMB system.

C. Controller parameter modification

According to the analysis results in the previous subsection, the current saturation is the main causes of

pitchfork bifurcation. In this subsection, the controller parameter adjustment is conducted to avoid the current saturation and pitchfork bifurcation phenomenon during system operation.

　　Through the analysis results in subsection B, it is found that controller parameters can influence the severity of current saturation. The smaller proportional gain p' is, the more serious the current saturation. While the differential gain d' has the opposite effect that the larger differential gain is, the more serious current saturation becomes. As pitchfork bifurcation appears, the rotor's maximal instantaneous displacement becomes larger, which has an adverse effect on system stability. In order to keep the system stable, the bifurcation should be prevented by increasing proportional gain p' and decreasing differential gain d'. In the actual system, the modification of controller parameters is also limited by other factors.

　　In the next analysis, controller parameters are modified to be $p' = 4.461 \times 10^{-5}$, $d' = 4.117 \times 10^{-5}$ based on the operating condition of the actual system. The change of rotor displacements at Poincaré map points versus exciting magnitude for two different initial conditions is shown in Fig. 13. Compared with Fig. 6, the pitchfork bifurcation disappears after controller parameter modification. The rotor vibrates at the zero equilibrium position for all exciting forces and vibration amplitude tends to be larger with the increase of exciting force. Also take $\left| \tilde{F}_d \right| = 16.83$ as an example to show the current and electromagnetic force in this case, as shown in Fig. 14 and Fig. 15, respectively. It can be seen the current saturation doesn't appear and electromagnetic force doesn't distort. These dynamic behaviors of the system prove that modified controller parameters are very effective to avoid the pitchfork bifurcation, which is detrimental to the stability of the rotor-AMB system.
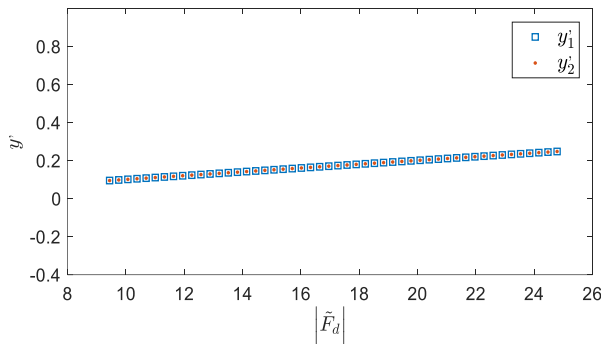
Fig. 13. The rotor displacements at Poincaré map points versus exciting magnitude after controller parameter modification.
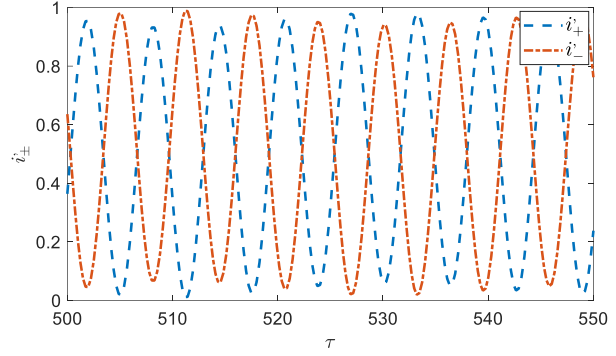
Fig. 14. The partial enlarged detail of current for $\left| \tilde{F}_d \right| = 16.83$ after controller parameter modification.
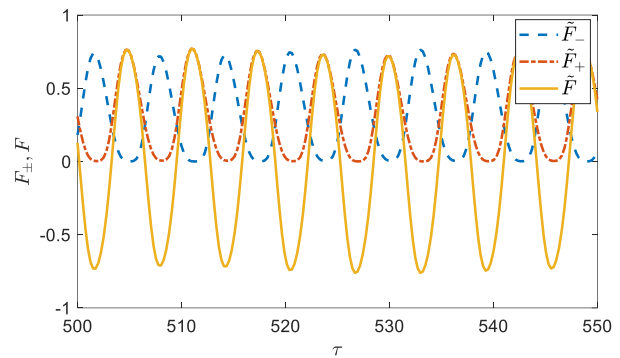
Fig. 15. The partial enlarged detail of electromagnetic force for $\left| \tilde{F}_d \right| = 16.83$ after controller parameter modification.

　　In summary, the large air gap between the rotor and stator provides the possibility of pitchfork bifurcation. And extreme operating conditions, such as heavy load and large disturbance, lead to the phenomenon. The find of pitchfork bifurcation shows that nonlinear dynamic analysis makes sense in full speed range of the rotor-AMB system. And nonlinear phenomena adverse to system performance can be prevented through proper controller adjustment.

IV. CONCLUSIONS AND PROSPECTS

　　In this paper, the rotor-AMB with a PD controller is investigated numerically and the nonlinearity of electromagnetic force and current saturation effect are taken into account in the analysis. The nonlinear dynamic behaviors of the rotor-AMB system in both resonance and non-resonance regions are analyzed in detail. And the effects of the exciting force and the current saturation on the dynamic behaviors of the rotor-AMB system

are illustrated and the specific controller parameter optimization is conducted based on analysis results. The results reveal that:

(1) There are a soft-spring characteristic and jump phenomenon in the resonance region. Compared with the linear system, the rotor vibration amplitude has a saltation when the rotor passes the resonant frequency.

(2) There is a supercritical pitchfork bifurcation in the non-resonance region. With the increase of exciting force, the zero equilibrium solution loses its stability and two new equilibrium solutions come up. In the case of pitchfork bifurcation, the equilibrium positions and vibration amplitude affects the rotor displacement which has a key effect on the system stability.

(3) The effects of exciting force and current saturation on the nonlinear dynamics are illustrated in detail and optimized controller parameters can suppress the occurrence of bifurcation effectively. So appropriate controller design can prevent complicated nonlinear phenomena and keep the system stable.

The future work of this paper is to apply some special numerical integration methods to investigate the nonlinear dynamic behaviors more precisely [22]. In fact, in this paper, the governing equation is solved by Runge-Kutta 5(4) algorithm. However, the precision of Runge-Kutta 5(4) method is not sufficient in some cases including solving the stiff equations. And in numerical integration, the conservation laws of the mechanical quantities may be infringed. Therefore, some different numerical integration methods should be utilized in nonlinear dynamic analysis of rotor-AMB system.

ACKNOWLEDGMENT

REFERENCES

[1] G. Schweitzer and E. H. Maslen, *Magnetic Bearings: Theory, Design, and Application to Rotating Machinery*. Springer, 2009.

[2] Z. Sun, J. Zhao, Z. Shi, and S. Yu, "Identification of Flexible Rotor Suspended by Magnetic Bearings," *Proceeding of 21st International Conference on Nuclear Engineering*, 2013.

[3] Z. Sun, Y. He, J. Zhao, Z. Shi, L. Zhao, and S. Yu, "Identification of active magnetic bearing system with a flexible rotor," *Mechanical Systems & Signal Processing*, vol. 49, no. 1-2, pp. 302-316, 2014.

[4] N. A. Saeed, M. Eissa, and W. A. El-Ganini, "Nonlinear oscillations of rotor active magnetic bearings system," *Nonlinear Dynamics*, vol. 74, no. 1-2, pp. 1-20, 2013.

[5] J. Ji and C. H. Hansen, "Non-linear oscillations of a rotor in active magnetic bearings," *Journal of Sound & Vibration*, vol. 240, no. 4, pp. 599-612, 2001.

[6] A. Hu, L. Hou, and L. Xiang, "Dynamic simulation and experimental study of an asymmetric double-disk rotor-bearing system with rub-impact and oil-film instability," *Nonlinear Dynamics*, vol. 84, no. 2, pp. 1-19, 2015.

[7] L. Xiang, X. Gao, and A. Hu, "Nonlinear dynamics of an asymmetric rotor-bearing system with coupling faults of crack and rub-impact under oil-film forces," *Nonlinear Dynamics*, vol. 86, no. 2, pp. 1-11,2016.

[8] T. Inoue, Y. Sugawara, and M. Sugiyama, "Modeling and nonlinear vibration analysis of a rigid rotor system supported by the magnetic bearing (effects of delays of both electric current and magnetic flux)," *Neuroimage*, vol. 13, no. 13, pp. 1203-1203, 2010.

[9] J. Ji, "Stability and Hopf bifurcation of a magnetic bearing system with time delays," *Journal of Sound & Vibration*, vol. 259, no. 4, pp. 845-856, 2013.

[10] K. Kang and A. Palazzolo, "Homopolar magnetic bearing saturation effects on rotating machinery vibration," *IEEE Transactions on Magnetics*, vol. 48, no. 6, pp. 1984-1994, 2012.

[11] W. Zhang and X. Zhan, "Periodic and chaotic motions of a rotor-active magnetic bearing with quadratic and cubic terms and time-varying stiffness," *Nonlinear Dynamics*, vol. 41, no. 4, pp. 331-359, 2005.

[12] M. J. Jang and C. K. Chen, "Bifurcation analysis in flexible rotor supported by active magnetic bearing," *International Journal of Bifurcation & Chaos*, vol. 11, no. 08, pp. 2163-2178, 2001.

[13] J. I. Inayat-Hussain, "Geometric coupling effects on the bifurcations of a flexible rotor response in active magnetic bearings," *Chaos Solitons & Fractals*, vol. 41, no. 5, pp. 2664-2671, 2009.

[14] J. I. Inayat-Hussain, "Nonlinear dynamics of a statically misaligned flexible rotor in active magnetic bearings," *Communications in Nonlinear Science & Numerical Simulation*, vol. 15, no. 3, pp. 764-777, 2010.

[15] W. Zhang, M. Yao, and X. Zhan, "Multi-pulse chaotic motions of a rotor-active magnetic bearing system with time-varying stiffness," *Chaos Solitons & Fractals*, vol. 27, no. 1, pp. 175-186, 2006.

[16] F. Sorge, "Stability analysis of rotor whirl under nonlinear internal friction by a general averaging approach," *Journal of Vibration & Control*, vol. 16, no. 4, pp. 301, 2015.

[17] F. Sorge, "Approach to rotor-shaft hysteretic whirl using Krylov-Bogoliubov techniques," *Journal of Vibration & Control*, vol. 21, no. 5, pp. 883-895, 2013.

[18] T. Inoue, Y. Ishida, and S. Murakami, "Theoretical

analysis and experiments of the nonlinear vibration in a vertical rigid rotor supported by the magnetic bearing system," *Journal of System Design & Dynamics*, vol. 1981, no. 1, pp. 295-306, 2007.

[19] M. Kamel and H. S. Bauomy, "Nonlinear study of a rotor–AMB system under simultaneous primary-internal resonance," *Applied Mathematical Modelling*, vol. 34, no. 10, pp. 2763-2777, 2010.

[20] Z. Sun, X. Zhang, T. Fan, X. Yan, J. Zhao, L. Zhao, and Z. Shi, "Nonlinear dynamic characteristics analysis of active magnetic bearing system based on cell mapping method with a case study," *Mechanical Systems & Signal Processing*, vol. 117, pp. 116-137, 2019.

[21] J. R. Dormand and P. J. Prince, "A family of embedded Runge-Kutta formulae," *Journal of Computational & Applied Mathematics*, vol. 6, no. 1, pp. 19-26, 1980.

[22] B. Leimkuhler and S. Reich, *Simulating Hamiltonian Dynamics*. Cambridge University Press, 2004.

Xiaoshen Zhang (1993.03), Ph.D. candidate of Institute of Nuclear and New Energy Technology, Tsinghua University, Beijing, China. His research interests are the nonlinear dynamics analysis and control of the rotor-AMB system.

Tianpeng Fan (1993.07-) received his Bachelor's degree in Engineering in 2016 from School of Energy Science and Engineering of Harbin Institute of Technology, Harbin. He is studying for a Master's degree in the Institute of Nuclear and New Energy Technology, Tsinghua University. His research interests are unbalance control of rotor and system identification.

Applied Adaptive Controller Design for Vibration Suppression in Electromagnetic Systems

Zhizhou Zhang

College of Aerospace Science
National University of Defense Technology, Changsha 410073, Hunan, People's Republic of China
zhangzhizhou@nudt.edu.cn

Abstract ─ In engineering tests, the vehicle-track coupled vibration is very easy to occur on the elastic support beams for a magnetic levitation (maglev) system. The fundamental waves, higher order harmonics, and other components related to the mode of track vibrations are often observed in the gap, acceleration and current sensors. This paper aims to design an adaptive filter to suppress these vibration components and improve the ride comfort for the passengers. Firstly, an adaptive self-turning filter is designed to filter out wideband signals and noise from the original signals, and enhance the strength of the fundamental wave and the harmonic components related to the mode of track vibration. Secondly, a narrow-band bandpass filter is presented to extract these enhanced periodical signals related to the track mode, and then the enhanced signals are configured as the reference inputs of the subsequent adaptive noise canceller. Thirdly, the adaptive noise canceller filters out periodical vibration components related to the track mode. Finally, the designed digital adaptive filter is applied to a real maglev system and suppresses coupled vibration on the elastic support beams effectively.

Index Terms ─ Adaptive notch filter, magnetic levitation system, noise canceller, self-turning filter, vibration control.

I. INTRODUCTION

Engineering tests show that when as a magnetic levitation (maglev) system is stationary suspension or slowly running on an elastic track, the system can easily induce a coupled vibration between the vehicle and track. These elastic tracks may be the cantilever beams and steel beams outside the garage, or switches in the maintenance platform. The vehicle-track coupled vibration may cause the instability of the maglev system, which directly affects normal operation of maglev train [1,2]. For example, strong vehicle-track coupled vibration occurs in Japan HSST04, German TR04, and US AMT trains [3]. In the process of commercialization of maglev trains, China has encountered similar vibration problem on the elastic beams [4].

In the past studies, in order to avoid the coupled vibration between vehicle and track, the main way is to increase the track stiffness or reduce the static suspension time to avoid the excitation of vibration [3]. Increasing track stiffness will add the system cost while reducing the static suspension time will not fundamentally solved the problem of vehicle-track coupled vibration.

Studies have shown that the vehicle-track coupled vibration is caused by elastic deformation of the track [3]. Thus, the vibration mechanism can be investigated from the perspective of dynamical behavior of maglev system. However, the effect of elastic deformation of the track are rarely taken into account in previous studies [4-6].They often regard the elastic deformation of the track as 0 to simplify the problem when studying the bifurcation behavior of the maglev system, which is closely related to the vehicle-track coupled vibration. Some researchers have established a five-order system by taking elastic deformation into account [7,8], and preliminarily investigated the Hopf bifurcation type of the complicated system as well as the corresponding periodical solution considering the time delay of the sensors [4-6].

To solve the engineering problem of vehicle-track coupled vibration in maglev systems, several researchers have attempted to suppress vehicle-track coupled vibrations from the perspective of signal processing technology. Zhang [9], Li [10], and Han [11] have designed the band-stop filters or differentiators respectively to suppress the coupled vibration of maglev systems to a certain degree. Zhang [12] designed an FPGA-based gap differentiator with full and rapid convergence, which can suppress vehicle- track coupled vibration on the fixed elastic track but shows poor adaptability to different elastic tracks.

Test results show that when the vehicle-track coupled vibration occurs on beams with different stiffness, the periodical signals with different frequencies appear in the sensor signals. The basic frequencies of this periodical signal are inconsistent and generally distributed in the range of 45 to 60 Hz. The second and third harmonica components are generally distributed in the range of 90 to 120 Hz and 135 to 180 Hz, respectively. An intuitive

hypothesis is that if the periodical signal related to the vibration frequency in the sensor is largely weakened, the vehicle-track coupled vibration may be suppressed significantly.

Because the vibration frequency of periodical signals related to the track mode changes depending on different elastic tracks, those notch filters with fixed central frequency cannot suppress these vibrations with variable frequencies. This paper aims to design an adaptive filter to suppress these vibration components and improve ride comfort for the passengers. An adaptive self-turning filter is designed to enhance the strength of the fundamental wave and the harmonic components related to the mode of track vibration. And a narrow-band bandpass filter is presented to extract these enhanced periodic signals above and then the enhanced signals are configured as the reference inputs of the subsequent adaptive noise canceller. Then the adaptive noise canceller filters out periodic vibration signals related to the track mode. Finally, the simulation and experiment results show that the designed digital adaptive filter can suppresses basic frequency, second harmonic, third harmonic, and other vibration components on the elastic support beams effectively.

II. SYSTEM MODEL AND ADAPTIVE FFILTER ARCHITECTURE

The maglev system with an electromagnet considering the elastic deformation of the track is shown in Fig. 1. Here, where z_m and z_G denote the vertical (direction of OZ) displacements of the electromagnet and the track, respectively, and z is the suspension gap. F and mg denote separately the electromagnetic force and the weight of the electromagnet. u, R and i are the voltage, resistor and current of the electromagnet winding.

Considering the first-order vibration mode of the track, the model of maglev system with flexible track can be presented as following [8]:

$$\begin{cases} z = z_m - z_G \\ (m+M)g - C_1\dfrac{i^2}{z^2} = m\ddot{z}_m \\ u = Ri + 2\dfrac{C_1}{z}\dot{i} - \dfrac{2C_1 i}{z^2}\dot{z} \\ \ddot{z}_G + 2\eta_1\omega_1\dot{z}_G + \omega_1^2 z_G = C_2\dfrac{i^2}{z^2} \end{cases} \tag{1}$$

where M is the mass of carriage, η_1 and ω_1 are the

damping ratio and natural frequency of fist-order mode respectively, $C1$, $C2$ are the system parameters.
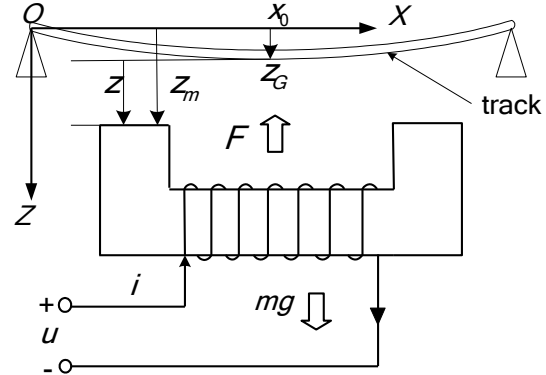
Fig. 1. The maglev system with flexible track.

In order to make the electromagnet suspend at the certain air gap z_e, a state feedback control algorithm can be adopted as follows [8]:

$$u = u_e + k_g z + k_v\dot{z} + k_i i , \tag{2}$$

where k_g, k_v, k_i are the control parameters of suspension gap, velocity and current, respectively. v_e is the initial voltage of the electromagnet.

From (8), we can find that the deformation of the elastic track in the control law can't be ignored. As mentioned above, the vibration components related to the track mode can be supressed by some filter technology.

In this section, an architecture of an adaptive filter for suppressing the vehicle-track coupled vibration with multiple vibration frequencies is presented in Fig. 2. It contains an adaptive self-tuning filter, a narrow-band bandpass filter, and an adaptive noise canceller.

In Fig. 2, the adaptive self-tuning filter is to filter out the wideband signals and noises from the original signal and enhance the strength of the basic wave and various components related to the track vibration mode. The narrow-band bandpass filter is to extract periodical signals related to the track mode for use as reference signals of the adaptive noise filter. Finally, the adaptive noise canceller is to filter out the periodical vibration signals related to the track mode.

The following sections discuss the working principles of the adaptive self-tuning filter and adaptive noise canceller.
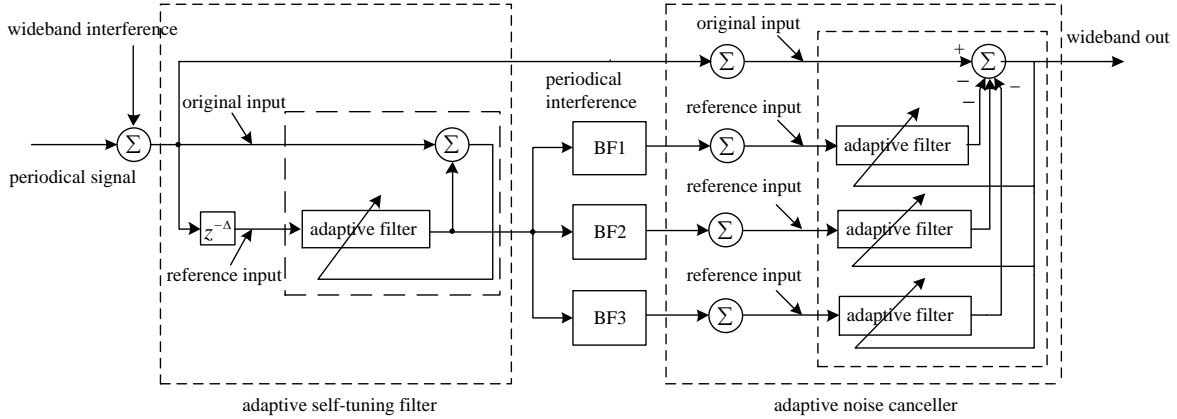
Fig. 2. Architecture of the adaptive filter with multiple central frequencies.

III. DESIGN OF THE ADAPTIVE SELF-TUNING FILTER WITHOUT REFERENCE INPUT

In an actual maglev system, the frequency of time-varying periodical interference in a single gap is variable and unknown. Thus, no related outside reference input signal can be used. In this section, an adaptive self-tuning filter without outside reference input is presented. This filter can extract periodical gap fluctuation signal, including the baseband signal, second harmonic, and third harmonic related to the track vibration mode. Therefore, this filter can be considered a spectral linear enhancer. The structure of the adaptive self-tuning filter is shown in Fig. 3.
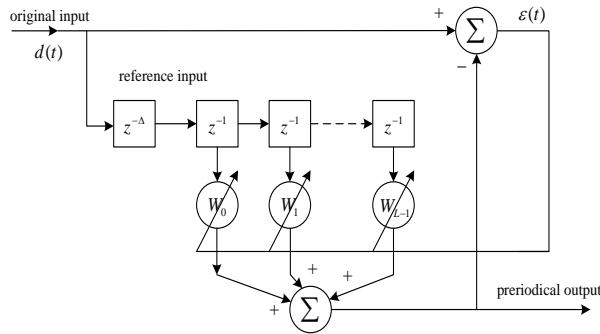

Fig. 3. The adaptive self-tuning filter with original sensor output.

We denote the original sensor signal of the maglev system as following [13]:

$$d(t) = s(t) + n(t) = \sum_{i=1}^{M} A_i e^{j(\omega_i t + \theta_i)} + n(t), \qquad (3)$$

where $s(t)$ is the periodical component, $n(t)$ is the wideband component with stable Gauss white noise. A_i, ω_i, θ_i refer to the amplitude, frequency, and starting

phase of the i_{th} sinusoidal signal, respectively.

We select a proper Δ, such that,

$$E\{n(t)n(t-\Delta)\} = 0. \qquad (4)$$

From (4), the broadband signal component $n(t)$ and $n(t-\Delta)$ are decorrelated. However, the components of vibration interference $s(t)$ and $s(t-\Delta)$ are still related to each other because of their periodicity.

If the mean power of noise $n(t)$ is given as $M\delta_0^2$, the mean power of the i_{th} sinusoidal signal is $\delta_i^2 = A_i^2 / 2$, and its input signal-to-noise ratio is:

$$SNR_i = \frac{\delta_i^2}{\delta_0^2}. \qquad (5)$$

Here X represents the vector composed of the signals of all taps in the delay line, and a weight vector represents the adaptive filter with length L. Thus,

$$X^T = [x_0 \quad x_1 \quad ... \quad x_{L-1}]^T, W^T = [w_0 \quad w_1 \quad ... \quad w_{L-1}]^T. \qquad (6)$$

The output of adaptive tuning filter is given by:

$$y(t) = W^T X = X^T W. \qquad (7)$$

The system error signal is expressed as:

$$\varepsilon(t) = d(t) - y(t) = d(t) - W^T X. \qquad (8)$$

A common criterion for filter design is minimization of the mean-square error between filter output and expected response, that is,

$$E\{| \varepsilon(t) |^2\} \to \min. \qquad (9)$$

Substituting Eq. (8) into (9), $\overline{d}(t)$ is used to represent the conjugant of $d(t)$, such that we obtain:

$$E\{| \varepsilon(t) |^2\} = E\{[d(t) - W^T X]^2\}$$
$$= E\{d(t)\overline{d}(t) - d(t)\overline{W}^T \overline{X} - \overline{d}(t)W^T X \qquad (10)$$
$$+ W^T X \overline{X}^T \overline{W}\}$$

If $P = E\{d(t)\overline{X}\}$, the autocorrelative matrix of filter tap input X is:

$$R_{X\overline{X}} = E\{X\overline{X}^{T}\} = E\{XX^{H}\}, \qquad (11)$$

where $X^{H} = \overline{X}^{T}$ refers to the conjugate transpose matrix of X. $R_{X\overline{X}}$ is generally a symmetric matrix that is definitely positive.

Eq. (8) can be rewritten as:

$$E\{|\varepsilon(t)|^{2}\} = E\{d(t)\overline{d}(t) - 2\operatorname{Re}(W^{H}P) + W^{T}R_{XX}\overline{W}\}. \quad (12)$$

In the above equation, $\operatorname{Re}(W^{H}P)$ refers to the real part of $W^{H}P$.

Based on the LMS (Least mean square) criterion, the optimal weight vector (Wiener solution) of this filter is:

$$W^{*} = R_{X\overline{X}}^{-1}P. \qquad (13)$$

The above equation shows that if this filter aims to adaptively track input signals, the matrix R_{XX}^{-1} must be calculated in real-time. To avoid the inconvenience of matrix inversion in real-time signals, we can update the weight vector by using the steepest descent LMS algorithm [13,14].

The expected value of the weight vector can be obtained in the main coordinates if and only if:

$$0 < \mu < \lambda_{\max}^{-1}, \qquad (14)$$

where μ is the converging factor refers to a gain constant for controlling adaptive speed and stability, $\lambda_{\max}$ refers to the maximal eigenvalue of input-related matrix $R_{X\overline{X}}$. The parameter $\lambda_{\max}$ is not higher than the trace of the input-related matrix $R_{X\overline{X}}$ (the sum of the diagonal elements), and the convergence of the weight vector can be ensured by the following equation:

$$0 < \mu < (trR)^{-1}. \qquad (15)$$

In the equation above, the diagonal elements of the input-related matrix $R_{X\overline{X}}$ (i.e., the input power) are easier to estimate than the eigenvalue of $R_{X\overline{X}}$ and can easily be used in practice.

In the following section, we deduce the transfer function of the self-tuning filter. This function can be obtained on the basis of the steady impulse response of the filter through discrete Fourier transform.

The steady impulse response function of filter is given by:

$$W_{k}^{i} = \sum_{i=1}^{N} A_{i}e^{j\omega_{n}k}, \quad k=0,1,2,...,L-1. \qquad (16)$$

Thus,

$$
\begin{aligned}
H(\omega) &= \sum_{k=0}^{L-1} W_{k}^{i}e^{-j\omega(\Delta+k)} \\
&= \sum_{k=0}^{L-1}\sum_{i=1}^{M} A_{i}e^{j\omega_{i}} e^{-j\omega(\Delta+k)} \\
&= \sum_{i=1}^{M} A_{i}e^{-j\omega\Delta}\sum_{k=0}^{L-1} e^{j(\omega_{i}-\omega)k} \\
&= \sum_{i=1}^{M} A_{i}e^{-j\omega\Delta}\frac{1-e^{j(\omega_{i}-\omega)L}}{1-e^{j(\omega_{i}-\omega)}}
\end{aligned}
\qquad (17)
$$

If L is very high, no relation exists among M sine waves. Thus,

$$A_{i} = \frac{e^{j\omega_{i}\Delta}}{L + \delta_{0}^{2}/\delta_{i}^{2}}. \qquad (18)$$

The transfer function of the filter is:

$$H(\omega) = \sum_{i=1}^{M}\frac{e^{j(\omega_{i}-\omega)\Delta}}{L+\dfrac{\delta_{0}^{2}}{\delta_{i}^{2}}}\frac{1-e^{j(\omega_{i}-\omega)L}}{1-e^{j(\omega_{i}-\omega)}}. \qquad (19)$$

Equation (19) shows that this self-tuning filter is equivalent to the sum of M bandpass filters with central frequency ω_{i}.

The above equation shows that the amplitude/frequency response of the i_{th} filter is:

$$H_{i}(\omega) = \frac{1}{L+\delta_{0}^{2}/\delta_{i}^{2}}\left|\frac{1-e^{j(\omega_{i}-\omega)L}}{1-e^{j(\omega_{i}-\omega)}}\right|. \qquad (20)$$

If $\omega \to \omega_{i}$, $\dfrac{1-e^{j(\omega_{i}-\omega)L}}{1-e^{j(\omega_{i}-\omega)}}$ in the above equation refers to $\dfrac{0}{0}$ type, and $\dfrac{(1-e^{j(\omega_{i}-\omega)L})'}{(1-e^{j(\omega_{i}-\omega)})'} = L$. Thus, the maximum amplitude-frequency response of the i_{th} filter is:

$$H_{i}(\omega)_{\max} = \frac{L}{L+\delta_{0}^{2}/\delta_{i}^{2}} = \frac{L(SNR)_{i}}{1+L(SNR)_{i}}. \qquad (21)$$

To verify the performance of the self-tuning filter, the input signal is given as $x(t) = s(t) + n(t)$, with the periodical signal being $s(t) = \sin(2\pi \cdot 50 \cdot t) + 0.7\sin(2\pi \cdot 100 \cdot t) + 0.4\sin(2\pi \cdot 150 \cdot t) + 1$. The wideband signal of random noise is $n(t) = 0.56 randn(1, N)$. The sampling frequency is 2000 Hz. The order of the self-tuning filter is 96, the sample data comprise 10000 points, and $\mu = 0.002$. When the delay time is set to $\Delta = 256$, the spectrograms of the input and output signal can be obtained as shown in Fig. 4.
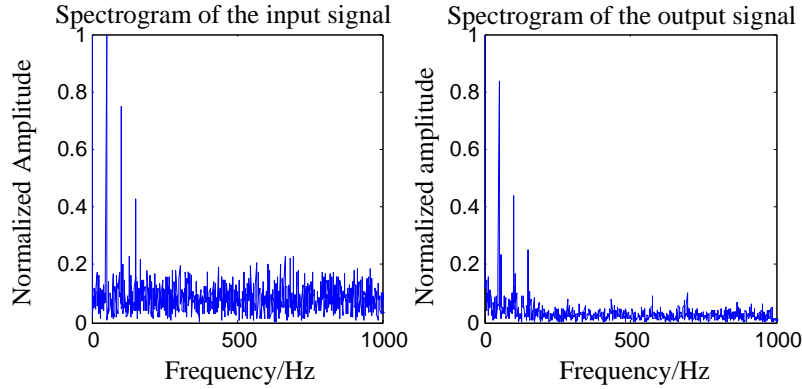
Fig. 4. Spectrogram of input and output signal of self-tuning filter with a delay time 256.

Figure 4 shows that when the delay time is 256, the spectral lines of the output at 50 Hz, 100 Hz, and 150 Hz are enhanced and the wideband signals with noise is weakened. Then we can adopt the self-tuning filter to filter out the wideband signals and noises from the original signal, and enhance the strength of the vibration components related to the track mode for the maglev system.

IV. DESIGN OF THE ADAPTIVE NOISE CANCELLER WITH MULTIPLE REFERENCE INPUTS

We suppose that the original input signal of the maglev system is arbitrary, that is, it can be random, determinate, continuous, or transient. When a vehicle-track coupled vibration occurs, it may even be a combination of the basic wave and various components related to the track vibration mode.

The architecture of the adaptive noise canceller with multiple frequecies is presented in Fig. 5. The rationality of the algorithm is discussed below.

The reference input signal with any single frequency can be denoted as:

$$x_i(t) = A_i \cos(2\pi f_i t + \varphi_i), i = 1, 2, 3. \tag{22}$$

In Fig. 5, for the first reference input signal with the single frequency, the input of the first weight can be directly obtained from reference input, and the input of the second weight is obtained after a 90-degree phase shift of the first weight input, that is,

$$x_{i1k} = A_i \cos(k\omega_i t + \varphi_i), x_{i2k} = A_i \sin(k\omega_i t + \varphi_i), \tag{23}$$

where T refers to the sampling period and $\omega_i = 2\pi f_i T$.

Weight is iterated by using the LMS algorithm [13,15]. The flowchart of the adaptive noise canceller is presented in Fig. 6.

For simplicity, the feedback loop from G to B is disconnected in Fig. 6 during analysis of the open-loop transmission characteristics of the adaptive noise canceller, that is, the isolated impulse response from error C to G. We suppose that a discrete unit impulse function is inputted in C at $k = m$, such that,

$$\varepsilon_{ik} = \delta(k - m). \tag{24}$$

To reach D in the upper branch passing through a multiplier, the multiplier at I is a signal composed of multiple sinusoidal functions such that the system is determined to be a time-varying system. The output response is:

$$h_{i1} = \begin{cases} A_i \cos(m\omega_i t + \varphi_i), & k = m \\ 0, & k \neq m \end{cases}. \tag{25}$$

A digital integrator exists from D to E with the transfer function $2\mu / (z - 1)$. The impulse response is:

$$h_{i2} = 2\mu u(k - 1), \tag{26}$$

where $u(k)$ refers to the discrete unit step function. The parameters h_{i1}, h_{i2} are used for the convolution operation, and the output response at E is:

$$\omega_{i1k} = h_{i1} \otimes h_{i2} = 2\mu A_i \cos(m\omega_i + \varphi_i). \tag{27}$$

In the above equation, $k \geq m + 1$. This function is multiplied by the multiplication factor x_{i1k} at H such that the output response at F is:

$$y_{i1k} = 2\mu u(k - m - 1)A_i \cos(m\omega_1 + \varphi_1) \cdot A_i \cos(k\omega_1 + \varphi_1). \tag{28}$$

Similarly, the output response at J is:

$$y_{i2k} = 2\mu u(k - m - 1)A_i \sin(m\omega_i + \varphi_i) \cdot A_i \sin(k\omega_i + \varphi_i). \tag{29}$$

By combining the two equations above, the response at the output end G of the filter can be obtained as:

$$y_{ik} = y_{i1k} + y_{i2k} = 2\mu u(k - m - 1)A_i^2 \cos[(m - k)\omega_i]. \tag{30}$$
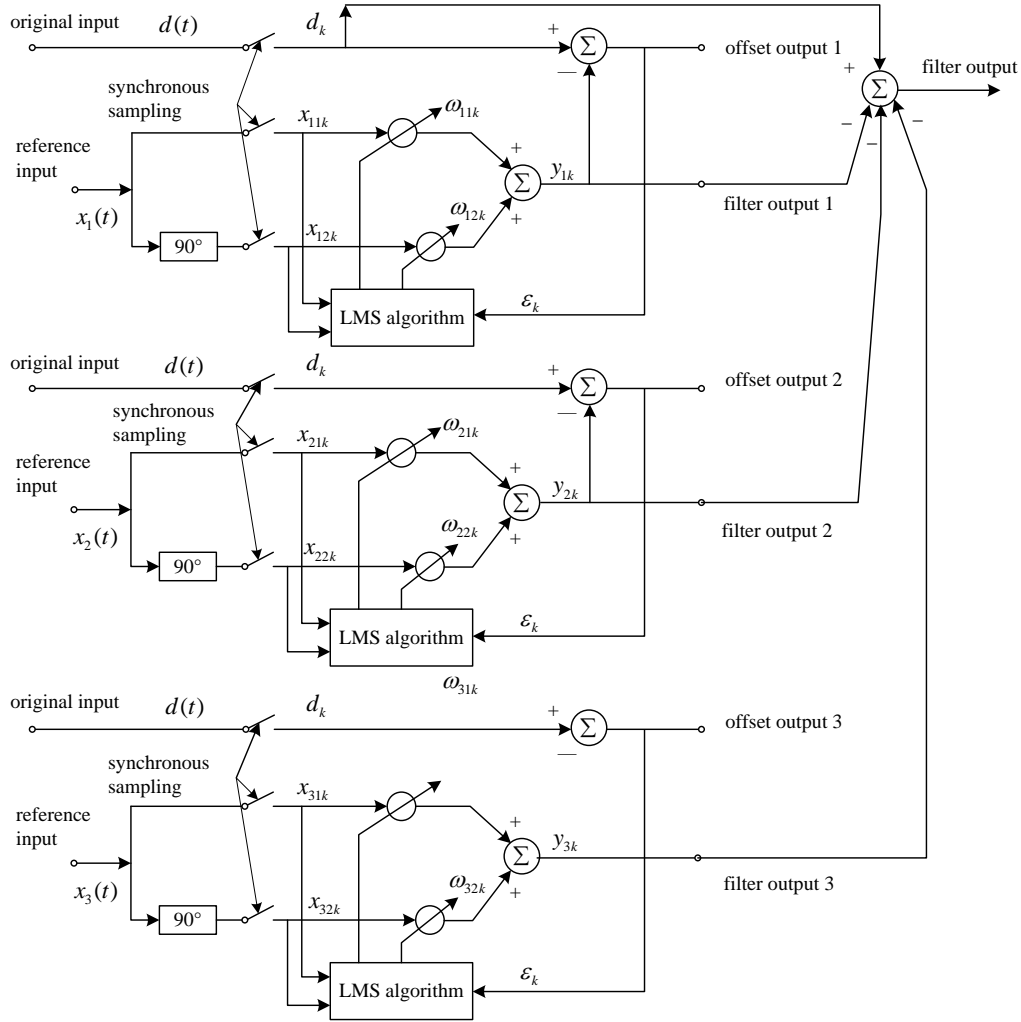
Fig. 5. Adaptive noise canceller with multiple reference frequency.
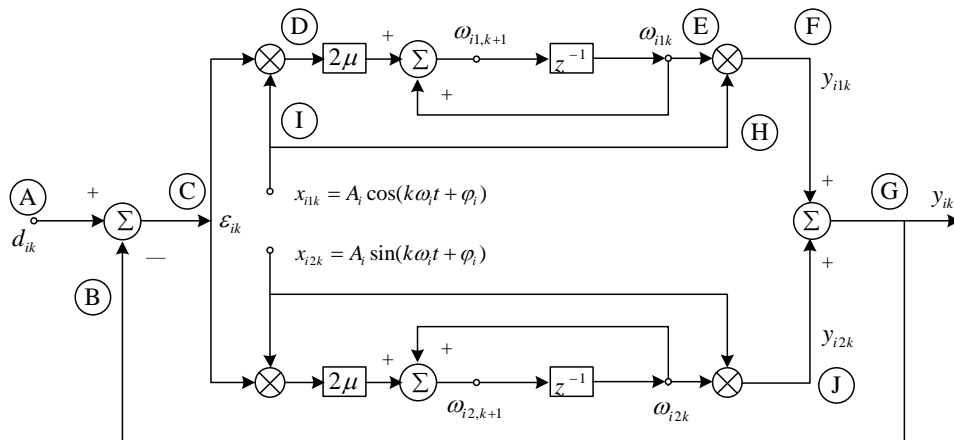
Fig. 6. Signal transmission flowchart of LMS algorithm.

The equation above is a function related to $k-m$. If the impulse moment m is taken as 0, the open-loop impulse response from C to G can be obtained as:

$$y_{ik} = y_{i1k} + y_{i2k} = 2\mu u(k-1)A_i^2 \cos(k\omega_i). \tag{31}$$

The transfer function from C to G in this channel is the z conversion of the above equation, that is,

$$G(z) = 2\mu A_i^2 \frac{z\cos\omega_i - 1}{z^2 - 2z\cos\omega_i + 1}. \qquad (32)$$

In fact, the above-mentioned open-loop system is an unsteady system. Now, we connect the feedback loop from G to B to be closed. Thus, we can obtain a closed-loop transfer function from original input A to noise cancel output C:

$$H(z) = \frac{1}{1+G(z)} = \frac{z^2 - 2z\cos\omega_i + 1}{z^2 - 2(1-\mu A_i^2)z\cos\omega_i + 1 - 2\mu A_i^2}. \qquad (33)$$

The above equation is a canceller with a single frequency. A zero point is found at the reference frequency f_i and accurately located at $z = e^{\pm j\omega_i}$ inside the unit circle in the Z plane. The poles are located at:

$$z_{ip} = (1-\mu A_i^2)\cos\omega_i \pm j[(1-2\mu A_i^2) - (1-\mu A_i^2)^2\cos^2\omega_i]^{0.5}. \qquad (34)$$

Two conjugate poles may be easily found inside the unit circle. Thus, the above closed-loop system is stable. Based on the above equation, the module of this pole is $(1-2\mu A_i^2)^{0.5}$, and its angle is:

$$z_{ip} = (1-2\mu A_i^2)^{\pm j0.5\arccos[(1-\mu A_i^2)(1-2\mu A_i^2)^{-0.5}\cos\omega_0]}$$
$$= (1-\mu A_i^2)^{\pm j\arccos[(1-\mu A_i^2)(1-2\mu A_i^2)^{-0.5}\cos\omega_0]}. \qquad (35)$$

For a slow adaptive process, μA_i^2 in the above equation is very small, and the factor in the exponential term can be arranged as:

$$\frac{1-\mu A_i^2}{(1-2\mu A_i^2)^{0.5}} = [\frac{1-2\mu A_i^2 + \mu^2 A_i^4}{1-2\mu A_i^2}]^{0.5}$$
$$= [1+\mu^2 A_i^4 + \cdots]^{0.5} = 1 + \frac{\mu^2 A_i^4}{2} + \cdots. \qquad (36)$$

The equation above suggests that the pole can be approximately represented as:

$$z_{ip} = (1-\mu A_i^2)^{\pm j\omega_0}. \qquad (37)$$

Therefore, the angle of the pole is almost equal to that of the zero point under actual circumstances. The pole points and zero points of the transfer function are shown in Fig. 7 (a). The zero points are on the unit circle, so the transfer function is infinitely deep at $\omega = \omega_0$. The sharpness of the notch is determined by the distance μA_i^2 from pole to zero. The distance between half-power points along the unit circle is defined as the arc length, that is, the bandwidth of the notch filter. We find that [14,15]:

$$BW = 2\mu A_i^2 \ rad/s = \frac{\mu A_i^2}{\pi T} \ Hz. \qquad (38)$$

Notch sharpness is represented by a quality factor, which is defined as the ratio of central frequency to band width, that is,

$$Q = \frac{\omega_0}{2\mu A_i^2}. \qquad (39)$$

Thus, when the reference input contains multiple sine wave signals, the adaptive noise cancelling process is equal to a filter with many central notch frequencies, as shown in Fig. 7 (b).


Fig. 7. The characteristics of the adaptive noise canceller with many reference frequencies.

Figure 7 clearly shows that when the reference frequency is slowly changed, the adaptive notch process can be adjusted to the phase relation required by cancellation.

Here, the zero point of the transfer function of the whole filter is on the unit circle. However, the distribution of poles is not completely regular. If the sum of various harmonic signals that serve as output from the adaptive filter is regarded as the reference signal, the subsequent adaptive process is not necessarily convergent. For example, the sum of three sine wave signals is used as the reference input and the Matlab software is adopted for numerical analysis. We find out that improperly set parameters can easily cause the adaptive noise canceller to become unstable. Analysis shows that the adaptive noise canceller is actually an IIR filter and the pole

is close to the unit circle, so improper coefficient quantization is easily to cause the filter to be unstable. Also, the high-order IIR filtering process is often unstable, so we should properly set the gain of each link to prevent the filter from experiencing divergence in the cascade form of two-order IIR filters [16,17].

To verify the performance of the adaptive filter, we set the input signal as $x(t) = s_1(t) + s_2(t) + s_3(t) + n(t)$, adopt a signal-to-noise ratio of 10 dB, and assign the three periodical reference signals as $s_1(t) = \sin(2\pi \cdot 50 \cdot t)$, $s_2(t) = 0.7\sin(2\pi \cdot 100 \cdot t)$, $s_3(t) = 0.4\sin(2\pi \cdot 150 \cdot t)$. Here, the wideband signal with random noise is $n(t) = 0.56 randn(1, N) + 1$. The order of the three adaptive noise cancellers is 2. The amplitude-phase characteristic curves of the adaptive noise canceller are shown in Fig. 8. When the frequencies of three sine wave reference signals are known, the amplitude-frequency curves for the adaptive noise canceller described above are similar to the filter with three notches.
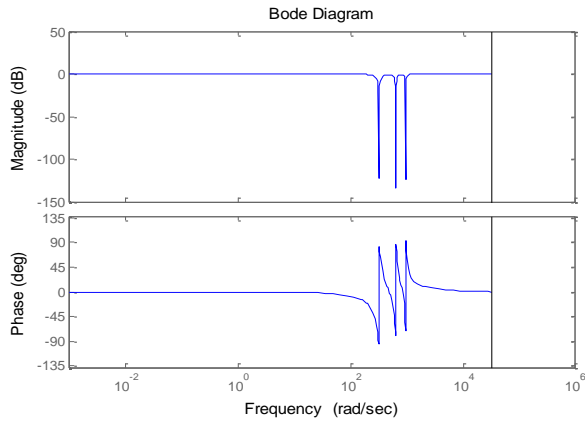

Fig. 8. Amplitude-frequency characteristic curves of the adaptive noise canceller.

V. EXPERIMENTAL VERIFICATION

Engineering tests show that when the vehicle is suspended statically on the steel girders, cantilever beams, turnouts or running at a speed lower than 5 km/h, the vehicle-track coupled vibration is prone to occur. There are 60 suspension control systems in a low-speed maglev train, and each control system needs to collect three displacement signals, one acceleration signal and one current signal in real-time. Because of the massive real-time sensor data from the whole train system, we use a high-speed CAN bus equipment to collect these sensor data from all 60 controllers. Here, each controller sends its own sensor data including displacement, acceleration and current to the CAN bus, and the train operation control equipment store the real-time data of the sensors on-line. The sampling frequency of these data is 2500 Hz and it is convenient for on-line fault diagnosis or off-line

data analysis for the maglev train.

Figure 9 is the curve of the sensors of a vehicle-track coupled vibration for 5 seconds, including the vehicle's suspending process and low-speed operation process.
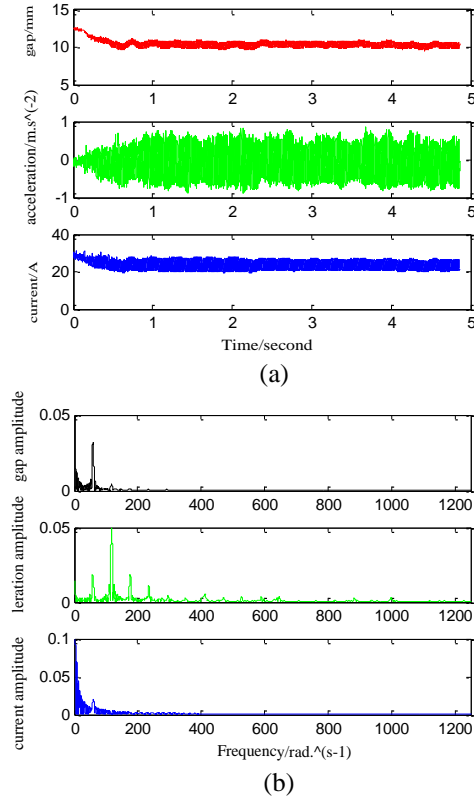

Fig. 9. Sensor output curves and spectrum of a vehicle-track coupled vibration.

From Fig. 9 (a), when a vehicle-track coupled vibration occurs, the gap fluctuation is more than 0.5 mm, the acceleration fluctuation is higher than 0. $6m/s^2$, and the current fluctuation is higher than 7.7A. In Fig. 9 (b), it contains obvious periodical signals such as fundamental frequency 58Hz, second harmonic 117Hz and third harmonic 174Hz.

When the vehicle is suspended on the same elastic track, we introduce the adaptive filter to the control system, and acquire the curves of the signals of gap, acceleration, and current sensors as shown in Fig. 10.

Figure 10 (a) shows that when the adaptive filter with multiple central frequencies is applied to the system, the vehicle-track coupled vibration no longer occurs while the vehicle is levitated statically in the garage. The gap fluctuation is no higher than 0.3 mm, the acceleration fluctuation is no higher than 0.06m/s², and the current fluctuation is no higher than 0.7A. In Fig. 10 (b), there are no obvious periodical signal is observed from the gap, acceleration, or current signals. Starting

from 35 s, the vehicle enters the landing process and lands on the track at 37 s. The current of the magnet drops to 0 A at 38 s. It shows that coupled vibration has been suppressed effectively.

In the same way, while the vehicle is levitated statically or runs at a low-speed on other elastic beams, there is no obvious periodical signal related to the track mode. It indicates that that the adaptive filter without frequency measurement can effectively suppress the vehicle-track coupled vibration for different elastic tracks to a certain extent.


(a)

(b)
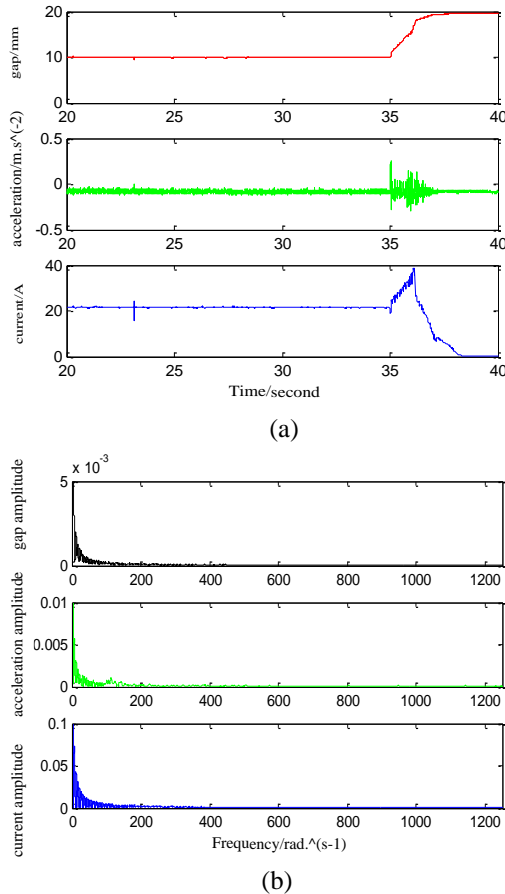
Fig. 10. Sensor output curves and spectrum of the adaptive filter with multiple central frequencies.

VI. CONCLUSION

This study aims to solve the vehicle-track coupled vibration problem that occurs during levitation or low-speed running of the maglev system from the perspective of signal processing. The fundamental waves, higher order harmonics, and other components related to the mode of track vibrations are often found in the gap, acceleration, and current sensors. An adaptive filter is designed to suppress these vibration components and improve the ride comfort for the passengers.

The adaptive filter with multiple central frequencies

doesn't need outside reference input signals. This filter effectively filters out the wideband signals and noises from the original signal and enhances the strength of the basic wave and various components related to the track vibration mode.

The narrow-band bandpass filter extracts the periodical signals related to the track mode for use as reference signals of the adaptive noise filter. And the adaptive noise canceller filters out the periodical vibration signals related to the track mode. It should be noted that the self-tuning process must be convergent.

Experimental results show that the designed digital filter effectively suppresses vehicle-track coupled vibration on different elastic beams. In the next step, we will further improve the stability proof of the algorithm.

REFERENCES

[1] H. W. Lee, K. C. Kim, and J. Lee, "Review of maglev train technologies," *IEEE Trans. on Magnetics*, vol. 42, pp. 1917-1925, 2006.

[2] M. Nagai, "The control of magnetic suspension to suppress the selfexcited vibration of a flexible track," *Jpn. Soc. Mech. Eng.*, vol. 30, no. 260, pp. 365-366, 1987.

[3] L. H. She, Z. Z. Zhang, D. S. Zou, et al., "Multi-state feedback control strategy for maglev elastic vehicle-guideway-coupled system," *Advanced Science Letters*, vol. 5, no. 2, pp. 587-592, 2012.

[4] H. P. Wang, J. Li, and K. Zhang, "Stability and Hopf bifurcation of the maglev system with delayed speed feedback control," *Acta Automatica Sinica*, vol. 33, no. 8, pp. 829-834, 2007.

[5] L. L. Zhang, L. H. Huang, and Z. Z. Zhang, "Stability and Hopf bifurcation of the maglev system with delayed position and speed feedback control," *Nonlinear Dyn.*, vol. 57, no. 1-2, pp. 197-207, 2009.

[6] L. L. Zhang, L. H. Huang, and Z. Z. Zhang, "Hopf bifurcation of the maglev time-delay feedback system via pseudo-oscillator analysis," *Mathematical and Computer Modelling*, vol. 52, no. 5-6, pp. 667-673, 2010.

[7] D. S. Zou, L. H. She, Z. Z. Zhang, and W. S. Chang, "Maglev system controller design based on the feedback linearization methods," *2008 IEEE International Conference on Information and Automation,*

Zhangjiajie, China, 2008.

[8] Z. Z. Zhang and L. L. Zhang, "Hopf bifurcation of time-delayed feedback control for maglev system with flexible track," *Applied Mathematics and Computation*, vol. 219, no. 11, pp. 6106-6112, 2013.

[9] D. Zhang, Y. G. Li, H. K. Liu, et al., "Restrain the effects of vehicletrack dynamic interaction: bandstop filter method," *Maglev2008 Proceedings*, 2008.

[10] H. Li and R. M. Goodall, "Linear and non-linear skyhook damping control laws for active railway suspensions," *Control Eng. Pract.*, vol. 7, no. 7, pp. 843-850, 1999.

[11] Q. J. Han, "From PID to active disturbance rejection control," *IEEE Trans. Ind. Electron.*, vol. 56, no. 3, pp. 900-906, 2009.

[12] L. L. Zhang, Z. Z. Zhang, and L. H. Huang, "Hybrid nonlinear differentiator design for permanent-electromagnetic suspension maglev system," *Signal Processing*, vol. 6, no. 6, pp. 559-567, 2012.

[13] S. Haykin, *Adaptive Filter Theory*. 5th Edition, Pearson Education Inc., 2013.

[14] Z. W. Liu, R. S. Chen, and J. Q. Chen, "Using adaptive cross approximation for efficient calculation of monostatic scattering with multiple incident angles," *The Applied Computational Electromagnetics Society*, vol. 26, pp. 325-333, Apr. 2011.

[15] S. Xue, Z. Q. Long, N. He, and W. S. Chang, "A high precision position sensor design and its signal processing algorithm for a maglev train," *Sensors*, vol. 12, pp. 5225-5245, 2012.

[16] L. L. Zhang and J. H. Huang, "Stability analysis for a flywheel supported on magnetic bearings with delayed feedback control," *The Applied Computational Electromagnetics Society*, vol. 32, no. 8, pp. 642-649, 2017.

[17] L. Y. Xiang, S. G. Zuo, and L. C. He, "Electric vehicles to reduce vibration caused by the radial force," *The Applied Computational Electromagnetics Society*, vol. 29, pp. 340-350, Sep. 2014.

Zhizhou Zhang received the B.S. degree in Automation from Northeastern University, China, in 2004. He received the M.S. and Ph.D. degrees in Control Science and Engineering from National University of Defense Technology, China, in 2006 and 2011. Since 2011, he works at the College of Aerospace Science, National University of Defense Technology. His research interest is maglev control.

Experimental Verification of Nonlinear Position-Flux Zero-Bias Control for Heteropolar Active Magnetic Bearing

Arkadiusz Mystkowski* and Andrzej Kierdelewicz

Bialystok University of Technology, Department of Automatic Control and Robotics, Bialystok, Poland
a.mystkowski@pb.edu.pl, a.kierdelewicz@doktoranci.pb.edu.pl

Abstract ─ This study presents experimental verification of a nonlinear position-flux control for active magnetic bearing (AMB) system operated with zero-bias flux. Recently developed controllers for nonlinear flux-controlled AMB applications are complicated and inherently difficult to implement. Therefore, three designs of low-order controllers are proposed using nonlinear feedback tools including Lyapunov-based techniques and control Lyapunov functions (CLFs). The control objective is to globally stabilize the rotor mass position in the AMB system. Responses of the AMB system states to initial condition and to external load disturbance are presented and the simulation and experimental results for transient responses are compared. The overshoots are compensated for the zero neighbourhood, and the rotor position amplitude does not exceed 2.5% of the air gap.

Index Terms ─ Active magnetic bearing, control Lyapunov function, nonlinear flux controller, zero-bias control.

I. INTRODUCTION

The bias-current or bias-flux are frequently used to linearize active magnetic bearing (AMB) dynamics, i.e., see author references [1, 2, 3]. However, large bias-current or bias-flux implies power losses, more heat dissipation and high bearing stiffness. In order to improve the energy efficiency of the AMB system, low- or zero-bias flux control can be applied [4, 5, 6, 7, 8]. The low- or zero-bias flux-controlled AMB dynamics become strongly nonlinear. Therefore, nonlinear control methods based on position-current or position-flux state feedbacks can be applied [9, 10, 11, 12]. In particular, in [10] the uncertain nonlinear flux-controlled AMB system operated with zero-bias is stabilized and so-called *small gain theorem* is used to calculate the robust stability.

The Lyapunov-based technique, such as control Lyapunov function (CLF) was introduced by Artstein and Sontag in 1983 [13, 14]. The idea of CLF-based control is to select a Lyapunov function $V(x)$ and then to try to find a feedback control $u(x)$ that renders $dV(x,u)/dt$, defined negatively. Therefore, for suitable $V(x)$, we can find a stabilizing control law $u(x)$ for the system feedback [15]. The CLF-based control concept was extended to dynamic systems with known disturbance [16, 17, 18], where $V(x)$ is the RCLF (a robust CLF), if, for a bounded disturbance, ω ensures that $\dot{V}(x,u,\omega) < 0$ [19, 20].

Recently the Lyapunov functions are used in the control application to the AMBs and electric machines. The nonlinear Lyapunov-based observer for the induction motor dynamics with saturation of the iron core is presented [21]. The observer is used to estimate the rotor flux amplitude and phase under varying conditions. The simulation and experimental results show good convergence of the observer comparing with the full-order Luenberger observer. Similarly, in [22] the authors designed a Lyapunov-based fuzzy adaptive controller in order to estimate the dynamic system uncertainties. The adaptive sliding-mode controller is designed for the position of rotor axial direction based on Lyapunov function and radial basis function is given in [23]. Simulations and experimental validation show a promising position tracking of the AMB rotor based on the designed control algorithm under different operating conditions, such as rotor position and force disturbance. The Lyapunov-based model predictive (MPC) scheme for permanent-magnet synchronous machine (PMSM) drive systems is presented in [24]. This system is shown to be asymptotically stable using the convex control set (CCS) input constraint with space vector or pulse width modulation and asymptotically set stable using the finite control set (FCS) input constraint.

The purpose of this paper is to provide the experimental verification of the CLF-based control designs. The experimental results proof that proposed controllers improve the zero-bias flux-controlled AMB performance and are comparable with more complicated approaches, i.e., based on Artstein-Sontag's theorem [4] or passivity-based ideas [5]. In comparison with previous solutions [4, 5], the obtained control laws ensure similar or even better transient responses and better external disturbance attenuation.

The paper is organized as follows. Section 2 presents

a nonlinear one-dimensional AMB model. Section 3 formulates conditions for Lyapunov-based AMB control and proposes CLF-controllers. Section 4 provides simulation of the zero-flux AMB system with CLF states feedbacks. The description of the experimental test rig and experimental results are given in Section 5. Section 6 states the concluding remarks.

II. ZERO-BIAS AMB SYSTEM

Consider a simplified 1–DOF (one-degree-of-freedom) AMB model, that consists of two opposite and presumably identical electromagnets with resistance R_1, R_2 [Ω] and currents i_1, i_2 [A], respectively (see Fig. 1). These electromagnets generate fluxes ϕ_1, ϕ_2 [Wb] and further the attractive forces F_1, F_2 [N], acting on the rotor with mass m [kg]. In order to control the position x [m] of the rotor to the stable state $x = 0$, the voltage inputs of the electromagnets, v_1 and v_2 [V], are used. The cross sectional area of the air-gap is denoted by A [m^2] and N is the number of turns of the coil of each electromagnet, respectively.
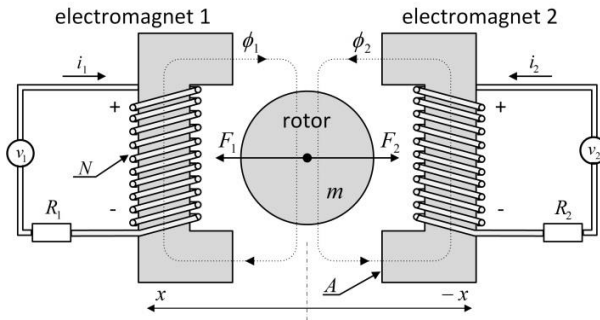

Fig. 1. Simplified one-dimensional AMB.

In order to represent the dynamics of the AMB system operated with zero-bias we follow the approach given in [4, 5]. Let us introduce the following non-dimensionalized state and control variables along with a non-dimensionalized time:

$$x_1 := \frac{x}{g_0}, x_2 := \frac{\dot{x}}{\Phi_{sat}\sqrt{g_0/\mu_0 mA}}, x_3 := \frac{\phi}{\Phi_{sat}}$$
$$u := \frac{v\sqrt{g_0\mu_0 mA}}{N\,\Phi_{sat}^2}, \tau := t\,\frac{\Phi_{sat}}{\sqrt{g_0\mu_0 mA}}, \tag{1}$$

where g_0 [m] is the nominal air-gap, $\dot{x}$ [m/s] is the velocity of the rotor mass, $\phi := \phi_1 - \phi_2$ [Wb] is the generalized electromagnetic flux, Φ_{sat} [Wb] is the saturation flux, u is the non-dimensionalized control variable, $v = v_1 - v_2$ [V] is the generalized control voltage, μ_0 is the permeability of free space (=1.25×10^{-6} H/m), τ denotes a non-dimensionalized time, t [s] is the original time.

In zero-bias flux control, the generalized control voltage v changes under the following flux-dependent condition:

$$v_1 = v, \quad v_2 = 0 \quad \text{when } \phi \geq 0,$$
$$v_2 = -v, \quad v_1 = 0 \quad \text{when } \phi < 0. \tag{2}$$

The switching scheme allows us to minimize the control power since at least one of the control voltages v_1 or v_2 and as well as fluxes ϕ_1 or ϕ_2 is zero at the time. The dynamics of the 1–DOF AMB model with zero-bias flux may be presented in terms of (1) as:

$$\begin{cases} \frac{d}{d\tau}x_1 = x_2, \\ \frac{d}{d\tau}x_2 = x_3|x_3|. \\ \frac{d}{d\tau}x_3 = u. \end{cases} \tag{3}$$

Equation (3) shows that the AMB system has strongly nonlinear dynamics provided by the singularity.

III. LYAPUNOV-BASED AMB CONTROL

In this section we will find the CLF that will make the AMB system globally stable. Consider the continuous-time system:

$$\dot{x} = f(x) + g(x)u, \tag{4}$$

where $u \in \mathbb{R}$ – control input, and vector $f: \mathbb{R}^3 \to \mathbb{R}^3$ and $g: \mathbb{R}^3 \to \mathbb{R}^3$, are given by $f(x) = \begin{bmatrix} x_2 & x_3^{[2]} & 0 \end{bmatrix}^T$, $g(x) = \begin{bmatrix} 0 & 0 & 1 \end{bmatrix}^T$, with $x_3^{[2]} := x_3^2 \mathrm{sgn}(x_3) = x_3|x_3|$. Recall that system (4) is asymptotically stabilizable with respect to the equilibrium pair (x_0, u_0), where $x_0 = x(0)$, if there exists a feedback law $u = \alpha(x)$, $\alpha(x_0) = u_0$, defined on a neighbourhood U_{x_0} of x_0 such that α is continuously differentiable on $U_{x_0} \setminus \{x_0\}$, for which the closed-loop system $\dot{x}(t) = (f + \alpha g)(x(t))$ is locally asymptotically stable (with respect to x_0). Recall also that (see [14, 25]) a real continuous function defined on open set $X \subset R^n$ is a local control Lyapunov function for closed-loop system if it satisfies the following properties:

(i) V is proper at x_0, i.e., $\{x \in X : V(x) \leq \varepsilon\}$ is a compact subset of some neighborhood U_{x_0} of x_0 for each sufficiently small $\varepsilon > 0$.

(ii) V is positive defined on U_{x_0}: $V(x_0) = 0$ and $V(x) > 0$ for each $x \in U_{x_0}$, $x \neq x_0$.

(iii) $L_f V(x) < 0$ for each $x \neq x_0, x \in U_{x_0}$, such that $L_g V(x) = 0$, where $L_g V(x) := \nabla V(x) \cdot g(x)$ denotes the Lie derivative of V with respect to g, and $L_f V(x)$ is the Lie derivative of V with respect to f.

The pair (f, g) of vector fields f and g that satisfies conditions (i)-(iii) is called *a control Lyapunov pair*. If the origin of (4) has CLF, then there exists a control law that renders the system asymptotically stable. We assume that for all $x \neq 0$ there is a positive, proper function $V \in \mathbb{R}_+$ such that:

$$\nabla V(x)[f(x) + g(x)u] < 0. \tag{5}$$

Let us assume that CLF describes the kinetic energy of system (3) is $V = \frac{1}{2}(3x_1^2 + 2x_2^2 + x_3^2)$. Then the

control laws, which fulfil inequality (5), are as follows:

$$u_1 = -3x_1^2 x_3 - 2x_2|x_3| - 3x_1 x_2 x_3 - x_3 + u_0,$$
$$u_2 = \frac{1}{2}(3x_1^2 + 2x_2 x_3|x_3| + 3x_1 x_2 - x_3) + u_0, \quad (6)$$
$$u_3 = -x_2|x_3| - x_3 - x_1 x_2 x_3 + u_0,$$

where $u_0 = -k_1 x_1 - k_2 x_2$ with k_1=0.92 k_2=9.94 were optimized and evaluated earlier in [12]. These gains are kept constant for all simulations and experiments. Regarding Eq. (6), it should be noted that theoretically there are an infinite number of functions. Each of them must to fulfill inequality (5). In our work, we have examined three functions u_1, u_2 and u_3 that were optimized due the kinetic energy of the system. Detailed information for evaluation of the controller u_1 can be found in [7], u_2 in [6], and u_3 in [8], respectively.

IV. SIMULATION RESULTS

This section presents simulation results obtained for zero-bias AMB system (3), described in Section 2, after applying zero-bias flux control with switching scheme (2). The results are presented for three state-feedback controllers u_1, u_2, u_3 (6) and for AMB true states: x [m] position, $\dot{x}$ [m/s] velocity and ϕ [Wb] flux. The AMB specifications are collected in Table 1. All simulations were carried out with sample time of 0.0001 s.

Table 1: AMB specifications

Symbol	Value	Meaning
$|x|_{max}$ [m]	0.0002	Rotor position limit
g_0 [m]	0.0004	Nominal width of air-gap
m [kg]	2.5	Rotor mass in the bearing plane
N	60	Number of coil turns
R [Ω]	0.26	Coil resistance
A [m^2]	0.00036	Electromagnet pole area
Φ_{sat} [Wb]	0.0022	Saturation flux
i_{sat} [A]	± 10	Saturation current

The AMB model detailed in Section 2, with parameters given in Table 1 was applied in Matlab/ Simulink® software, and the control structure is presented in Fig. 2.

The AMB system trajectories and controller outputs are illustrated for the given sinusoidal disturbances d_1 and d_2 with amplitude of ± 1 V and frequency of 10 and 20 Hz respectively, which are constant for all simulations. The disturbance is the external load/force acting on the rotor supported by AMB. This force is used to test the rotor stability. For simplicity we represent the disturbance as voltage. The power amplifier converts this voltage into the disturbance current with amplitude ± 1 A, resulting in the disturbance force generated by the electromagnets. The disturbances d_1 and d_2 are given in Fig. 3.
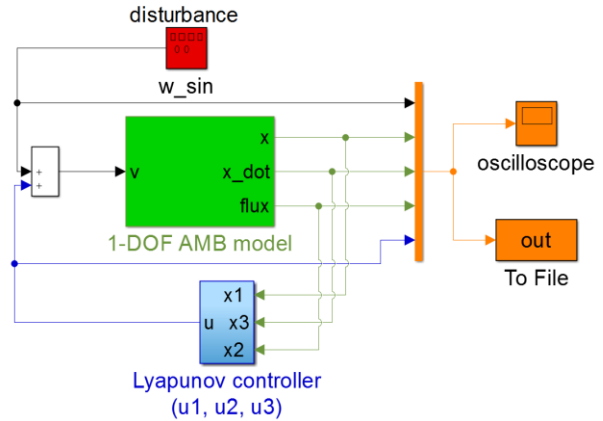

Fig. 2. Simulink control structure.
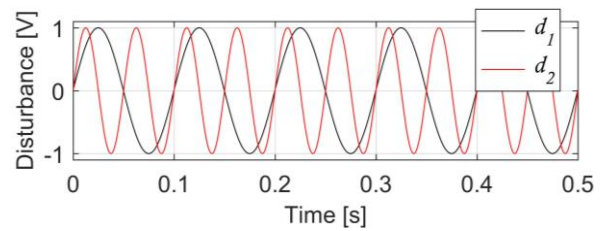
Fig. 3. Sinusoidal disturbances d_1 and d_2 of control voltage.

The AMB state responses to disturbance d_1, in zero-bias mode with controllers (6) are presented in Fig. 4, respectively. The disturbance d_1 is successfully attenuated by the controller in all cases. The lowest amplitude of the rotor positon response is given for controller u_1, but the flux amplitude is also the highest.
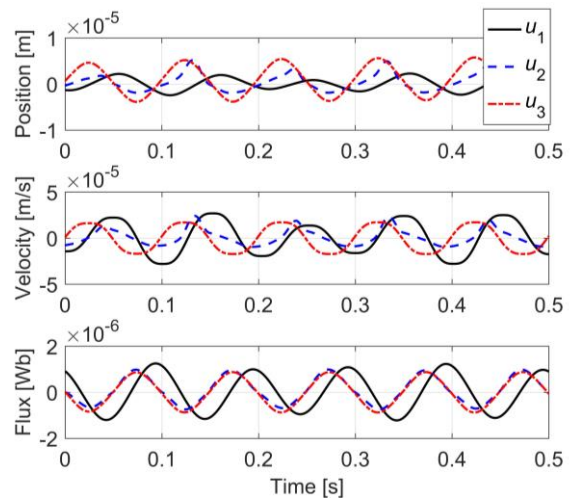

Fig. 4. Responses of closed-loop system with zero-bias to disturbance d_1 employing control laws: u_1, u_2 and u_3.

Figure 5 presents the control voltages responses to disturbance d_1 for controllers (6). One can be observed, that the voltage amplitude does not exceed ± 2 V (peak-to-peak). Maximum absolute voltage is about 1.9 V for control law u_2 and minimum equals 0.8 V for u_3. Although the controller output u_2 has the biggest amplitude (peak-to-peak), the system's response is worse, compared to the controls u_1 and u_3 (see Fig. 4).
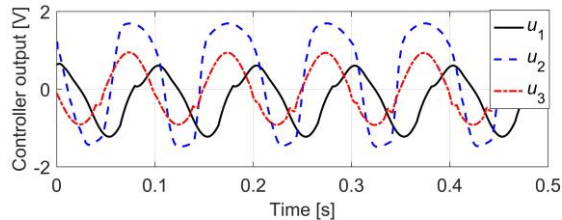

Fig. 5. Comparison of controller outputs responses to disturbance d_1 for controllers u_1, u_2, u_3.

Comparing control voltages responses given in Fig. 5 with results shown in Fig. 4, we can observe that the shapes of the voltage curves coincide with the rotor displacement values. Similarly with the rotor velocity and flux, which correspond to the displacement values obtained from simulation tests. The smoothest responses were obtained at the lowest values of the control signal. However, the control error was not reduced to zero, while in the case of u_1 and u_2 control, after reaching the extreme position – minimum or maximum, the error was compensated to zero, then again reaching the extreme position and finally stabilize near to zero. According to the assumption, using more electric energy (greater control voltage value) to stabilize the position takes place faster than in the opposite case.

V. EXPERIMENTAL VALIDATION

In this section the performance of the CLF-based AMB state-feedbacks, which simulation results are presented in Section 4, are verified via experimental measurements. The experimental research was carried out using a laboratory stand located in the Bialystok University of Technology where it was designed and fabricated [26].

The AMB system consists of two radial heteropolar active magnetic bearings which support the shaft. The shaft is connected with AC spindle motor by flexible coupling. The total mass of shaft equals 6 kg, and spindle AC motor with inverter enables to the system operated with speed range of $0 \div 24\ 000$ r/min. The radial AMBs are enclosed by a housing which consists of the stator, two-axes eddy-current displacement sensors, and auxiliary ball bearings. Main components of the experimental test rig are given in Fig. 6.
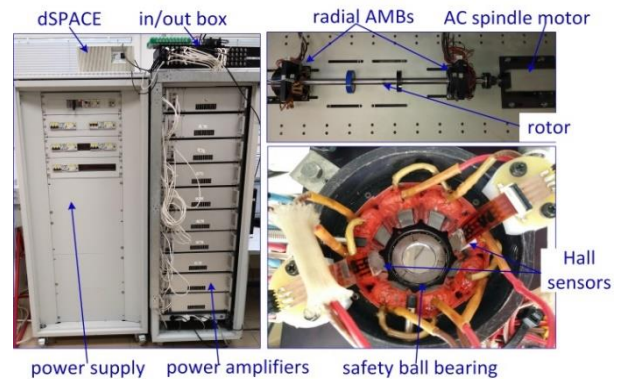
Fig. 6. Experimental setup: PWM power amplifiers, AMB rotor, radial AMB with sensors.

The control laws (6) are implemented in the real-time Digital Signal Processor (DSP) of dSpace. The control algorithms are implemented as the discrete-time models using the Real-Time Interface (RTI) and the Real-Time Workshop (RTW) provided by Matlab/Simulink environment. The signal acquisition is realized using ControlDesk environment of dSPACE. The DSP box consists also 14 bits analog-to-digital (A/D) and digital-to-analog (D/A) converts. The control voltage is the command input signal to the pulse width modulation (PWM) amplifiers. The switching frequency of the PWM amplifiers equals 18 kHz and the PWM voltage is equal to ± 180 V. The PWM amplifiers have inherent current control loops which ensure that the coil current i is proportional to the DSP output voltage command, with the gain 1 A/V. The output control currents which drive the AMB coils are limited to ± 10 A (peak-to-peak) with frequency bandwidth up to 1 kHz. The AMB current noise does not exceed the 0.1 A (peak-to-peak). The radial rotor displacement is measured using contact-less eddy-current sensor with accuracy up to 1 μm. The position sensor output is connected to the proximitor converter to ensure stable voltage output which is proportional to the rotor displacement with the gain 7.87 V/mm $\pm 5\%$. The displacement sensor output is filtered using anti-aliasing filters in order to cut-off any noise in the channel above *Nyquist* frequency (above 2 kHz). In order to obtain rotor velocity, the displacement derivative was used. Noisy signal was smoothed with 1st degree Bessel filter. Flux measurement is provided by ultra-thin (130 μm) Kapton-foil flexible Hall sensors. Two Hall sensors are mounted on opposite poles in the x axis of the AMB. Fabricated conditioning system was used to amplify the Hall voltage outputs. The AMB configuration during measurements and signal connections are shown in Fig. 7.
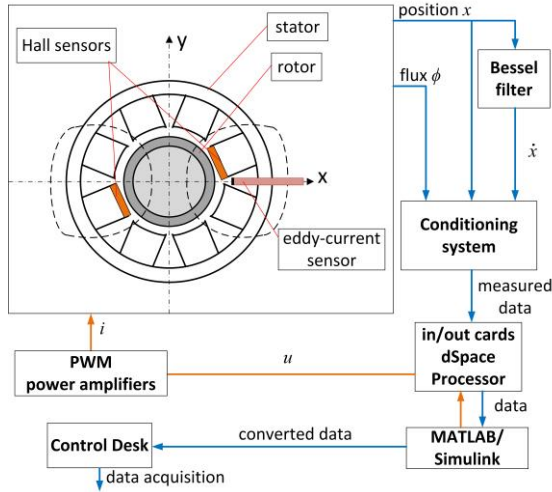
Fig. 7. Measurement configuration.

The experimental tests were divided into two groups: AMB states response to the sinusoidal disturbance d_1/d_2 (presented in Figs. 8÷11) and AMB trajectories response to displacement initial condition $x = 0.0002$ m (given in Figs. 12 and 13). The first set of the results are given for control u_1. The initial condition response of the AMB system with disturbance d_1 and d_2 is given in Fig. 8. In particular, in Fig. 8 the experimental results are plotted together with simulation responses. According to results given in Fig. 8, it is demonstrated that, the disturbance effect of two different frequencies is compensated with controller voltage output amplitudes.
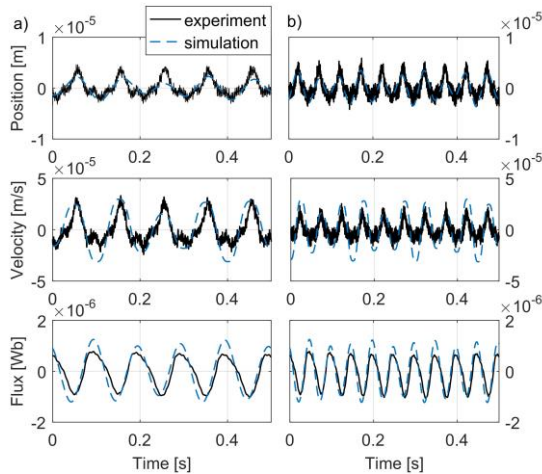

Fig. 8. Comparison of the simulation and experimental transient responses of AMB states with the controller u_1 and disturbances: (a) d_1; (b) d_2.

Figure 9 shows the AMB states responses to disturbance d_1 with control u_2, and Fig. 10 presents the AMB trajectories for controller u_3.
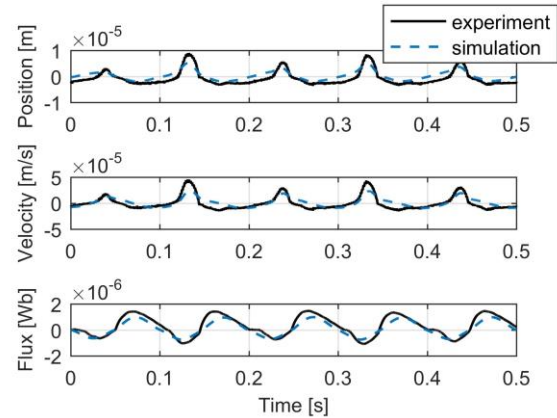
Fig. 9. Experimental and simulation responses of the AMB states to disturbance d_1 with controller u_2.
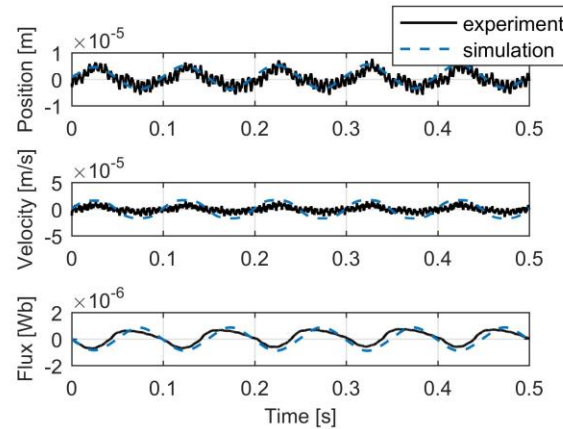

Fig. 10. Experimental and simulation responses of the AMB states to disturbance d_1 with controller u_3.

The voltage outputs v_1, v_2 for controllers u_1, u_2, u_3 are presented in Fig. 11 in case of both disturbances d_1/d_2.
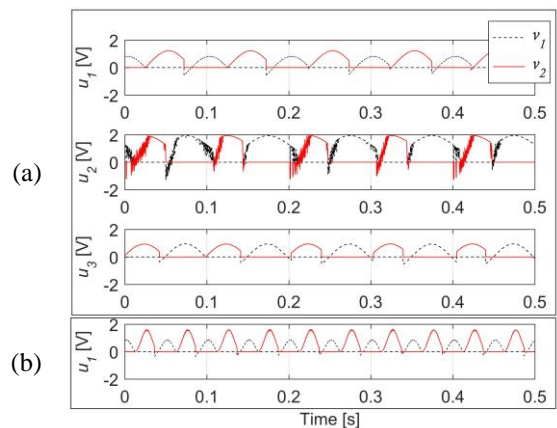

Fig. 11. Control voltages responses to disturbances: (a) d_1 for controllers u_1, u_2, u_3; (b) d_2 for controller u_1.

To summarize, the results presented in Figs. 8–10 indicate that the overshot is compensated to zero neighbourhood, and the max rotor position amplitude does not exceed 10 μm that is 2.5% of the air-gap, despite the desired initial conditions and different disturbances. Moreover, the experimental results of the rotor position responses fit to the simulation one. In the case of u_3 control (Fig. 10), the error is not reduced to zero, but the disturbance is less compensated. In Fig. 11, we can observe the results of the voltage v_1 and v_2 switching operation under the flux-dependent condition (2), where at any given time only one electromagnet is activated. The control voltage amplitude does not exceed 2 V, for controller u_1, u_2, and u_3. The AMB system response to the initial condition, where the rotor is stabilized from the auxiliary bearing (when $x = 0.0002$) to the origin at $x = 0$, is given in Figs. 12 and 13. In particular, Figs. 12 (a) and 12 (b) give the generalized flux ϕ responses and voltage outputs v_1 v_2 responses for controllers u_1, u_2 and u_3.

(a) Electromagnetic flux

(c) Cost function

(b) Voltage outputs
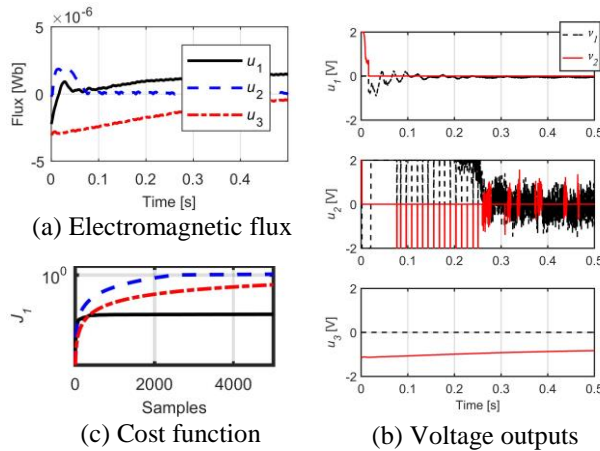
Fig. 12. AMB system responses to the initial condition for controllers u_1, u_2, u_3, without disturbance.

In order to assess the energy requirements for controllers u_1, u_2 and u_3, the quadratic cost function of the controller output $J_1 = \int_0^\infty u^2 \, dt$ is used. The cost function for all controllers is compared and results are shown in Figure 12c. One may observe that the highest total energy is required by the controller u_2. Figure 13 presents comparison of AMB rotor position responses to the initial condition for three controllers: u_1, u_2 and u_3.

Stabilization time is less than about 0.1 s for each controller. However the shortest setting time of 0.05 s is achieved with control u_2, while the setting time of 0.1 s is achieved for controllers u_1 and u_3 with less energy requirements. The energy demand is the lowest in the case of controller u_1, see Figs. 12 (b) and 12 (c), but the rotor position stabilizes slower (about 0.1 s), see Fig. 13.
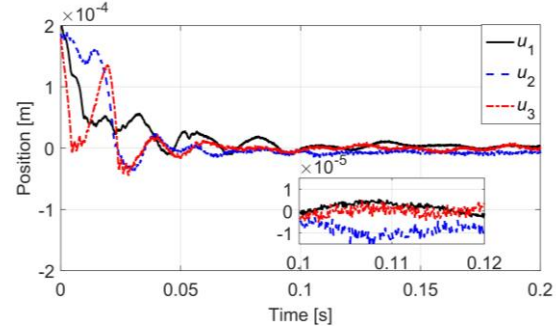

Fig. 13. Comparison of AMB system responses to the initial condition without disturbance.

To conclude the experimental results, we can notice that the zero-bias control design for the AMB is challenging cause of the loss of linear controllability near the origin, when $x = 0$. Thus, in order to produce a low control electromagnetic force we need a large voltage commands v_1 and v_2, see i.e., output voltages for controller u_2 in Fig. 12. Moreover, we need to notice, that in the experimental measurements, we can observe the influence of the other disturbances which are not addressed (see zoo window in Fig. 13). These disturbances can be divided into external part, i.e., noise in the control voltage and in the measured rotor position or flux, and into internal, such as: self-excited vibrations. The total noise of the measured rotor position is about 1.2 μm (peak-to-peak), that is 0.3% of the air-gap According to the high sensitivity of the AMB rotor dynamics, these disturbances provide to system perturbations and more power consumption.

VI. CONCLUSION

In this paper we have presented three control Lyapunov function (CLF) designs for the flux-controlled AMB system operated with zero-bias. The proposed designs are experimentally validated. The results showed global asymptotic stability of the nonlinear AMB system with the singularity near the origin. The AMB states transient responses to initial condition and to the external load disturbance are presented and compared. The Matlab/ Simulink simulation results fit with experimental measurements. Moreover, the low-order CLF-based state controllers gave equivalent results compared with the high-order complex control, i.e., based on Artstein-Sontag's theorem [4]. One of the future goals is to address Lyapunov-based nonlinear feedback controllers for the MIMO system. In the case of 5–DOF AMB flux-controlled rotor dynamics, the decoupling control can be applied.

REFERENCES

[1] Z. Gosiewski and A. Mystkowski, "Robust control of active magnetic suspension: analytical and experimental results," *Mechanical Systems & Signal Processing*, vol. 22, pp. 1297-1303, 2008.

[2] A. Mystkowski, "Mu-synthesis for magnetic bearings of flywheel," *Proc. in Applied Mathematics and Mechanics (PAMM)*, Wiley Online Library, vol. 9, pp. 631-632, 2009.

[3] A. Mystkowski, "μ-synthesis control of flexible modes of AMB rotor," *Acta Mechanica et Automatica*, vol. 4, pp. 83-90, 2010.

[4] P. Tsiotras and B. C. Wilson, "Zero- and low-bias control designs for active magnetic bearings," *IEEE Trans. Contr. Syst. Technol.*, vol. 11, pp. 889-904, 2003.

[5] P. Tsiotras and M. Arcak, "Low-bias control of AMB subject to voltage saturation: state-feedback and observer designs," *Proc. of the 41st IEEE Conf. on Decision and Contr.*, Las Vegas, NV, USA, pp. 2474-2479, 10-13 Dec. 2002.

[6] A. Mystkowski and A. E. Pawluszewicz, "Nonlinear position-flux zero-bias control for AMB system with disturbance," *Applied Computational Electromagnetics Society Journal*, vol. 32, no. 8, pp. 650-656, 2017.

[7] A. Mystkowski and E. Pawluszewicz, "Remarks on some robust nonlinear observer and state-feedback zero-bias control of AMB," *IEEE The 16th Int. Carpathian Control Conf.*, Szilvásvárad, Hungary, pp. 328-333, 2015.

[8] A. Mystkowski, E. Pawluszewicz, and R. P. Jastrzebski, "Nonlinear position-flux zero-bias control for AMB system," *IEEE 20th Int. Conf. on Methods and Models in Automation and Robotics*, Międzyzdroje, Poland, pp. 24-27, 24-27 Aug. 2015.

[9] H. Bleuler, D. Yischer, G. Schweitzer, et al., "New concepts for cost-effective magnetic bearing control," *Automatica*, vol. 30, pp. 871-876, 1994.

[10] A. Charara, J. De Miras, and B. Caron, "Nonlinear control of a magnetic levitation system without premagnetization," *IEEE Trans. Contr. Syst. Technol.*, vol. 4, pp. 513-523, 1996.

[11] R. P. Jastrzebski, A. Smirnov, A. Mystkowski, and O. Pyrhönen, "Cascaded position-flux controller for AMB system operating at zero bias," *Energies*, vol. 7, pp. 3561-3575, 2014.

[12] A. Mystkowski, E. Pawluszewicz, and E. Dragašius, "Robust nonlinear position-flux zero-bias control for uncertain AMB system," *Int. J. of Contr.*, vol. 88, pp. 1619-1629, 2015.

[13] Z. Artstein, "Stabilization with relaxed controls," *Nonlinear Analysis*, vol. 7, pp. 1163-1173, 1983.

[14] E. D. Sontag, "A Lyapunov-like characterization of asymptotic controllability," *SIAM Journal of Control and Optimization*, vol. 21, pp. 462-471, 1983.

[15] E. D. Sontag, "A universal construction of Artstein's theorem on nonlinear stabilization," *Systems and Control Letters*, vol. 13, pp. 117-123, 1989.

[16] R. A. Freeman and P. V. Kokotović, "Inverse optimality in robust stabilization," *SIAM Journal of Control and Optimization*, vol. 34, pp. 1365-1391, 1996.

[17] R. A. Freeman and P.V. Kokotović, *Robust Nonlinear Control Design – State–Space and Lyapunov Techniques*, Boston: Birkhäuser, 1996.

[18] R. A. Freeman and P. V. Kokotović, "Design of 'softer' robust nonlinear control laws," *Automatica*, vol. 29, pp. 1425-1437, 1996.

[19] F. Clarke, "Lyapunov functions and feedback in nonlinear control, optimal control, stabilization and nonsmooth analysis," *Lecture Notes in Control and Information Science*, vol. 301, pp. 267-282, 2004.

[20] I. Kanellakopoulos, P. V. Kokotović, and A. S. Morse, "A toolkit for nonlinear feedback design," *Systems and Control Letters*, vol. 18, pp. 83-92, 1992.

[21] F. Alonge, M. Cirrincione, M. Pucci, and A. Sferlazza, "A nonlinear observer for rotor flux estimation of induction motor considering the estimated magnetization characteristic," *IEEE Trans. on Industry Applications*, vol. 53, no. 6, pp. 5952-5965, 2017.

[22] J. Fei and J. Zhou, "Robust adaptive control of MEMS triaxial gyroscope using fuzzy compensator," *IEEE Sys., Man. and Cybernetics Society*, vol. 42, no. 6, pp. 1599-1607, 2012.

[23] H. S. Zad, T. I. Khan, and I. Lazoglu, "Design and adaptive sliding-mode control of hybrid magnetic bearings," *IEEE Trans. on Industrial Electronics*, vol. 65, no. 3, pp. 2537-2547, 2018.

[24] M. Preindl, "Robust control invariant sets and Lyapunov-based MPC for IPM synchronous motor drives," *IEEE Trans. on Ind. Electronics*, vol. 63, no. 6, pp. 3925-3933, 2016.

[25] A. Bressan and B. Piccoli, "Introduction to the mathematical theory of control," *Springfield: American Institute of Mathematical Sciences*, *Applied Math*, vol. 2, 2007.

[26] Z. Gosiewski and A. Mystkowski, "The robust control of magnetic bearings for rotating machinery," *Solid State Phenomena*, vol. 113, pp. 125-130, 2006.

Calculation and Experiment of Electromagnetic Force of the Axial AMB used in HTR-PM Main Helium Blower Prototype and its Dual Material Selection Method

Xingnan Liu, Zhengang Shi, Ni Mo, Jingjing Zhao, and Guojun Yang*

Institute of Nuclear and New Energy Technology, Tsinghua University, Beijing, 100084, China
Collaborative Innovation Center of Advanced Nuclear Energy Technology, Beijing, 100084, China
The Key Laboratory of Advanced Reactor Engineering and Safety, Ministry of Education, Beijing, 100084, China
liuxingnan@tsinghua.edu.cn, shizg@tsinghua.edu.cn, moni@tsinghua.edu.cn, zhao-jj@tsinghua.edu.cn,
yanggj@tsinghua.edu.cn*

Abstract ─ The Active Magnetic Bearing (AMB) is used in the main helium blower in the High Temperature Reactor-Pebble-bed Modules (HTR-PM) which is being constructed in Shandong province, China. The axial AMB is very large and works under extreme conditions. The calculation deviation of the electromagnetic force of the axial AMB was studied experimentally. Through measuring *B-H* curve of the material in large range of magnetic field intensity, considering flux leakage in calculation, and considering residual magnetism and the change of the gas gap in measurement, the calculation deviation reduces to 10%, with most values less than 5%. The material selection method of the axial AMB working under extreme conditions was studied experimentally. Through measuring the electromagnetic force when the stator and the thrust disc are made of different materials, it's found that the force mostly depends on the stator. Combined with the analysis of the stress distribution of the stator and the thrust disc under working condition, the dual material selection method is proposed. That is, the stator material should have good magnetic properties and its mechanical properties are not very important, however, the thrust disc material should have good mechanical properties, and its magnetic properties are not very important.

Index Terms ─ Active magnetic bearing, axial bearing, calculation deviation, electromagnetic force, extreme conditions, material selection.

I. INTRODUCTION

The Active Magnetic Bearing (AMB) suspends the rotor by electromagnetic force. Compared with traditional mechanical bearing, the AMB has advantages such as no-contact, long-life and controllability [1]. In the High Temperature Reactor- Pebble-bed Modules (HTR-PM) which is being constructed in Shandong province, China, the AMB is used in the main helium blower [2,3]. A prototype of the main helium blower is manufactured for research, and its AMB is designed by Tsinghua University [4,5]. The AMB of the blower prototype is large. The diameter of the axial bearing is about 600 mm. The axial load is about 10 tons, and the bearing will work in extreme conditions, which is near magnetic saturation. So the calculation of the electromagnetic force during design should be quite accurate.

Many researchers calculated the electromagnetic force using the Maxwell Stress Tensor Method (MSTM) and the Finite Element Method (FEM), and reduced the calculation errors from point of elements and nodes [6-8]. Nehl and Field [6] improved the force calculation accuracy for electromagnetic devices with small air gaps by adaptive mesh refinement using first order tetrahedral element using MSTM. Onuki et al. [7] proposed a smoothing method to calculate electromagnetic force more accurately using the Boundary Element Method (BEM) as a complement to the FEM and MSTM. Shi and Rajanathan [8] improved the force calculation accuracy of MSTM by selecting appropriate integration path and the potential interpolation points within the FEM. Except the MSTM, other methods are adopted by the researchers to calculate the electromagnetic force, such as the Reluctance Network Method (RNM) [9] and Lorentz Force Method (LFM) [10]. However, commercial software usually uses Virtual Work Method (VWM) and FEM to calculate the electromagnetic force, such as ANSYS Maxwell [11] and MagNet [12]. Compared with other methods, the VWM can deal with complex problems and is not sensitive to the integration path. As the algorithm improves, the calculation results by the commercial software are more and more accurate, and are usually regarded as reference values [13,14].

Unfortunately, the calculation results by ANSYS Maxwell have large deviation in the authors' early work of designing the axial AMB used in the main helium blower prototype. Theoretically, the deviation between

the calculated force and the actual value comes from both calculation and measurement. The calculation error mainly composes of two parts. The first part is the magnetic properties of the materials used in calculation, which could be looked up in the handbooks, such as literature [15]. These properties may be different from the actual ones. The second part is the calculation model, which usually ignores flux leakage for simple. The measurement error depends on specific experiment and is rarely mentioned in other literatures [6-10]. It will be discussed below.

In this paper, firstly, the deviation between the calculated force and the experimental value of the axial AMB used in the main helium blower prototype is studied. Both the calculation error and the measurement error are considered. At first, the *B-H* curve of the materials are measured, especially under large magnetic field intensity. Then, the leakage flux is considered in the calculation model. At last, the actual value is measured carefully in the experiment. The deviation then is reduced by considering the above factors.

Secondly, material selection method for the axial AMB working under extreme conditions is studied. It's difficult to find a kind of material with both good mechanical properties and good magnetic properties [15]. Research about material selection for the axial AMB is rare, some papers that seem relevant don't concern this problem [16,17]. In this paper, different materials are used to make the bearing stator and the thrust disc, and the different influences of the stator and the thrust disc are researched by experiment. The stress distribution of the stator and the thrust disc is analyzed under working condition. At last, the materials selection method for the large axial bearing working in extreme condition is proposed.

II. EXPERIMENT AND CALCULATION

A. Measurement of *B-H* curve of the materials

The most important magnetic properties of a material for calculating the electromagnetic force is *B-H* curve, where *B* is the magnetic flux density, and *H* is the magnetic field intensity.

Materials of the axial AMB stator and thrust disc used in the blower prototype are the same, a kind of low alloy steel, denoted by M-steel. The *B-H* curve of this material could be looked up in handbook [15]. However, the low alloy steel has complex composition and heat treatment process, and both of them will change the *B-H* curve [15]. So the data from handbook is usually different from the actual one. At the same time, the data from handbook is only for low-intensity magnetic field, however the axial bearing of the blower prototype will work under high-intensity magnetic field. During calculation, the extension part of the curve will be deduced with some method, and then some error may be

produced. To reduce the calculation error, the *B-H* curve of M-steel should be measured practically in large range of magnetic intensity.

In this paper, including M-steel, the *B-H* curves of used materials are measured with a soft magnetic tester, MATS-2010SD [18]. The sample is made into a ring and its size is shown in Fig. 1.
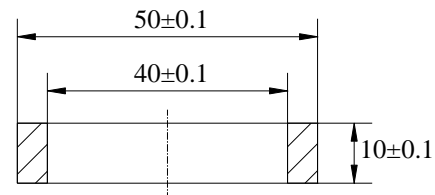

Fig. 1. Size of the magnetic material sample ([mm]).

B. Experiment for electromagnetic force

An equipment is established to measure the electromagnetic force, shown in Fig. 2. The equipment has the same size as the axial AMB of the blower prototype, with a thrust disc having a diameter of 600 mm. Actually, the equipment is also used to prove the design of the axial AMB. The thrust disc is fixed on a foundation with a magnetic isolation shim between them which is made of stainless steel. A bearing stator is also fixed on the foundation through three force testing sensors. When the coils in the stator have current, the force between the stator and the thrust disc could be measured by the sensors. It should be noted that the actual force is the sum of these three sensors' values. The current in stator is from 0 to 60 A, and the electromagnetic force is about from 0 to 10^5 N. The gas gap is from 0.7 mm to 1.5 mm.

In this paper, the measurement error of the electromagnetic force under certain current and certain gas gap comes from two aspects. The first one is residual force under zero current coming from gravity of the stator and the residual magnetism. The second one is the change of the gas gap under large electromagnetic force. In this paper the residual force is subtracted, and the gas gap is the actual value adjusted by the nuts under a certain current. Through these efforts, the measurement error is reduced.

In some experiments, the stator and the thrust disc are made of the same material, e.g., M-steel, which is used to prove the design of the AMB and to be compared with the calculation. In some other experiments, they are made of different materials to study the different influences of the stator and the thrust disc on the electromagnetic force. It will be discussed below.

C. Calculation for electromagnetic force

For simple, the magnetic flux density *B* in the gas gap shown in Fig. 2 could be calculated by equation (1),

ignoring magnetic field in metal [1]:

$$B = \mu_0 NI/(2s), \qquad (1)$$

where μ_0 is permeability of vacuum, N is number of windings in a single groove of the stator, I is current in the windings, and s is gas gap. And then the electromagnetic force would be calculated by equation (2):

$$F = B^2 A/(2\mu_0), \qquad (2)$$

where F is the magnetic force, and A is the projected area of the flux. The above method has large error in equation (1) and it's only fit for initial design of the AMB.

In this paper, the electromagnetic force is calculated by the commercial software, ANSYS Maxwell [11]. A model as same as the actual experiment equipment is established, as shown in Fig. 3. The magnetic field in the metal, the actual *B-H* curve of the material, and the flux leakage are all considered in the model.
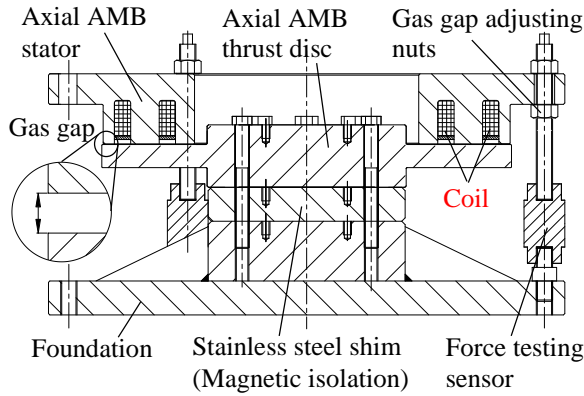

Fig. 2. The experiment equipment.
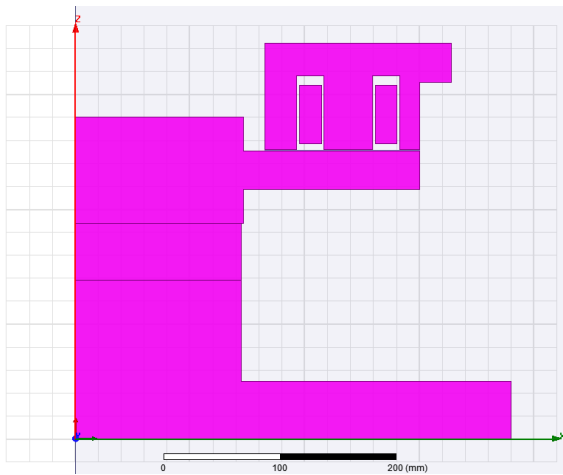
Fig. 3. Calculation model of the axial AMB for electromagnetic force.

D. Material selection method

In this section the stator and the thrust disc are made of different materials to study their different influences on the electromagnetic force. Two kinds of materials are used, as shown in Fig. 4. DT4C is a kind of soft magnetic iron with better magnetic properties and worse mechanical properties [19]. 20CrMo is a kind of low alloy steel with better mechanical properties [20] and worse magnetic properties, named 4120 in ASTM [21]. Their mechanical properties are shown in Table 1.

The stress distributions of the stator and the thrust disc under working conditions are analyzed. The stator is static, however, the thrust disc rotates under a speed of maximum 4,800 rpm [4,5] and has interference fit with the mandrel [22]. At the same time, there is an attractive force of most 10 tons between them. The stress is calculated by the commercial software, ANSYS Mechanical APDL [23], with the same material properties for both the stator and the thrust disc, such as Young's modulus of 210 GPa, Passion's ratio of 0.3, and density of 7850 kg/m³.

According to the different influences on the force and the different stress distributions under working condition, the material selection method for the axial AMB is determined.
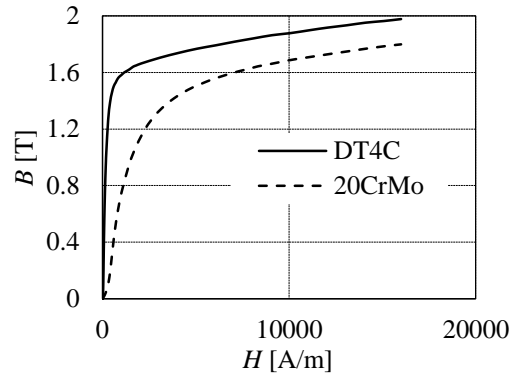

Fig. 4. *B-H* curves of DT4C and 20CrMo from measurement.

Table 1: Mechanical properties of DT4C and 20CrMo [19, 20]

Properties	DT4C	20CrMo
Tensile stress / MPa	≥265	≥885
Yield strength / MPa	≈100	≥685
Hardness (HV)	≤195	≥300
Young's modulus / GPa	≈210	≈210
Poisson's ratio	0.25~0.3	0.25~0.3

III. RESULTS AND DISCUSSION

A. Comparison of *B-H* curves of material between handbook and measurement

The *B-H* curve of the material M-steel is shown in Fig. 5. The values from handbook [15] and from measurement have large difference especially under high magnetic intensity, which would result in large deviation between calculation and experiment. There is similar

phenomenon in Figs. 6~8, showing the *B-H* curve of C45 carbon steel, DT4C and 20CrMo respectively. C45 carbon steel is a kind of common carbon structural steel, which is used to make the foundation shown in Fig. 2. As a matter of fact, it's a general phenomenon that the values from handbook are accurate enough under low magnetic intensity, but not fit for accurate calculation under high magnetic intensity. The main reason of these difference is that both the composition and the heat treatment process of the material will change its magnetic properties.

Another problem of the values from handbook [15] is lack of data under magnetic field of more than 16000 A/m. ANSYS Maxwell [11] will extend the range of *B-H* curve with interpolation method, which will bring some certain error, as shown in Fig. 9. So measured *B-H* curve in the range of working conditions should be supplied for accurate calculation. In the blower prototype, the axial AMB worked under high-intensity filed, so the *B-H* curve of M-steel are measured up to 24000 A/m, as shown in Fig. 5. That ensured the accuracy of the calculation.
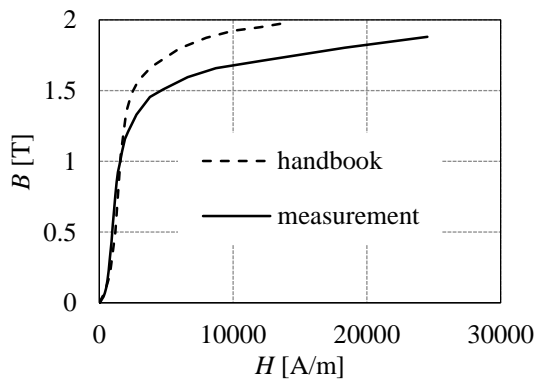

Fig. 5. *B-H* curve of M-steel, from handbook [15] and from measurement.
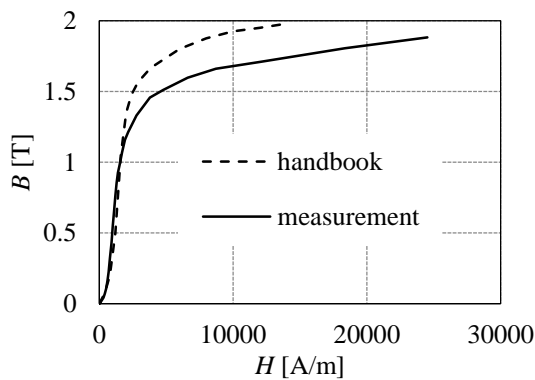

Fig. 6. *B-H* curve of C45 carbon steel, from handbook [15] and form measurement.
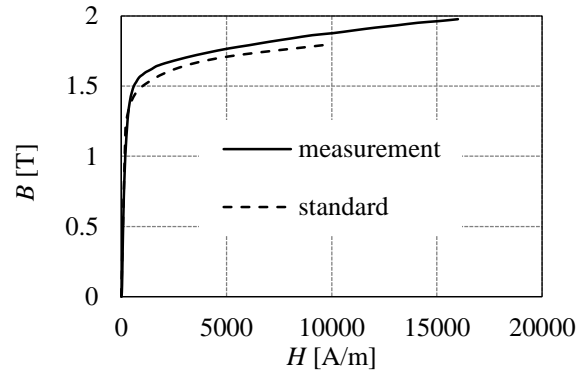
Fig. 7. *B-H* curve of DT4C, from standard [19] and from measurement.
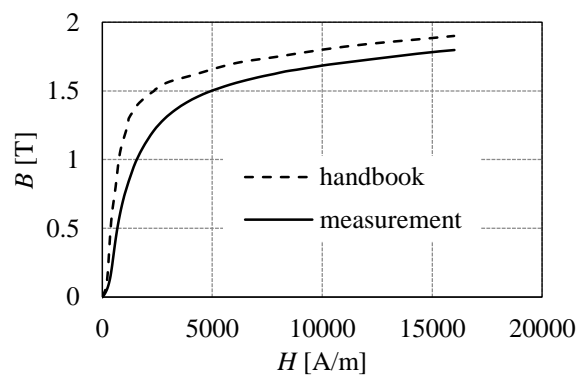
Fig. 8. *B-H* curve of 20CrMo, from handbook [15] and from measurement.
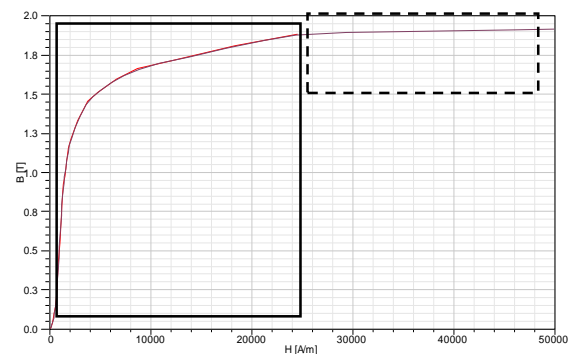
Fig. 9. Extended *B-H* curve of M-steel, produced by ANSYS Maxwell [11] with interpolation method, whose measured data is in solid line box and extended part is in dash line box.

B. Deviation of electromagnetic force between calculation and experiment

The typical distribution of the magnetic flux in the stator and the thrust disc is shown in Fig. 10, calculated with the model shown in Fig. 3. The experiment and

calculation of the electromagnetic force of the axial AMB used in the blower prototype is shown in Fig. 11. The gas gaps are 0.8 mm and 1.1 mm, and the current is from 5 A to 60 A.

It's shown that, through efforts mentioned above, including measuring *B-H* curve of M-steel in large range of magnetic intensity, considering flux leakage in calculation, and considering residual force and the change of the gas gap in experiment, the deviation of the calculation values could be smaller than 10%. For most values, it's less than 5%. Because the magnetic tester's measurement accuracy for the *B-H* curve is about 1%~2% [18], the limitation of the calculation deviation is about 4% according to equation (2). That is to say, for most values, the deviation of the calculation is close to the limitation.
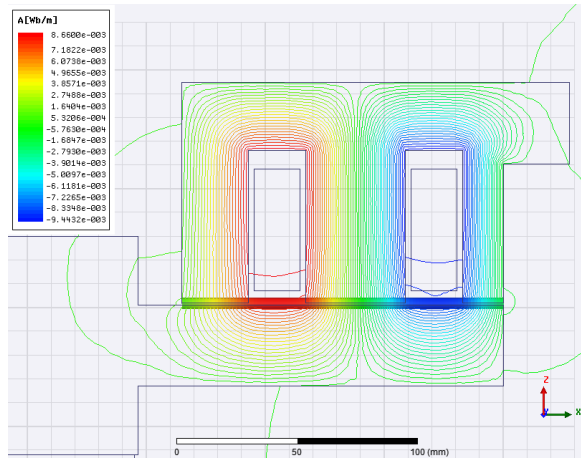

Fig. 10. Distribution of the magnetic flux in the axial AMB.
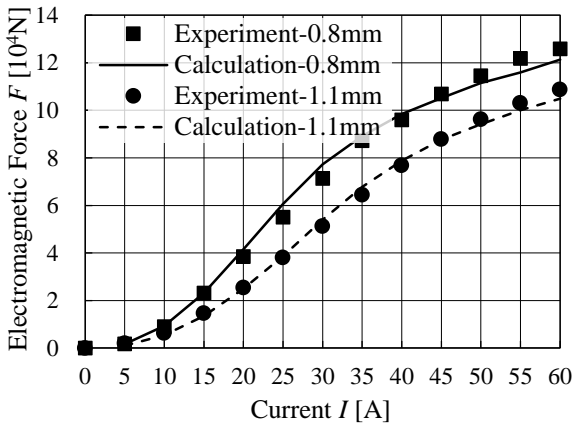
Fig. 11. Comparison between calculation and experiment of electromagnetic force, under two gas gaps, 0.8 mm and 1.1 mm.

C. Different influence on electromagnetic force and different stress distributions of bearing stator and thrust disc

In this section, two kinds of materials, DT4C and 20CrMo, are used to make the stator and the thrust disc. Their *B-H* curves from measurement are shown in Fig. 4. It can be seen that the permeability of DT4C is quite larger than the one of 20CrMo.

Measured electromagnetic force is shown in Fig. 12, with the stator and the thrust disc are made of DT4C or 20CrMo, and 0.8 mm gas gap. It can be seen that the force mostly depends on the material of the stator. That is to say, the stator material should have good magnetic properties to obtain large electromagnetic force. However, the magnetic properties of the thrust disc are not very important.
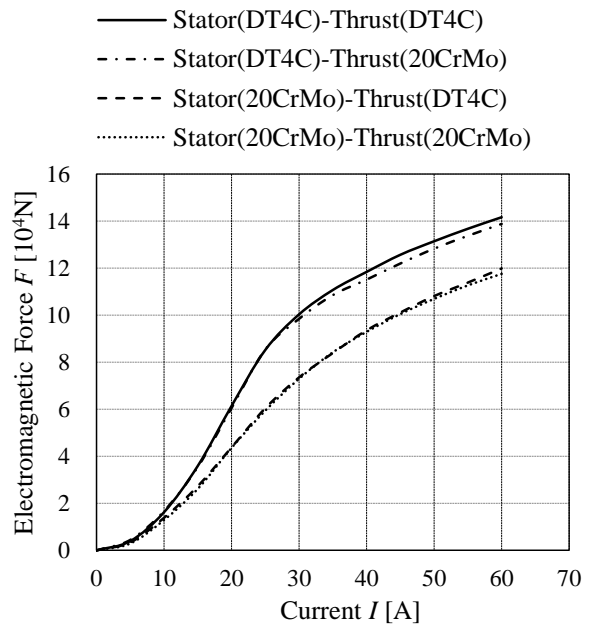
Fig. 12. Measured electromagnetic force, with the stator and the thrust disc made of DT4C or 20CrMo, under 0.8 mm gas gap.

The stress distributions of the stator and the thrust disc under working conditions are shown in Figs. 13 and 14 respectively. The working conditions include attractive electromagnetic force of 10 tons between the stator and the thrust disc, a rotation speed of 4,800 rpm for the thrust disc, and the interference fit of 0.25 mm in diameter between the thrust disc and the mandrel. Both the stator and the thrust disc have the same material properties, including Young's modulus of 210 GPa, Passion's ratio of 0.3, and density of 7850 kg/m^3.

It can be seen, the maximum Mises stress of the thrust disc is about 210 MPa; however the one of the

stator is only 14.4 MPa. Considering a safety factor of 1.5~2.0, the yield strength of the thrust disc material should be larger than 350~400 MPa, and the one of the stator material should be larger than only 22~29 MPa.
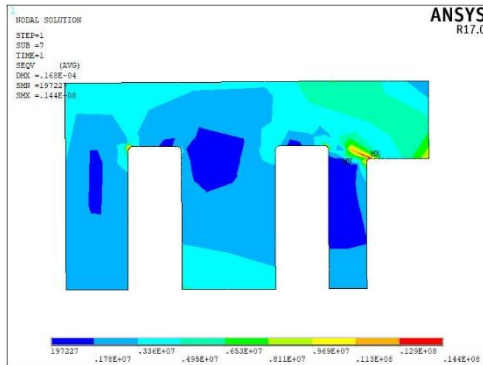
Fig. 13. Mises stress distributions of the stator under working condition.
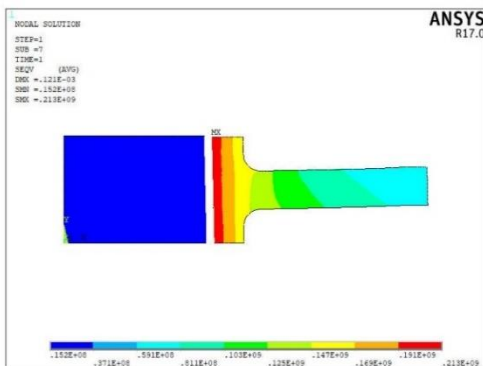
Fig. 14. Mises stress distributions of the thrust disc under working condition.

D. Dual material selection method

According to section III. C, the axial AMB stator has more important influence on the electromagnetic force, so its material should have good magnetic properties. And it doesn't need very good mechanical properties. However, the thrust disc should have good mechanical properties because of harder working condition, and doesn't need very good magnetic properties. The above description is called "dual material selection method" for the axial AMB.

Under extreme working condition like the blower prototype, it's difficult to find a kind of material with both good magnetic properties and good mechanical properties. In the blower prototype, the stator and the thrust disc used the same material, M-steel. As a matter of fact, M-steel is expensive and has complex heat treatment to improve the magnetic properties. So it's not the optimal solution. With the dual material selection method proposed in this paper, the stator and the thrust

disc all have more options.

IV. CONCLUSION

Through some efforts, including measuring *B-H* curve of the material in large range of magnetic field intensity, considering flux leakage in calculation, and considering residual force and the change of the gas gap in measurement, the calculation deviation of the electromagnetic force of the axial AMB used in the main helium blower prototype is reduced to 10%. For most calculation values, the deviation is less than 5%, close to the limitation depending on measurement accuracy of the magnetic tester.

When the axial AMB stator and the thrust disc use different materials, the electromagnetic force is mostly depended on the material of the stator. The stator material should have good magnetic properties, and its mechanical properties are not very important. However, the thrust disc material should have good mechanical properties, and its magnetic properties are not very important. This "dual material selection method" make the materials of the stator and the thrust disc have more options.

REFERENCES

[1] G. Schweizer, H. Bleuler, and A. Traxler (L. Yu and C. J. Yuan. translated), *Active Magnetic Bearings—Basics, Properties and Application of Active Magnetic Bearings*. New Time Press, Beijing, 1997.

[2] Z. Y. Zhang, Y. D. Dong, F. Li, et al., "The Shandong Shidao Bay 200 MWe high-temperature gas-cooled reactor pebble-bed module (HTR-PM) demonstration power plant: An engineering and technological innovation," *Engineering*, vol. 2, no. 1, pp. 112-118, Mar. 2016.

[3] Z. Y. Zhang, Z. X. Wu, D. Z. Wang, et al., "Current status and technical description of Chinese 2×250 MWth HTR-PM demonstration plant," *Nuclear Engineering and Design*, vol. 239, no. 7, pp. 1212-1219, Feb. 2009.

[4] G. J. Yang, Z. G. Shi, and N. Mo, "Technical design and engineering prototype experiment of active magnetic bearing for helium blower of HTR-PM," *Annals of Nuclear Energy*, vol. 71, pp. 103-110, Apr. 2014.

[5] G. J. Yang, Z. G. Shi, N. Mo, and L. Zhao, "Research on active magnetic bearing applied in Chinese modular high-temperature gas-cooled reactor," *Progress in Nuclear Energy*, vol. 77, pp.

352-360, Nov. 2014.

[6] T. W. Nehl and D. A. Field, "Accuracy of force calculations using first order tetrahedra for electromagnetic devices with small air gaps," *IEEE Transactions on Magnetics*, vol. 27, no. 5, pp. 4249-4253, Sept. 1991.

[7] T. Onuki, S. Wakao, and H. Saito, "Improvement in the calculation of electromagnetic force by the FEM," *IEEE Transactions on Magnetics*, vol. 30, no. 4, pp. 1863-1866, July 1994.

[8] Z. W. Shi and C. B. Rajanathan, "A method of reducing errors in the calculation of electromagnetic forces by Maxwell stress summation method," *IEEE Transactions on Magnetics*, vol. 35, no. 3, pp. 1358-1361, May 1999.

[9] J. Worotynski, M. Turowski and E. A. Mendrela, "The accuracy of calculation of magnetic fields, inductance and forces in electromagnetic devices using the reluctance network method (RNM)," *COMPEL - The International Journal for Computation and Mathematics in Electrical and Electronic Engineering*, vol. 13, no. 1, pp. 159-162, Mar. 1994.

[10] D. Xu, X. S. Liu, K. Fang, and H. Y. Fang, "Calculation of electromagnetic force in electromagnetic forming process of metal sheet," *Journal of Applied Physics*, vol. 107, no. 12, pp. 124907, Dec. 2010

[11] ANSYS Maxwell, ver. 16, ANSYS Corporation, Pittsburgh, PA, 2013.

[12] "MagNet User's Manual," Infolytica Corp., 2008.

[13] A. Shiri and D. E. Moghadam, "Analytical and FEM based calculation of electromagnetic forces exerted on cylindrical coils due to their own current," *Applied Computational Electromagnetics Society Journal*, vol. 27, no. 11, pp. 866-872, Nov. 2012.

[14] Y. Chen and K. L. Zhang, "Electromagnetic force calculation of conductor plate double Halbach permanent magnet electrodynamic suspension," *Applied Computational Electromagnetics Society Journal*, vol. 27, no. 11, pp. 916-922, Nov. 2014.

[15] *Technical Qualification Appraisal Committee of the Weapon Industry Nondestructive Testing Personnel, The Commonly used Steel Magnetic Characteristic Curve Handbook*. China Machine Press, Beijing, 2003.

[16] M. N. Recheis, B. Schweighofer, P. Fulmek, and H. Wegleiter, "Selection of magnetic materials for bearingless high-speed mobile flywheel energy storage systems," *IEEE Transactions on Magnetics*, vol. 50, no. 4, pp. 8000604, Apr. 2014.

[17] C. T. Liu, P. C. Shih, S. C. Yen, H. N. Lin, Y. W. Hsu, and S. Y. Lin, "Theoretical and experimental investigations of the electromagnetic steel compositions for synchronous reluctance motors,"

IEEE Transactions on Industry Applications, vol. 54, no. 3, pp. 2947-2954, May/June 2018.

[18] http://www.linkjoin.com/

[19] GB/T 6893-2008, *Soft Magnetic Iron*. Beijing: Standards Press of China, 2008.

[20] GB/T 3077-2015, *Alloy Structure Steel*. Beijing: Standards Press of China, 2016.

[21] ASTM A29 /A29M 2012, *Standard Specification for Steel Bars, Carbon and Alloy, Hot-Wrought, General Requirements for, ASTM International*, West Conshohocken, PA, 2012.

[22] X. N. Liu, G. J. Yang, Y. Xu, et al., "Interference fit design for rotor components of the active magnetic bearing," *International Conference on Nuclear Engineering, Proceedings, ICONE 21st*, 2013.

[23] ANSYS Mechanical APDL, ver. 17, ANSYS Corporation, Pittsburgh, PA, 2015.

Xingnan Liu received his Ph.D. in Materials Science and Engineering at Tsinghua University in 2011. He is now working at Institute of Nuclear and New Energy Technology, Tsinghua University, Beijing, China. His researching subject includes structure design of the active magnetic bearing, magnetic field analysis, rotor dynamics, and insulation of helium gas.

Zhengang Shi received his Ph.D. in Nuclear Science and Technology at Tsinghua University in 2003. He is now working at Institute of Nuclear and New Energy Technology, Tsinghua University, Beijing, China. Shi's research subject is magnetic bearing.

Guojun Yang received his Ph.D. from the Department of Astronautic Engineering and Mechanics of Harbin Institute of Technology of China in 2001, and worked on the study of Active Magnetic Bearing at the Institute of Nuclear and New Energy Technology of Tsinghua University of China since 2001. The main research field: auxiliary bearings, rotor dynamics, and mechanical design.

Loss Calculation and Thermal Analysis of Axial AMB in HTR-PM Helium Circulator

Haoyu Zuo [1,2,3], Zhengang Shi [1,2,3], Yangbo Zheng [1,2,3], Jinpeng Yu [1,2,3], Tianpeng Fan [1,2,3], and Ni Mo [*1,2,3]

[1] Institute of Nuclear and New Energy Technology
Tsinghua University, Beijing 100084, China

[2] Collaborative Innovation Center of Advanced Nuclear Energy Technology
Tsinghua University, Beijing 100084, China

[3] The Key Laboratory of Advanced Reactor Engineering and Safety
Ministry of Education, Beijing, 100084, China
zuohy16@mails.tsinghua.edu.cn, moni@tsinghua.edu.cn*

Abstract ─ The helium circulator is one of the important components of the High Temperature Gas-cooled Reactor Pebble Bed Module (HTR-PM). It uses the electromagnetic suspension technology to support the rotor, the so-called magnetic bearing technology. Considering the performance and safety issues on the axial active magnetic bearing(AMB) caused by potential high temperature, this paper calculates copper loss, iron loss and wind loss in axial AMB and simulates temperature field under a normal operating condition, and compares the results with the experimental data.

Index Terms ─ Axial magnetic bearing, copper loss, helium circulator, iron loss, temperature field, wind loss.

I. INTRODUCTION

The HTR-PM is one of the most promising candidates for the next generation reactors. It's renowned for its inherent safety, system simplification and high power generation efficiency.

The helium circulator is the key equipment in the primary loop of the HTR-PM and installed at the output at the steam generator. It drives helium coolant with an average temperature of 750℃ to circulate in the primary loop for heat exchange released by the nuclear reaction [1]. Figure 1 shows a cross section of the HTR-PM reactor.

The rotor of helium circulator is supported by axial active magnetic bearings (AMB) instead of mechanical bearings for its excellent performance of non-contact, non-polluting and high-speed characteristics [2]. But there still exist copper loss, iron loss and wind loss in magnetic bearings, leading to an increase in temperature

and affecting the performance of the AMB system under some special conditions. Therefore, it is necessary to calculate the losses and the temperature field of the axial AMB in HTR-PM.
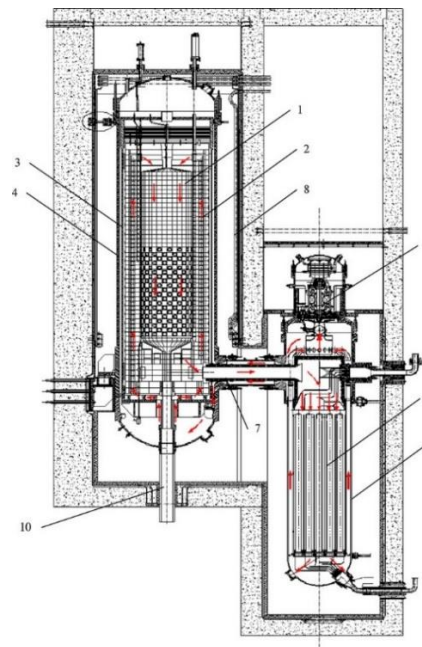

Fig. 1. Cross section of the primary loop of the HTR-PM (1. reactor core; 2. side reflector and carbon thermal shield; 3. core barrel; 4. reactor pressure vessel; 5. steam generator; 6. steam generator vessel; 7. coaxial gas duct; 8. water-cooling panel; 9. blower; 10. fuel discharging tube).

Researches have been done including theoretical and experimental studies on iron loss of laminated magnets: Karsarda proposed the calculation formulas for eddy current and hysteresis loss of laminated magnets [3-4]; Marinescu [5] discussed the possibility of calculating the eddy current loss of permanent magnet bearings in two dimensions. For solid axial bearings with a single-coil structure, Sun [6-7] proposed analytical solutions and finite element solutions for eddy current losses considering electromagnet temperature coupling.

As for the research of AMB temperature field, Sun [6-7] solved the temperature field while neglecting the wind loss and considering eddy current losses as an even distributed internal heat source in the mathematical model of the temperature field.

In this paper, based on the actual operation current data of the HTR-PM axial AMB, the losses of the axial bearing are studied. Furthermore, the temperature field is modeled and theoretically analyzed on ANSYS platform. The theoretical simulation analysis results are compared with the actual temperature data. The simulation results are in accordance with the actual operating data, which provides a theoretical model support and an effective calculation method for the subsequent optimization design of the axial AMB.

II. GEOMETRIC MODEL OF AXIAL AMB IN HTR-PM

The HTR-PM axial bearing is used to support the gravity of the rotor in the helium circulator. The rotor has a length of 3.3 meters and a mass of 4000 kg. The speed at normal operation is 4000 r/min. The structure of axial magnetic bearing is shown in Fig. 2, including 4 main sections: thrust disk, stators, coils and rotor. The parameter is shown in Table 1.
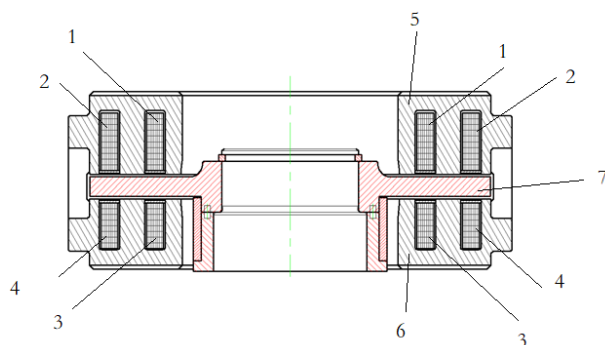

Fig. 2. Structure of the axial AMB (1. upper stator inner coil; 2. upper stator outer coil; 3. lower stator inner coil; 4. lower stator outer coil; 5. upper stator; 6. lower stator; 7. thrust disk).

Table 1: Parameters of the axial AMB

Parameter	Unit	Value
Gap between stator and rotor	mm	1
Inner magnetic pole area, A_i	mm^2	7868.8
Central magnetic pole area, A_c	mm^2	15009.2
Outer magnetic pole area, A_o	mm^2	9982.1
Trust disk diameter	mm	300
Vacuum permeability, μ_0	N/A^2	$4\pi\times10^{-7}\approx$ 1.256637×10^{-6}
Winding turns	-	78, 78

The actual HTR-PM axial bearing structure is complex. In order to save computing resources, the geometric model used in this paper simplifies the connecting nuts between the components, the chamfers, and the disassembly tooling of the thrust disk, and the windings are processed solidly. The model is shown in Fig. 3 below. The following three assumptions are the bases for the loss calculation and temperature field analysis:

(1) The eddy current has the same effect on each strand of the axial AMB, and the loss is evenly distributed on the wingdings;

(2) The temperature difference inside the bearing is not large and the radiation is neglected;

(3) The actual solid surface is ideally flat and the thermal contact resistance is ignored.
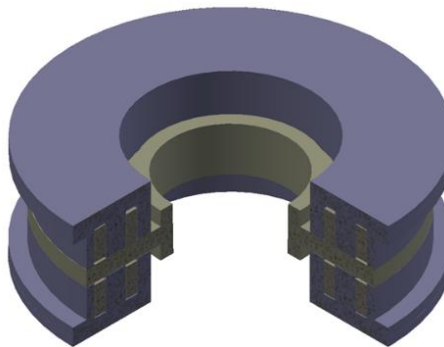

Fig. 3. Geometric model of axial AMB.

III. LOSSES CALCULATION

While the axial AMB realizes the stable support of the rotor in HTR-PM, the winding needs a large current to generate the electromagnetic force that balances the gravity and aerodynamic force of the rotor, and there will also be current fluctuations in the actual operation. During

high-speed rotating, there will be copper loss and iron loss in the stator and thrust disk, and wind loss on the surface of the thrust disk. Based on the actual operating condition and current data, the copper loss, iron loss, and wind loss of the axial AMB are analyzed.

A. Operating condition

Excluding start, shutdown and some special abnormal conditions, the HTR-PM helium circulator are usually in normal operating conditions, the following analysis and calculation are based on this condition. The operating parameters of the HTR-PM helium circulator are shown in Table 2.

Table 2: Main operating parameters of helium circulator

Parameter	Unit	Value
Medium	-	Helium
Rated speed	r/min	4000
Mass flow	kg/s	96
Inlet pressure	Mpa	7
Speed range	%	20~105
Medium density	kg/m3	6.33
Circulator chamber ambient temperature	°C	65

B. Copper loss

The gravitational force and aerodynamic force of the rotor are balanced by the electromagnetic force generated by the winding's current. The loss caused by the current passing through the winding is called the copper loss. The actual electrical parameters of the upper and lower coils are measured at 25°C and the results are shown in Table 3, and the copper loss of the axial bearings can be calculated by formula (1):

$$P_{Cu} = Ri^2. \tag{1}$$

Among them, P_{cu} is the copper loss of axial bearings in W, R is the resistance of the winding in Ω, i is the current in A.

Table 3: Resistance of axial AMB

Parameters	Unit	Value
Upper winding inner coil resistance	Ω	0.38
Upper winding outer coil resistance	Ω	0.37
Lower winding inner coil resistance	Ω	0.38
Lower winding outer coil resistance	Ω	0.37

The measured average value of the upper and lower winding currents under normal operation is 36.5A and 23.7A respectively. Through the calculation of formula (1), the copper loss during normal operation are shown in Table 4.

Table 4: Copper losses of axial AMB

Parameters	Unit	Value
Upper stator inner coil copper loss	W	506
Upper stator outer coil copper loss	W	492
Lower stator inner coil copper loss	W	213
Lower stator outer coil copper loss	W	207

C. Iron loss

The classic theory of iron loss point that iron loss can be divided into eddy current loss, hysteresis loss and other losses. Eddy current loss is the energy loss caused by the induced current generated in the conductor when it moves in a non-uniform magnetic field or is in a time-varying magnetic field. Hysteresis loss refers to the energy consumed by the hysteresis of the ferromagnetic magnet during repetitive magnetization.

Iron loss mainly exists in the stator and thrust disks of the axial AMB, which material is 40CrNiMoA soft magnetic material. Because of manufacturing processes and other reasons, axial AMB are made in solid structure, for which means the eddy current loss is relatively large compared with the hysteresis loss. Therefore, only the eddy current losses are considered in the calculation of iron loss, which can be described by equation (2):

$$p_{iron} = p_{eddy}(x, y, z). \tag{2}$$

Among them, P_{iron} is the iron loss of axial bearings in W, P_{eddy} is the eddy current loss of axial bearings in W.

In order to accurately calculate the three-dimensional distribution of the eddy current loss in the solid double-coil axial AMB, the actual speed and the current data are obtained from actual parameters under normal operating conditions as the bases of calculation.

The Fourier-transformation of the upper and lower axial bearing current data in the running state is performed, and the main frequency is extracted. The results are shown in Fig. 4 and Fig. 5, which show the actual current of the axial bearing has a significant dominant frequency of 56 Hz.
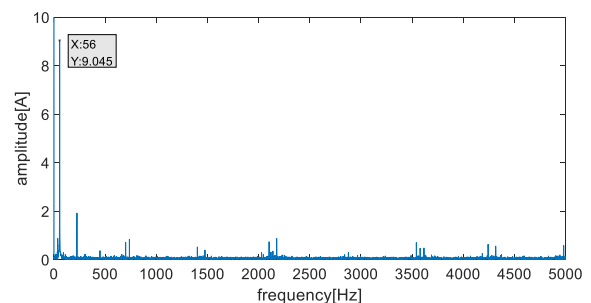

Fig. 4. Fourier Transform of upper axial AMB current.
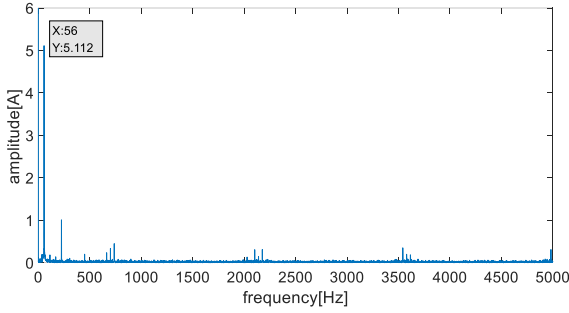
Fig. 5. Fourier Transform of lower axial AMB current.

The fitting current function and the comparison between fitting current and the actual current are shown in Table 5, Fig. 6 and Fig. 7.

Table 5: Fitted currents

| Current	Fitting Function
Upper axial AMB current	$I = 36.64 + 8.18\cos 352.2t - 18.55\sin 352.2t$
Lower axial AMB current	$I = 23.74 - 5.37\cos 353.4t - 10.13\sin 353.4t$
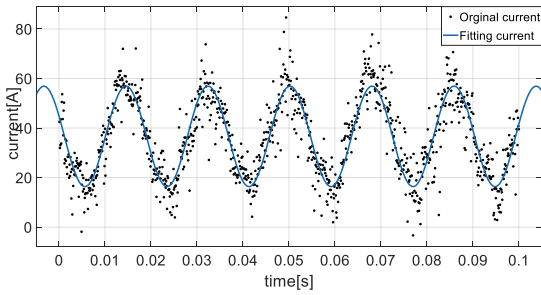
Fig. 6. Upper fitted current curve and original current.
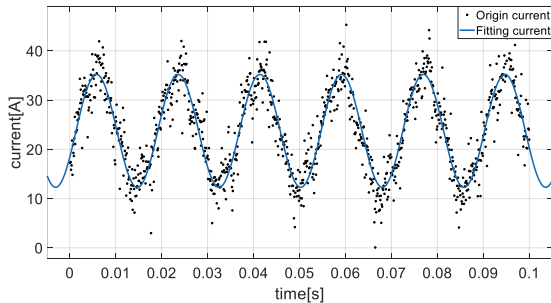
Fig. 7. Lower fitted current curve and original current.

The eddy current loss distribution of the stator and thrust disk is obtained by the finite element method. The results are shown in in Fig. 8 to Fig. 10, the eddy current loss is concentrated around the windings in the stator and concentrated on the corresponding positions of the windings on the thrust disk.
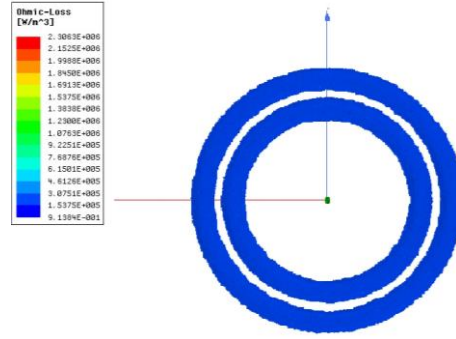
Fig. 8. Eddy current loss distribution in upper stator.
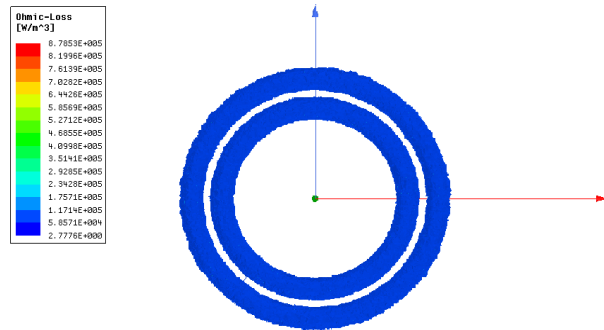
Fig. 9. Eddy current loss distribution in lower stator.
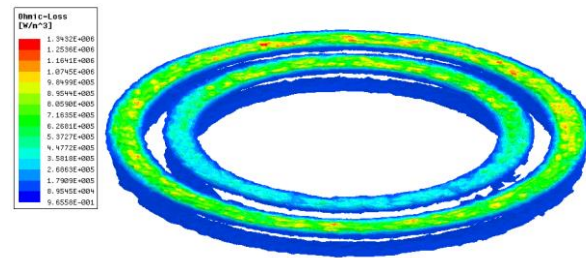
Fig. 10. Eddy current loss distribution in thrust disk.

The eddy current loss in each part is calculated as Table 6:

Table 6: Eddy current loss calculation

Part	Unit	Eddy Current Loss
Upper stator	W	2622
Lower stator	W	787
Thrust disk	W	559

D. Wind loss

As shown in Fig. 1, the high-speed rotating thrust disk is supported by the axial AMB, so there is a forced flow of gas in the air gap. The friction generated between the gas and the rotor is wind loss. Wind losses mainly exist on the disk surfaces and end surfaces of high-speed rotating thrust disks. The wind loss is not related to the electrical parameters of the axial AMB, the calculation

of the wind loss can refer to the research of the rotating machine.

End-face wind loss can be based on the empirical formula of Von Karman's plate turbulence model as formula (3):

$$P_w = [0.074 \rho_g L \pi R^4 \left(\frac{v}{2\pi R^2} \right)^{0.2}] \omega^{2.8}. \quad (3)$$

Among them, ρ_g is the density of the gas in kg/m^3, v is the kinematic viscosity of the gas in m^2/s, R is the radius of the thrust disk in m, L is the length of thrust disk in m, ω is the rotational angular velocity in rad/s.

For the disc surface, the formula for different flow patterns are proposed by Etemad [8], the formula (4) is based on the turbulence model:

$$P_w = 0.311 \left(\frac{s}{r} \right)^{-1/4} \mu^{1/4} \rho^{3/4} \omega^{11/4} r^{9/2}. \quad (4)$$

Among them, s is the air gap width in m, r is the radium of the disk in m, and μ is the dynamic viscosity of the gas in Pa·s. The calculation is measured on one side.

The parameter for wind loss calculation and results are shown in Table 7 and Table 8.

Table 7: Parameter for wind loss calculation

Parameters	Unit	Value
Ambient helium temperature	°C	65
Helium pressure	MPa	7
Helium density	kg/m^3	9.686420455
Helium dynamic viscosity	Pa·s	2.1592×10-5
Helium kinematic viscosity	m^2/s	2.2291×10-6
Radium of thrust disk, r	mm	300
Length of thrust disk, L	mm	32
Air gap width	mm	0.8
Rotational angular velocity	rad/s	418.67

Table 8: Wind loss results

Parameters	Unit	Value
Wind loss on end surface	W	1673
Wind loss on one disk surface	W	2089

E. Results analysis

Through calculation and analysis of the copper loss, iron loss and wind loss of the HTR-PM helium circulator axial AMB under normal operating conditions, the results are shown in Table 9. The total loss in the axial bearing is 9446W, among which the wind loss accounted for the largest proportion, followed by the proportion of iron loss, and the copper loss accounted for the smallest proportion. The results are in good agreement with the

actual project conditions.

Table 9: Percentage of each loss

Loss	Unit	Value	Percentage
Iron loss	W	3968	42.0%
Copper loss	W	1418	15.0%
Wind loss	W	4060	43.0%
Total loss	W	9446	100%

IV. TEMPERATURE FIELD ANALYSIS AND CALCULATION

Based on the results of the losses of the axial bearings in the HTR-PM helium circulator, the mathematical model of temperature field is established for the analysis.

A. Mathematical model of temperature field

According to the law of Fourier heat conduction, the three-dimensional steady-state temperature field of an axial AMB can be described as a differential conduction equation in Cartesian coordinates, as shown in equation (5):

$$\rho C_p \frac{\partial T}{\partial t} = \lambda \left(\frac{\partial^2 T}{\partial x^2} + \frac{\partial^2 T}{\partial y^2} + \frac{\partial^2 T}{\partial z^2} \right) + p_v. \quad (5)$$

Among them, ρ is the density in kg/m^3, C_p is the constant-pressure specific heat in J/(kg·K), λ is the thermal conductivity in W/(m·K), P_v is the inner heat source in W/m^3.

The eddy current loss is unevenly distributed, and the copper loss is evenly distributed in the conductors formed by each strand:

$$p_v = p_{eddy}(x, y, z) + p_{copper}. \quad (6)$$

The boundary conditions for the mathematical model of the temperature field include fixed heat flux and convection heat transfer boundaries:

$$q_s = const, \quad (7)$$

$$-\lambda \frac{\partial T}{\partial n} = h(T_w - T_f). \quad (8)$$

Among them, q_s is the fixed heat flux, h is the convective heat transfer coefficient.

The fixed heat flux q_s is equal to the wind loss q_w caused by the rotation in formula (3) and (4), and the convection heat transfer coefficient in formula (8) is calculated by the corresponding correlation [9].

B. Results and analysis

The temperature field results shown in Figs. 11 to 13 are obtained by solving equation (1)-(8) by the ANSYS under normal operating condition.

The temperature of the upper axial AMB is shown in the Fig. 11: axially, the temperature of the upper axial bearing increases from the surface close to the thrust disk to the surface far away from the thrust disk, because the high speed rotating causes a large forced convective heat

transfer coefficient; radially, there are relatively high temperature areas at the tooth between the two slots and outer coil, because copper loss and eddy current loss are concentrated in this location. The maximum temperature of the upper axial bearing is 75.42°C.
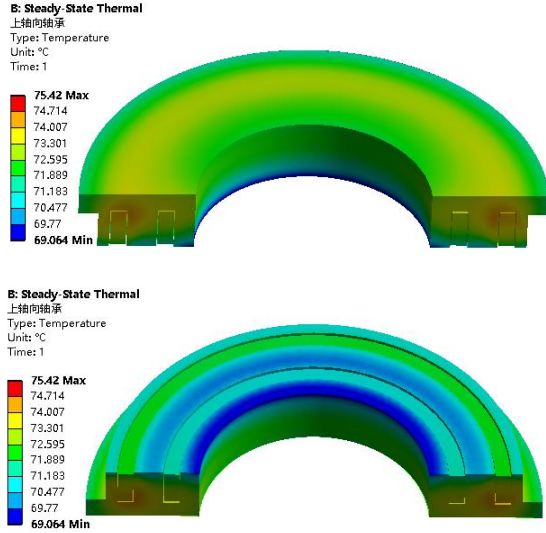

Fig. 11. Temperature field of upper Axial AMB.

The temperature field of the lower axial AMB is shown in the Fig. 12: the lower axial bearing have a similar temperature gradient distribution with the upper axial bearing. Because the lower axial bearing generates less copper loss and iron loss compared to the upper one, the temperature is slightly lower and the maximum temperature of the lower axial bearing is 71.56°C.
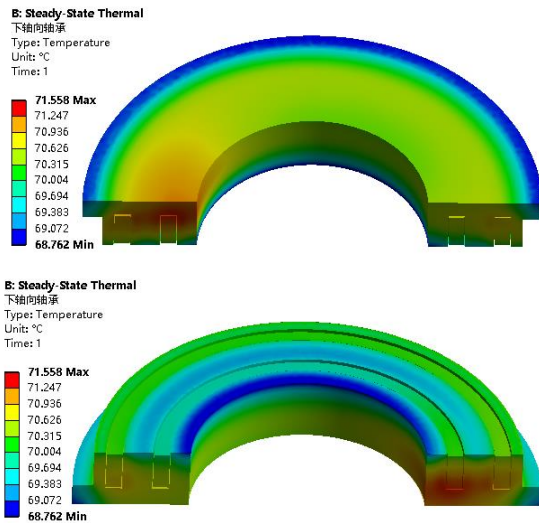

Fig. 12. Temperature field of lower Axial AMB.

The temperature field of the thrust disk is shown in

the Fig. 13. The average temperature of the upper surface of the thrust plate is higher than the lower surface, and due to the distribution of iron loss on the surface of the thrust plate, there are obvious high temperature areas on the upper and lower surfaces of the thrust disk. The high temperature areas are mainly concentrated on the thrust disk surface facing the coils on the stator, which is about 2°C higher than the average temperature on the surface. The maximum temperature of the thrust disk is 75.46°C.
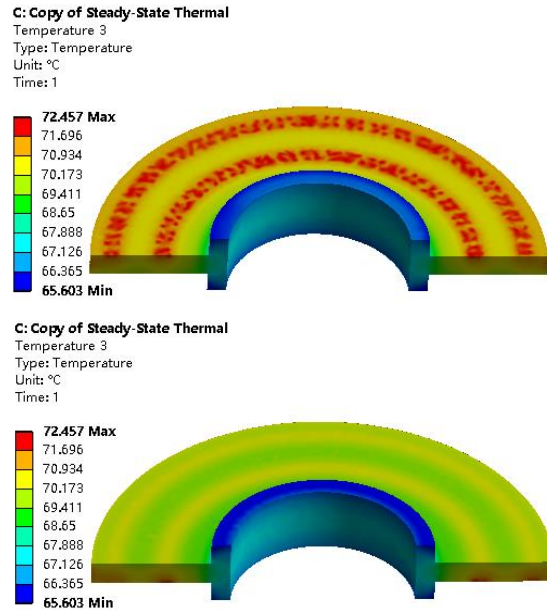
Fig. 13. Temperature field of thrust disk.

Four test points are arranged near the inner and outer coils of the upper and lower axial AMB of the helium circulator, and the speed of the rotor during experiment is 3710r/min.

The test point temperature under the test condition and the maximum temperature in the calculation are shown in Table 10, both are below the allowable temperature limitation 150°C.

Table 10: Comparison of simulation and experimental results

Measuring Point	Experiment Results/°C	Calculation Results/°C (Maximum)	Relative Error/%
Upper axial AMB inner coil temperature	85.0	75.4	-11.08%
Upper axial AMB outer coil temperature	82.6	74.0	-10.41%

There is certain error between the experimental results and the calculation results. The main reasons for

the are as follows:

(1) Windings are affected by factors such as the outsourcing insulating varnish, and the actual windings are different from solid copper which assumed in this article.

(2) When considering the copper loss, the effect of temperature increase on the resistance is ignored.

(3) The corresponding convective heat transfer coefficient at a specific location is inconsistent with the actual situation. Therefore, the calculation results will deviate from the actual situation.

V. CONCLUSION

(1) The article calculates the loss of the axial AMB of the HTR-PM helium circulator under the normal operating condition. The results show that there are concentrated areas of eddy current loss on the stator and the thrust disk, and the wind loss of the axial AMB can't be ignored.

(2) In this paper, ANSYS is used to calculate the steady-state temperature field of the axial AMB in HTR-PM helium circulator under normal operation, the results show that the temperature is below the allowable temperature limitation. Comparing with the results of field tests, the calculated results are basically consistent with the experimental results, which show the correctness of the model and method, and thus can provide a reliable basis for the design of an axial AMB in helium circulation.

(3) From the simulation results, it can be seen that the upper stator temperature is higher than the lower stator temperature, the temperature is higher in the area where iron loss concentrates inside the axial bearing stator. There is also a higher temperature area where the iron loss concentrates on the surface of the thrust disk.

ACKNOWLEDGMENT

REFERENCES

[1] Y. Zheng, J. Lapins, E. Laurien, L. Shi, and Z. Zhang, "Thermal hydraulic analysis of a pebble-bed modular high temperature gas-cooled reactor with attica3d and thermix codes," *Nuclear Engineering and Design*, 246 (2012/05/01/2012): 286-97.

[2] G. Yang, S. Zhengang, and Ni Mo, "Technical design and engineering prototype experiment of active magnetic bearing for helium blower of Htr-Pm," *Annals of Nuclear Energy*, 71 (2014/09/01/2014): 103-10.

[3] M. E. F. Kasarda, P. E. Allaire, E. H. Maslen, et al., "High-speed rotor losses in a radial eight-pole magnetic bearing: Part 1-Experimental measure-ment," *ASME J. Eng. Gas Turbines Power*, vol. 120, pp. 110-114, Jan. 1998.

[4] M. E. F. Kasarda, P. E. Allaire, E. H. Maslen, et al., "High-speed rotor losses in a radial eight-pole magnetic bearing: Part 2-Analytical/empirical models and calculations," *ASME J. Eng. Gas Turbines Power*, vol. 120, pp. 110-114, Jan. 1998.

[5] M. Marinescu, N. Marinescu, and W. Bernreuther, "A 2-D treatment of the eddy currents induced by transversal oscillations of permanent magnet rings in conducting axisymmetric plates," *IEEE Transactions on Magnetics*, vol. 28, no. 2, pp. 1386-89, 1992.

[6] S. Shouqun, G. Haipeng, and G Keqian, 'Transient temperature field in active thrust magnetic bearing," *Chinese Journal of Mechanical Engineering*, no. 04, pp. 575-78, 2005.

[7] S. Shouquan and Z. Guoquan, "Analysis of eddy current loss inthrust magnetic bearing considering electormagento temperature coupling," *University of Shanghai for Science and Technology*, no. 03, pp. 194-97+202, 2005. (In Chinese).

[8] M. R. Etemad, K. Pullen, C. B. Besant, et al., "Evaluation of windage losses for high-speed disc machinery," *Proc. Instn. Mech. Engrs.*, vol. 206, pp. 149-157, 1992.

[9] I. Shevchuk, "Convective heat and mass transfer in rotating disk systems," vol. 45, 2009. doi:10.1007/978-3-642-00718-7.

Haoyu Zuo graduated from Power Engineering Department of North China Electric Power University, and now is a second year Master candidate in Institute of Nuclear and New Energy Technology of Tsinghua University. His main research is loss calculation and temperature analysis in helium circulator.

Zhengang Shi received his Ph.D. in Nuclear Science & Technology at Tsinghua University in 2003. He is now working at Institute of Nuclear and New Energy Technology, Tsinghua University, Beijing, China. Shi's research subject is magnetic bearing.

Theory and Simulation of Linearized Force Coefficients for Active Magnetic Bearings with Multiple Magnetic Poles

Tianpeng Fan [1,2,3], Jinpeng Yu [1,2,3], Zhe Sun[*1,2,3], Xingnan Liu [1,2,3], Xiaoshen Zhang [1,2,3], Jingjing Zhao [1,2,3], Xunshi Yan [1,2,3], Haoyu Zuo [1,2,3], and Zhengang Shi [1,2,3]

[1] Institute of Nuclear and New Energy Technology of Tsinghua University
[2] Collaborative Innovation Center of Advanced Nuclear Energy Technology
[3] Key Laboratory of Advanced Reactor Engineering and Safety of Ministry of Education
Beijing, 100084, China
ftp16@mails.tsinghua.edu.cn, sun_zhe@mail.tsinghua.edu.cn*

Abstract ─ Active magnetic bearing (AMB) is a kind of typical mechatronic product which is widely used due to its high performance. Since the electromagnetic force is strongly nonlinear, the force-displacement coefficient and the force-current coefficient need to be linearized in the process of controlling the AMB. This paper analyzes the three most common magnetic bearings and gives their linearized force formulas. Simulations show that the formulas have high precision. In addition, the source of errors is also analyzed in this paper.

Index Terms ─ Active magnetic bearing, ANSYS Maxwell simulation, error analysis, force coefficient, multiple magnetic poles.

I. INTRODUCTION

Industrially, active magnetic bearings have been widely used because of the excellent properties, such as high speed, long system life, adaptability to extreme temperature and corrosion condition [1]. Nevertheless, due to the open-loop instability and multiple nonlinearities of the AMB system, applicable feedback is required making the rotor stable to operate [2]. In the control process, the force-current coefficient and force-displacement coefficient of the bearing are very important quantities, which directly affect the control accuracy and system performance.

For the magnetic bearing with eight magnetic poles, Schweitzer et al. gave the linearization formula [3]. This formula is widely accepted, for example in [4,5]. But in this paper, a more accurate coefficient including an extra angle factor is given. Three types of magnetic bearings researched in this paper were introduced in [6], but corresponding linearization results were not given. In [7], the force-current coefficient of a 16-pole magnetic bearing was analyzed and the result was verified experimentally. Unlike the arc-shaped magnetic pole surface in this paper, in [8], the magnetic pole surface is considered to be plane, which will introduce an additional angle factor. For the papers mentioned above, there is no complete set of unified formulas for the magnetic bearings of each structure. Especially for magnetic bearings with different magnetic pole structures and distributions, the amount of air gap changes between the rotor and the stator are not the same as the rotor moves, resulting in a more complex formula for the linearized force.

This paper gives the linearization results of the AMB force including the bearings with eight, twelve, and sixteen magnetic poles, and carries out simulation verification using ANSYS Maxwell model. Material saturation, hysteresis, and magnetic leakage have all been ignored, and a new linear material has been set up to represent the main characteristics of the rotor and stator. This paper illustrates that for a particular structure of a magnetic bearing, its force-displacement coefficient and force-current coefficient can be calculated according to the formulas given in this paper. The simulation results show that these formulas have higher accuracy. Moreover, it should be noted that the model and theoretical calculations are obtained under very ideal conditions. However, for actual magnetic bearing models, the results obtained in this paper can be concluded that the factors neglected in this paper have little influence on the accuracy of magnetic bearing force calculation. The formulas in this paper can reflect the main aspects. Therefore, the formulas and the modeling method proposed in this paper have remarkable meaning and can be used to solve engineering problems, such as the control of unbalancing rotor and the coaxiality detection of the AMB system.

This paper consists of five sections. Section 2 gives the formulas for electromagnetic force linearization. Section 3 analyzes the two kinds of force coefficients of three types of magnetic bearings respectively. Section 4 analyzes the source of errors for linearization forces. Section 5 is the conclusion.

II. LINEARIZED MAGNETIC FORCE FORMULA

Figure 1 is the schematic diagram of a couple of magnetic poles and a rotor. For a magnetic bearing, the force between the rotor and the stator depends on the magnetic induction in the air gap, which is generated by the current in the coil [9]. The two magnetic poles are respectively enwound with coils of different directions to form a closed magnetic field in the rotor, magnetic poles, and the air gaps, which generate force effect to the rotor.
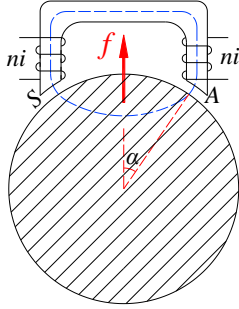

Fig. 1. A couple of magnetic poles and a rotor.

According to [3], the force generated by a couple of magnetic poles can be expressed as follows:

$$f = k\frac{i^2}{s^2}\cos\alpha , \qquad (1)$$

where i is the coil current, s the air gap width between the magnetic pole and the rotor, α the angle between the magnetic pole center and the vertical direction, k the intermediate quantity including the vacuum permeability μ_0, the number of turns n of the coil, and the area A of the magnetic pole. For the magnetic bearing of this structure, $k=\mu_0 n^2 A$, $\mu_0 =4\pi\times10^{-7}$ N·A^{-2}.

Suppose the initial distance between the rotor and the magnetic pole is s_0. When the rotor moves up a distance x, the distance between the magnetic pole and the rotor is shortened to $s_0-x\cos\alpha$. Notice that the vertical direction is defined as x direction in this paper and only the vertical rotor displacement is discussed. An identical couple of magnetic poles is located at the lower symmetrical side of the rotor. The upper and lower magnetic poles adopt a differential driving mode. The current flowing through the coil is composed of bias current i_0 and control current i_x. Therefore, the resultant force in the vertical direction is:

$$f = k\left(\frac{(i_0+i_x)^2}{(s_0-x\cos\alpha)^2}-\frac{(i_0-i_x)^2}{(s_0+x\cos\alpha)^2}\right)\cos\alpha . \qquad (2)$$

According to the Taylor formula for the multivariate function, we have:

$$f = f(i_0,s_0)+f_i'(i_0,s_0)(i-i_0)+f_x'(i_0,s_0)(s-s_0)+\cdots .(3)$$

After eliminating high-order terms, the formula

becomes:

$$f_+ =k\left(\frac{i_0^2}{s_0^2}+\frac{2i_0}{s_0^2}\cdot i_x+\frac{2i_0^2}{s_0^3}\cos\alpha\cdot x\right)\cos\alpha , \qquad (4)$$

$$f_- = k\left(\frac{i_0^2}{s_0^2}+\frac{2i_0}{s_0^2}\cdot(-i_x)+\left(-\frac{2i_0^2}{s_0^3}\cos\alpha\right)\cdot x\right)\cos\alpha . \qquad (5)$$

Then,

$$f = \frac{4ki_0}{s_0^2}\cos\alpha\cdot i_x+\frac{4ki_0^2}{s_0^3}\cos^2\alpha\cdot x , \qquad (6)$$

where the force-current coefficient and force-displacement coefficient are:

$$k_i = \frac{4ki_0}{s_0^2}\cos\alpha,\ k_x = \frac{4ki_0^2}{s_0^3}\cos^2\alpha . \qquad (7)$$

III. ANALYSIS OF DIVERSE BEARINGS

A. Bearing with eight magnetic poles

Figure 2 is the schematic diagram of the force of magnetic bearing with eight magnetic poles, where the rotor displacement and control current are drawn in one picture. For the sake of clarity, the air gaps between the rotor and the magnetic poles are abnormally amplified while the practical air gaps are usually in the millimeter order of magnitude. Such an alteration has a significant influence on the calculation accuracy, which will be explained in the following section.
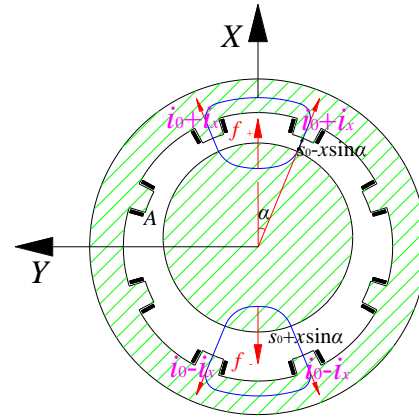
Fig. 2. Force schematic of bearing with eight poles.

A two-dimensional ANSYS Maxwell model is built, as shown in Fig. 3. In the model, the rotor radius is 104 mm, the air gap is 1 mm, the angle of magnetic pole with respect to the rotor center is 11°, α=22.5°. There is a coil enwinding on each of the magnetic poles to supply the current. For a two-dimensional figure, the width of a magnetic pole represents area A, because the axial length is set to 1m by default. So, the magnetic pole area is:

$$A = \alpha r = \frac{11^\circ}{180^\circ}\pi\cdot0.105 \approx 0.0202\text{m}^2 . \qquad (8)$$

A new material, Steel_1, with relative permeability and bulk conductivity of 10,000 and 2,000,000 S·m^{-1}, respectively, is provided, and the material of stator and rotor is set to this "new" material. The N-pole and S-pole of magnetic poles can be altered by setting the winding direction of the coil so each of the two pairs of magnetic poles in the vertical direction can form a closed magnetic field to generate force to the rotor.
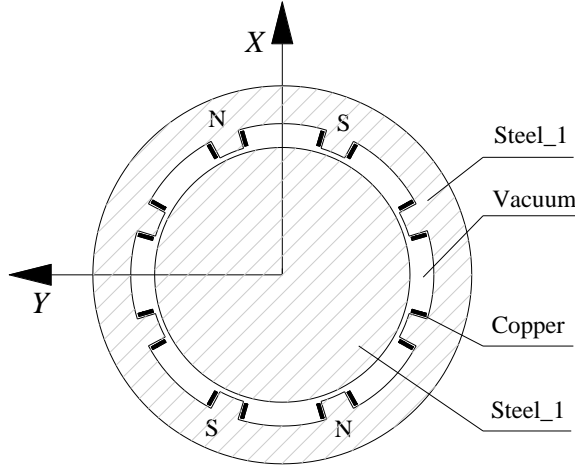
Fig. 3. ANSYS Maxwell model of eight-pole bearing.

Consider the two coefficients separately, i.e., when calculating the force-current coefficient, let $x=0$; when calculating the force-displacement coefficient, let $i_x=0$. For the sake of simplicity, only the vertical direction is considered, so two pairs of magnetic poles in the horizontal direction do not supply current. The maximum length of the grid in the model is limited to 1mm, and other parameters are set to default.

1) Force-current coefficient
Take $n=100$, $i_0=5$A, $i_x=0.1$A, so in Maxwell $NI_U=n\cdot(i_0+i_x)=510$A, $NI_D=n\cdot(i_0+i_x)=490$A; $x=0$. The theoretical value and the calculation result are 469.04N and 474.03N respectively, which the error is 1.06%.

2) Force-displacement coefficient
Take $n=100$, $i_0=5$A, $x=0.1$mm, so in Maxwell $NI_U=NI_D=n\cdot i_0=500$A. The theoretical value and the calculation result are 2167N and 2178N respectively, which the error is 0.51%.

B. Bearing with twelve magnetic poles
Figure 4 is the schematic diagram of the force of magnetic bearing with twelve magnetic poles where the angles of large and small magnetic poles are $\theta_L=30°$ and $\theta_S=15°$ respectively, and the angle between two magnetic poles is $\theta_A=10°$.
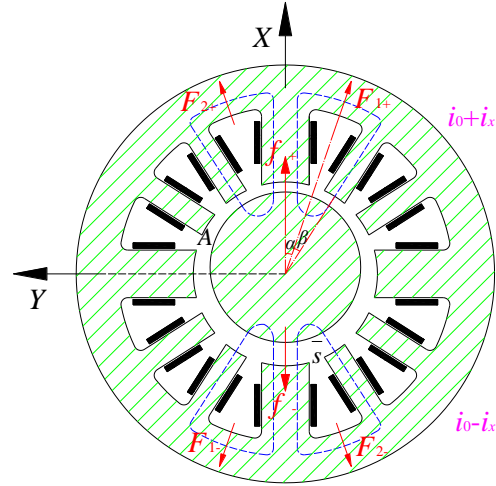

Fig. 4. Force schematic of bearing with twelve poles.

In ANSYS Maxwell model, the radius of the rotor is 109mm and the air gap is 1mm. As shown in Fig. 4, half of a large magnetic pole and a small magnetic pole generate a complete magnetic field, so A is the area of a small magnetic pole whose value is:

$$A = \alpha r = \frac{15°}{180°}\pi \cdot 0.11 \approx 0.0288 \text{m}^2 . \qquad (9)$$

The calculation of the coefficients should be divided into two steps. In the first step, a small magnetic pole and half of a large magnetic pole generate forces F_1 and F_2; in the second step, F_1 and F_2 are merged into a vertical force F.

Unlike the bearing with eight magnetic poles, the changes in the air gaps at the large and small magnetic poles are not the same when the rotor moves. When there is a displacement x of the rotor in the vertical direction, the average air gaps for large and small poles are $s_1=s_0\pm x\cdot\cos(\theta_L/4)$ and $s_2=s_0\pm x\cdot\cos(\theta_L/2+\theta_A+\theta_S/2)$ respectively. Hence, for a complete magnetic circuit, the average air gap is:

$$\bar{s} = s_0 \pm \frac{x}{2}\left(\cos\frac{\theta_L}{4} + \cos\left(\frac{\theta_L}{2} + \theta_A + \frac{\theta_S}{2}\right)\right) \qquad (10)$$
$$= s_0 \pm x\cos\alpha\cos\beta.$$

Then F_1 or F_2, whose direction has an angle α with the vertical axis is:

$$f = k\left(\frac{(i_0+i_x)^2}{(s_0 - x\cos\alpha\cos\beta)^2} - \frac{(i_0-i_x)^2}{(s_0 + x\cos\alpha\cos\beta)^2}\right)\cos\beta .(11)$$

According to the Taylor formula, we have:

$$f = \frac{4ki_0}{s_0^2}\cos\beta\cdot i_x + \frac{4ki_0^2}{s_0^3}\cos^2\beta\cos\alpha\cdot x , \qquad (12)$$

where the force-current coefficient is the same as the previously obtained one while the force-displacement

coefficient contains an extra cosα. The ANSYS Maxwell model is shown in Fig. 5.
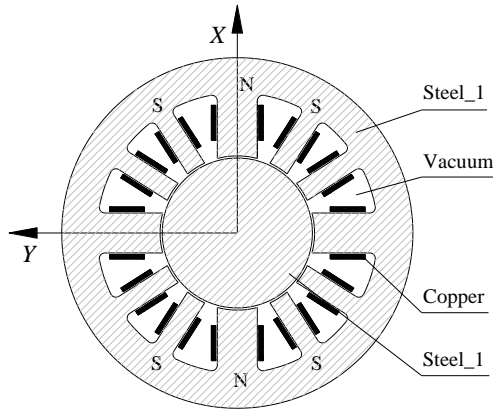
Fig. 5. ANSYS Maxwell model of twelve-pole bearing.

1) Force-current coefficient
Take n=100, i_0=5A, i_x=0.1A, so in Maxwell NI_U=$n\cdot(i_0+i_x)$=510A, NI_D= $n\cdot(i_0+i_x)$=490A; x=0. The theoretical value and the calculation result are 1328.0N and 1310.7N respectively, which the error is 1.30%.

2) Force-displacement coefficient
Take n=100, i_0=5A, x=0.1mm, so in Maxwell NI_U=NI_D=$n\cdot i_0$=500A. The theoretical value and the calculation result are 6090.0N and 5998.4N respectively, which the error is 1.50%.

C. Bearing with sixteen magnetic poles
Figure 6 is the schematic diagram of the force of magnetic bearing with sixteen magnetic poles, where the angles of large and small magnetic poles are θ_L=18° and θ_S=9° respectively, and the angle between two magnetic poles is θ_A=9°. Hence, β=0.5×($\theta_S+\theta_A$)=9°, α=$\theta_L+\theta_A$=27°.
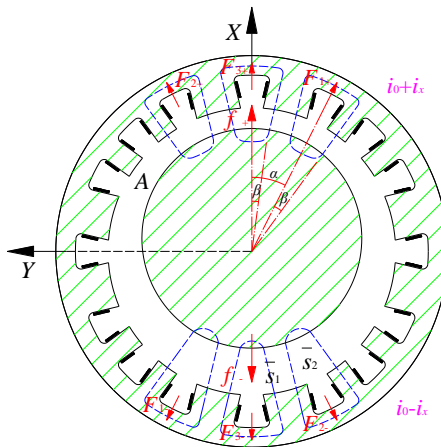

Fig. 6. Force schematic of bearing with sixteen poles.

As shown in Fig. 6, the force generated by the bearing with 16 magnetic poles consists of two parts: half of a large magnetic pole and one small magnetic pole form two magnetic fields, and the direction of the force between its direction and the vertical axis is α; two halves of the two large magnetic poles form another magnetic field. The total force is the superposition of the three.

In ANSYS Maxwell model, the radius of the rotor is 109mm and the air gap is 1mm. A is the area of a small magnetic pole whose value is approximate 0.0173m^2.

The calculation of the coefficients should be divided into three steps. In the first step, a small magnetic pole and half of a large magnetic pole generate a pair of forces F_1 and F_2; in the second step, two halves of the two large magnetic poles generate F_3; in the third step, F_1, F_2, and F_3 generate a vertical force F. Fig. 7 is the ANSYS Maxwell model.
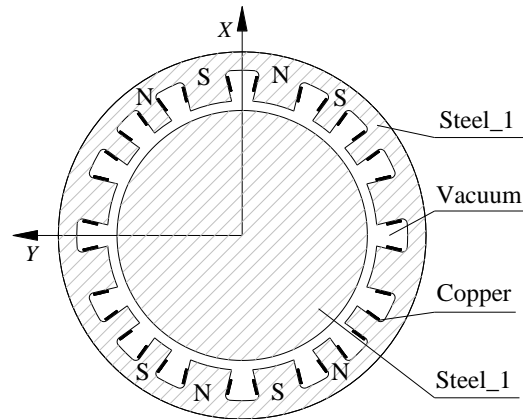
Fig. 7. ANSYS Maxwell model of sixteen-pole bearing.

1) Force-current coefficient
Take n=100, i_0=5A, i_x=0.1A, so in Maxwell NI_U=$n\cdot(i_0+i_x)$=510A, NI_D= $n\cdot(i_0+i_x)$=490A; x=0. Then,

$$F_1 = F_2 = F_3 = \frac{4\mu_0 n^2 A i_0}{s_0^2}\cos\beta\cdot i_x, \quad (13)$$

$$f=(F_1+F_2)\cos\alpha+F_3. \quad (14)$$

The theoretical value and the calculation result are 1328.0N and 1310.7N respectively, which the error is 1.30%.

2) Force-displacement coefficient
Similar to the bearing with 12 poles, when the rotor has a displacement x in the vertical direction, the changes in the air gap at different poles are different. For the middle magnetic circuit, the average air gap is $\bar{s}_1 = s_0 \pm x\cos\beta$. For the magnetic circuit on both sides, the average air gap of large magnetic poles is s_{2L}=$s_0\pm x\cos(\alpha-\theta_A/2-\theta_L/4)$, and the average air gap of

small magnetic poles is $s_{2S}=s_0\pm x\cos(\alpha+\beta)$; therefore, the average air gap:

$$\bar{s}_2 = s_0 \pm \frac{x}{2}\left(\cos\left(\alpha - \frac{\theta_A}{2} - \frac{\theta_L}{4}\right) + \cos(\alpha + \beta)\right) \quad (15)$$
$$= s_0 \pm x\cos\alpha\cos\beta$$

Analogy available, when $i_x=0$, take $n=100$, $i_0=5$A, $x=0.1$mm, so in Maxwell $NI_U=NI_D=n\cdot i_0=500$A. Then,

$$F_1 = F_2 = \frac{4ki_0^2}{s_0^3}\cos^2\beta\cos\alpha\cdot x, \quad (16)$$

$$F_3 = \frac{4ki_0^2}{s_0^3}\cos^2\beta\cdot x, \quad (17)$$

$$f=(F_1+F_2)\cos\alpha+F_3. \quad (18)$$

The theoretical value and the calculation result are 5488.1N and 5569.2N respectively, which the error is 1.5%.

IV. ERROR ANALYSIS

A. Air gap

The air gap is an important parameter of the magnetic bearing. Hence, the influence of the air gap on the computational accuracy is taken into considered. In theory, the larger the air gap and the smaller the rotor displacement, the better the linearization of the model, and the more accurate the theoretical and computational results. However, several air gap values are given and it is found that this was not the case.

Taking a bearing with twelve poles as an example, in the simulation, the air gap value is adjusted by changing the radius of the rotor. Ten simulations are performed, where $n=100$ and $i_0=5$A. Table 1 gives the comparison of theoretical and ANSYS results. In this section, theoretical value T is regarded as the true value and error e represents the degree of deviation of ANSYS result C, i.e., $e=(T-A)/T\times100\%$, which e might be positive or negative.

Table 1: Effect of air gap on calculation error of 12-pole bearing

Air Gap	k_x ($x=0.1$mm, $i_x=0$)			k_i ($i_x=0.1$A, $x=0$)		
	Theory/N	ANSYS/N	Error	Theory/N	ANSYS/N	Error
1mm	6090.0	5998.4	-1.50%	1328.0	1310.7	-1.30%
2mm	761.25	769.27	1.05%	332	338.71	2.02%
3mm	225.56	232.28	2.98%	147.56	153.09	3.75%
4mm	95.16	99.453	4.51%	83	86.856	4.65%
5mm	48.72	51.519	5.75%	53.12	55.743	4.97%
6mm	28.194	30.098	6.75%	36.889	38.637	4.74%
7mm	17.755	19.097	7.56%	27.102	28.227	4.15%
8mm	11.895	12.826	7.83%	20.75	21.418	3.22%
9mm	8.3539	9.0675	8.54%	16.395	16.723	2.00%
10mm	6.0900	6.6234	8.76%	13.28	13.351	0.53%

The two types of errors are plotted in a graph, and the trends can be seen, as shown in Fig. 8.

From Fig. 8, we can see that for the force-displacement coefficient, the error has a significant upward trend with the increase of the air gap value. This is probably because when the air gap is too large, part of the magnetic induction lines will close directly through the vacuum between the magnetic poles without passing through the rotor. However, for the force-current coefficient, the error first increases to a maximal value, and then decreases as the air gap increases. The increasing trend of force-current error has the same reason with force-displacement error. However, as the air gap continues to increase, the total amount of magnetic induction lines passing through the rotor decreases, resulting in a significant drop in force. Moreover, the residual magnetic induction lines are sparser. Therefore, the proportion of the residual magnetic induction line that does not pass through the rotor reduces, which reduces the error. It also can be seen that too small air gap does not improve the calculation accuracy.
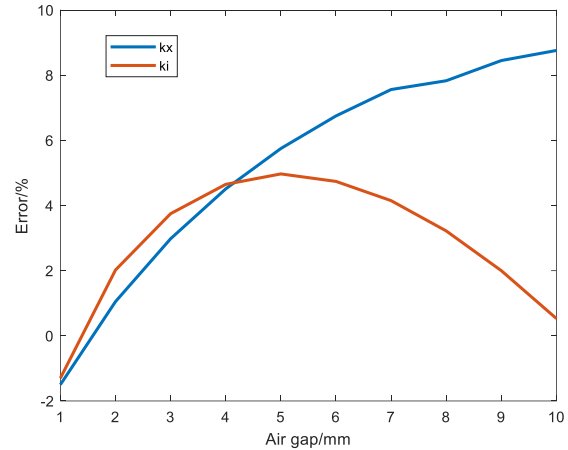

Fig. 8. Effect of air gap on errors of k_i and k_x.

However, the air gap width in this paper is not universal for all magnetic bearings, because for larger bearings, the tolerable air gap values become

correspondingly larger. For the twelve-pole bearing in this paper, the circumferential distance of the two poles at the air gap is 0.0288m. As can be seen from the figure, when the air gap value is 1.5mm, the errors are small. A general ratio $\delta=s_0/l$ can be defined for the air gap s_0 and the partial circumferential distance l between two poles at the air gap. In this paper, the ratio of the two is 5.2%. Therefore, in order to ensure good computational accuracy, it is recommended that the δ not be larger than 5% to ensure both types of errors are close to zero.

B. Rotor displacement

Obviously, as the rotor displacement increases, the linearization formulas will no longer be accurate. For this reason, the scope of application of the force-displacement formulas is studied in this paper. From Section 4.A, taking 12 magnetic-pole bearing as an example, take the air gap as 1.5mm, $n=100$, $i_0=5A$, and analyze the force-displacement coefficient computational accuracy. The rotor displacements, theoretical and ANSYS results are listed in Table 2. The error trend is shown in Fig. 9.

Table 2: Effect of rotor displacement on calculation error of 12-pole bearing

| Rotor Displacement	Theory/N	ANSYS/N	Error	Rotor Displacement	Theory/N	ANSYS/N	Error
0.025mm	451.11	447.32	-0.84	0.3mm	5413.3	5742.4	6.08
0.05mm	902.22	895.95	-0.70	0.4mm	7217.8	8084.9	12.0
0.075mm	1353.3	1347.1	-0.46	0.5mm	9022	10864	20.4
0.1mm	1804	1802	-0.11	0.6mm	10827	14298	32.1
0.125mm	2255.6	2261.9	0.28	0.7mm	12631	18718	48.2
0.15mm	2706.7	2728.3	0.80	0.8mm	14436	24661	70.9
0.175mm	3157.8	3202.4	1.41	0.9mm	16240	33054	104
0.2mm	3608.9	3685.7	2.13	1mm	18044	45621	153
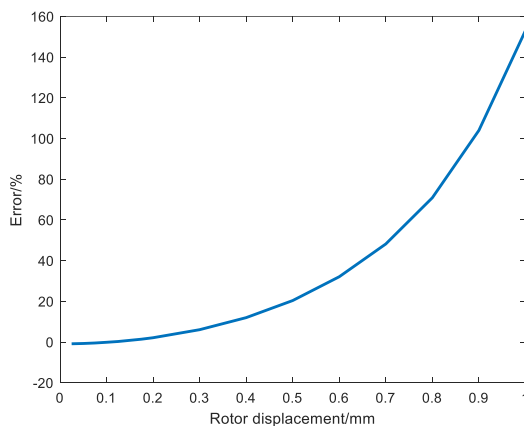
Fig. 9. Effect of rotor displacement on error of k_x.

From the table, it can be seen that when the rotor displacement exceeds 0.3 mm, the error will be greater than 6% and will increase sharply as the rotor displacement increases. Define a general ratio $\varepsilon=x/s_0$ for the rotor displacement x and air gap width s_0. In this paper, it can be considered that the linearization formula has an effective ε limit of 20%. Hence, for all sizes of bearings, the rotor displacement coefficient ε should not exceed this value.

V. CONCLUSION

In this paper, the linearized force-current and force-displacement formulas of magnetic bearings with eight, twelve, and sixteen poles are given. Simulation shows that the linearized formulas has high accuracy. The work in this paper shows that for some magnetic bearings of specific structures, the linearized coefficients can be accurately calculated based on their parameters. The source of errors is also analyzed and two referenced parameters are given to meet the engineering needs.

REFERENCES

[1] S. E. Mushi, Z. Lin, and P. E. Allaire, "Design, construction, and modeling of a flexible rotor active magnetic bearing test rig," *IEEE/ASME Transactions on Mechatronics*, vol. 17, no. 6, pp. 1170-1182, 2012.

[2] J. Witte, H. M. N. K. Balini, and C. W. Scherer, "Experimental results with stable and unstable LPV controllers for active magnetic bearing systems," *IEEE International Conference on Control Applications IEEE*, pp. 950-955, 2010.

[3] G. Schweitzer and E. H. Maslen, *Magnetic Bearings: Theory, Design, & Application to Rotating Machinery*. 2009.

[4] W de Boer, *Active Magnetic Bearings: Modelling & Control of a Five Degrees of Freedom Rotor*. Diss. Eindhoven University of Technology, 1998.

[5] Y. A. Amer and U. H. Hegazy, "Resonance behavior of a rotor-active magnetic bearing with time-varying stiffness," *Chaos, Solitons & Fractals*, vol. 34, no. 4, pp. 1328-1345, 2007.

[6] S. Bouaziz, et al., "A theoretical model for analyzing the dynamic behavior of a misaligned rotor with

active magnetic bearings," *Mechatronics*, vol. 21, no. 6, pp. 899-907, 2011.

[7] X. Zhang, et al., "Force-current factor investigation of a radial active magnetic bearing with large load capacity," *Transportation Electrification Asia-Pacific (ITEC Asia-Pacific), 2014 IEEE Conference and Expo. IEEE*, 2014.

[8] J. C. Ji and C. H. Hansen, "Non-linear oscillations of a rotor in active magnetic bearings," *Journal of Sound and Vibration*, vol. 240, no. 4, pp. 599-612, 2001.

[9] M. Autila, E. Lantto, and A. Arkkio, "Determination of forces and linearized parameters of radial active magnetic bearings by finite element technique," *IEEE Transactions on Magnetics*, vol. 34, no. 3, pp. 684-694, 1998.

Jinpeng Yu received his B.Sc. degree in 2015 from Dalian University of Technology. Now he is studying for a Ph.D. at the Institute of Nuclear and New Energy Technology, Tsinghua University. He is mainly engaged in active magnetic bearing and its application in flywheel system.

Tianpeng Fan (1993.07-) received his bachelor's degree in Engineering in 2016 from School of Energy Science and Engineering of Harbin Institute of Technology, Harbin. He is studying for a Master's degree in the Institute of Nuclear and New Energy Technology, Tsinghua University. His research interests are unbalance control of rotor and system identification.

Disturbance Rejection for a Zero-bias Controlled Active Magnetic Bearing Based on Disturbance Observer and Notch Filter

Hai Rong and Kai Zhou

Department of Mechanical Engineering
Tsinghua University, Beijing, 100084, China
rongh14@mails.tsinghua.edu.cn, zhoukai@mail.tsinghua.edu.cn

Abstract ─ This paper introduces a nonlinear disturbance observer plus general notch filter based zero-bias control strategy to handle disturbance and reduce power consumption for the radial magnetic bearing in the magnetically suspended spindle. The zero-bias control is used to decrease the power consumption of magnetic bearings, as large power consumption causes temperature rise of system and temperature drift of sensor. The suspension of the rotor is affected by complicated disturbance including non-periodic and periodic disturbance. In order to reduce the deviation of rotor brought by external disturbance, the nonlinear disturbance observer is used. However, since the response lag to the disturbance, the nonlinear disturbance observer cannot suppress the periodic imbalance force well. Therefore, the general notch filter is introduced to reduce the periodic vibration. The effectiveness on the disturbance suppression and power reduction of the proposed method is verified by experiment results.

Index Terms ─ Active magnetic bearing, disturbance rejection, general notch filter, nonlinear disturbance observer, zero-bias control.

I. INTRODUCTION

As well known, one of the main characteristics of active magnetic bearing (AMB) system is nonlinearity [1–5]. The conventional bias controlled way to handle the high nonlinearity is using the Taylor series expansion to linearize it [1], however, constant bias current is generated. Generally, large bias current is set to improve the stiffness, which causes large copper and eddy current losses, brings the temperature rise of system and temperature drift of sensors [6]. The zero-bias current control algorithm has been proposed to reduce the power consumption of the AMB [7–10]. Sivrioglu adopted the zero-bias control method in the control of a magnetic suspension flywheel [7]. However, the controller is much difficult to design for the zero-bias current control as the system nonlinearity. One linear control structure for a cascaded position-flux controller operating at zero bias is proposed [8], which uses a flux observer to estimate the flux state. A cascaded position-force controller structure is proposed to control the AMB under zero-bias, which means the position controller can use any linear or nonlinear control strategies, and applications adopting the linear algorithms such as H∞ control [10] can be found in the literature, however, no complicated disturbance is considered.

The suspension of the rotor is affected by kinds of disturbance. For the magnetically suspended spindle, when the cutting tool enters and leaves the work piece, the suspension of the rotor suffers from non-periodic disturbance such as step and impulse forces. However, due to the randomness and uncertainty of disturbance, it is hard to predict and suppress it. H∞ [11] or μ synthesis [12] algorithms have been used in the AMB systems, nevertheless, the high requirement of modeling accuracy and algorithm complexity limit the range of applications. Sliding mode control (SMC) method has been applied in maglev suspension application [13] for the advantages of quick response and insensitivity to parameter uncertainties. Nevertheless, SMC method is short of dealing with disturbance with unknown bound. The adaptive backstepping sliding mode control [14] is therefore proposed to handle the unknown disturbance, whereas, it estimates the disturbance simply via an integral of the state variables, which asymptotically converges slowly, therefore, the disturbance should be slowly varied. Disturbance observer based control (DOBC) approach which combines the disturbance observer with basic control method has been proposed [15–16]. Under this control framework, the normal control part is designed to achieve basic performance for the whole system, while the disturbance observer is developed to eliminate the effects caused by disturbance. With the co-operation of normal control part and disturbance observer, the DOBC approach can handle the non-periodic disturbance well.

Due to the eccentricity from the mass center to the geometric center, the rotation axis of the rotor and the inertial axis cannot coincide, the imbalance force is

therefore generated. The disturbance observer loses its effectiveness to handle imbalance force as the response lag to the disturbance, especially in high frequencies. There are two main control strategies to handle imbalance force – imbalance compensation and automatic balancing. Automatic balancing is commonly used since it significantly reduces the possibility of saturation of the power amplifier, while imbalance compensation could easily lead to saturation of the power amplifier. Therefore, automatic balancing is the better choice for zero-bias control. Many researches have investigated the active suppression of imbalance vibration, most are based on biased current controlled mode, such as the iterative learning control (ILC) [17]. However, the imbalance suppression methods under zero-bias control are rare in the literature. The generalized notch filters are widely used in the imbalance suppression applications [18], due to the simple structure and easy realization. Therefore, it can be used in the circumstances of zero-bias controlled mode.

In this paper, a new zero-bias control structure of the AMB system based on the nonlinear disturbance observer and generalized notch filter has been proposed and studied, which uses the zero-bias control strategy to reduce power consumption, and achieves suppression of non-periodic disturbance and imbalance vibration force via nonlinear disturbance observer and generalized notch filter respectively. The suspension control law is designed by state feedback control algorithm. Finally, the effectiveness of the proposed method is verified by experiment results.

The paper is organized as follows: Section II focuses on the system model and description; Section III provides the controller design process; Section IV shows the experiment platform and the corresponding experiment results; Conclusions are given in Section V.

II. MODEL OF THE ZERO-BIAS AMB SYSTEM

The radial support system of the magnetically suspended spindle is composed of two radial AMBs. The diagram of the radial AMBs system is shown in Fig. 1. Due to the movement of rotor between the axial and radial degrees can be decoupled, the influence of axial movement to the radial motion can be ignored. Therefore, the dynamic equations of the rotor for the radial four degrees of freedoms (4–DOFs) are:

$$M\ddot{q} + G\dot{q} = Bu_f + f_d$$
$$q_b = T_s q \qquad , \qquad (1)$$
$$y = Cq$$

define the mass matrix M, the gyroscopic matrix G, the control input matrix B, the transform matrix T_s, the output matrix C, the center of gravity (COG) coordinates q, the AMB coordinates q_b, the sensor coordinates y, the

external disturbance f_d, the electromagnetic force u_f.

Fig. 1. The diagram of the radial AMBs system.

Since the rotor normally operates within the range of rigid frequencies and the sensor centers are close to the AMB centers, to simplify the modeling process, assume that the output matrix C equals to the transform matrix T_s, namely, Equation (1) can be rewritten as:

$$MT_s^{-1}\ddot{q}_b + GT_s^{-1}\dot{q}_b = T_s^T u_f + f_d$$
$$y = q_b \qquad . \qquad (2)$$

For the slender rotor considered in this research, the transverse mass moments of inertia are significantly larger than the polar mass moment of inertia, the gyroscopic effect and coupling of two AMBs in the same direction can be ignored [18]. Besides, the design parameters for the front and rear AMBs are not the same, the max design force for the front AMB are much larger than the rear AMB, as the front AMB is the main part to bear external load in the radial directions. The suspension accuracy of the front AMB is more important than that of the rear AMB. That means the AMB systems can be modeled separately for each DOF. Since the above reasons, the 4-DOFs AMBs system can be built as the following form:

$$m\ddot{x}_i = b_i f_{ui} + f_{di}, \ i = xA, xB, yA, yB, \qquad (3)$$

where, f_{ui} and f_{di} denote the electromagnetic force and the lumped disturbance for each DOF respectively, b_i is the force distribution coefficient. Due to the limits of space, the detail descriptions about the derivation process are not given, more details can be found in Ref. 16. Therefore, decentralized control strategy can be used for two AMBs. Take the front AMB A into consideration, the state space form of the AMB in the AY direction is:

$$\begin{cases} \dot{x}_1 = x_2 \\ \dot{x}_2 = (bf_u + f_d)/m \, , \\ y = x_1 \end{cases} \qquad (4)$$

where, x_1 and x_2 represent the displacement and velocity of the rotor separately, y is system output, f_u denotes the electromagnetic force in AY direction, f_d represents the

lumped disturbance (including the equivalent imbalance force, non-periodic external force and the gravity, etc), b is the force distribution coefficient in AY direction, m is the mass of rotor.

Then based on the Maxwell's law, the electromagnetic force can be presented as:

$$f_u = k[\frac{i_1^2}{(g_0 - y)^2} - \frac{i_2^2}{(g_0 + y)^2}], \ k = \frac{\mu_0 A N^2}{4}, \quad (5)$$

where k represents the electromagnetic force coefficient, i_1, i_2 are the coil currents, N is the turn of coil, A is the area of stator pole, g_0 is the normal air gap, μ_0 represents the magnetic field constant in vacuum, which equals to $4\pi \times 10^{-7}$ Vs/Am.

From Equations (4) and (5), it can be known that the whole system is a nonlinear one when the coil current is considered as system input. Besides, there are two control outputs whereas only one input, which is not desired. Treat the electromagnetic force as the system input instead of current, then the AMB system becomes a linear one. Therefore, a new equivalent force controlled zero-bias AMB system can be written as:

$$\begin{cases} \dot{x}_1 = x_2 \\ \dot{x}_2 = g(x_1)u + d \, . \\ y = x_1 \end{cases} \quad (6)$$

Define u as the new system input, $g(x_1) = b/m$ is the input coefficient, and d denotes the lumped disturbance, $d = f_d / m$. Then the excitation current of the coil can be calculated via the following transform relationship:

$$\begin{cases} i_1 = 0, i_2 = (g_0 + y)\sqrt{\dfrac{u}{k}}, \ u \geq 0 \\ i_1 = (g_0 - y)\sqrt{\dfrac{-u}{k}}, i_2 = 0, \ u < 0 \end{cases} \quad (7)$$

The zero-bias AMB system in Equation (6) is a linear one, therefore, linear or nonlinear control strategies can be used. To maintain the normal suspension and suppress disturbance well, a DOBC approach is proposed and designed. Before the controller design, define the tracking error and its derivatives as:

$$\begin{aligned} e &= x_1 - x^* \\ \dot{e} &= \dot{x}_1 - \dot{x}^* \\ \ddot{e} &= \ddot{x}_1 - \ddot{x}^* = g(x_1)u + d - \ddot{x}^* \end{aligned} \quad (8)$$

where x^*, $\dot{x}^*$, $\ddot{x}^*$ are the reference position, velocity and acceleration of the rotor respectively.

Let $\lambda = [\lambda_1 \quad \lambda_2]^T = [e \quad \dot{e}]^T$, then Equation (6) can be written into a state-space form as:

$$\dot{\lambda} = \begin{bmatrix} \lambda_2 \\ g(x_1)u - \ddot{x}^* \end{bmatrix} + \begin{bmatrix} 0 \\ 1 \end{bmatrix} d \, . \quad (9)$$

Define $G_d = [0 \quad 1]^T$ and,

$$\boldsymbol{\eta} = \begin{bmatrix} \lambda_2 \\ g(x_1)u - \ddot{x}^* \end{bmatrix} = \begin{bmatrix} \eta_1 \\ \eta_2 \end{bmatrix}. \quad (10)$$

Then system Equation (9) changes to:

$$\lambda = \boldsymbol{\eta} + G_d d \, . \quad (11)$$

III. CONTROLLER DESIGN

A. Nonlinear disturbance observer based state feedback controller design

In order to handle the non-periodic disturbance, a nonlinear disturbance observer (NDO) is proposed [15], which observes the disturbance as well as its derivatives. For the convenience of realization, the first two-order derivatives of disturbance are considered here, and an assumption is made that the feasibility of NDO is existing if only the lumped disturbance meets the following assumption:

Assumption: The lumped disturbance d and its first two-order derivatives are continuous and bounded, namely:

$$|\frac{\partial^j d(t)}{\partial (t)^j}| \leq \mu, \quad for \ j = 0, 1, 2 \, , \quad (12)$$

where μ is a positive constant, μ can be unknowable.

Based on the definitions and deductions above, the NDO is designed as:

$$\begin{cases} \hat{d} = p_1 + q_1(\lambda_1 + \lambda_2) \\ \dot{p}_1 = -q_1(\eta_1 + \eta_2) - q_1\hat{d} + \hat{\dot{d}} \\ \hat{\dot{d}} = p_2 + q_2(\lambda_1 + \lambda_2) \\ \dot{p}_2 = -q_2(\eta_1 + \eta_2) - q_2\hat{d} \end{cases}, \quad (13)$$

where $\hat{d}$ and $\hat{\dot{d}}$ are estimations of d and its derivative respectively, p_1 and p_2 are auxiliary functions, and q_1, q_2 are positive constants. $\boldsymbol{D}$

Let $\boldsymbol{D} = [d \quad \dot{d}]^T$, then Equation (13) is reformed as:

$$\begin{cases} \hat{\boldsymbol{D}} = \boldsymbol{p} + \boldsymbol{q}(\lambda_1 + \lambda_2) \\ \dot{\boldsymbol{p}} = -\boldsymbol{q}(\eta_1 + \eta_2) + \boldsymbol{Q}\hat{\boldsymbol{D}} \end{cases}, \quad (14)$$

where $\hat{\boldsymbol{D}} = \begin{bmatrix} \hat{d} \\ \hat{\dot{d}} \end{bmatrix}$, $\boldsymbol{p} = \begin{bmatrix} p_1 \\ p_2 \end{bmatrix}$, $\boldsymbol{q} = \begin{bmatrix} q_1 \\ q_2 \end{bmatrix}$, $\boldsymbol{Q} = \begin{bmatrix} -q_1 & 1 \\ -q_2 & 0 \end{bmatrix}$.

According to Equation (14), the derivative of $\hat{\boldsymbol{D}}$ is yielded as:

$$\begin{aligned} \dot{\hat{\boldsymbol{D}}} &= \dot{\boldsymbol{p}} + \boldsymbol{q}(\dot{\lambda}_1 + \dot{\lambda}_2) \\ &= -\boldsymbol{q}(\eta_1 + \eta_2) + \boldsymbol{Q}\hat{\boldsymbol{D}} + \boldsymbol{q}(\eta_1 + \eta_2 + d) \, . \\ &= \boldsymbol{Q}\hat{\boldsymbol{D}} + \boldsymbol{q}d \end{aligned} \quad (15)$$

Then the estimation error can be defined as follows:

$$\tilde{\boldsymbol{D}} = [\tilde{d} \quad \tilde{\dot{d}}]^T = \boldsymbol{D} - \hat{\boldsymbol{D}} \, . \quad (16)$$

The observer error dynamics can be written as

$$\dot{\tilde{D}} = \dot{D} - \dot{\hat{D}}$$

$$= \begin{bmatrix} \dot{d} & \ddot{d} \end{bmatrix}^{T} - (Q\hat{D} + qd),$$ (17)

$$= Q\tilde{D} + E\ddot{d}$$

where $E = \begin{bmatrix} 0 & 1 \end{bmatrix}^{T}$.

Suppose that q_1 and q_2 are chosen to guarantee that the eigenvalues of Q are in the left hand plane (LHP), then for any given positive definite matrix R, a positive definite symmetric matrix P can be found to satisfy the following relationship:

$$Q^{T}P + PQ = -R,$$ (18)

then the observer is asymptotically stable. The details of stability analysis can be seen in Ref. 15. Therefore, the norm of the extended disturbance estimation error $\tilde{D}$ is ultimately bounded and the bounds can be lowered by choosing q_1, q_2, P and R appropriately.

Remark: The NDO has strong ability to handle disturbance since the derivative of the disturbance is also estimated. Meanwhile, it should be mentioned that the bound of disturbance is unnecessary to know. Since that, stronger ability to handle non-periodic disturbance can be expected. Though the bound value can be unknown, in fact, it affects the suspension accuracy of the rotor a lot. Therefore, strategies to lower the bound value such as removing the gravity from the unknown disturbance are meaningful.

With the disturbance observer, the equivalent disturbance for the system becomes $\tilde{d}$, which is much smaller than d, then the system can be presented as the following state space form:

$$\dot{x} = Ax + Bu + G_{d}\tilde{d},$$ (19)

$$y = Cx$$

where $x = \begin{bmatrix} x_1 \\ x_2 \end{bmatrix}, A = \begin{bmatrix} 0 & 1 \\ 0 & 0 \end{bmatrix}, B = \begin{bmatrix} 0 \\ g(x_1) \end{bmatrix}, C = \begin{bmatrix} 0 \\ 1 \end{bmatrix}^{T}.$

Also system (11) changes to:

$$\dot{\lambda} = \eta + G_{d}\tilde{d}.$$ (20)

According to the DOBC design framework [15], the structure of the controller for the zero-bias AMB system can be divided into two parts – the disturbance compensation part and the normal suspension part. As the effect caused by the unknown disturbance is eliminated via disturbance observer, then a suspension controller needs to be designed.

Based on the state feedback control law [19], it can be deduced that the whole system is controllable. Then a state feedback controller is deigned to realize the normal suspension of rotor.

$$u_{f} = -K\lambda,$$ (21)

where, $K = \begin{bmatrix} k_1 & k_2 \end{bmatrix}$ is the feedback coefficient matrix.

Then the whole control output can be presented as:

$$u = u_{f} + u_{b}$$

$$= -K\lambda - \hat{d} / g(x_1)$$ (22)

where u and u_b are the whole control output and the output of the disturbance observer. The DOBC method combining nonlinear disturbance observer with state feedback control can be abbreviated as SF+NDO.

B. The general notch filter based imbalance force rejection controller design

Although the disturbance observer can well restrain disturbance, the state feedback controller based on disturbance observer itself is still feedback closed-loop control, that means there remains response lag to the disturbance, and with the increase of disturbance frequency, the response lag is more obvious. Therefore, the disturbance observer functions as a low-pass filter, it is only effective on the low frequency range, and it cannot handle the imbalance force well under high spinning speed. Besides, the value of the unknown upper bound of disturbance μ affects the accuracy of suspension a lot. With the limits of response frequency of the power amplifier, the generalized notch filter (GNF) based minimum current compensation control strategy is therefore proposed to deal with the periodic imbalance force. The principle of the GNF N is shown in Fig. 2. The core of the notch filter is the notch feedback item N_f, its central frequency can vary with the change of rotating speed, the convergence factor ε determines the convergence rate and bandwidth of the notch filter.
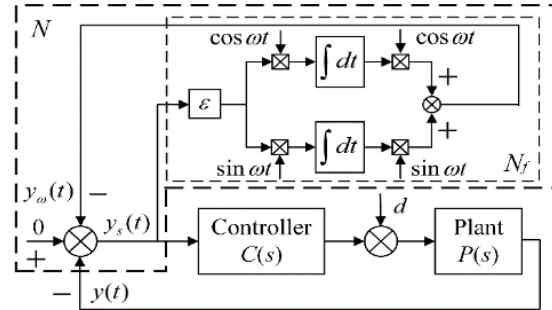

Fig. 2. The principle of the generalized notch filter N.

Assume $y_s(t)$ and $y_\omega(t)$ to be the input and output of the notch feedback item respectively, then $y_\omega(t)$ equals to:

$$y_\omega(t) = \varepsilon \begin{bmatrix} \sin \omega t & \cos \omega t \end{bmatrix} \begin{bmatrix} \int y_s(t)\sin \omega t dt \\ \int y_s(t)\cos \omega t dt \end{bmatrix}.$$ (23)

The transfer function of the notch feedback item can be written as

$$N_f(s) = \frac{Y_\omega(s)}{Y_s(s)} = \frac{\varepsilon s}{s^2 + \omega^2} . \quad (24)$$

Then transfer function from system output $Y(s)$ to the notch filter output $Y(s)$ is:

$$N(s) = \frac{Y_s(s)}{Y(s)} = \frac{s^2 + \omega^2}{s^2 + \varepsilon s + \omega^2} . \quad (25)$$

When $\varepsilon \neq 0$, let $s = j\omega_r$, the following equation can be established:

$$\begin{cases} N(j\omega_r) \approx 1, & \left[\omega_r \in (0, \ \omega - \Delta\omega) \cup \right. \\ & \left. (\omega + \Delta\omega, \ \infty)\right] \\ N(j\omega_r) = 0, & \left[\omega_r \in (\omega - \Delta\omega, \ \omega + \Delta\omega)\right] \end{cases} . \quad (26)$$

Therefore, as long as $\varepsilon \neq 0$, the output of the notch feedback item tends to the component with the frequency of ω in the system output $y(t)$. By subtracting the original displacement signal to the signal estimated by the notch filter, the same frequency component caused by the imbalance force in the original signal $y(t)$ is filtered out, in other words, the same frequency current generated by the controller is eliminated, and thus the imbalance force is suppressed.
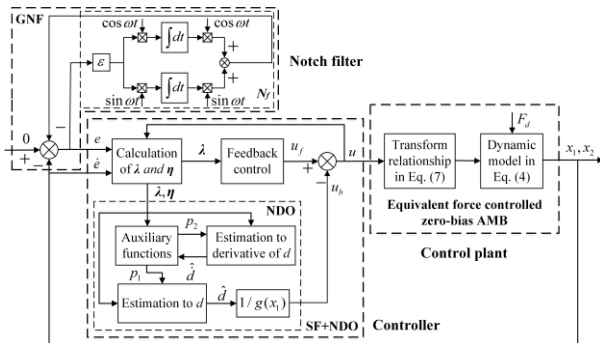

Fig. 3. The whole control system based on SF+NDO+GNF.

Since that, with the co-function of the disturbance observer and the notch filter, the imbalance force and non-periodic disturbance can be well restrained. The whole control system for nonlinear disturbance observer based state feedback control plus general notch filter (SF+NDO+GNF) is described as Fig. 3.

IV. EXPERIMENTS

A. Experimental platform construction

As shown in Fig. 4, a 5 degree of freedoms (5–DOFs) magnetically suspended spindle system is built, which consists of two radial AMBs, one axial AMB and the drive motor mainly. Figure 5 shows the structure of the front radial AMB. In this paper, the main attention is

paid on the front AMB, for which is the main part to bear external load in the radial directions. The whole control system for the magnetic bearing is based on a FPGA chip – the EP4CE15F17C8 manufactured by ALTERA. The proposed control methods employ the cascaded structure with position and current feedback. As well known, for the zero-bias control, the magnetic force slue rate near the origin is zero. In order to produce a small force, a large change is needed in control current. To overcome this problem, firstly, large current (equals to 20 A) and small turns of coil (equals to 40) for AMB are designed to improve the force bandwidth of actuators, then hysteretic current control is adopted to realize the fast response of current, therefore the largest force bandwidth can be held. Parameters of the front radial AMB system are shown in Table 1.
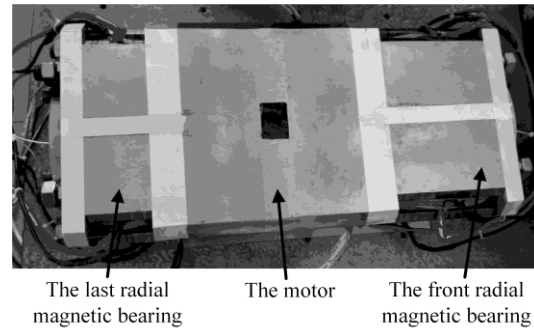

Fig. 4. 5–DOFs magnetically suspended spindle system.
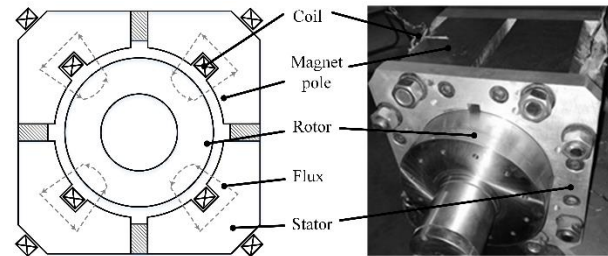
Fig. 5. The structure of the front radial AMB.

Table 1: Parameters of the front radial AMB system

Parameter (Symbol)	Value
Mass of the rotor (m)	55 kg
Transverse mass moments of inertia (I_x, I_y)	0.817 kg×m^2
Polar mass moment of inertia (I_z)	0.139 kg×m^2
Magnetic pole area (A)	5.04×10^{-3} m^2
Electromagnetic force coefficient (k)	2.53×10^{-6} N×m^2/A^2
Nominal air gap (g_0)	0.3 mm
Auxiliary gap (g_a)	0.1 mm
Turns of coil (N)	40
Max current (i_{max})	20 A

Fig. 6. Displacement curves during initial lift up.

Fig. 8. Displacement curves under the constant load.
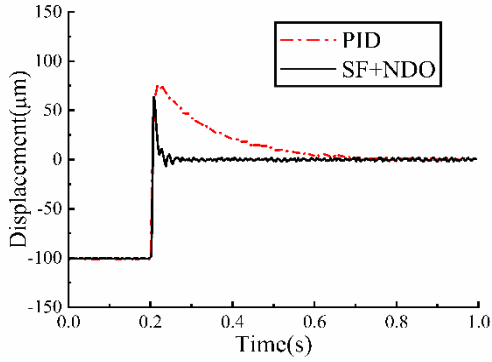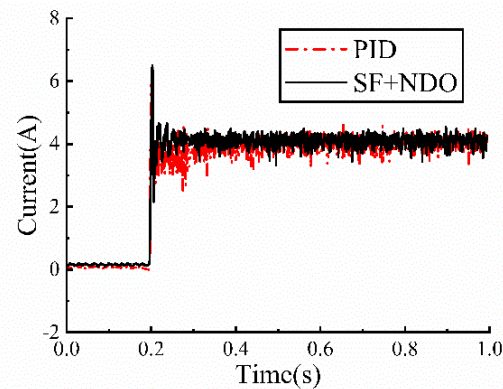
Fig. 7. Current curves during initial lift up.
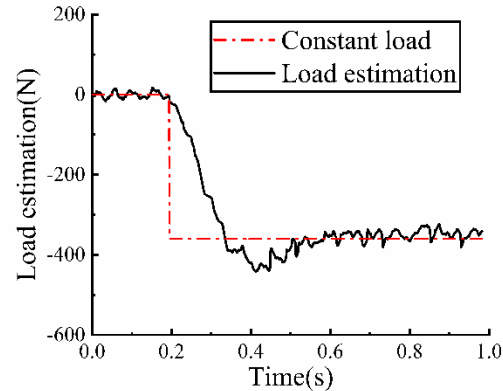
Fig. 9. Load estimation curve under the constant load.

B. Experimental tests for SF+NDO based control

Firstly, researches on the non-periodic disturbance rejection are carried out under static condition. The effectiveness of the SF+NDO control is verified under two kinds of circumstances, namely the initial lift up process and adding a constant load. In order to verify the effectiveness of the proposed algorithm, the commonly used proportional-integral-derivative (PID) strategy is compared. Figures 6–8 show the displacement and current curves under two kinds of disturbance in Y direction respectively. Firstly, Fig. 6 shows the displacement curves during initial lift up process, the maximum overshoots and adjusting time of the rotor for the SF+NDO method and PID are 63 μm / 0.06 s and 75 μm / 0.52 s respectively. It is demonstrated in Fig. 8 that when a 360 N constant load is applied to the rotor, the maximum deviations and recovery time of the rotor for SF+NDO and PID are 7 μm / 0.25 s and 44 μm / 0.4 s respectively. Therefore, compared with PID control strategy, the SF+NDO control strategy has stronger ability to restrain the non-periodic disturbance. In addition, the load estimation curve for the disturbance observer can be obtained as shown in Fig. 9.

Then, at 2400 rpm, the dynamic performances for the SF+NDO method and PID control are compared. Figure 10 describes the displacement curves in Y direction. It is demonstrated that the maximum deviations of the rotor for SF+NDO and PID are 9 μm and 17 μm respectively. Therefore, it can be seen that the SF+NDO control strategy can suppress the harmonic vibrations well. Though the proposed SF+NDO method can suppress disturbance, there are still residual vibrations caused by the imbalance force, as described in Fig. 11. Therefore, a new strategy is needed to suppress the imbalance force.

C. Experimental tests for SF+NDO+GNF based control

On the basis of the SF+NDO method, the imbalance force is further suppressed by introducing the GNF. At 2400 rpm, the performances of suspension under the three kinds of methods are obtained, as shown in the Fig. 12. The results demonstrate that the basic values of displacement are about 2.4 μm, 2.0 μm and 0.85 μm for PID, SF+NDO and SF+NDO+GNF respectively. Finally, the proposed SF+NDO+GNF method is compared with biased control (the biased current is 4A) using PID

method at the same speed, and it shows in Fig. 13 that the vibrations also decreased with the proposed method.

Besides, the copper losses for the front radial magnetic bearing are calculated for the proposed control method and biased control method (the biased current is 4A) respectively, Fig. 14 shows the relationship between copper losses and the rotating speed. It demonstrates that zero bias control reduces the power consumption by at least 40% compared with the biased control. Therefore, zero bias control is helpful to increase the running time of AMB system.
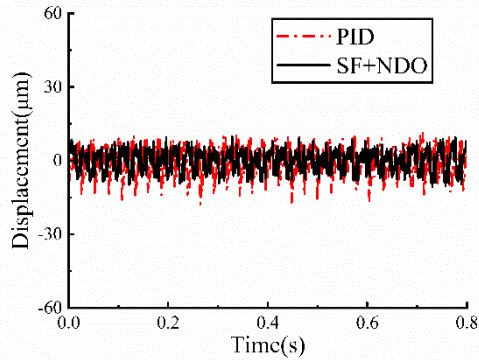

Fig. 10. Displacement curves at 2400 rpm.
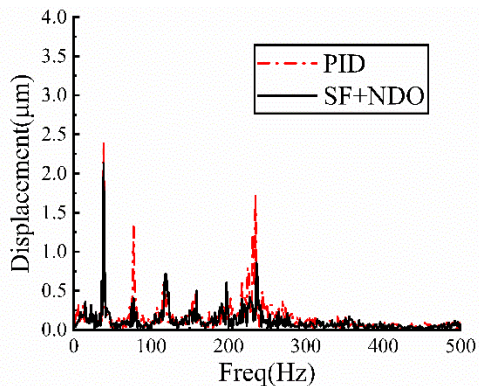
Fig. 11. The spectrum curves of displacement at 2400 rpm.
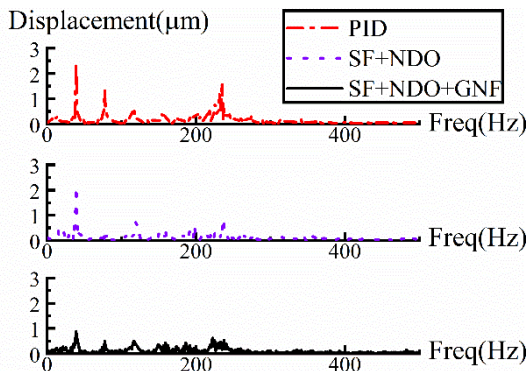

Fig. 12. The spectrum curves of displacement for the three methods at 2400 rpm.
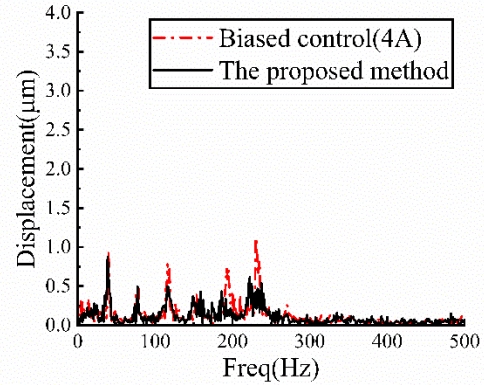
Fig. 13. The spectrum curves of displacement for biased control and the proposed method at 2400 rpm.
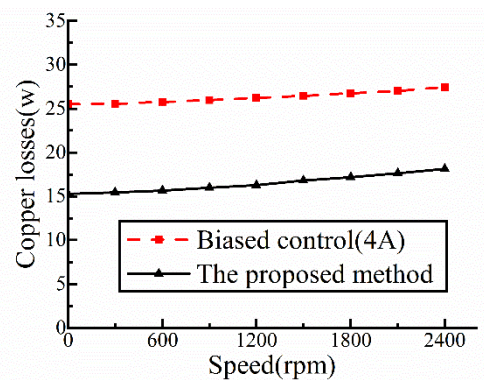
Fig. 14. Copper losses for biased control and the proposed method.

From above, it can be seen that the proposed SF+NDO+GNF method for zero bias controlled AMB system shows excellent performance on comprehensive disturbance suppression and power reduction. Therefore, the effectiveness of the proposed method is verified.

V. CONCLUSIONS

In this paper, a nonlinear disturbance observer plus notch filter based zero-bias control strategy is proposed for the radial AMBs in a magnetically suspended spindle. An equivalent electromagnet force controlled model is introduced to handle the nonlinearity brought by zero-bias current strategy. The nonlinear disturbance observer is adopted to restrain the non-periodic disturbance such as step forces. The periodic imbalance force is suppressed by introducing the general notch filter. Various experiments have been performed to verify the effectiveness of the approach. Besides, the proposed SF+NDO+GNF method is compared with biased control using PID method, it also show excellent performance in vibrations suppression and power reduction. Since the strong ability both in power reduction and disturbance restraint for the proposed method, it can also be adopted to other AMB applications where low power consumption

and suppression of disturbance are needed.

REFERENCES

[1] G. Schweitzer and E. H. Maslen, *Magnetic Bearings: Theory, Design, and Application to Rotating Machinery*. Berlin Heidelberg: Springer–Verlag, 2009.

[2] S. L. Chen and K. Y. Liu, "Sensorless control for a three-pole active magnetic bearing system," *ACES Journal*, vol. 32, no. 8, pp. 720-725, Aug. 2017.

[3] L. L. Zhang and J. H. Huang, "Stability analysis for a flywheel supported on magnetic bearings with delayed feedback control," *ACES Journal*, vol. 32, no. 8, pp. 642-649, Aug. 2017.

[4] C. Dumont, V. Kluyskens, and B. Dehez, "Performance of yokeless heteropolar electrodynamic bearings," *ACES Journal*, vol. 32, no. 8, pp. 685-690, Aug. 2017.

[5] Z. Jun, D. D. Song, Q. L. Han, J. M. Wang, G. H. Li, and S. L. Li, "Optimization of T-shaped suspension magnetic ring for vertical axis wind turbine," *ACES Journal*, vol. 33, no. 7, pp. 781-789, July 2018.

[6] D. G. Li, S. Q. Liu, and B. Bian, "Automatic thermal expansion compensation of the precise grinding machine AMB spindle," *Applied Mechanics and Materials*, vol. 130-134, no. 2, pp. 3221-3224, 2011.

[7] S. Sivrioglu, "Adaptive backstepping for switching control active magnetic bearing system with vibrating base," *IET Control Theory and Applications*, vol. 1, no. 4, pp. 1054-1059, 2007.

[8] R. P. Jastrzebski, A. Smirnov, A. Mystkowski, and O. Pyrhönen, "Cascaded position-flux controller for an AMB system operating at zero bias," *Energies*, vol. 7, no. 6, pp. 3561-3575, 2014.

[9] A. Mystkowski and E. Pawluszewicz, "Nonlinear position-flux zero-bias control for AMB system with disturbance," *ACES Journal*, vol. 32, no. 8, pp. 650-656, Aug. 2017.

[10] S. Sivrioglu, K. Nonami, and M. Saigo, "Low power consumption nonlinear control with H∞ compensator for a zero-bias flywheel AMB system," *Journal of Vibration and Control*, vol. 10, no. 8, pp. 1151-1166, 2004.

[11] F. Matsumura, T. Namerikawa, K. Hagiwara, and M. Fujita, "Application of gain scheduled H ∞ robust controllers to a magnetic bearing," *IEEE Transactions on Control System Technology*, vol. 4, no. 5, pp. 484-493, 1996.

[12] M. Chen and C. R. Knospe, "Control approaches to the suppression of machining chatter using active magnetic bearings," *IEEE Transactions on Control Systems Technology*, vol. 15, no. 2, pp. 220-232, 2007.

[13] M. S. Kang, J. Lyou, and J. K. Lee, "Sliding mode control for an active magnetic bearing system subject to base motion," *Mechatronics*, vol. 20, no. 1, pp. 171-178, 2010.

[14] H. Rong and K. Zhou, "Nonlinear zero-bias current control for active magnetic bearing in power magnetically levitated spindle based on adaptive backstepping sliding mode approach," *Proceedings of the Institution of Mechanical Engineers Part C Journal of Mechanical Engineering Science*, vol. 231, no. 20, pp. 3753-3765, 2017.

[15] D. Ginoya, P. D. Shendge, and S. B. Phadke, "Sliding mode control for mismatched uncertain systems using an extended disturbance observer," *IEEE Transactions on Industrial Electronics*, vol. 61, no. 4, pp. 1983-1992, 2014.

[16] L. F. Xiao and Y. Zhu, "Sliding mode output feedback control based on tracking error observer with disturbance estimator," *ISA Transactions*, vol. 53, no. 4, pp. 1061-1072, 2014.

[17] B. Shafai, S. Beale, P. Larocca, and E. Cusson, "Magnetic bearing control systems and adaptive forced balancing," *IEEE Transactions on Control Systems Technology*, vol. 14, no. 2, pp. 4-13, 1994.

[18] Q. Chen, G. Liu, and S. Q. Zheng, "Suppression of imbalance vibration for AMBs controlled driveline system using double-loop structure," *Journal of Sound and Vibration*, vol. 337, pp. 1-13, 2015.

[19] H. Wei, Y. C. Ouyang, and J. Hong, "Vibration control of a flexible robotic manipulator in the presence of input deadzone," *IEEE Transactions on Industrial Informatics*, vol. 13, no. 1, pp. 48-59, 2017.

Hai Rong was born in 1993. He received B.S. degree in Mechanical Engineering and Automation from Huazhong University of Science and Technology (HUST) in 2014. He is currently pursuing a Ph.D. degree in Tsinghua University. His research focuses on magnetic bearing control and magnetic bearing systems design.

Kai Zhou was born in 1954. He received Ph.D. degree in Mechanical Engineering from Tsinghua University. He is currently a Full Professor in the Department of Mechanical Engineering, Tsinghua University. His research focuses on magnetically suspended systems, CNC systems, high speed motors and servo control.

The Interaction Forces in Magnetic Support Systems of Vertical Type

E. Frishman

Department of Electrical Engineering
Jerusalem College of Technology

Abstract — In this article, the vertical and horizontal forces of the interaction of permanent magnets in a Magnetic Suspension (support) System of Vertical Type (MSVT) are considered. The magnetic support system contains multi-row magnetic bands (strips), which have alternating polarity. The magnetization vector, $\vec{M}$, is directed horizontally, as opposed to classical support systems where $\vec{M}$ is directed vertically. The results of the comparison of the vertical and lateral forces for the classic Magnetic System of Horizontal Type (MSHT) and the MSVT are presented too. An effectiveness factor, $\mu_{eff} = f_z / mg$, is adopted (where f_z is the vertical force per unit length of magnetic band and mg is its weight) and is used as the principle criterion for comparison. In this paper it is shown that when the vertical displacement of the moving part of the support system of MSVT causes the vertical force, f_z, to reach its maximum, the lateral force f_y is at its minimum.

Index Terms — Horizontal and vertical types of magnetic suspension, permanent magnets, stability, suspension effectiveness factor, vertical and horizontal forces.

I. INTRODUCTION

Well known systems of magnetic support (magnetic suspension) on permanent magnets of horizontal type (MSHT), are illustrated in Fig. 1 (a). Magnetic strips and their polar faces are located in the horizontal plane. The magnets of the mobile and fixed parts are mounted on a ferromagnetic base. The magnetic substrate (magnetically soft material) reduces scattering fluxes. This simplifies the installation of magnetic strips and also causes a significant increase in the vertical force, i.e., bearing capacity of the magnetic support. This is a very desirable effect that even takes into account the mass of the ferromagnetic base for magnets.

The effectiveness of the support (suspension) can be determined by the index $\mu_{eff} = f_z / mg$, where $f_V = f_z$ is the vertical force of interaction (repulsive force) of the magnets located on the fixed and on the movable parts of the support system. The vertical force is defined as the

interaction force and is calculated per unit length of one pair of magnetic strips of the system; mg- is the weight of the magnets per unit length, [1]. The support system can contain many strips arranged in a certain way and at a certain distance from each other. For example, in Fig. 1 (a) there are two magnetic bands on the mobile and fixed parts of the support.

The bands are located in the same plane (MSHT) and have alternating polarity.

In Fig. 1 (b), the support has a step-like character (and is said to be a Magnetic Support of Step Type – MSST) with relative vertical shifts of neighboring strips [2].
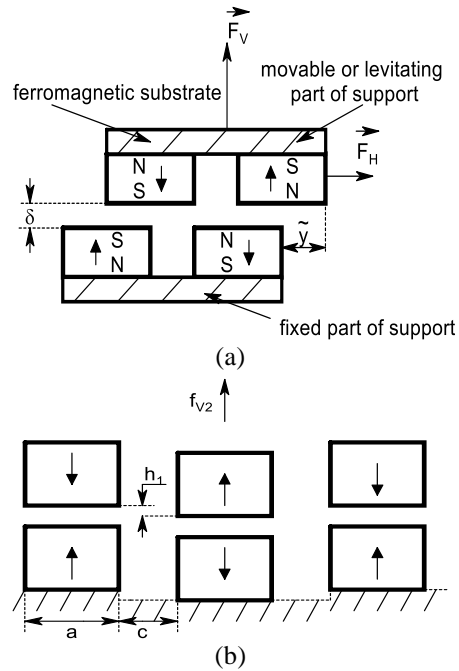

Fig. 1. (a) MSHT with ferromagnetic substrate, and (b) the scheme with the vertical displacement (MSSS).

The paper [2] also introduced a stability factor index $\gamma = f_V / f_H$, which is the ratio of vertical and lateral forces. This index is calculated for different values of lateral displacement.

The value μ_{eff} can be chosen as the objective function for determining the optimum sizes of the cross section of the magnetic strip and the distance between them.

Different Permanent Magnet (PM) configurations have been proposed in the scientific literature with the objective to improve figures of merit similar to γ and μ_{eff} for magnetic bearings and force magnetic gears [3]-[5].

II. MAGNETIC SUSPENSION (SUPPORT) SCHEMES OF THE VERTICAL TYPE

A fundamentally different structure has a magnetic support system of vertical type on permanent magnets, Fig. 2 (a) and Fig. 2 (b). The first scheme proposed by Iskanderov [6] and the second by the author of this paper. The main advantages of these supports are: a small gap δ, and the elimination of the impact of the magnets of the stationary and moving parts under dynamic loads, which leads to displacements in the vertical plane. The placement of the magnetic strips can be carried out with high accuracy due to the use of rolling channels, T-bars, etc., serving simultaneously as structural components and magnetic flux concentrators. The increased accuracy of the placement of magnetic strips and the independence of the gap from vertical movements makes it possible to achieve significantly lower values of the working gap and, consequently, an increase in the bearing (vertical) support capacity and efficiency index μ_{eff}. In addition, in this paper it is shown that when the maximum vertical load on the moving part is reached, the lateral force tends to its minimum, and, consequently, the forces acting on the stabilizing mechanical (or electrodynamic) system reduce to a minimum. As a consequence of the reduction of the instability forces, the external stabilization system is simpler and cheaper to design. In contrast, levitation configurations, characterized by high destabilizing forces, require high-performance, complex and expensive stabilization systems [7]-[11].

The results of a theoretical analysis of the vertical and lateral forces acting in the MSVT, Fig. 2 (a) and Fig. 2 (b) are presented in this paper. The considered suspension system does not work on repulsion, as in does the classical system (Fig. 1), but on attraction. System 2, shown in Fig. 2 (b) differs from system 1; Fig. 2 (a) in that the magnets in the middle of the support "work" with both pole faces. The lateral (or horizontal) force destabilizing the suspended part depends on the accuracy of the placement of magnetic strips and ideally (if the system is symmetrical) is zero. In the initial position, when the magnetic strips are exactly opposite one another ($\tilde{y} = z = 0$, see Fig. 2 (a) and Fig. 2 (b)), the vertical force acting on the moving part of the system is zero.

It is clear that the mobile and fixed parts of the support system can be swapped (depending on the technical requirements imposed on the MP system). As the load increases, the moving part moves down, the vertical force, balancing the weight of the moving part, increases to a certain maximum, and the lateral force (if the system is not exactly symmetrical) decreases. Such a picture of interaction takes place within certain limits of vertical displacement: $z_{max} > z > 0$. For the MSVT systems, shown in Fig. 2 (a) and Fig. 2 (b), the use of a ferromagnetic substrate leads to the same effect as for the MSHT, but in the case of Fig. 2 (b) a fixed part of the magnetic flux is used on both sides (without placing the magnets on a ferromagnetic base). In order to increase the bearing capacity, the systems shown in Figs. 2 (a) and 2 (b) can be transformed into multi-row systems.
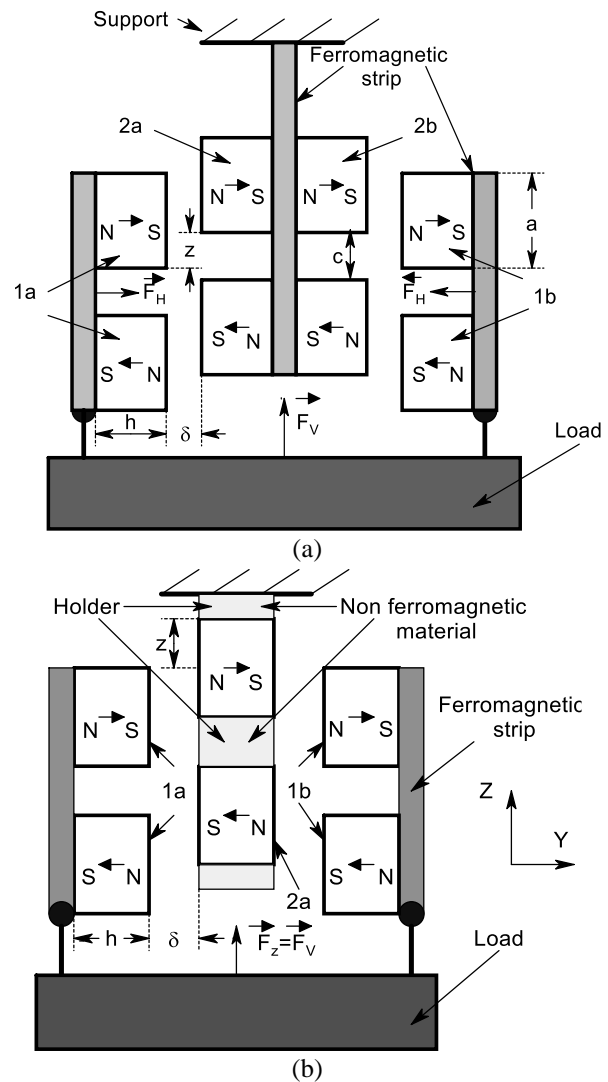

Fig. 2. (a) Scheme 1 MSVT, and (b) scheme 2 MSVT.

III. INTERACTION ANALYSIS FOR MSVT SYSTEMS

The forces of vertical and horizontal interaction in the magnetic systems can be determined using the expression for the potential energy of a permanent magnet that is located in an external magnetic field [2]:

$$E_p = \mu_0 \iiint_V \vec{M} \cdot \vec{H} \cdot dV . \tag{1}$$

In (1) $\vec{M}$ is the magnetization vector (e.g., the magnet *1a* or *1b*) and $\vec{H}(y, z)$ is the vector of magnetic field intensity (of the external magnetic field), created, for example, by the magnet *2a* or *2b*; V is the volume of the magnet, $\mu_0 = 4\pi \cdot 10^{-7} \, H/m$. Expressions for the interaction forces of permanent magnets can be obtained using the equation $\vec{F} = -\vec{\nabla} E_p$. For the vertical and horizontal components of the force, this formula gives:

$$\vec{F}_z = -\hat{z} \frac{\partial E_p}{\partial z} , \qquad \vec{F}_y = -\hat{y} \frac{\partial E_p}{\partial y} . \tag{2}$$

The efficiency μ_{eff} of support schemes shown in Fig. 2 (a) and Fig. 2 (b) can be estimated using the following expression [2]:

$$\mu_{eff} = f_z / mg , \tag{3}$$

in which $f_z (N / m) = f_V$ is the vertical interaction force per the unit length of the system that includes magnets *1* and *2*, and *mg* is the weight per unit length of the same magnets.

To find the interaction force of magnetic systems, we must first determine the magnetic field intensity $H(z, y)$ in those systems. Each magnet has a rectangular cross-section and can be represented by two faces (strips), each with a uniformly distributed fictitious magnetic charge with a surface density [1]: $\sigma = \pm \mu_0 \cdot M$. In [2] the two-dimensional potential of the magnetic field produced by the "face-charge" at any point $P(y, z)$, Fig. 3 (a) was obtained and can be represented as:

$$\phi(y, z) = -\frac{\sigma}{4\pi \cdot \mu_0} \int_0^a \ln\left[z^2 + (y - u)^2 \right] \cdot du , \tag{4}$$

u is the variable of integration.

The components of the intensity of the magnetic field are determined by the following expression:

$$H_y(y, z) = -\frac{\partial \phi(y, z)}{\partial y} ; H_z(y, z) = -\frac{\partial \phi(y, z)}{\partial z} . \tag{5}$$

By substituting (4) into (5), we obtain the expressions for the intensity of the magnetic field at the point $P(y, z)$:

$$H_y(y, z) = \frac{\sigma}{4\pi\mu_0} \left[\ln(y^2 + z^2) - \ln((a - y)^2 + z^2) \right], \tag{6}$$

$$H_z(y, z) = \frac{\sigma}{2\pi\mu_0} (arctg \frac{y}{z} - arctg \frac{y - a}{z}). \tag{7}$$
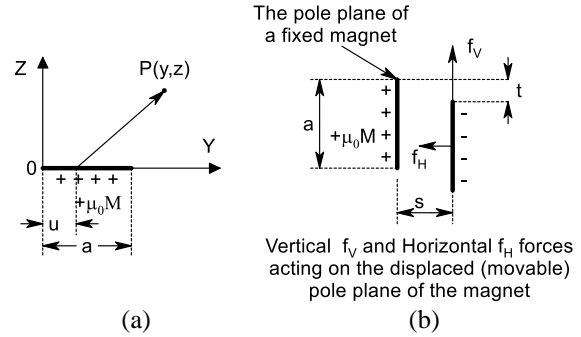

Fig. 3. (a) Charged strip, and (b) calculated scheme.

In contrast to the scheme in Fig. 1 (a) (or Fig. 1 (b)), in the proposed new schemes (Fig. 2 (a) and Fig. 2 (b)), the pole faces are arranged vertically. The calculation scheme for the interaction of two pole faces in this case is shown in Fig. 3 (b). Now:

$$H_y(y, z) = H_{Vertical} = H_V$$
$$H_z(y, z) = H_{Horizontal} = H_H .$$

In other words, the coordinates *y* and *z* change places (including in (4)).

The vertical force of interaction of two charged faces (repulsive force) obtained for horizontally located "charged" pole surfaces (for the scheme in Fig. 1 (b)) is now a lateral destabilizing force (for MSVT). Conversely, the lateral destabilizing force in the MSHT schemes is now a "holding" or supporting force in schemes with vertically arranged pole faces. Taking (1) and (2) into account, the forces of interaction of the faces, can be represented as:

$$f_H = \sigma \int_t^{t+a} H_H \cdot dy ; \quad f_V = \sigma \int_t^{t+a} H_V \cdot dy . \tag{8}$$

After substituting (6) and (7) into (8) and integrating, we obtain expressions for the vertical f_V and horizontal f_H interaction forces of a unit length of two charged faces:

$$f_V(t, s) = \frac{\mu_0 \cdot M^2}{4\pi} \left\{ 2s\,(arctg \frac{t + a}{s} + \right.$$
$$+ arctg \frac{t - a}{s} - 2arctg \frac{t}{s} - 2t \ln(t^2 + s^2) +$$
$$+ (t + a) \ln\left[(t + a)^2 + s^2 \right] +$$
$$\left. + (t - a) \ln\left[(t - a)^2 + s^2 \right] \right\}, \tag{9}$$

$$f_H(t,s) = \frac{\mu_0 \cdot M^2}{2\pi} \left\{ (t+a)(arctg \frac{t+a}{s} - \right.$$

$$-2t \, arctg \frac{t}{s} + (t-a) \, arctg \frac{t-a}{s} +$$

$$+ \frac{s}{2} \ln \frac{(s^2+t^2)^2}{\left[s^2+(t-a)^2\right]\left[s^2+(t+a)^2\right]} \left. \right\}, \qquad (10)$$

where t and s are given in Fig. 3 (b). To obtain expressions for the interaction forces of the magnetic systems of the moving and bearing parts of the suspension system (support), it is necessary to sum (taking into account the signs) the interaction forces of the corresponding pole faces. For example, the vertical force for the scheme in Fig. 2 (a) (or in Fig. 4) is composed of the interaction of the faces: (1 and 2) minus the faces (1 and 3); the result is multiplied by 4. Of course, for a more accurate calculation of the vertical force, it is necessary to take into account the interaction of face 1 with faces 4 and 5. Similar calculations must be made with faces 6 and 2,3,4,5. In accordance with the calculated data, it suffices to take into account the first image. The error does not exceed 4-5%.

As for the lateral force of interaction, it can be neglected if the magnetic strips along the fixed (bearing) and suspended parts of the system are fairly accurately placed (i.e., when the gaps δ in the left and right parts of the support system are approximately equal). When calculating the vertical and horizontal interaction forces of the MSTV system shown in Fig. 2 (a), only the first images of the faces of the magnets with respect to the central ferromagnetic strip (the axis of symmetry) were taken into account.

Calculations of the vertical and horizontal forces of interaction of the MSTV system shown in Fig. 2 (a) were performed considering only the first images of the faces of the magnets relative to the central ferromagnetic strip (the axis of symmetry). The effect of subsequent images is negligible.

As an example, the expression for the vertical force f_V, calculated for the case of interaction of two-row systems (Fig. 2 (a) or Fig. 4) is given below:

$$f_V = 2f(z,\delta) - 4f(z,\delta+2h) + 2f(z,\delta+4h) -$$

$$-2f(z,3\delta+4h) - f(a+c+z,\delta) +$$

$$+2f(a+c+z,\delta+2h) - f(a+c+z,\delta+4h) -$$

$$-f(a+c-z,3\delta+4h) + f(a+c-z,\delta) - \qquad (11)$$

$$-2f(a+c-z,\delta+2h) + f(a+c-z,\delta+4h) +$$

$$+f(a+c+z,3\delta+4h).$$
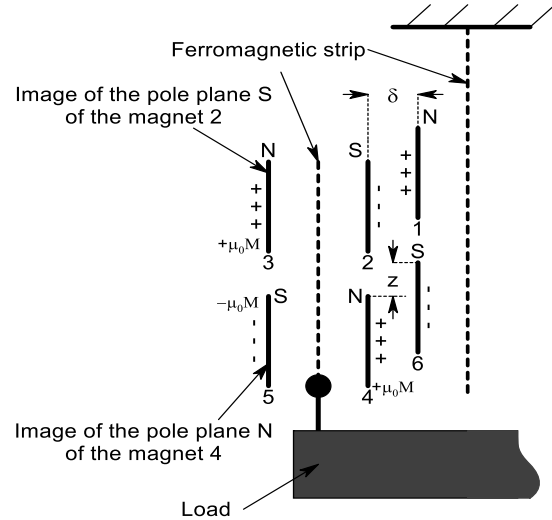
Fig. 4. Calculation scheme (corresponding to left side of Fig. 2 (a).

To quantify the quality of the scheme, we consider only the left-hand side of the support, i.e., asymmetrical support Fig. 5.
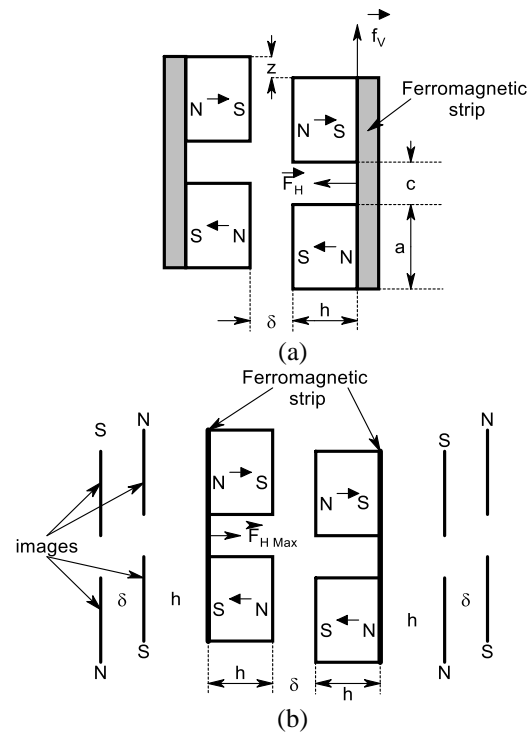

Fig. 5. (a) The support (or suspension) scheme, and (b) the calculation scheme.

The results of calculations f_V, f_H and μ_{eff} for

$a = 0.021m$, $h = 0.014m$, $M = 230A/m$ are given in the following Table 1. Figure 6 shows the dependencies $f_V(z)$ H $f_H(z)$.

Table 1: Calculation results

| δ, mm	z, mm	$f_V, N/m$	$f_H, N/m$	μ_{eff}
6	0	0	237	0
	5.0	138	200	9.1
	10.0	208	113	15.3
	15.0	239	0	17.6
	20.0	213	-107	15.7
10	0	0	167	0
	5.0	82	145	6.04
	10.0	141	88	10.4
	15.0	165	14	12.2
	20.0	153	-59	11.3
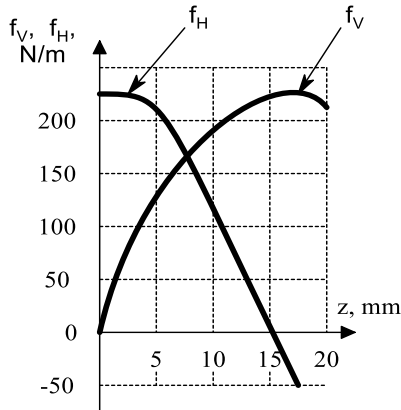
Fig. 6. Dependencies of the vertical and horizontal forces from vertical displacement at $\delta = 6mm$.

IV. CONCLUSION

The vertical and horizontal forces of interaction between permanent magnets in a magnetic support system of vertical type (MSVT) have been investigated. The main results of the investigations are briefly summarized below.

1. The systems of magnetic support (magnetic suspension) of vertical type with permanent magnets MSVT-1 (Fig. 2 (a) and MSVT-2 (Fig. 2 (b)) considered here, seem to be a very promising direction for their creating. They can be realized with relatively small gaps ($\delta = 5 \div 7mm$ or less) and therefore allow to achieve high values of effectiveness factor μ_{eff}.

2. The analysis of the obtained data for the MSVT-1 and MSVT-2 indicates that the investigated magnetic suspension systems outperform the classic horizontal system MSHT, (Fig. 1 (a)).

3. The ratio $\gamma = f_V / f_H$ increases with increasing

z (vertical displacement of the movable part of the support) indicating a reduction of the instability of the support system in the horizontal plane.

4. When the lateral force is close to 0, the vertical force (for the size of the magnetic system shown in the table) increases to hundreds of units, reaching its maximum (Fig. 6); which is an undoubted advantage of MSVT, since the requirements for a stabilizing system (roller, electromagnetic or electrodynamic) are substantially less stringent. This is also true for other correctly chosen sizes of the magnetic system.

REFERENCES

[1] W. Baran, "Berechnung von anziehungs-und haftkraften fur magnet emit reinpolteilung," *Techn. Mitt. Krupp Forsch. - Ber*, vol. 21, p. 7283, 1963.

[2] E. Frishman, "A stepped magnetic suspension system (SMSS)," *The Applied Computational Electromagnetics Society Journal*, vol. 32, no. 8, pp. 731-735, Aug. 2017.

[3] F. Di Puccio, R. Bassani, E. Ciulli, A. Musolino, and R. Rizzo, "Permanent magnet bearings: Analysis of plane and axisymmetric V-shaped element design," *Prog. Electromagn. Res. M*, vol. 26, pp. 205-223, 2012.

[4] M. Van Beneden, V. Kluyskens, and B. Dehez, "Optimal sizing and comparison of permanent magnet thrust bearings," *IEEE Trans. on Mag.*, vol. 53, no. 2, Feb. 2017.

[5] E. Diez-Jimenez, R. Sanchez-Montero, and M. Martinez-Muñoz, "Towards miniaturization of magnetic gears: Torque performance assessment," *Micromachines*, vol. 9, no. 16, 2018. doi:10.3390/mi9010016.

[6] A. Iskanderov, "Magnetic suspension for a vehicle," Patent number: 4711182, 1987.

[7] A. Musolino, M. Raugi, R. Rizzo, and E. Tripodi, "Stabilization of a permanent-magnet MAGLEV system via null-flux coils," *IEEE Trans. on Plasma Sci.*, vol. 43, no. 5, pp. 1242-1247, 2015.

[8] F. Di Puccio, A. Musolino, R. Rizzo, and E. Tripodi, "A self-controlled maglev system," *Prog. In Electromagn. Res. M*, vol. 26, pp. 187-203, 2012.

[9] K. D. Bachovchin, J. F. Hoburg, and R. F. Post, "Stable levitation of a passive magnetic bearing," *IEEE Trans. on Mag.*, vol. 49 no. 1 pp. 609-617, 2013.

[10] A. Musolino, R. Rizzo, L. Sani, and E. Tripodi, "Null-flux coils in permanent magnets bearings," *IEEE Trans on Plasma Sci.*, vol. 45, no. 7, pp. 1545-1552, 2017.

[11] V. Di Dio and L. Sani, "Coupled electromechanical analysis of a permanent-magnet bearing," *The Applied Computational Electromagnetics Society Journal*, vol. 32, no. 8, pp. 736-741, Aug. 2017.

Analysis and Experimental Study on Uncertain Fault of Active Magnetic Bearing Displacement Sensor

Yangbo Zheng [1,2,3], Xingnan Liu [1,2,3], Guojun Yang [1,2,3], Haoyu Zuo [1,2,3], Zhe Sun [1,2,3], and Zhengang Shi [1,2,3,*]

[1] Institute of Nuclear and New Energy Technology of Tsinghua University, Beijing, China, 100084
[2] Collaborative Innovation Center of Advanced Nuclear Energy Technology
[3] The Key Laboratory of Advanced Reactor Engineering and Safety, Ministry of Education
zhengyb17@mails.tsinghua.edu.cn, liuxinnan@tsinghua.edu.cn, yanggj@tsinghua.edu.cn,
zuohy16@mails.tsinghua.edu.cn, sun_zhe@tsinghua.edu.cn, *shizg@tsinghua.edu.cn

Abstract — Active magnetic bearing (AMB) has been gradually applied to high speed rotating equipment to suspend rotor as it has many advantages, but some uncertain faults always appeal in the process of application. Meanwhile, displacement sensor is a key equipment of AMB control system, but when it is used in high speed atomizer, some uncertain problems are happened, such as expected range cannot be adjusted, and data characteristics cannot match well in the X-Y direction. In view of these problems, we gather electrical parameters in different frequencies, and establish the corresponding equivalent circuit models, to analyze the reasons of uncertain faults. Then we propose the high frequency electrical parameters characteristic analysis method to realize reliable judgment and reveal the essence of uncertain faults. Finally, comparative experiments are carried to verify the analysis methods, the results show that the electrical parameters of fault characteristic analysis method established for uncertain faults of displacement sensor has good theoretical and practical value.

Index Terms — AMB, data characteristic, displacement sensor, uncertain fault.

I. INTRODUCTION

As the greatest potential and high-efficiency bearing, AMB has lots of advantages, such as contactless, no need of lubrication, no wear, low noise, and can reach very high rotation speed [1], so it has important application values in the field of rotary machinery and equipment. The closed loop control system is essential to stably suspend the rotor because AMB is an open loop unstable system. Therefore, the reliability of control system is a basic guarantee for the system operation. High precision displacement sensor is one of the key components of system, but it is always influenced by uncertain factors that exist in some abnormal states in the process of design, manufacture, commissioning and operation.

Such as expected range cannot be adjusted, and data characteristics cannot match well in the X-Y direction, which would bring huge risk to AMB. So these uncertain faults must be effectively solved in the actual application.

Meanwhile, the study on fault diagnosis of AMB displacement sensor is very important as it is applied to the industrial area, and some great research results are obtained [2-4]. Article [3] proposed an on-line diagnosis scheme for sensor faults in an active magnetic bearing system equipped with built-in force transducers. Article [4] introduced wavelet transform to fault diagnosis of redundant displacement sensor for AMB. However, these diagnosis methods are only suitable to the deterministic faults, but cannot be used to solve uncertain faults.

Therefore, aiming to solve uncertain faults of atomizer AMB displacement sensor, different frequency equivalent circuit models are built, and data characteristics of high frequency electrical parameter are analyzed, which would be used to diagnose some uncertain faults of displacement sensor. Apparently, this research work is innovative and pioneering to the study and diagnose of the uncertain fault of the AMB displacement sensor.

II. AMB APPLIED IN ATOMIZER

There are many factories that require tail gas treatment, for example, the desulphurization and denitrification of tail gas in thermal power plants, the absorbent is usually atomized in order to achieve better purification. The principle of atomizer described in this article is to atomize the absorbent by virtue of the centrifugal force, which is generated via the high speed motor, as shown in Fig. 1.

As centrifugal force is the basis of the atomizer, so the design speed of the atomizer is usually very high, basically reaching more than 10000r/min. However, the traditional rolling bearing is easily damaged at high speed and cannot meet the application requirements. Therefore, AMB is the best technical choice for rotor levitation in such high speed device. From the perspective of the

atomizer structure as shown in Fig. 1, the rotor is vertical layout, therefore, the axial AMB should produce force to balance the gravity of the rotor and atomization wheel, and the corresponding AMB structure is shown in Fig. 2.



Fig. 1. High speed atomizer.
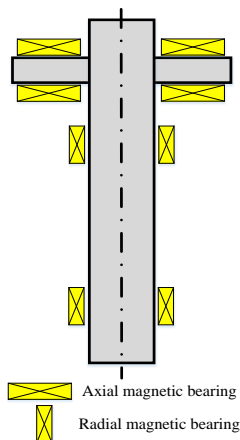
Fig. 2. The AMB structure of atomizer.

III. UNCERTAIN FAULTS DESCRIPTION OF AMB IN ATOMIZER

Displacement sensor commissioning is the basic work for AMB control system. According to the atomizer control demand, five degrees of freedom need to install the displacement sensors [1]. Actually, in order to reduce the nonlinear error, we usually adopt the differential transformer type displacement sensor, and the structure is shown in Fig. 3.

In the process of commissioning, we found a series of uncertain faults, such as the expected range cannot be adjusted in the Y direction in the bottom of AMB displacement sensor, and X-Y direction data characteristic cannot match well within the same sensor, here we refer to the radial magnetic bearing.

In fact, uncertain fault refers to a kind of unpredictable fault which has the characteristics of randomness, fuzziness and greyness, and the evolution mechanism is not clear and occurrence process is gradual. The diagnosis of uncertain faults often needs field expert

experience, but recent years, random mathematics [5], fuzzy theory [6], and mathematical methods (such as grey theory [7] and evidence theory), have been introduced to the study of uncertain problems to predict failures.
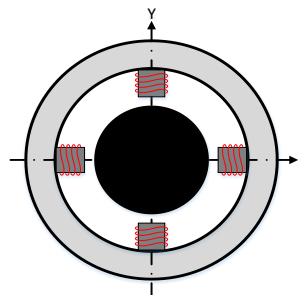

Fig. 3. The structure of differential transformer type displacement sensor used in AMB.

In this paper, uncertain faults happened in AMB displacement sensor of the atomizer are described as:

1) Even if the circuit amplification factor is adjusted in the whole range, Y direction cannot achieve the target range.

2) In the same frequency, the electrical parameters of the inductor coil cannot match well between X and Y direction.

Unlike conventional deterministic faults, uncertain faults have the characteristics of progressive and latent. Thus, traditional fault analysis methods have been unable to solve the uncertain problems. Otherwise, if uncertain faults are not properly confirmed and solved scientifically, it would bring great safety risk to the operation of the AMB system.

IV. ANALYSIS ON THE UNCERTAIN FAULT MECHNISM OF DISPLACEMENT SENSOR

A. Equivalent circuit model of winding

In order to solve the above problems of AMB displacement sensor, it is necessary to analyze the equivalent circuit model and electrical parameter characteristics. A single pole inductor is shown in Fig. 4. In addition to inductance L, it is usually accompanied by loss resistance R_L and distributed capacitance C_L. C_L usually has little impact on circuit in DC or low frequency state, but it cannot be ignored in high frequency state. So according to the working frequency of the circuit, a single pole inductor has three equivalent circuit models, which are described as below.
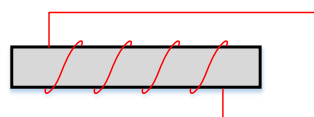

Fig. 4. A single pole inductor.

B. DC steady state equivalent circuit model of single pole inductor winding

When an inductor winding is connected to the DC circuit that reaches a steady state, the winding can be regarded as an ideal resistance R_L. The corresponding equivalent circuit model is shown in Fig. 5, and the equivalent impedance is expressed as (1):

$$Z_e = R_L. \tag{1}$$
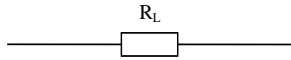
Fig. 5. DC steady state equivalent circuit model.

C. Low frequency equivalent circuit model of single pole inductor winding

When an inductance winding is connected into low frequency AC circuits, the winding can be regarded as an ideal resistance R_L in series with an inductance L. The corresponding equivalent circuit model is shown in Fig. 6, and the equivalent impedance is expressed as (2):

$$Z_e = R_L + j\omega L. \tag{2}$$

Fig. 6. Low frequency equivalent circuit model.

D. High frequency equivalent circuit model of single pole inductor winding

When an inductance winding is connected into high frequency AC circuits, in addition to an ideal resistance R_L in series with an inductance L, there exists a distributed capacitance C_L. Especially when the winding has turn-to-turn short circuit, the distributed capacitance effect would be much more serious. The corresponding equivalent circuit model is shown in Fig. 7 and the equivalent impedance is expressed as (3):

$$Z_e = \frac{(R_L + j\omega L)\frac{1}{j\omega C_L}}{R_L + j\omega L + \frac{1}{j\omega C_L}}$$

$$= \frac{R_L}{(1-\omega^2 LC_L)^2 + (\omega C_L R_L)^2} + j\omega \frac{L(1-\omega^2 LC_L) - R_L^2 C_L}{(1-\omega^2 LC_L)^2 + (\omega C_L R_L)^2}. \tag{3}$$
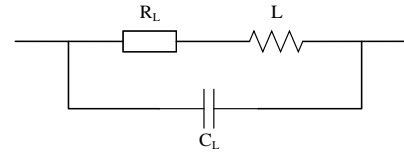
Fig. 7. High frequency equivalent circuit model.

In (1) (2) (3), $\omega = 2\pi f$. Where, f is the working frequency of circuit. Here (1) (2) (3) can be written as the standard formula of reactance, as shown in (4):

$$Z_e = R_e + jX_e. \tag{4}$$

Therefore, Quality Factor (Q) of the circuit is calculated as (5):

$$Q = \frac{X_e}{R_e}. \tag{5}$$

Q is an important parameter to measure inductance components, which is the ratio of reactance (X_e) to equivalent loss resistance (R_e) refer to the AC at a particular frequency. Certainly, Q is influenced by the winding DC resistance, skeleton, dielectric loss, and the core material. But in the same AMB displacement sensor, all poles have the same inductor winding, so the data characteristic of all electrical parameters are basically consistent.

E. Analysis of winding electrical parameter

According to field expert experience, electrical parameters of the displacement sensor installed in the atomizer are measured via handheld LCR meter and analyzed in 0.1 kHz, 1 kHz, 10 kHz and 100 kHz. Here we mainly analyzed inductance L, quality factor Q, DC resistance DCR and equivalent reactance $Z_e = R_e + jX_e$ in four directions, the results are shown in Table 1, Fig. 8, Fig. 9, Fig. 10 and Fig. 11.

Table 1: Electrical parameters of displacement sensor used in atomizer

Frequency	0.1 kHz					1 kHz				
Parameters	$R_e(\Omega)$	L(mH)	$X_e(\Omega)$	Q	DCR(Ω)	$R_e(\Omega)$	L(mH)	$X_e(\Omega)$	Q	DCR(Ω)
X+	2.106	0.811	0.510	0.242	2.103	2.169	0.809	5.083	2.343	2.102
X-	2.094	0.790	0.496	0.237	2.086	2.148	0.788	4.951	2.305	2.083
Y+	2.064	0.782	0.491	0.238	2.061	2.126	0.781	4.907	2.308	2.060
Y-	2.108	0.738	0.464	0.220	2.106	*2.598*	*0.727*	*4.568*	*1.758*	2.105
Frequency	10 kHz					100 kHz				
Parameters	$R_e(\Omega)$	L(mH)	$X_e(\Omega)$	Q	DCR(Ω)	$R_e(\Omega)$	L(mH)	$X_e(\Omega)$	Q	DCR(Ω)
X+	6.080	0.783	49.197	8.092	2.101	112.727	0.603	378.876	3.361	2.100
X-	5.892	0.763	47.941	8.136	2.082	109.152	0.591	371.336	3.402	2.081
Y+	5.833	0.757	47.564	8.154	2.058	109.608	0.583	366.309	3.342	2.060
Y-	*20.981*	*0.377*	*23.688*	*1.129*	2.103	*98.786*	*0.197*	*123.779*	*1.253*	2.102

**Note:** the abnormal data is marked with bold italic and underscore, such as *2.598*.
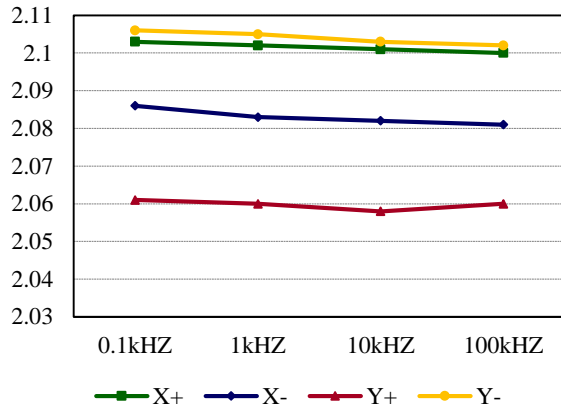
Fig. 8. DCR (Ω) comparison diagram.

It can be seen from Fig. 8 that the DC steady state resistances DCR of the four poles are basically the same, which indicates that the windings have no open circuit fault.
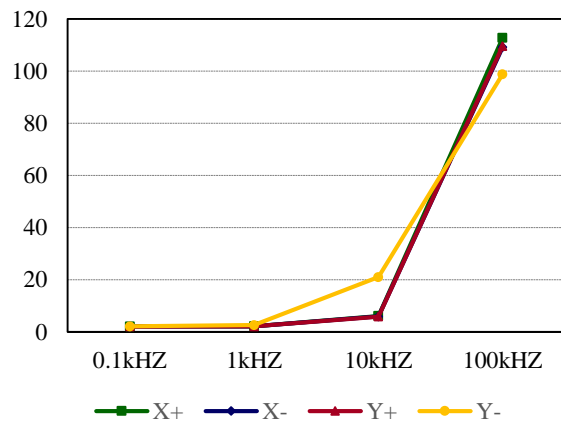

Fig. 9. R_e (Ω) comparison diagram.
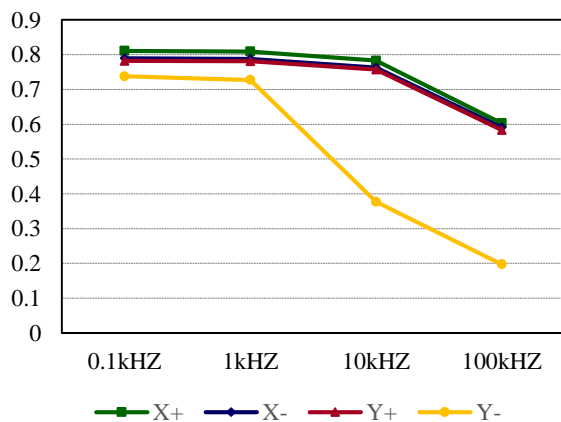
Fig. 10. L (mH) comparison diagram.
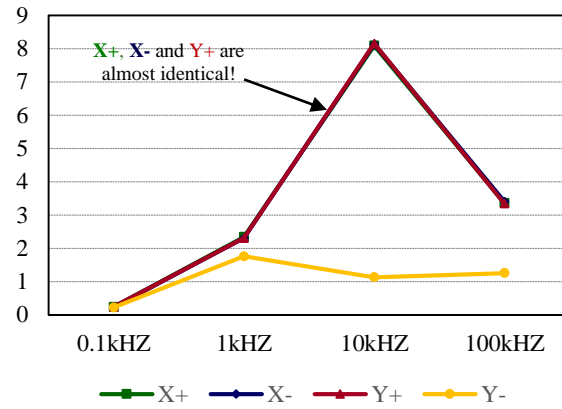
Fig. 11. Q comparison diagram.

Figure 9 and Fig. 10 indicate that in the low frequency, equivalent resistance R_e and inductance L of the four poles are not very different with each other. But as the frequency increases, the gaps between Y-direction and the other three directions is increasing rapidly, which means it exists abnormal condition. When the inductance L and the distributed capacitance C_L of the circuit meet certain conditions, the circuit will resonate. And the resonant frequency f_0 can be obtained by setting the imaginary part of equation (3) to zero, as shown in (6) and (7):

$$L(1 - \omega_0{}^2 LC_L) - R_L{}^2 C_L = 0, \qquad (6)$$

$$f_0 = \frac{\omega_0}{2\pi} . \qquad (7)$$

When the working frequency of the circuit f is greater than f_0, the inductance L will be significantly less, so the corresponding Q also decreases sharply, as shown in Fig. 11. According to Fig. 7 and equation (3), we can found that the higher the frequency of the circuit (f), the smaller the equivalent inductive reactance (X_e), which is because the greater the distributed capacitance (C_L).

Combined with the circuit theory [8] and the above analysis, as the frequency increases, the Y-direction in the equivalent resistance (Re), equivalent inductance (L) and quality factor (Q) do not match with the other three poles. And the main reason is that the Y-inductor has a larger capacitance (C_L), which eventually leads to the range cannot be adjusted to expected goal. Although the actual inductor winding will not work in high frequency, analysis on characteristics of high frequency electrical parameters can provide a very useful way to solve this kind of uncertain faults.

V. EXPERIMENTAL STUDY ON UNCERTAIN FAULT OF DISPLACEMENT SENSOR

A. Experimental design and data analysis

In order to further verify the conclusion of uncertain

faults analysis on AMB displacement sensor. Firstly, we rebuilt two fully functional displacement sensors for comparative analysis, then we intentionally damaged the insulation layer of X+ direction winding of one displacement sensor and marked it as A, another one was marked B that maintained functional integrity.

In accordance with Table 1, we used the same methods to test and analyze the same electrical parameters of A and B, the results are shown in Table 2 and Table 3.

Table 2: Electrical parameters of displacement sensor A

Frequency	0.1 kHz					1 kHz				
Parameters	$R_e(\Omega)$	L(mH)	$X_e(\Omega)$	Q	DCR(Ω)	$R_e(\Omega)$	L(mH)	$X_e(\Omega)$	Q	DCR(Ω)
X+	2.391	0.799	0.502	0.210	2.388	***4.248***	***0.697***	***4.397***	***1.031***	2.388
X-	2.269	0.791	0.497	0.219	2.265	2.342	0.789	4.957	2.117	2.264
Y+	2.294	0.814	0.511	0.223	2.287	2.367	0.811	5.096	2.153	2.289
Y-	2.392	0.788	0.495	0.207	2.394	2.468	0.786	4.939	2.001	2.393
Frequency	10 kHz					100 kHz				
Parameters	$R_e(\Omega)$	L(mH)	$X_e(\Omega)$	Q	DCR(Ω)	$R_e(\Omega)$	L(mH)	$X_e(\Omega)$	Q	DCR(Ω)
X+	***24.074***	***0.382***	***24.002***	***0.997***	2.388	***83.114***	***0.159***	***99.903***	***1.202***	2.388
X-	6.554	0.758	47.627	7.267	2.264	117.191	0.592	371.964	3.174	2.264
Y+	6.809	0.777	48.820	7.170	2.287	119.286	0.606	380.761	3.192	2.286
Y-	6.725	0.754	47.375	7.045	2.392	116.795	0.590	370.708	3.174	2.392

Note: the abnormal data is marked with bold italic and underscore, such as ***4.248***.

Table 3: Electrical parameters of displacement sensor B

Frequency	0.1 kHz					1 kHz				
Parameters	$R_e(\Omega)$	L(mH)	$X_e(\Omega)$	Q	DCR(Ω)	$R_e(\Omega)$	L(mH)	$X_e(\Omega)$	Q	DCR(Ω)
X+	2.355	0.802	0.504	0.214	2.350	2.429	0.800	5.027	2.069	2.349
X-	2.237	0.794	0.499	0.223	2.232	2.310	0.792	4.976	2.154	2.232
Y+	2.279	0.816	0.513	0.225	2.268	2.348	0.814	5.115	2.178	2.268
Y-	2.367	0.791	0.497	0.210	2.355	2.434	0.789	4.957	2.037	2.355
Frequency	10 kHz					100 kHz				
Parameters	$R_e(\Omega)$	L(mH)	$X_e(\Omega)$	Q	DCR(Ω)	$R_e(\Omega)$	L(mH)	$X_e(\Omega)$	Q	DCR(Ω)
X+	6.764	0.766	48.129	7.115	2.350	119.784	0.603	378.876	3.163	2.347
X-	6.562	0.760	47.752	7.277	2.232	118.520	0.594	373.221	3.149	2.232
Y+	6.818	0.779	48.946	7.179	2.266	120.556	0.609	382.646	3.174	2.265
Y-	6.723	0.756	47.500	7.065	2.355	118.347	0.592	371.965	3.143	2.353

Table 2 indicates that the electrical parameters of A cannot keep the consistency. The reason is that C_L of X+ direction impacts on the circuit is much greater than other poles, and much more serious in high frequency. The experimental results is consistent with characteristic of atomizer.

Table 3 indicates that the electrical parameters of B can keep the consistency as B is a fully functional displacement sensor.

Therefore, insulation layer damaged in inductor winding would lead the C_L is much greater, which results in the electrical parameters be inconsistent, and other uncertain problems.

B. Commissioning and operation analysis

After individual testing and analyzing of A and B, we installed A and B to the atomizer respectively, and found that only B can meet the requirements of the atomizer, and operational state as shown in Fig. 12.

Conversely, A failed to achieve the intended range adjustment problems. The results indicate that the two uncertain faults described in part III have intrinsic relevance, and the essential reason is that excessive distributed capacitance exists between inductance windings.
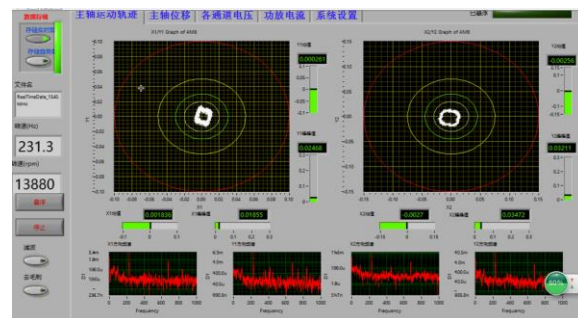

Fig. 12. Operational state of the atomizer.

VI. CONCLUSION

Uncertain faults are common problems of the AMB displacement sensor. Due to latent and progressive characteristics, uncertain faults are often difficult to be found in normal condition, and it may lay hidden danger to the safe and stable operation of the AMB. Based on AMB used in atomizer, combining with the expert experience and electrical parameters characteristic analysis technology, this article reveals the fundamental reasons of two uncertain faults of displacement sensor, and solves the problem of uncertain fault in actual application. In addition, the analyze method based on the characteristics of high frequency electrical parameter for inductive displacement sensor proposed in this article provides a new solution and diagnosis method to solve this kind of uncertain faults in AMB. Furthermore, the experimental results show that the method has certain theoretical and practical value.

ACKNOWLEDGMENT

REFERENCES

[1] G. Schweitzer and E. H. Maslen, *Magnetic Bearings: Theory Design and Application to Rotating Machinery*. Springer-Verlag Berlin Heidelberg, 2009.

[2] F. L. Osch, "Detection and correction of actuator and senor faults in active magnetic bearing systems," *The 8ᵗʰ International Symposium on Magnetic Bearing, Mito*, Japan, 2002.

[3] S. J. Kim and C. W. Lee, "Diagnosis of sensor faults in active magnetic bearing system equipped with built-in force transducers," *IEEE ASME Transactions on Mechatronics*, vol. 4, pp. 180-186, July 1999.

[4] H. Jun, H. Yefa, C. Xin, S. Shao, and C. Qiang, "Fault diagnosis of redundant displacement sensor for magnetic bearings based on wavelet transform," *Manufacturing Automation*, vol. 39, pp. 79-83, 2017.

[5] A. Pelc, "Optimal diagnosis of heterogeneous systems with random faults," *IEEE Transactions on Computers*, vol. 47, pp. 298-304, Mar. 1998.

[6] I. H. Brahim and D. Mehdi, "Robust fault detection for uncertain T-S fuzzy system with unmeasurable premise variables: Descriptor approach," *International Journal of Fuzzy Systems*, vol. 20, pp. 416-425, Feb. 2018.

[7] A. Chatterjee and N. K. Roy, "Applying grey theory prediction model on the DGA data of the transformer oil and using it for fault diagnosis," *WSEAS Transactions on Power Systems*, vol. 4, pp. 43-52, Feb. 2009.

[8] J. Bird, *Electrical Circuit Theory and Technology*. The 2nd Edition , 2003.

Yangbo Zheng is now a Ph.D. candidate at Institute of Nuclear and New Energy Technology, Tsinghua University, Beijing, China. Zheng's research subject is active magnetic bearing control technology.

Zhengang Shi received his Ph.D. in Nuclear Science & Technology at Tsinghua University in 2003. He is now working at Institute of Nuclear and New Energy Technology, Tsinghua University, Beijing, China. As the header of magnetic bearing laboratory, Shi's research subject is magnetic bearing technology.